ADVANCED NANOMATERIALS FOR SENSING APPLICATIONS

EDITED BY: Zhongchang Wang, Wen Zeng and Zhenyu Li
PUBLISHED IN: Frontiers in Chemistry

frontiers Research Topics

ISSN 1664-8714
ISBN 978-2-88963-123-0
DOI 10.3389/978-2-88963-123-0

About Frontiers

Frontiers is more than just an open-access publisher of scholarly articles: it is a pioneering approach to the world of academia, radically improving the way scholarly research is managed. The grand vision of Frontiers is a world where all people have an equal opportunity to seek, share and generate knowledge. Frontiers provides immediate and permanent online open access to all its publications, but this alone is not enough to realize our grand goals.

Frontiers Journal Series

The Frontiers Journal Series is a multi-tier and interdisciplinary set of open-access, online journals, promising a paradigm shift from the current review, selection and dissemination processes in academic publishing. All Frontiers journals are driven by researchers for researchers; therefore, they constitute a service to the scholarly community. At the same time, the Frontiers Journal Series operates on a revolutionary invention, the tiered publishing system, initially addressing specific communities of scholars, and gradually climbing up to broader public understanding, thus serving the interests of the lay society, too.

Dedication to Quality

Each Frontiers article is a landmark of the highest quality, thanks to genuinely collaborative interactions between authors and review editors, who include some of the world's best academicians. Research must be certified by peers before entering a stream of knowledge that may eventually reach the public - and shape society; therefore, Frontiers only applies the most rigorous and unbiased reviews.
Frontiers revolutionizes research publishing by freely delivering the most outstanding research, evaluated with no bias from both the academic and social point of view. By applying the most advanced information technologies, Frontiers is catapulting scholarly publishing into a new generation.

What are Frontiers Research Topics?

Frontiers Research Topics are very popular trademarks of the Frontiers Journals Series: they are collections of at least ten articles, all centered on a particular subject. With their unique mix of varied contributions from Original Research to Review Articles, Frontiers Research Topics unify the most influential researchers, the latest key findings and historical advances in a hot research area! Find out more on how to host your own Frontiers Research Topic or contribute to one as an author by contacting the Frontiers Editorial Office: researchtopics@frontiersin.org

ADVANCED NANOMATERIALS FOR SENSING APPLICATIONS

Topic Editors:
Zhongchang Wang, International Iberian Nanotechnology Laboratory (INL), Portugal
Wen Zeng, Chongqing University, China
Zhenyu Li, Southwest Petroleum University, China

Citation: Wang, Z., Zeng, W., Li, Z., eds. (2019). Advanced Nanomaterials for Sensing Applications. Lausanne: Frontiers Media. doi: 10.3389/978-2-88963-123-0

Table of Contents

frontiers in Chemistry

ORIGINAL RESEARCH
published: 17 December 2018
doi: 10.3389/fchem.2018.00628

One-Dimensional Zinc Oxide Decorated Cobalt Oxide Nanospheres for Enhanced Gas-Sensing Properties

Hang Zhou, Keng Xu, Yong Yang, Ting Yu, Cailei Yuan*, Wenyan Wei, Yue Sun and Wenhui Lu*

Jiangxi Key Laboratory of Nanomaterials and Sensors, Jiangxi Normal University, Nanchang, China

In this study, one-dimensional (1D) zinc oxide was loaded on the surface of cobalt oxide microspheres, which were assembled by single-crystalline porous nanosheets, via a simple heteroepitaxial growth process. This elaborate structure possessed an excellent transducer function from the single-crystalline feature of Co_3O_4 nanosheets and the receptor function from the zinc oxide nanorods. The structure of the as-prepared hybrid was confirmed via a Scanning Electron Microscope (SEM), X-ray diffraction (XRD), and a Transmission Electron Microscope (TEM). Gas-sensing tests showed that the gas-sensing properties of the as-designed hybrid were largely improved. The response was about 161 (R_a/R_g) to 100 ppm ethanol, which is 110 and 10 times higher than that of Co_3O_4 ($R_g/R_a = 1.47$) and ZnO ($R_a/R_g = 15$), respectively. And the as-designed ZnO/Co_3O_4 hybrid also showed a high selectivity to ethanol. The superior gas-sensing properties were mainly attributed to the as-designed nanostructures that contained a super transducer function and a super receptor function. The design strategy for gas-sensing materials in this work shed a new light on the exploration of high-performance gas sensors.

Keywords: gas sensing, transducer function, receptor function, ethanol detection, single-crystalline

OPEN ACCESS

Edited by:
Wen Zeng,
Chongqing University, China

Reviewed by:
Yan Wang,
Henan Polytechnic University, China
Ming Ying Xu,
Heilongjiang University, China
Shunping Zhang,
Huazhong University of Science and Technology, China

****Correspondence:***
Keng Xu
xukeng@163.com
Cailei Yuan
clyuan@jxnu.edu.cn

Specialty section:
This article was submitted to Nanoscience, a section of the journal Frontiers in Chemistry

Received: *10 October 2018*
Accepted: *03 December 2018*
Published: *17 December 2018*

Citation:
Zhou H, Xu K, Yang Y, Yu T, Yuan C, Wei W, Sun Y and Lu W (2018) One-Dimensional Zinc Oxide Decorated Cobalt Oxide Nanospheres for Enhanced Gas-Sensing Properties. Front. Chem. 6:628. doi: 10.3389/fchem.2018.00628

INTRODUCTION

Metal oxides, as a type of predominant gas sensing material, have provoked considerable attention because of their low cost, excellent electrical properties and controllable preparation (Korotcenkov, 2007; Li et al., 2016; Dong et al., 2018). It is well accepted that the gas-sensing processes of metal oxides, contain not only gas diffusion and gas reaction on its surface, but also signal transformation that transforms the surficial chemical signal into an electrical resistance variation (Rai et al., 2013). In this regard, gas-sensing performances of metal oxides depend largely on the structure factors of sensing materials such as surface area, morphology, as well as signal transmission channels (Zhu et al., 2018). Nowadays, many studies have reported that the gas-sensing properties of metal oxides can be improved by the creation of heterojunctions, which can provide tunable morphologies and compositions (Miller et al., 2014; Cao et al., 2017; Gong et al., 2018). For example, the In_2O_3/Co_3O_4 composites synthesized by Mirzaei et al., exhibited superior gas-sensing performances than pristine In_2O_3 did (Mirzaei et al., 2017). However, up to now, most related studies have been based on mechanical mixed composites or inhomogeneous structures, resulting in randomly distributed

heterojunctions. In particular, the gas-sensing processes of composites that contain gas diffusion, gas reaction, and signal transformation still need to be further improved.

In this paper, ZnO nanorods anchored on the surface of Co_3O_4 nanospheres were synthesized by an epitaxial growth method. ZnO and Co_3O_4 have been widely investigated in the field of gas-sensing application, because of their chemical and physical stability and abundance in raw materials (Tan et al., 2017; Zhu and Zeng, 2017). We chose the ZnO nanorods and Co_3O_4 microspheres because of their large surface area for gas reaction and because of the effective accesses for gas diffusion (Park et al., 2016). Moreover, the Co_3O_4 nanospheres consisted of single-crystalline porous nanosheets which provided effective electrical pathways for charge-carrier transfer and was more beneficial to the signal transformation process (Singh et al., 2011; Zhang et al., 2015). Therefore, these ZnO nanorods acted as "trigger hairs," while Co_3O_4 microspheres acted as "channels." And the p-n heterojunctions between ZnO and Co_3O_4 also led to an extended depletion region and a high initial resistance, which is more beneficial for the transducer function (Li et al., 2015).

EXPERIMENT

Synthesis of ZnO/Co_3O_4 Hybrid

All the chemical reagents were purchased from Sinopharm Chemical Reagent and used without further purification. During the synthesis processes (Xu et al., 2017), a mixed solution (80 ml) composed of distilled water and ethylene glycol (1: 79) was added at 0.05 g PVP, as well as 1 g cobalt acetate. The mixed solution was then stirred and poured into a Teflon-lined stainless-steel autoclave (100 mL). The resulting precipitate was collected and washed repeatedly at least seven times and thereafter maintained at 180°C for 12 h. The final powder was then annealed at 350°C for 2 h in air atmosphere. To prepare the ZnO/Co_3O_4 hybrid, 0.03g as-prepared Co_3O_4 and 0.32 g zinc acetate dehydrate was added in methanol through the assistance of ultrasonication. A KOH methanol solution (60 ml) was then also added to the above mixture. After 2 h of stirring, the mixture was centrifuged at 3,000 rpm and washed several times. The powder obtained, was then was added into a mixed solution composed of $Zn(NO_3)_2$ (0.89 g) and HMT (0.42 mol/L) by vigorous stirring. The final as-designed hybrid was obtained after being refluxed at 95 °C for 6 h.

Sensor Fabrication and Measurements

To fabricate a gas sensor, a certain number of as-prepared samples were uniformly dispersed in ethanol, by ultrasonication for 15 min, to form a suspension. The suspension was then coated onto a ceramic flat, which had been coated with Pt interdigitated electrodes and a Pt heat element (about 500 μm). The obtained film was sintered at 500°C for 2 h and aged at 300°C for 3 days in air atmosphere. Gas-sensing performances were measured in a static testing instrument which was purchased from Wuhan Hua Chuang Rui Ke Co. Ltd. This equipment includes a test chamber (about 30 L in volume) and a personal computer. During the gas-sensing tests, the target gases were introduced into the test chamber by injecting their corresponding liquid, with a calculated amount, which was then vaporized by a heater. The desired concentrations of the testing gases are calculated by the following formula:

$$Q = \frac{V \times \varphi \times M}{22.4 \times d \times \rho} \times 10^{-9} \times \frac{273 + T_R}{273 + T_B}$$

where Q (ml) is the liquid volume of the volatile compound, V (ml) is the volume of the testing chamber, ϕ is the required gas volume fraction, M (g. mol^{-1}) is the molecular weight, d (g. cm^{-3}) is the specific gravity, and ρ is the purity of the volatile testing liquid, T_R and T_B (°C) are the temperatures at ambient and the test chamber, respectively. For example, the liquid volume of ethanol is calculated at about 13.05 μL that corresponds to 100 ppm. Two electric fans installed in the chamber were used to make the test gas homogeneous. After a few minutes, the chamber was lifted to introduce ambient air (humidity: 16∼22%). In the meantime, the resistances of the sensors were recorded by a personal computer.

RESULTS AND DISCUSSION

The crystalline phases of as-prepared samples were characterized by XRD (**Figure 1A**). As can be seen, beside the peaks that belong to Co_3O_4 (JCPDS No. 42-1467), all the diffraction peaks left in the pattern of hybrids can be indexed to the reflections of ZnO (JCPDS No. 36–1451).The morphology of Co_3O_4 is shown in the **Figures 1B,C**. It is seen that the Co_3O_4 is composed of numerous uniform microspheres with a diameter of 2–4 μm. These microspheres are composed of many crossed 2D nanosheets with numerous pores, as shown in the enlarged images (**Figure 1C**). It is worth mentioning that the individual nanosheets containing numerous pores are single crystals, since each nanosheet consisted of coherent lattice fringes regardless of the pore in the inset of **Figure 1C**. The single crystal can provide effective electrical pathways for charges, which benefits the gas-sensing performances (Meng et al., 2015). Accordingly, the morphology of ZnO/Co_3O_4 was also characterized (**Figures 1D–F**). **Figure 1D** reveals that the ZnO/Co_3O_4 hybrids were also composed of numerous microspheres. However, its diameter was much larger than that of pristine Co_3O_4. The enlarged images (**Figures 1E,F**) reveal a hedgehog-like structure of ZnO/Co_3O_4 where ZnO nanorods were formed on the surface of Co_3O_4 as trigger hairs. The ZnO/Co_3O_4 hybrids were further characterized through EDS (**Figure S1**). Only O, Zn, Co, together with C elements were detected. The average atomic ratio of Zn and Co was about 1:6.5. The distributions of O, Zn and Co are presented in **Figures S1A–D**. It was revealed that the elements O, Zn, and Co were distributed homogeneously. The growth processes of ZnO on the surface of cobalt oxide were displayed under different time conditions as shown in **Figure S2**. The preparation processes of ZnO/Co_3O_4 are thus illustrated in **Figures 1G,H**. As seen in step 1, the as-obtained Co_3O_4 microspheres are composed of many single-crystalline porous nanosheets. These Co_3O_4 microspheres

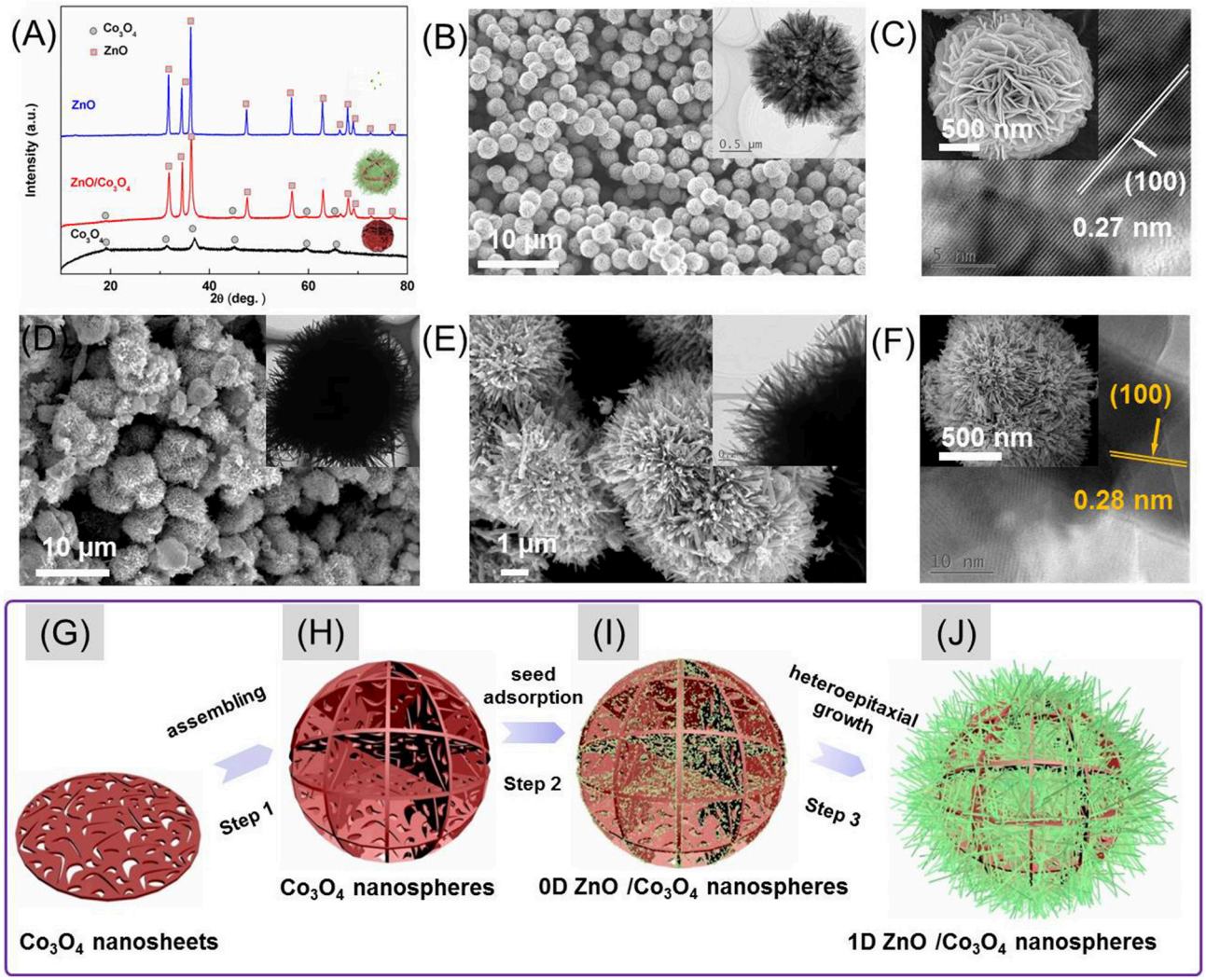

FIGURE 1 | (A) XRD spectra of Co_3O_4, ZnO, and ZnO/Co_3O_4. **(B,C)** SEM and TEM (inset) of Co_3O_4. **(D–F)** SEM and TEM (inset) of ZnO/Co_3O_4. **(G–J)** Schematic illustration of the formation processes of ZnO/Co_3O_4 hybrid.

were then anchored with ZnO crystal seeds by soaking them into a pre-prepared ZnO colloid solution as shown in step 2 (**Figure 1I**). Finally, via a heteroepitaxial growth process, ZnO nanorods were grown on the surface of Co_3O_4 microspheres (**Figure 1J**).

The responses of these sensors to 100 ppm ethanol at different operating temperatures are shown in **Figure 2A**. It can be observed that the optimal operating temperature is 300°C for ZnO/Co_3O_4. The response was about 161 (R_a/R_g) to 100 ppm ethanol, which is 110 and 10 times higher than that of Co_3O_4 (R_g/R_a = 1.47) and ZnO (R_a/R_g = 15), respectively. Gas-sensing tests of ZnO/Co_3O_4 toward other gases (100 ppm) were carried out as shown in **Figure 2B**. It was found that the responses to ethanol was much higher than to other gases. This could be due to the different volatilities and chemical properties of gases, which prompt the sensors to exhibit different adsorption and catalytic performances toward them. Therefore, the polarity, molecular weight and structure of these gases can exert great effect on the gas-sensing response. The difference between ethanol and methanol in this work may be the molecular weight. Alcohol with larger molecules can be more easily adsorbed and can release more electrons. On the other hand, different constituents and structures with various surface properties are also believed to influence the selectivity of sensing material, due to the diverse chemisorption abilities, which induce different selectivity behaviors between Co_3O_4, ZnO/Co_3O_4, and ZnO. The responses to 1∼100 ppm ethanol were tested as shown in **Figure 2C**. Evidently, exposure to ethanol gas led to an increase in resistance for Co_3O_4, while it led to a decrease for ZnO and ZnO/Co_3O_4, indicating that Co_3O_4 exhibits a p-type semiconducting behavior while ZnO and ZnO/Co_3O_4 exhibits an n-type behavior. **Figure 2D** present the responses of Co_3O_4 and ZnO/Co_3O_4 as a function of the ethanol concentrations (1–100 ppm), from

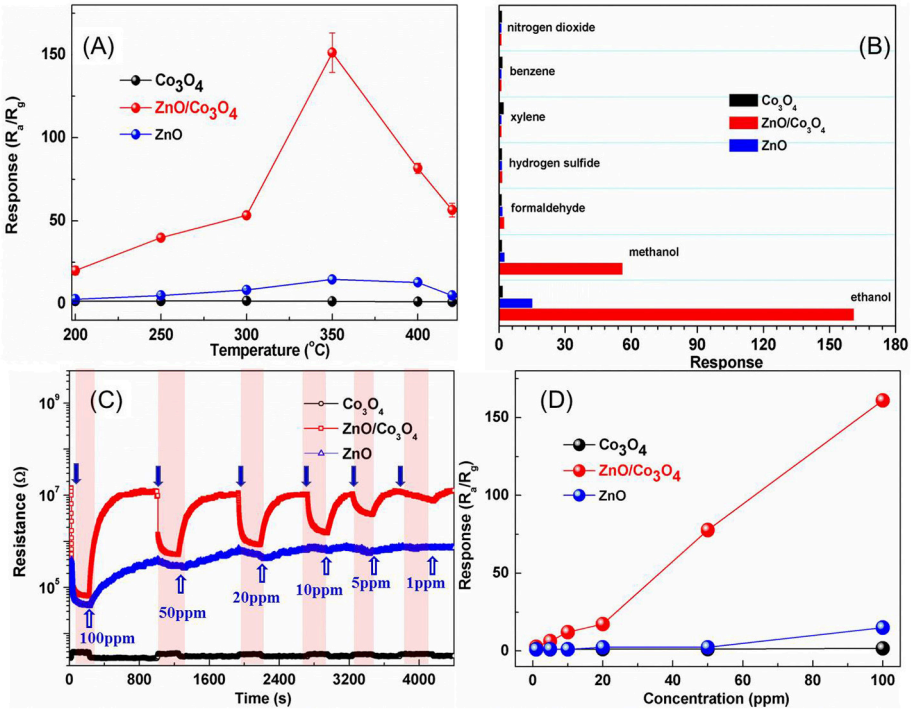

FIGURE 2 | (A) Responses of Co_3O_4, ZnO, and ZnO/Co_3O_4 microspheres to 100 ppm ethanol at different operating temperatures. **(B)** Responses to different gases with a concentration of 100 ppm. **(C)** The dynamic gas response patterns to ethanol with different concentration. **(D)** The response as a function of concentration.

which the gas responses increase almost linearly with the gas concentration.

The real-time responses of Co_3O_4, ZnO, and ZnO/Co_3O_4 to 100 ppm ethanol with three cycles are displayed in **Figure S3**. The resistance patterns reveal the similar continuous recycles, indicating all of the samples exhibit good repeatability. The response and recovery time are also important parameters in the fields of gas detection. It was revealed that the response time of Co_3O_4, ZnO, and ZnO/Co_3O_4 are 6, 17, and 13 s, respectively. And the recovery times of Co_3O_4, ZnO, and ZnO/Co_3O_4 were 12, 405, and 168 s, respectively. The fast response and recovery of Co_3O_4 can be attributed to its single-crystalline porous structure which benefits the gas-diffusion process and charge-transfer process. Compared with pure ZnO, the response and recovery process of ZnO/Co_3O_4 were accelerated because of its super single-crystalline porous structure. In addition, the response and recovery speeds of ZnO/Co_3O_4 to ethanol with low concentrations was much faster than those in ethanol with high concentrations, because of the slow diffusion speed of ethanol molecules to the active site at a low concentration.

The excellent gas-sensing properties of the ZnO/Co_3O_4 to ethanol, are mainly due to the many benefits of the as-designed structure. First, the ZnO nanorods and Co_3O_4 microspheres provide numerous channels for gas diffusion and an extremely high surface area for gas reaction. Furthermore, the single-crystalline feature of Co_3O_4 nanosheets provides a fast transport of charge carrier, another main factor to improve the signal transformation process of a hybrid. Moreover, the p-n heterojunctions between ZnO and Co_3O_4 can enlarge the response signal. Because the conduction band edge of Co_3O_4 is more negative than that of ZnO, band bending, and depletion regions are formed at the heterojunctions (Jana et al., 2015). By increasing the initial resistance, due to the as-established depletion region, the modulation of resistance will become more evident (Kim et al., 2017).

CONCLUSIONS

In this paper, ZnO nanorods anchored on the surface of Co_3O_4 nanospheres were synthesized. ZnO nanorods and porous Co_3O_4 microspheres provided numerous channels for gas diffusion and a large surface area for gas reaction. The Co_3O_4 nanospheres consisted of single-crystalline porous nanosheets to provide effective electrical pathways for charge-carrier transfer. And the p-n heterojunctions between ZnO and Co_3O_4 also led to an extended depletion region and a high initial resistance. As expected, this as-designed hybrid exhibited excellent gas-sensing properties with an extremely high response ($R_a/R_g = 161$) and a high selectivity to ethanol.

AUTHOR CONTRIBUTIONS

HZ performed the experiments and analyzed the data with the help from YY, TY, CY, WW, YS, and WL. KX wrote the manuscript with input from all authors. All authors read and approved the manuscript.

FUNDING

This work was supported by the National Natural Science Foundation of China (Grant No. 51461019, 51661012, 51761017, 51702140, 51602134, 61664005).

SUPPLEMENTARY MATERIAL

The Supplementary Material for this article can be found online at: https://www.frontiersin.org/articles/10.3389/fchem.2018.00628/full#supplementary-material

REFERENCES

Cao, J., Gong, Y., Wang, Y., Zhang, B., Zhang, H., Sun, G., et al. (2017). Cocoon-like ZnO decorated graphitic carbon nitride nanocomposite: Hydrothermal synthesis and ethanol gas sensing application. *Mater. Lett.* 198, 76–80. doi: 10.1016/j.matlet.2017.03.143

Dong, X., Cheng, X., Zhang, X., Sui, L., Xu, Y., Gao, S., et al. (2018). A novel coral-shaped Dy_2O_3 gas sensor for high sensitivity NH_3 detection at room temperature. *Sens. Actuators B: Chem.* 255, 1308–1315. doi: 10.1016/j.snb.2017.08.117

Gong, Y., Wang, Y., Sun, G., Jia, T., Jia, L., Zhang, F., et al. (2018). Carbon nitride decorated ball-flower like Co_3O_4 hybrid composite: hydrothermal synthesis and ethanol gas sensing application. *Nanomaterials* 8:132. doi: 10.3390/nano8030132

Jana, T. K., Pal, A., and Chatterjee, K. (2015). Magnetic and photocatalytic study of Co3O4–ZnO nanocomposite. *J. Alloys Comp.* 653, 338–344. doi: 10.1016/j.jallcom.2015.09.040

Kim, J. H., Lee, J. H., Mirzaei, A., Kim, H. W., and Kim, S. S. (2017). Optimization and gas sensing mechanism of n-SnO_2-p-Co_3O_4 composite nanofibers. *Sens. Actuators B* 248, 500–511. doi: 10.1016/j.snb.2017.04.029

Korotcenkov, G. (2007). Metal oxides for solid-state gas sensors: what determines our choice? *Mater. Sci. Eng. B* 139, 1–23. doi: 10.1016/j.mseb.2007.01.044

Li, F., Gao, X., Wang, R., Zhang, T., Lu, G., and Barsan, N. (2016). Design of core-shell heterostructure vanofibers with different work function and their sensing properties to trimethylamine. *ACS Appl. Mater. Interfaces* 8, 19799–19806. doi: 10.1021/acsami.6b04063

Li, T., Zeng, W., and Wang, Z. (2015). Quasi-one-dimensional metal-oxide-based heterostructural gas-sensing materials: a review. *Sens. Actuators B* 221, 1570–1585. doi: 10.1016/j.snb.2015.08.003

Meng, F., Hou, N., Ge, S., Sun, B., Jin, Z., Shen, W., et al. (2015). Flower-like hierarchical structures consisting of porous single-crystalline ZnO nanosheets and their gas sensing properties to volatile organic compounds (VOCs). *J. Alloys Compd.* 626, 124–130. doi: 10.1016/j.jallcom.2014.11.175

Miller, D. R., Akbar, S. A., and Morris, P. A. (2014). Nanoscale metal oxide-based heterojunctions for gas sensing: a review. *Sens. Actuators B* 204, 250–272. doi: 10.1016/j.snb.2014.07.074

Mirzaei, A., Park, S., Kheel, H., Sun, G.-J., Ko, T., Lee, S., et al. (2017). Acetone sensors based on in_2O_3-Co_3O_4 composite nanoparticles. *J. Nanosci. Nanotechno.* 17, 4087–4090. doi: 10.1166/jnn.2017.13408

Park, S., Sun, G. J., Jin, C., Kim, H. W., Lee, S., and Lee, C. (2016). Synergistic effects of a combination of Cr_2O_3-functionalization and UV-irradiation techniques on the ethanol gas sensing performance of ZnO nanorod gas sensors. *ACS Appl. Mater. Interfaces* 8, 2805–2811. doi: 10.1021/acsami.5b11485

Rai, P., Kwak, W. K., and Yu, Y. T. (2013). Solvothermal synthesis of ZnO nanostructures and their morphology-dependent gas-sensing properties. *ACS Appl. Mater. Interfaces* 5, 3026–3032. doi: 10.1021/am302811h

Singh, N., Ponzoni, A., Gupta, R. K., Lee, P. S., and Comini, E. (2011). Synthesis of In_2O_3-ZnO core–shell nanowires and their application in gas sensing. *Sens. Actuators B* 160, 1346–1351. doi: 10.1016/j.snb.2011.09.073

Tan, J., Dun, M., Li, L., Zhao, J., Tan, W., Lin, Z., et al. (2017). Synthesis of hollow and hollowed-out Co_3O_4 microspheres assembled by porous ultrathin nanosheets for ethanol gas sensors: responding and recovering in one second. *Sens. Actuators B* 249, 44–52. doi: 10.1016/j.snb.2017.04.063

Xu, K., Zou, J., Tian, S., Yang, Y., Zeng, F., Yu, T., et al. (2017). Single-crystalline porous nanosheets assembled hierarchical Co_3O_4 microspheres for enhanced gas-sensing properties to trace xylene. *Sens. Actuators B* 246, 68–77. doi: 10.1016/j.snb.2017.02.071

Zhang, J., Zeng, D. W., Zhu, Q., Wu, J. J., Xu, K., Liao, T. G., et al. (2015). Effect of grain-boundaries in NiO nanosheet layers room-temperature sensing mechanism under NO_2. *J. Phys. Chem. C* 119, 17930–17939. doi: 10.1021/acs.jpcc.5b04940

Zhu, L., Li, Y., and Zeng, W. (2018). Hydrothermal synthesis of hierarchical flower-like ZnO nanostructure and its enhanced ethanol gas-sensing properties. *Appl. Surf. Sci.* 427, 281–287. doi: 10.1016/j.apsusc.2017.08.229

Zhu, L., and Zeng, W. (2017). Room-temperature gas sensing of ZnO-based gas sensor: a review. *Sens. Actuators A* 267, 242–261. doi: 10.1016/j.sna.2017.10.021

Conflict of Interest Statement: The authors declare that the research was conducted in the absence of any commercial or financial relationships that could be construed as a potential conflict of interest.

frontiers in Chemistry

ORIGINAL RESEARCH
published: 06 November 2018
doi: 10.3389/fchem.2018.00540

Electrospun ZnO–SnO_2 Composite Nanofibers and Enhanced Sensing Properties to SF_6 Decomposition Byproduct H_2S

Zhaorui Lu[1], *Qu Zhou*[1,2*], *Caisheng Wang*[2*], *Zhijie Wei*[1], *Lingna Xu*[1] *and Yingang Gui*[1]

[1] College of Engineering and Technology, Southwest University, Chongqing, China, [2] Electrical and Computer Engineering Department, Wayne State University, Detroit, MI, United States

Hydrogen sulfide (H_2S) is an important decomposition component of sulfur hexafluoride (SF_6), which has been extensively used in gas-insulated switchgear (GIS) power equipment as insulating and arc-quenching medium. In this work, electrospun ZnO-SnO_2 composite nanofibers as a promising sensing material for SF_6 decomposition component H_2S were proposed and prepared. The crystal structure and morphology of the electrospun ZnO-SnO_2 samples were investigated by X-ray diffraction (XRD), scanning electron microscopy (SEM) and transmission electron microscopy (TEM), respectively. The composition of the sensitive materials was analyzed by energy dispersive X-ray spectrometers (EDS) and X-ray photoelectron spectroscopy (XPS). Side heated sensors were fabricated with the electrospun ZnO-SnO_2 nanofibers and the gas sensing behaviors to H_2S gas were systematically investigated. The proposed ZnO–SnO_2 composite nanofibers sensor showed lower optimal operating temperature, enhanced sensing response, quick response/recovery time and good long-term stability against H_2S. The measured optimal operating temperature of the ZnO–SnO_2 nanofibers sensor to 50 ppm H_2S gas was about 250°C with a response of 66.23, which was 6 times larger than pure SnO_2 nanofibers sensor. The detection limit of the fabricated ZnO–SnO_2 nanofibers sensor toward H_2S gas can be as low as 0.5 ppm. Finally, a plausible sensing mechanism for the proposed ZnO–SnO_2 composite nanofibers sensor to H_2S was also discussed.

Keywords: ZnO-SnO_2 nanofibers, electrospinning, H_2S, sensing properties, SF_6 decomposition components

OPEN ACCESS

Edited by:
Zhongchang Wang,
Laboratório Ibérico Internacional de Nanotecnologia (INL), Portugal

Reviewed by:
Yong Zhang,
Xiangtan University, China
Qi Qi,
Jilin University, China

***Correspondence:**
Qu Zhou
zhouqu@swu.edu.cn
Caisheng Wang
cwang@wayne.edu

Specialty section:
This article was submitted to Nanoscience, a section of the journal Frontiers in Chemistry

Received: *27 August 2018*
Accepted: *18 October 2018*
Published: *06 November 2018*

Citation:
Lu Z, Zhou Q, Wang C, Wei Z, Xu L and Gui Y (2018) Electrospun ZnO–SnO_2 Composite Nanofibers and Enhanced Sensing Properties to SF_6 Decomposition Byproduct H_2S. Front. Chem. 6:540. doi: 10.3389/fchem.2018.00540

INTRODUCTION

Sulfur hexafluoride (SF_6) insulating gas has excellent insulation performance and arc quenching. It is widely applied in gas-insulated switchgear (GIS) of power system as electrical insulator as well as arc-quenching medium (Beroual and Haddad, 2017; Zhang X. et al., 2017). However, partial discharge and disruptive discharge might occur in GIS equipment during the long run, accounting for the SF_6 gas decomposing to various decomposition components, such as H_2S, SO_2, SOF_2, SO_2F_2 (Tsai, 2007; Liu et al., 2017). Previous researches have reported that these typical decomposition components are able to accelerate the corrosion rate of the GIS equipment and increase the paralysis possibility of the power system (Zhang X. et al., 2016; Li et al., 2017). Therefore, accurate and effective detection of SF_6 gas decomposition components is significant to estimate and optimize the operation state of GIS power equipment.

Semiconductor metal oxides such as SnO_2 (Qi et al., 2014; Li et al., 2016; Shahabuddin et al., 2017; Zhou et al., 2018a), ZnO (Zhou et al., 2013; Zuo et al., 2013; Zhu et al., 2018), TiO_2 (Zeng et al., 2012; Park et al., 2017; Zhang Y. X. et al., 2018), NiO (Zhang Y. et al., 2016; Zhou et al., 2018b,c) are the most investigated group for gas sensors owing to their outstanding gas response and selectivity. Sensing nanostructure with high surface area and full electron depletion is advantageous to enhance the sensing performances (Hao et al., 2012; Miller et al., 2014). In particular, the 1D nanostructures such as nanofibers (Jiang et al., 2016), nanorods (Zhang et al., 2014; Zou et al., 2016), and nanotubes (Kong et al., 2015) have been extensively applied to improve gas sensing properties (Li T. M. et al., 2015; Long et al., 2018). Besides, many studies indicated that the selectivity and other important sensing parameters of semiconductor metal oxide nanomaterials can be enhanced by compositing semiconductor metal oxides (Zhou et al., 2015; Tomer and Duhan, 2016; Wang et al., 2017). Jae-Hun Kim et al. systematically investigated the sensing applications of $xSnO_2$-$(1-x)Co_3O_4$ composite nanofibers and reported that the $0.5SnO_2$-$0.5Co_3O_4$ sensor exhibited the most outstanding sensing characteristics (Kim et al., 2017). As one of the most important decomposition components of SF_6, H_2S has been widely studied in the past few years. A variety of composite metal oxides like Cu_2O-SnO_2 (Cui et al., 2013), CeO-SnO_2 (Fang et al., 2000), NiO-ZnO (Qu et al., 2016), and PdO-NiO (Balamurugan et al., 2017) have been reported as promising materials for H_2S gas sensing applications. However, the report of ZnO-SnO_2 composite nanofibers for H_2S gas sensing has been only investigated in a limited number of reports.

In this present work, we have successfully synthesized ZnO-SnO_2 nanofibers by electrospinning method and systematically investigated their sensing performances to H_2S gas. The prepared ZnO-SnO_2 nanofibers exhibited significantly improved sensing properties containing high response, low detection limit, low operating temperature and fast response/recovery times to H_2S gas detection, which can be ascribed to the large surface area of nanofiber structure and the formation of n-n heterojunctions at interface between ZnO and SnO_2. Finally, a plausible sensing mechanism for the proposed ZnO–SnO_2 composite nanofibers sensor to H_2S was also discussed.

EXPERIMENTAL

Materials Synthesis

Zinc nitrate hexahydrate ($Zn(NO_3)_2{\cdot}6H_2O$), stannic chloride pentahydrate ($SnCl_4{\cdot}5H_2O$), N,N-dimethylformamide (DMF), polyvinylpyrrolidone (PVP, Mw = 1,300,000) and ethanol were of analytical graded and used directly without further purification. All chemicals were purchased from Chongqing Chuandong Chemical Reagent Co., Ltd (Lu et al., 2018).

In the typical synthesis of ZnO-SnO_2 composite nanofibers, 0.7 g of $SnCl_4{\cdot}5H_2O$ and 0.6 g $Zn(NO_3)_2{\cdot}6H_2O$ (the molar ratio was 1:1) were dissolved in 5 ml of mixed solvents of ethanol and DMF (The volume ratio was 1:1) and stirred for 2 h. Then 2 g of PVP was added to the mixture and stirred for 24 h to form a viscous and homogeneous solution at room temperature. During electrospinning, the obtained mixture was delivered to a glass syringe. A voltage of 25 kV was applied between the flat aluminum foil and syringe at an electrode distance of 15 cm as shown in **Figure 1** and the flow rate is 0.7 ml/h. Finally, the electrospun nanofibers were transferred to a tube furnace and the specimens were annealed at 600°C for 3 h in air for the removal of PVP. For comparison, the pure SnO_2 nanofibers were also synthesized without adding $Zn(NO_3)_2{\cdot}6H_2O$. The schematic illustration of producing electrospun ZnO-SnO_2 composite nanofibers was shown in **Figure 1** (Bai et al., 2018).

Materials Characterization

To investigate the structures of electrospun ZnO-SnO_2 nanofibers, X-ray diffraction (XRD, D/Max-1200X, Rigaku, Japan) analysis was carried out at room temperature using a Rigaku D/Max-1200X diffractometry with Cu-Kα radiation (λ = 1.542 Å) over Bragg angles from 20° to 75° and the scanning speed of 2 deg/min. The morphologies of the electrospun nanofibers were investigated with a field emission scanning electronic microscopy (FESEM, JSM-6700F, JEOL, Japan) and transmission electron microscopy (TEM, JEM-2100, JEOL, Japan) operated at 120 kV. The energy dispersive X-ray spectrum analysis (EDS, Oxford INCA 250, JEOL, Japan) and X-ray photoelectron spectroscopy analysis (XPS, KRATOS X SAM800, Kratos, Kingdom) were tested to analyze the elemental compositions of the sample (Lu et al., 2018).

Gas Sensor Measurements

Gas sensors were fabricated with a side heated structure as shown in **Figure 2A** and a theoretic diagram of the test circuit was showed in **Figure 2B**. As shown in **Figure 2A**, there are two gold electrodes connected with platinum wire at both ends of the ceramic tube. Firstly, the as-prepared powder was mixed with appropriate amount of anhydrous ethanol and deionized water to form a homogeneous paste (Xu et al., 2015). Then the obtained paste was coated onto a prefabricated ceramic tube to form the sensing film and dried at room temperature for 2 h. Next a Ni–Cr heating wire was inserted into the ceramic tube to finish the side heated H_2S gas sensor. Finally, the stability of the sensing materials was improved by putting the sensor on the aging instrument of the side heated sensor at 120°C for 10 days. The sensor response was defined as $S = R_a/R_g$ (Zhang Q. Y. et al., 2017), where R_a and R_g were the resistances of the sensing material measured in air and in atmosphere containing target test gas H_2S, respectively (Zhu et al., 2017). Gas sensing properties of the obtained sensors were performed with the CGS-8 TP intelligent gas sensing analysis system (Chemical gas sensor-8, Beijing Elite Tech Co., Ltd., China). The response time was defined as the time required by the sensor to reach 90% of the final stable resistance when target gas in. The recovery time is the time required to return to 90% of its original baseline resistance when the sensor was exposed in air again (Nan et al., 2017). The sensing measurement were tested under laboratory condition with room temperature 25°C and constant humidity (50% relative humidity).

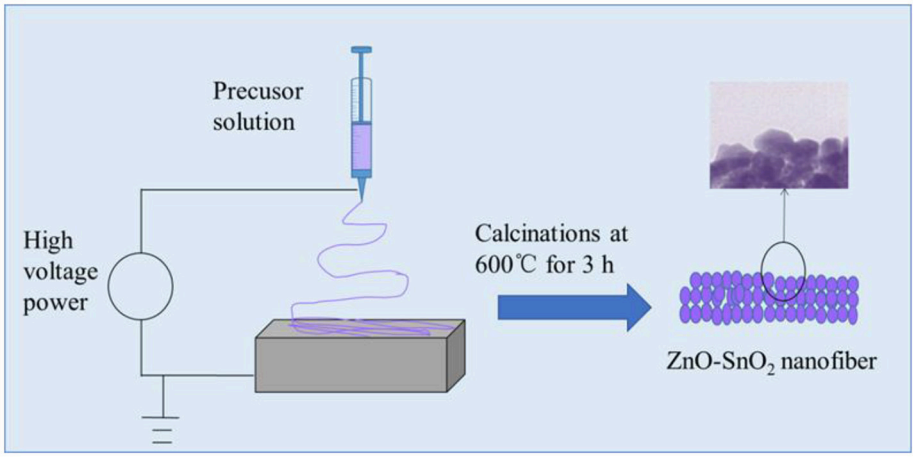

FIGURE 1 | Schematic illustration of producing electrospun ZnO-SnO_2 nanofibers.

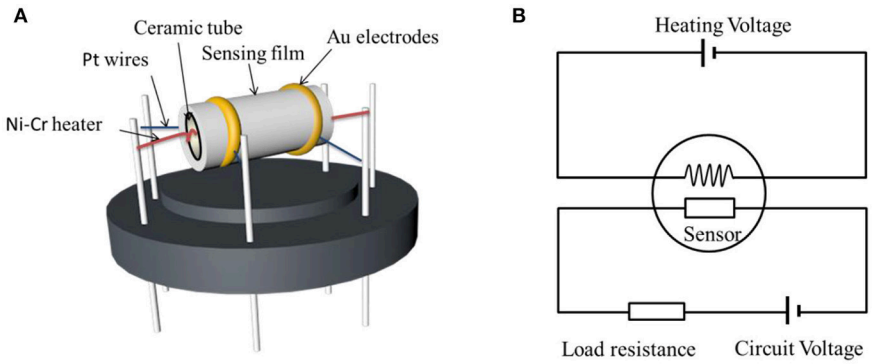

FIGURE 2 | (A) Schematic structure of the ZnO-SnO_2 nanofibers gas sensor and **(B)** theoretic diagram of the test circuit.

RESULTS AND DISCUSSION

Morphology and Structure

Figure 3 shows the XRD pattern of the electrospun ZnO-SnO_2 composite nanofibers. It can be seen from **Figure 3** that the XRD peaks are in accordance with the hexagonal wurtzite ZnO and tetragonal rutile SnO_2, compared with the standard pattern of JCPDS card No. 36-1451 and No. 41-1445, respectively. There is neither apparent peak shift nor any other phase corresponding SnO, $ZnSnO_3$ and Zn_2SnO_4, confirming that there are only SnO_2 and ZnO co-exist in the prepared material. The result shows a possibility of developing n–n heterojunction at the interface between ZnO and SnO_2 nanomaterial (Bai et al., 2018). The crystallite sizes of nanoparticels were calculated using Scherrer's equation ($D = k\lambda/\beta\cos\theta$) (Lu et al., 2018), and the average crystallite sizes of nanofibers were calculated by diffraction peaks (100), (101) for ZnO, and (110), (101), (221) for SnO_2. After calculation, the average crystallite size of ZnO is 20.1 nm, while it is 19.8 nm of SnO_2.

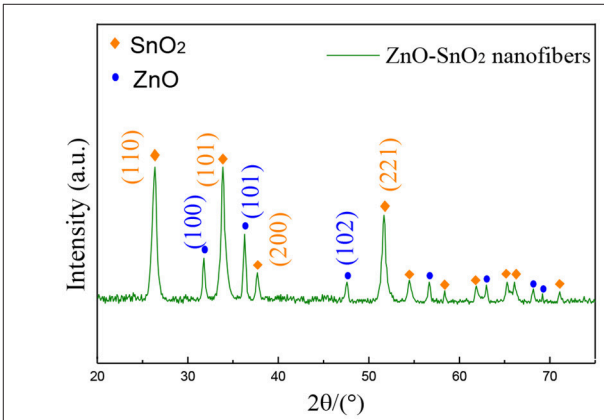

FIGURE 3 | XRD pattern of ZnO-SnO_2 nanofibers sensing material.

Figure 4 presents the FESEM and TEM images of the as-prepared ZnO-SnO_2 nanofibers after annealing. **Figure 4a** consists of randomly oriented nanofibers with diameters of 80–150 nm and lengths of 0.5–2 μm. Besides, the ZnO-SnO_2 nanofibers consist of nanoparticles and surface of nanofibers

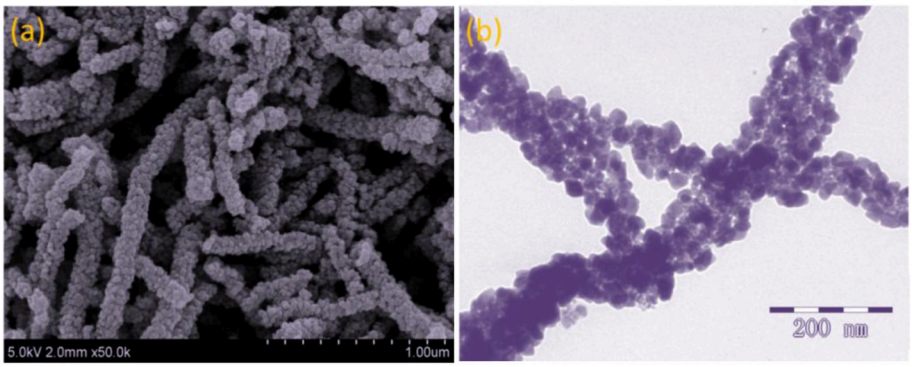

FIGURE 4 | (a) FESEM image and **(b)** TEM image of electrospun ZnO-SnO_2 nanofibers.

is rough, which can be attributed to thermal decomposition of PVP caused by annealing. More structural information of the ZnO-SnO_2 nanofibers is researched by TEM characterization as shown in **Figure 4b**, the single fiber is composed of grain-like nanoparticles with around 20 nm in size.

Figure 5 demonstrates the EDS spectrum of the electrospun ZnO-SnO_2 nanofibers. It can be seen that the ZnO–SnO_2 composite nanofibers are composed of Zn, Sn, and O elements and the atomic ratio of Zn and Sn is about 19.63:20.76.

To further analyze the compositions and element valences of the ZnO-SnO_2 nanofibers, XPS tests were investigated. **Figure 6A** shows the full range XPS survey spectra of the sample. It confirms the presence of Zn, O, Sn from prepared nanomaterial and C element which is due to the carbon contamination. The binding energies were calibrated using C 1 s hydrocarbon peak at 284.54 eV. **Figures 6B**,**C** demonstrate the high resolution spectra of the Zn 2p and Sn 3d energy state, respectively. The Zn 2p XPS spectrum (**Figure 6B**) presents the doublet peaks located at binding energies of 1045.6 eV and 1022.6eV, which corresponds to Zn $2p_{1/2}$ and Zn $2p_{3/2}$, respectively (Li W. Q. et al., 2015). The result indicates that the Zn^{2+} is the dominant species in the prepared material and in good agreement with the reported data for ZnO (Zhao et al., 2015). **Figure 6C** shows the binding energy of Sn $3d_{5/2}$, Sn $3d_{3/2}$ are 487.6eV and 496.1eV respectively, which are assigned to the highest oxidation state of Sn^{4+} for SnO_2 (Hamrouni et al., 2014; Chen et al., 2018). It further confirmed that ZnO and SnO_2 coexist in the samples.

Gas-Sensing Properties

The gas sensor responses of pure SnO_2 and ZnO-SnO_2 nanofibers sensors as a function of temperatures in the range of 100–375°C toward 50 ppm of H_2S gas were tested and shown in **Figure 7**. The sensing responses of all the prepared sensors increase with increasing temperature and attain a maximum value at 300 and 250°C for pure SnO_2 and ZnO-SnO_2 nanofibers sensor, respectively. With further increase in temperature, the sensing responses begin to decrease because desorption of H_2S is dominated and the amount of the adsorbed gas onto the surface decreases (Zhang et al., 2018). The response of gas sensor based on ZnO-SnO_2 nanofibers for 50 ppm H_2S gas at operating

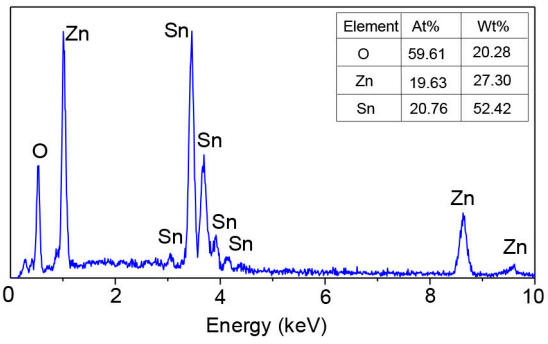

FIGURE 5 | EDS pattern of electrospun ZnO-SnO_2 nanofibers sample.

temperature of 250°C is 66.23, while it is 10.49 and 300°C for the pure SnO_2 nanofibers based sensor. The results indicate that ZnO-SnO_2 composite nanofibers can obviously improve the response to H_2S at different working temperatures and reduce the optimal operating temperature.

Figure 8 shows the H_2S gas responses of pure SnO_2 and ZnO-SnO_2 nanofibers based sensors to different concentration of H_2S in the range of 0.5–100 ppm at their optimal operating temperatures measured above. The measured results show that gas responses of the as-prepared gas sensors increase in a good linear relationship from 0.5 to 100 ppm. The linear relationship of the response and gas concentration satisfies linear equation $y = 1.1003x+6.90664$ for electrospun ZnO-SnO_2 nanofibers gas sensor. The higher response of ZnO-SnO_2 nanofibers can be explained by the formation of n-n heterojunctions at the interface between ZnO and SnO_2. Moreover, the sensor detection limit was defined as the target gas concentration value at which the response is above 3. The response of the ZnO-SnO_2 nanofibers sensor to 0.5 ppm H_2S gas can reach up to 3.45, indicating that the detection limit of the sensor for detecting H_2S gas is as low as sub-ppm level.

The dynamic response and recovery curve of the ZnO-SnO_2 nanofibers sensor for 1, 5, 30, and 50 ppm H_2S gas was performed and shown in **Figure 9**. The obtained sensing response values

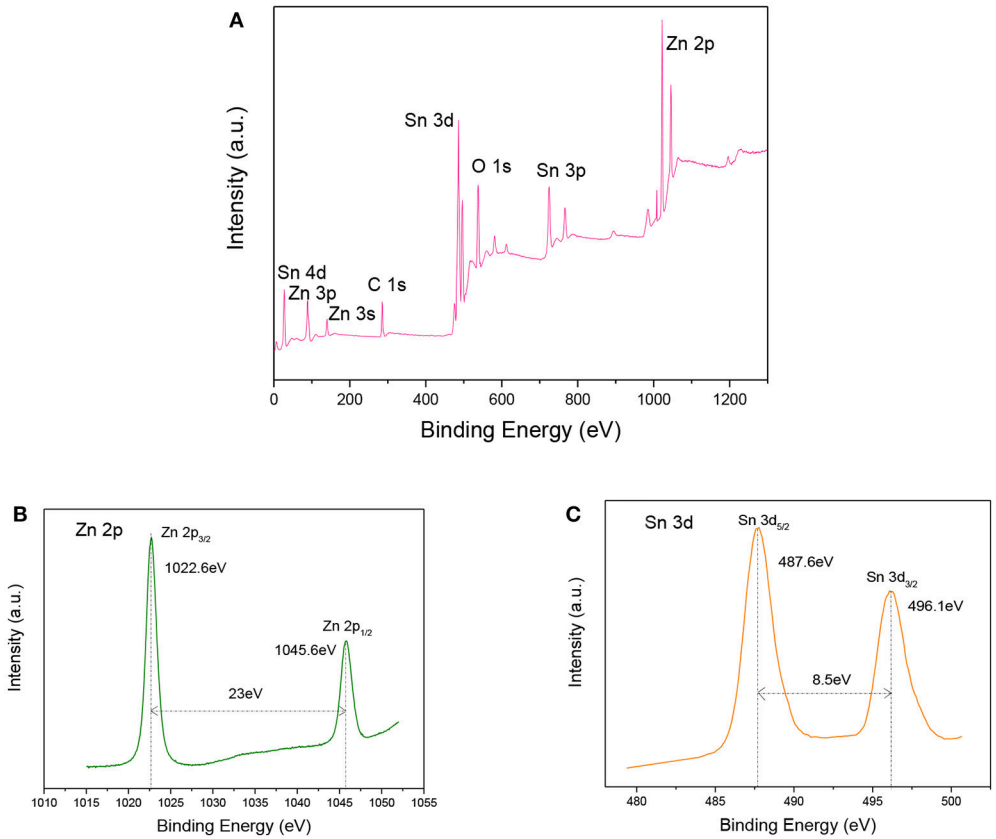

FIGURE 6 | (A) Survey, **(B)** Zn 2p, **(C)** Sn 3d XPS spectra of electrospun ZnO–SnO_2 nanofibers.

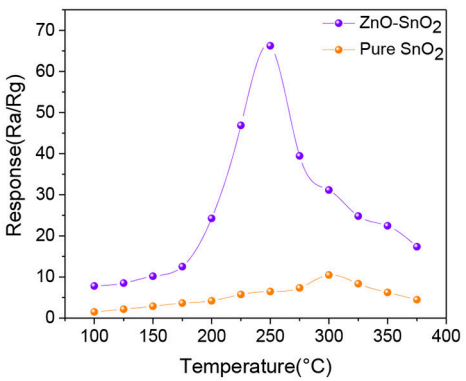

FIGURE 7 | Response to 50 ppm H_2S at different operating temperature of SnO_2 and ZnO-SnO_2 nanofibers sensors.

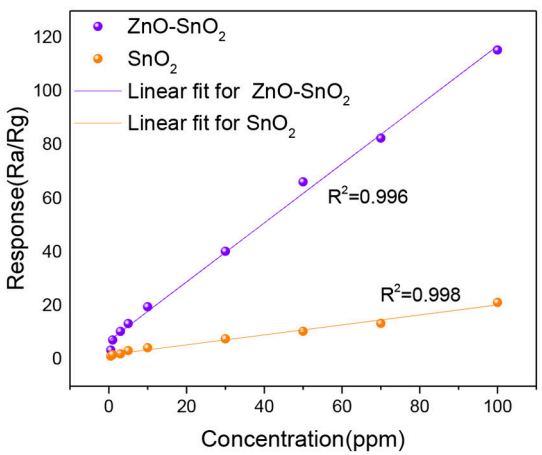

FIGURE 8 | Gas responses for H_2S gas (0.5–100 ppm) using pure SnO_2 and ZnO-SnO_2 nanofibers sensors at their optimal working temperature.

are about 7.25, 13.37, 40.31, and 66.23, respectively. The ZnO-SnO_2 nanofibers sensor responds rapidly and could recover to its initial value when it was exposed to air again, implying a satisfying stability and reproducibility of the proposed H_2S gas sensor.

Figures 10A,B illustrate the response-recovery curve of electrospun ZnO-SnO_2 nanofibers sensor and pure SnO_2 nanofibers sensor to 50 ppm of H_2S gas at their optimal operating temperature mentioned above. From the curves, it is observed that the response and recovery time of the ZnO-SnO_2 nanofibers sensor is about 18 and 32 s, respectively, whereas for pure

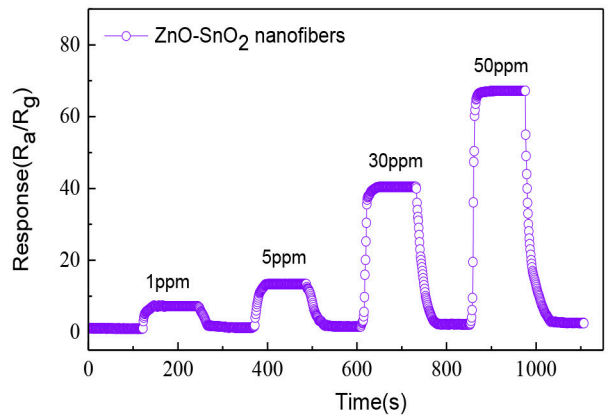

FIGURE 9 | Dynamic response-recovery curve of the sensor based upon ZnO-SnO_2 nanofibers at 250°C.

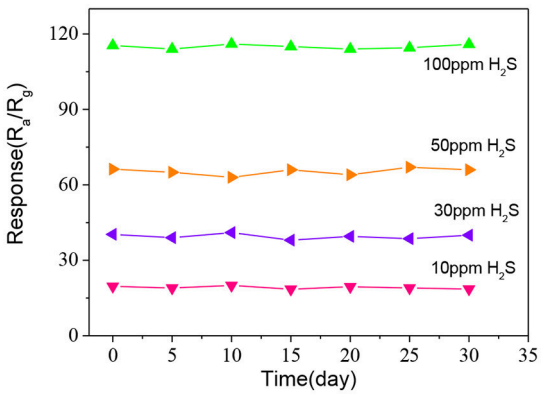

FIGURE 11 | Long term stability property of ZnO-SnO_2 nanofibers sensor.

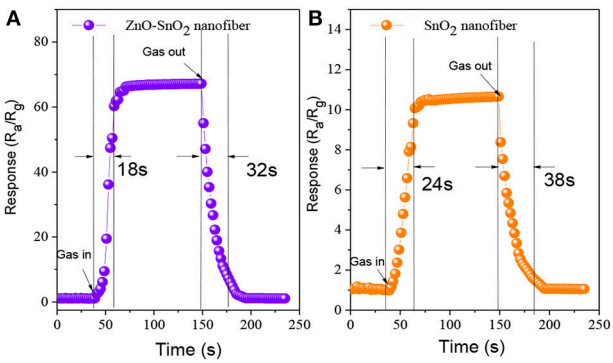

FIGURE 10 | Response-recovery curve of the sensor bases on **(A)** ZnO-SnO_2 nanofibers **(B)** pure SnO_2 nanofibers.

SnO_2 nanofibers sensor the corresponding values is 24 and 38 s, respectively.

Finally, the long-term stability of the fabricated ZnO-SnO_2 nanofibers sensor was measured to 10, 30, 50, and 100 ppm H_2S gas at 250°C for 30 days as shown in **Figure 11**. The measured results show that the response has little change for 30 days and confirm a good stability of the fabricated electrospun ZnO-SnO_2 nanofibers sensor.

Experimental results of ZnO-SnO_2 nanofibers sensor have been compared with the results reported by the other workers on H_2S sensors and presented in **Table 1**. It can be seen that electrospun ZnO-SnO_2 nanofibers sensor toward H_2S can reach a relatively higher response at lower temperature and the response time is relatively shorter than other sensors reported previously. The obtained results indicate that the electrospun ZnO-SnO_2 nanofibers sensor is promising for H_2S gas sensing.

Sensing Mechanism

ZnO and SnO_2 belong to typical n-type semiconductors, characterized by their high free carrier concentration (Hong et al., 2017; Zhou et al., 2018d). The gas sensing mechanism of ZnO-SnO_2 nanofibers is shown in **Figure 12**. Due to the sensing mechanism of ZnO-SnO_2 sensor follows the surface controlled type, the gas sensing properties are ascribed to the change of the surface resistance, which controlled by the adsorption and desorption of oxygen on the surface of sensing materials (Wei et al., 2014). When ZnO-SnO_2 nanofibers sensor is exposed to air (**Figure 12A**), the resistance of gas sensor depends on the amount of chemisorbed oxygen species (O^-, O_2^-, and O^{2-}). The free oxygen molecules are absorbed on the surface and capture electrons from the conduction band of the ZnO-SnO_2 nanofibers, which causes a depletion layer around the surface and the increasing the resistance (Cheng et al., 2014). When ZnO-SnO_2 nanofibers sensing materials are exposed to H_2S (**Figure 12B**), the target gas reacts with the adsorbed oxygen and then releases the captured electrons into the conduction band of ZnO-SnO_2 nanifibers to reduce the depletion layer and decrease the resistance.

It is well-known that the chemisorbed oxygen depends on the specific surface area of sensing materials and the operating temperature. ZnO-SnO_2 nanofibers show a big surface area as shown in **Figure 4**. It means that adsorption capability of ZnO-SnO_2 nanofibers was greatly enhanced (Zhang W. et al., 2017). Moreover, O^{2-} and O^- species are regarded as the most oxygen adsorption species at 250°C, and the following H_2S sensing reaction can be considered (Kolhe et al., 2017).

$$H_2S + 3O^- \rightarrow SO_2 + H_2O + 3e^- \quad (1)$$

$$H_2S + 3O^{2-} \rightarrow SO_2 + H_2O + 6e^- \quad (2)$$

In accordance with the definition about gas response ($S = R_a/R_g$), the increasing of R_a and decreasing of R_g cause that the response of ZnO-SnO_2 nanofibers is significantly enhanced. Additional electron consumption will occur at the boundaries of ZnO and SnO_2, which further enhances the gas response. The contact of ZnO and SnO_2 provides condition for electrons transfer from SnO_2 to ZnO, which has a higher work function of 5.2 eV compared to SnO_2 (4.9 eV). It results in the formation

TABLE 1 | Summary of the H_2S gas sensing performances of different gas sensor materials.

Sensor	H_2S (ppm)	Temp. (°C)	Response (R_a/R_g)	τ_{res} and τ_{rec}	References
Zn_2SnO_4 hollow octahedra	50	260	46	10 and 25 s	Ma et al., 2012
V doped In_2O_3	50	90	14	15 and 18 s	Liu et al., 2014
Co_3O_4-SWCNT composites	100	250	51	>100 s	Moon et al., 2016
Al-ZnO thin film	600	200	30	90 and 209 s	Kolhe et al., 2018
CuO-functionalized WO_3 nanowires	100	300	79.8	~30 and 20 s	Park et al., 2014
Fe_2O_3 -NiO nanoplate	200	200	26	11 and 18 s	Sun et al., 2016
TiO_2/SiO_2 composite aerogel film	50	250	13.5	21 and 600 s	Yang et al., 2018
micro/nanostructured In_2O_3 porous thin	50	300	30	16 and 30 s	Wang et al., 2016
Gold functionalized MoO_3 nano flake	15	400	260	60 and 480 s	Munasinghe Arachchige et al., 2018
ZnO-SnO_2 nanofibers	50	250	66.23	18 and 32 s	This work

Temp., the optimal working temperature. τ_{res} and τ_{rec} - response time and recovery time.

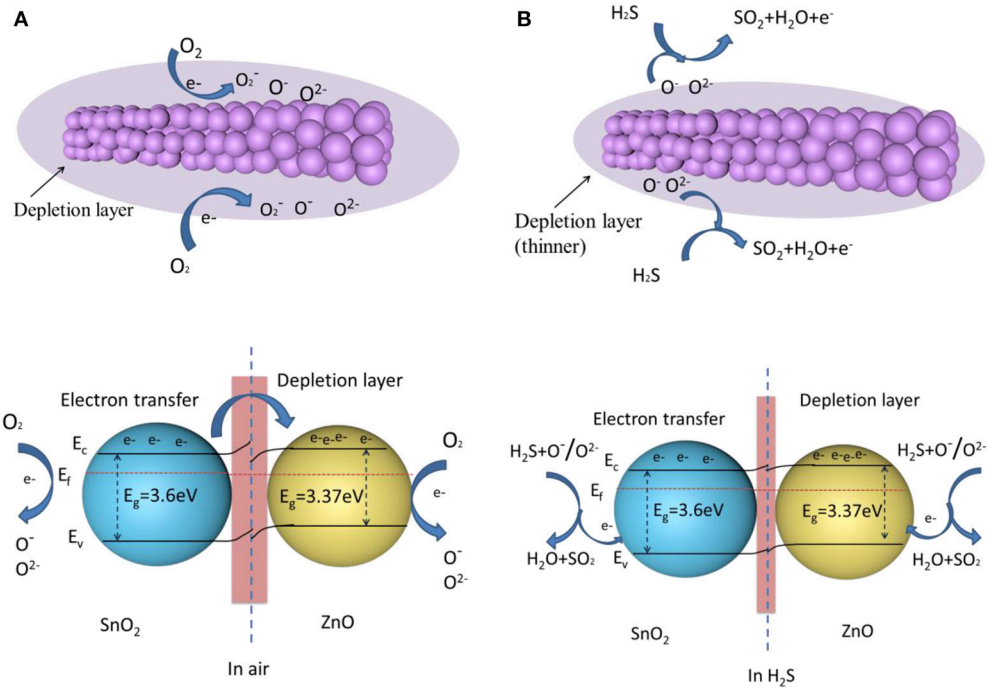

FIGURE 12 | A schematic of the H_2S sensing mechanism of the ZnO-SnO_2 nanofibers **(A)** when the gas sensor is exposed in air **(B)** when the gas sensor is exposed in H_2S (E_f is Fermi level; E_c is conduction band; E_v is valence band; E_g is band gaps).

of an additional depletion layer in the vicinity region between the ZnO and SnO_2, eventually generating a potential barrier for electron flow (Choi et al., 2013). The boundary barrier may decrease when the gas sensor is exposed in H_2S. More electrons of oxygen species transfer to the sensing material by reaction of H_2S with oxygen species, which results the resistance of the sensing material decreases and the response of the sensor increases. However, pure SnO_2 does not provide reaction interface, leading to lower gas response. So the ZnO–SnO_2 composite nanofibers exhibit better sensing properties than the SnO_2 nanofibers.

CONCLUSIONS

In summary, ZnO-SnO_2 composite nanofibers were successfully synthesized by electrospinning method and characterized by various techniques. H_2S sensing properties of the electrospun nanofibers sensor were also investigated. Compared to the pure SnO_2 nanofiber sensor, the ZnO-SnO_2 composite nanofibers sensor shows excellent gas sensing response for H_2S gas, which is attributed to the large specific surface and the heterojunctions between SnO_2 and ZnO. The proposed ZnO-SnO_2 composite

nanofibers sensor exhibits good linear relationship between sensing response and gas concentration in the range of 0.5∼100 ppm and its detection limit is as low as sub-ppm level. Moreover, the proposed sensor achieves good repeatability and long-term stability, making it a promising candidate for detecting H_2S gas.

AUTHOR CONTRIBUTIONS

ZL and ZW performed the experiments and analyzed the data with the help from LX and YG. ZL, QZ, and CW wrote and revised the manuscript with input from all authors. All authors read and approved the manuscript.

ACKNOWLEDGMENTS

This work has been supported in part by the National Natural Science Foundation of China (No. 51507144), the China Postdoctoral Science Foundation Project (Nos. 2015M580771, 2016T90832), the Chongqing Science and Technology Commission (CSTC) (No. cstc2016jcyjA0400) and the project of China Scholarship Council (CSC).

REFERENCES

Bai, S. L., Fu, H., Zhao, Y. Y., Tian, K., Luo, R. X., Li, D. Q., et al. (2018). On the construction of hollow nanofibers of ZnO-SnO_2 heterojunctions to enhance the NO_2 sensing properties. *Sensor. Actuat. B Chem.* 266, 692–702. doi: 10.1016/j.snb.2018.03.055

Balamurugan, C., Jeong, Y. J., and Lee, D. W. (2017). Enhanced H_2S sensing performance of a p-type semiconducting PdO-NiO nanoscale heteromixture. *Appl. Surf. Sci.* 420, 638–650. doi: 10.1016/j.apsusc.2017.05.166

Beroual, A., and Haddad, A. (2017). Recent advances in the quest for a new insulation gas with a low impact on the environment to replace sulfur hexafluoride (SF_6) gas in high-voltage power network applications. *Energies* 10:1216. doi: 10.3390/en10081216

Chen, Y., Qin, H., and Hu, J. (2018). CO sensing properties and mechanism of Pd doped SnO_2 thick-films. *Appl. Surf. Sci.* 428, 207–217. doi: 10.1016/j.apsusc.2017.08.205

Cheng, L., Ma, S. Y., Li, X. B., Luo, J., Li, W. Q., Li, F. M., et al. (2014). Highly sensitive acetone sensors based on Y-doped SnO_2 prismatic hollow nanofibers synthesized by electrospinning. *Sensor. Actuat. B-Chem.* 200, 181–190. doi: 10.1016/j.snb.2014.04.063

Choi, S.-W., Katoch, A., Sun, G.-J., and Kim, S. S. (2013). Synthesis and gas sensing performance of ZnO–SnO_2 nanofiber–nanowire stem-branch heterostructure. *Sensor. Actuat. B Chem.* 181, 787–794. doi: 10.1016/j.snb.2013.02.010

Cui, G., Zhang, M., and Zou, G. (2013). Resonant tunneling modulation in quasi-2D Cu_2O/SnO_2 p-n horizontal-multi-layer heterostructure for room temperature H_2S sensor application. *Sci. Rep.* 3:1250. doi: 10.1038/srep01250

Fang, G. J., Liu, Z. L., Liu, C. Q., and Yao, K. L. (2000). Room temperature H_2S sensing properties and mechanism of CeO_2-SnO_2 sol-gel thin films. *Sensor. Actuat. B-Chem.* 66, 46–48. doi: 10.1016/S0925-4005(99)00467-0

Hamrouni, A., Moussa, N., Parrino, F., Di Paola, A., Houas, A., and Palmisano, L. (2014). Sol–gel synthesis and photocatalytic activity of ZnO–SnO_2 nanocomposites. *J. Mol. Catal. A Chem.* 390, 133–141. doi: 10.1016/j.molcata.2014.03.018

Hao, D., Zhu, J. H., Jiang, J., Ding, R. M., Feng, Y. M., Wei, G. M., et al. (2012). Preparation and gas-sensing property of ultra-fine NiO/SnO2 nano-particles. *RSC Adv.* 2:10324–10329. doi: 10.1039/C2RA21121A

Hong, C., Zhou, Q., Lu, Z., Umar, A., Kumar, R., Wei, Z., et al. (2017). Ag-doped ZnO nanoellipsoids based highly sensitive gas sensor. *Mater. Exp.* 7, 380–388. doi: 10.1166/mex.2017.1388

Jiang, Z., Zhao, R., Sun, B., Nie, G., Ji, H., Lei, J., et al. (2016). Highly sensitive acetone sensor based on Eu-doped SnO_2 electrospun nanofibers. *Ceram. Int.* 42, 15881–15888. doi: 10.1016/j.ceramint.2016.07.060

Kim, J.-H., Lee, J.-H., Mirzaei, A., Kim, H. W., and Kim, S. S. (2017). Optimization and gas sensing mechanism of n-SnO_2-p-Co_3O_4 composite nanofibers. *Sensor. Actuat. B-Chem.* 248, 500–511. doi: 10.1016/j.snb.2017.04.029

Kolhe, P. S., Koinkar, P. M., Maiti, N., and Sonawane, K. M. (2017). Synthesis of Ag doped SnO_2 thin films for the evaluation of H_2S gas sensing properties. *Phys. B Condensed Matter.* 524, 90–96. doi: 10.1016/j.physb.2017.07.056

Kolhe, P. S., Shinde, A. B., Kulkarni, S. G., Maiti, N., Koinkar, P. M., and Sonawane, K. M. (2018). Gas sensing performance of Al doped ZnO thin film for H_2S detection. *J. Alloy. Compd.* 748, 6–11. doi: 10.1016/j.jallcom.2018.03.123

Kong, J., Rui, Z., Ji, H., and Tong, Y. (2015). Facile synthesis of ZnO/SnO_2 hetero nanotubes with enhanced electrocatalytic property. *Catal. Today* 258, 75–82. doi: 10.1016/j.cattod.2015.04.011

Li, L., Fan, X. P., Zhou, Y. Y., Tang, N., Zou, Z. L., Liu, M. Z., et al. (2017). Research on technology of online gas chromatograph for SF_6 decomposition products. *IOP Conf. Ser. Mater. Sci. Eng.* 274, 012–038. doi: 10.1088/1757-899X/274/1/012038

Li, T., Zeng, W., Long, H., and Wang, Z. (2016). Nanosheet-assembled hierarchical SnO_2 nanostructures for efficient gas-sensing applications. *Sensor. Actuat. B-Chem.* 231, 120–128. doi: 10.1016/j.snb.2016.03.003

Li, T. M., Zeng, W., and Wang, Z. C. (2015). Quasi-one-dimensional metal-oxide-based heterostructural gas-sensing materials: a review. *Sensor. Actuat. B-Chem.* 221, 1570–1585. doi: 10.1016/j.snb.2015.08.003

Li, W. Q., Ma, S. Y., Li, Y. F., Yang, G. J., Mao, Y. Z., Luo, J., et al. (2015). Enhanced ethanol sensing performance of hollow ZnO–SnO2 core–shell nanofibers. *Sensor. Actuat. B Chem.* 221, 392–402. doi: 10.1016/j.snb.2015.01.090

Liu, H. C., Zhou, Q., Zhang, Q. Y., Hong, C. X., Xu, L. N., Jin, L. F., et al. (2017). Synthesis, characterization and enhanced sensing properties of a NiO/ZnO p-n junctions sensor for the SF_6 decomposition byproducts SO_2, SO_2F_2, and SOF_2. *Sensors* 17:913. doi: 10.3390/s17040913

Liu, J., Guo, W., Qu, F., Feng, C., Li, C., Zhu, L., et al. (2014). V-doped In_2O_3 nanofibers for H_2S detection at low temperature. *Ceram. Int.* 40, 6685–6689. doi: 10.1016/j.ceramint.2013.11.129

Long, H. W., Zeng, W., Wang, H., Qian, M. M., Liang, Y. H., and Wang, Z. C. (2018). Self-Assembled biomolecular 1D nanostructures for aqueous sodium-ion battery. *Adv. Sci.* 5:1700634. doi: 10.1002/advs.201700634

Lu, Z., Zhou, Q., Xu, L., Gui, Y., Zhao, Z., Tang, C., et al. (2018). Synthesis and characterization of highly sensitive hydrogen (H2) sensing device based on Ag doped SnO2 nanospheres. *Materials* 11:E492. doi: 10.3390/ma11040492

Ma, G., Zou, R., Jiang, L., Zhang, Z., Xue, Y., Yu, L., et al. (2012). Phase-controlled synthesis and gas-sensing properties of zinc stannate ($ZnSnO_3$ and Zn_2SnO_4) faceted solid and hollow microcrystals. *CrystEngComm* 14, 2172–2179. doi: 10.1039/c2ce06272k

Miller, D. R., Akbar, S. A., and Morris, P. A. (2014). Nanoscale metal oxide-based heterojunctions for gas sensing: a review. *Sensor. Actuat. B Chem.* 204, 250–272. doi: 10.1016/j.snb.2014.07.074

Moon, S., Vuong, N. M., Lee, D., Kim, D., Lee, H., Kim, D., et al. (2016). Co_3O_4-SWCNT composites for H_2S gas sensor application. *Sensor. Actuat. B Chem.* 222, 166–172. doi: 10.1016/j.snb.2015.08.072

Munasinghe Arachchige, H. M. M., Zappa, D., Poli, N., Gunawardhana, N., and Comini, E. (2018). Gold functionalized MoO_3 nanoflakes for gas sensing applications. *Sensor. Actuat. B Chem.* 269, 331–339. doi: 10.1016/j.snb.2018.04.124

Nan, C., Li, Y. X., Deng, D. Y., Xu, L.,Xing, X. X., Xiao, X. C., et al. (2017). Acetone sensing performances based on nanoporous TiO_2 synthesized by a facile hydrothermal method. *Sensor. Actuat. B Chem.* 238, 491–500. doi: 10.1016/j.snb.2016.07.094

Park, J. Y., Kim, H. H., Rana, D., Jamwal, D., and Katoch, A. (2017). Surface-area-controlled synthesis of porous TiO_2 thin films for gas-sensing applications. *Nanotechnology* 28:095502. doi: 10.1088/1361-6528/aa5836

Park, S., Park, S., Jung, J., Hong, T., Lee, S., Kim, H. W., et al. (2014). H_2S gas sensing properties of CuO-functionalized WO_3 nanowires. *Ceram. Int.* 40, 11051–11056. doi: 10.1016/j.ceramint.2014.03.120

Qi, Q., Wang, P.-P., Zhao, J., Feng, L.-L., Zhou, L.-J., Xuan, R.-F., et al. (2014). SnO_2 nanoparticle-coated In_2O_3 nanofibers with improved NH3 sensing properties. *Sensor. Actuat. B Chem.* 194, 440–446. doi: 10.1016/j.snb.2013.12.115

Qu, Z., Fu, Y., Yu, B., Deng, P., Xing, L., and Xue, X. (2016). High and fast H_2S response of NiO/ZnO nanowire nanogenerator as a self-powered gas sensor. *Sensor. Actuat. B Chem.* 222, 78–86. doi: 10.1016/j.snb.2015.08.058

Shahabuddin, M., Umar, A., Tomar, M., and Gupta, V. (2017). Custom designed metal anchored SnO_2 sensor for H_2 detection. *Int. J. Hydrogen Energ.* 42, 4597–4609. doi: 10.1016/j.ijhydene.2016.12.054

Sun, G.-J., Kheel, H., Lee, J. K., Choi, S., Lee, S., and Lee, C. (2016). H_2S gas sensing properties of Fe_2O_3 nanoparticle-decorated NiO nanoplate sensors. *Surf. Coat. Tech.* 307, 1088–1095. doi: 10.1016/j.surfcoat.2016.06.066

Tomer, V. K., and Duhan, S. (2016). Ordered mesoporous Ag-doped TiO_2/SnO_2 nanocomposite based highly sensitive and selective VOC sensors. *J. Mater. Chem. A* 4, 1033–1043. doi: 10.1039/C5TA08336B

Tsai, W.-T. (2007). The decomposition products of sulfur hexafluoride (SF_6): reviews of environmental and health risk analysis. *J. Fluorine Chem.* 128, 1345–1352. doi: 10.1016/j.jfluchem.2007.06.008

Wang, C., Zeng, W., and Chen, T. (2017). Facile synthesis of thin nanosheet assembled flower-like NiO-ZnO composite and its ethanol-sensing performance. *J. Mater. Sci.* 28, 222–227. doi: 10.1007/s10854-016-5514-1

Wang, Y., Duan, G., Zhu, Y., Zhang, H., Xu, Z., Dai, Z., et al. (2016). Room temperature H_2S gas sensing properties of In_2O_3 micro/nanostructured porous thin film and hydrolyzation-induced enhanced sensing mechanism. *Sensor. Actuat. B Chem.* 228, 74–84. doi: 10.1016/j.snb.2016.01.002

Wei, S. H., Wang, S. M., Zhang, Y., and Zhou, M. H. (2014). Different morphologies of ZnO and their ethanol sensing property. *Sensor. Actuat. B Chem.* 192, 480–487. doi: 10.1016/j.snb.2013.11.034

Xu, L., Chen, N., Han, B. Q., Xiao, X. C., Chen, G., Djerdj, L., et al. (2015). Nanoparticle cluster gas sensor: Pt activated SnO_2 nanoparticles for NH_3 detection with ultrahigh sensitivity. *Nanoscale* 36, 14872–14880. doi: 10.1039/C5NR03585F

Yang, F., Zhu, J., Zou, X., Pang, X., Yang, R., Chen, S., et al. (2018). Three-dimensional TiO_2 /SiO_2 composite aerogel films via atomic layer deposition with enhanced H_2S gas sensing performance. *Ceram. Int.* 44, 1078–1085. doi: 10.1016/j.ceramint.2017.10.052

Zeng, W., Liu, T. M., and Wang, Z. C. (2012). Enhanced gas sensing properties by SnO_2 nanosphere functionalized TiO_2 nanobelts. *J. Mater. Chem.* 22, 3544–3548. doi: 10.1039/c2jm15017d

Zhang, H., Zeng, W., Zhang, Y., Li, Y. Q., Miao, B., Chen, W. G., et al. (2014). Synthesis and gas sensing properties of novel SnO_2 nanorods. *J. Mater. Sci. Mater. El.* 25, 5006–5012. doi: 10.1007/s10854-014-2264-9

Zhang, Q. Y., Zhou, Q., Yin, X. T., Liu, H. C., Xu, L. N., Tan, W. M., et al. (2017). The effect of PMMA pore-forming on hydrogen sensing properties of porous SnO_2 thick film sensor. *Sci. Adv. Mater.* 9, 1350–1355. doi: 10.1166/sam.2017.3111

Zhang, W., Xie, C., Zhang, G., Zhang, J., Zhang, S., and Zeng, D. (2017). Porous $LaFeO_3$/SnO_2 nanocomposite film for CO_2 detection with high sensitivity. *Mater. Chem. Phys.* 186, 228–236. doi: 10.1016/j.matchemphys.2016.10.048

Zhang, X., Cui, H., Gui, Y., and Tang, J. (2017). Mechanism and application of carbon nanotube sensors in SF_6 decomposed production detection: a review. *Nanoscale Res. Lett.* 12:177. doi: 10.1186/s11671-017-1945-8

Zhang, X., Gui, Y., and Dong, X. (2016). Preparation and application of TiO_2 nanotube array gas Sensor for SF_6-insulated equipment detection: a review. *Nanoscale Res. Lett.* 11:302. doi: 10.1186/s11671-016-1516-4

Zhang, Y., Wang, J., Wei, H., Hao, J., Mu, J., Cao, P., et al. (2016). Hydrothermal synthesis of hierarchical mesoporous NiO nanourchins and their supercapacitor application. *Mater. Lett.* 162, 67–70. doi: 10.1016/j.matlet.2015.09.123

Zhang, Y., Zeng, W., and Li, Y. (2018). The hydrothermal synthesis of 3D hierarchical porous MoS_2 microspheres assembled by nanosheets with excellent gas sensing properties. *J. Alloy. Compd.* 749, 355–362. doi: 10.1016/j.jallcom.2018.03.307

Zhang, Y. X., Zeng, W., Ye, H., and Li, Y. Q. (2018). Enhanced carbon monoxide sensing properties of TiO_2 with exposed (001) facet: a combined first-principle and experimental study. *Appl. Surf. Sci.* 442, 507–516. doi: 10.1016/j.apsusc.2018.02.036

Zhao, Y., Li, X., Dong, L., Yan, B., Shan, H., Li, D., et al. (2015). Electrospun SnO_2 –ZnO nanofibers with improved electrochemical performance as anode materials for lithium-ion batteries. *Int. J. Hydrogen Energ.* 40, 14338–14344. doi: 10.1016/j.ijhydene.2015.06.054

Zhou, Q., Chen, W., Xu, L., Kumar, R., Gui, Y., Zhao, Z., et al. (2018a). Highly sensitive carbon monoxide (CO) gas sensors based on Ni and Zn doped SnO_2 nanomaterials. *Ceram. Int.* 44, 4392–4399. doi: 10.1016/j.ceramint.2017.12.038

Zhou, Q., Chen, W., Xu, L., and Peng, S. (2013). Hydrothermal synthesis of various hierarchical ZnO nanostructures and their methane sensing properties. *Sensors* 13, 6171–6182. doi: 10.3390/s130506171

Zhou, Q., Lu, Z., Wei, Z., Xu, L., Gui, Y., and Chen, W. (2018b). Hydrothermal synthesis of hierarchical ultrathin NiO nanoflakes for high-performance CH_4 sensing. *Front. Chem.* 6:194. doi: 10.3389/fchem.2018.00194

Zhou, Q., Tang, C., Zhu, S. P., and Chen, W. G. (2015). NiO doped SnO_2 p-n heterojunction microspheres: preparation, characterisation and CO sensing properties. *Mater. Technol.* 30, 349–355. doi: 10.1179/1753555715Y.0000000010

Zhou, Q., Umar, A., Sodki, E., Amine, A., Xu, L. N., Gui, Y. G., et al. (2018c). Fabrication and characterization of highly sensitive and selective sensors based on porous NiO nanodisks. *Sensor. Actuat. B. Chem.* 259, 604–615. doi: 10.1016/j.snb.2017.12.050

Zhou, Q., Xu, L., Umar, A., Chen, W., and Kumar, R. (2018d). Pt nanoparticles decorated SnO_2 nanoneedles for efficient CO gas sensing applications. *Sensor. Actuat. B-Chem.* 256, 656–664. doi: 10.1016/j.snb.2017.09.206

Zhu, L., Li, Y. Q., and Zeng, W. (2017). Enhanced ethanol sensing and mechanism of Cr-doped ZnO nanorods: experimental and computational study. *Ceram. Int.* 43, 14873–14879. doi: 10.1016/j.ceramint.2017.08.003

Zhu, L., Zeng, W., Ye, H., and Li, Y. Q. (2018). Volatile organic compound sensing based on coral rock-like ZnO. *Mater. Res. Bull.* 100, 259–264. doi: 10.1016/j.materresbull.2017.12.043

Zou, C. W., Wang, J., and Xie, W. (2016). Synthesis and enhanced NO_2 gas sensing properties of ZnO nanorods/TiO_2 nanoparticles heterojunction composites. *J. Colloid Interf. Sci.* 478, 22–28. doi: 10.1016/j.jcis.2016.05.061

Zuo, Z. J., Wang, L., Liu, Y.-J., and Huang, W. (2013). The effect of CuO–ZnO–Al_2O_3 catalyst structure on the ethanol synthesis from syngas. *Catal. Commun.* 34, 69–72. doi: 10.1016/j.catcom.2013.01.008

Conflict of Interest Statement: The authors declare that the research was conducted in the absence of any commercial or financial relationships that could be construed as a potential conflict of interest.

frontiers in Chemistry

MINI REVIEW
published: 22 October 2018
doi: 10.3389/fchem.2018.00508

Gas Sensing Performances of ZnO Hierarchical Structures for Detecting Dissolved Gases in Transformer Oil: A Mini Review

He Zhang[1], Wei-Gen Chen[1]*, Yan-Qiong Li[2] and Zi-Hao Song[1]*

[1] State Key Laboratory of Power Transmission Equipment & System Security and New Technology, School of Electrical Engineering, Chongqing University, Chongqing, China, [2] School of Electronic and Electrical Engineering, Chongqing University of Arts and Sciences, Chongqing, China

Power transformer is one of the critical and expensive apparatus in high voltage power system. Hence, using highly efficient gas sensors to real-time monitor the fault characteristic gases dissolved in transformer oil is in pressing need to ensure the smooth functionalization of the power system. Till date, as a semiconductor metal oxide, zinc oxide (ZnO) is considered as the promising resistive-type gas sensing material. However, the elevated operating temperature, slow response, poor selectivity and stability limit its extensive applications in the field of dissolved gases monitoring. In this respect, rigorous efforts have been made to offset the above-mentioned shortcomings by multiple strategies. In this review, we first introduce the various ZnO hierarchical structures which possess high surface areas and less aggregation, as well as their corresponding gas sensing performances. Then, the primary parameters (sensitivity, selectivity and stability) which affect the performances of ZnO hierarchical structures based gas sensors are discussed in detail. Much more attention is particularly paid to the improvement strategies of enhancing these parameters, mainly including surface modification, additive doping and ultraviolet (UV) light activation. We finally review gas sensing mechanism of ZnO hierarchical structure based gas sensor. Such a detailed study may open up an avenue to fabricate sensor which achieve high sensitivity, good selectivity and long-term stability, making it a promising candidate for transformer oil monitor.

Keywords: ZnO, gas sensors, hierarchical structures, sensitivity, selectivity, stability, gas sensing mechanism

OPEN ACCESS

Edited by:
Zhongchang Wang, Laboratório Ibérico Internacional de Nanotecnologia (INL), Portugal

Reviewed by:
Ming-Guo Ma, Beijing Forestry University, China
Tianming Li, Leibniz-Institut für Festkörper-und Werkstoffforschung (IFW Dresden), Germany

****Correspondence:***
He Zhang
sophy305410@163.com
Wei-Gen Chen
weigench@cqu.edu.cn

Specialty section:
This article was submitted to Nanoscience, a section of the journal Frontiers in Chemistry

Received: *10 August 2018*
Accepted: *03 October 2018*
Published: *22 October 2018*

Citation:
Zhang H, Chen W-G, Li Y-Q and Song Z-H (2018) Gas Sensing Performances of ZnO Hierarchical Structures for Detecting Dissolved Gases in Transformer Oil: A Mini Review. Front. Chem. 6:508. doi: 10.3389/fchem.2018.00508

INTRODUCTION

Power transformer is one of the most critical and expensive devices in high voltage power system (Christina et al., 2018). Generally, oil is used inside the transformer for its operation and can release different fault characteristic gases, such as hydrogen (H_2), carbon oxides (CO, CO_2) and hydrocarbons (CH_4, C_2H_2, C_2H_4, and C_2H_6). Hence, real-time detection of dissolved gases in transformer oil is very essential in order to avoid unexpected failures (Mariprasath and Kirubakaran, 2018). At present, dissolved gas analysis (DGA) remains to be the simplest and most effective diagnostic method for checking latent faults of oil-immersed power transformers (Siada and Hmood, 2015; Fan et al., 2018). Therefore, using highly efficient gas sensors to real-time monitor these dissolved gases in transformer oil is a feasible way to ensure the stability and reliability of power system (Uddin et al., 2016).

Different types of gas sensors have already been applied in the online detection of dissolved gases in transformer oil, such as resistance-type (Benounis et al., 2008; Sun et al., 2015), optical-type (Ma et al., 2012) and electrochemical-type (Ding et al., 2014). Among diverse types of gas sensors, resistance-based sensors stand out owing to advantages like the small, cheap, high sensitivity and low power consumption (Bodzenta et al., 2002; Yang et al., 2011; Zhao et al., 2017; Xu et al., 2018). With the increasing demand for better gas sensors of higher sensitivity and selectivity (Sun et al., 2012; Gardon and Guilemany, 2013), countless endeavors have been poured on hunting for more suitable sensing nanomaterials. Semiconductor metal oxides (MOS), such as zinc oxide (ZnO), tin oxide (SnO_2), tungsten oxide (WO_3), etc., have received wide research for gas sensing applications and so on. Among these, the gas sensing performance of ZnO-based gas sensor was first investigated by Seiyama et al. (1962). As a typical n-type semiconductor material with a direct wide band gap (Eg $\approx$ 3.37 ev) and large excitation binding energy ($\sim$60 mev), ZnO has got important status in various MOS nanomaterials due to its high carrier mobility of conduction electrons, good chemical and thermal stability (Zeng et al., 2015; Das and Sarkar, 2017; Ganesh et al., 2017).

The gas sensing properties of ZnO greatly depend on its structure and morphology including surface area, size, orientation and crystal density (Cho et al., 2011). Therefore, tailoring the structure and morphology of ZnO is particularly important to optimize the gas sensing performances (Liao et al., 2008). In particular, the elaborate design of unique three-dimensional (3D) hierarchical architectures can fully achieve this, since such hierarchical structures possess high surface area and fast gas diffusion as well as reduce the agglomerated configuration of low dimensional structures.

ZnO-based gas sensors commonly have the shortcomings of slow response, poor selectivity and lack of long-term stability, which limits the wide applications. To acquire an efficient and reliable dissolved gases sensor, high sensitivity, selectivity, long-term stability, low response / recovery time, low fabrication cost are urgently needed (Wang et al., 2012). This review focuses on the factors that affect the performances (sensitivity, selectivity and stability), the methods to improve these sensor parameters and gas sensing mechanism of ZnO-based gas sensors.

GAS SENSING PERFORMANCES OF ZnO-BASED GAS SENSOR

Effects of Morphologies About ZnO Hierarchical Structures on Gas Sensing Performances

Three-dimensional (3D) hierarchical structures are generally recognized as the best candidate for gas sensing performances, compared with low-dimensional structures (Mo et al., 2008; Guo, 2016). They are defined as those assembled by zero-dimensional (0D), one-dimensional (1D) and two-dimensional (2D) components, which can be further classified into the following sub-sections. (1) Assembly of 0D structures: Li W. Q. et al. (2015) reported the synthesis of pure ZnO hollow nanofibers by electrospinning method. The walls of ZnO nanofibers consist of the aggregation of many individual nanoparticles, as shown in **Figure 1A**. The sensor based on ZnO hollow nanofibers exhibits excellent sensing performance for acetone detection, which can be attributed to the large aperture and small diameters provide higher specific surface area for gas adsorption. Chen H. et al. (2016) synthesized the uniformly monodispersed ZnO nanospheres via a simply hydrothermal route. In particular, all the microparticles on the surface are sphere-shapes and have a rough surface, as shown in **Figure 1B**. This unique porous structure exhibits perfect sensing performance toward ethanol. (2) Assembly of 1D structures: Lin et al. (2015) reported the hierarchical ZnO microstructures by hydrothermal method. The morphology of the sample likes a bunch of flowers which is made of uniform nanorods, as shown in **Figure 1C**. The sensor based on the sample shows a good response. Chen H. et al. (2016) reported the sea-urchin-like ZnO nanostructures by hydrothermal method. The sample is composed of many strips and radiates from the center, as shown in **Figure 1D**. The sensor based on the ZnO sample toward ethanol exhibits high sensitivity and quick response. (3) Assembly of 2D structures: Gu et al. (2011) reported the porous flower-like ZnO nanostructures by economical hydrothermal synthesis combined with subsequent calcination. Calcination of the precursors produced flower-like ZnO nanostructures which composed of interconnected porous ZnO nanosheets with high porosity, as shown in **Figure 1E**. The as-prepared flower-like ZnO nanostructures are highly promising candidate for applications of gas sensors. Han et al. (2016) reported the ZnO hollow spheres with high crystallinity via a simple template process, as shown in **Figure 1F**. The surfaces of these core-shell spheres are rough, suggesting that polystyrene sphere (PSS) core was coated by ZnO nanoparticles. The sensor based on ZnO hollow spheres exhibits good sensing performances.

In this part, the authors make a brief introduction with respect to the hierarchical structures. Hierarchical hollow or porous ZnO structures exhibit excellent properties for gas sensor applications (Guo et al., 2011, 2012, 2013). These unique hollow structures with large specific surface area and highly porous structures can provide excellent channel and "surface accessibility" for the gas transportation, which is very favorable for facilitating the interaction of ZnO surface with the gas molecules (Gu et al., 2011). No matter how complicated the hierarchical structure, it's all derived from low dimensional nanostructures as building blocks. Hence, the investigation about regulating the structure and morphology is a meaningful and challenge work.

A summary about factors affecting gas sensing performances of ZnO-based gas sensors and improvement approaches is shown in **Table 1**. The details are described in sections Factors affecting the sensitivity of ZnO hierarchical structure based Gas sensor, Factors affecting the selectivity of ZnO hierarchical structure based Gas sensor, and Factors affecting the long-term stability of ZnO hierarchical structure based Gas sensor as follows.

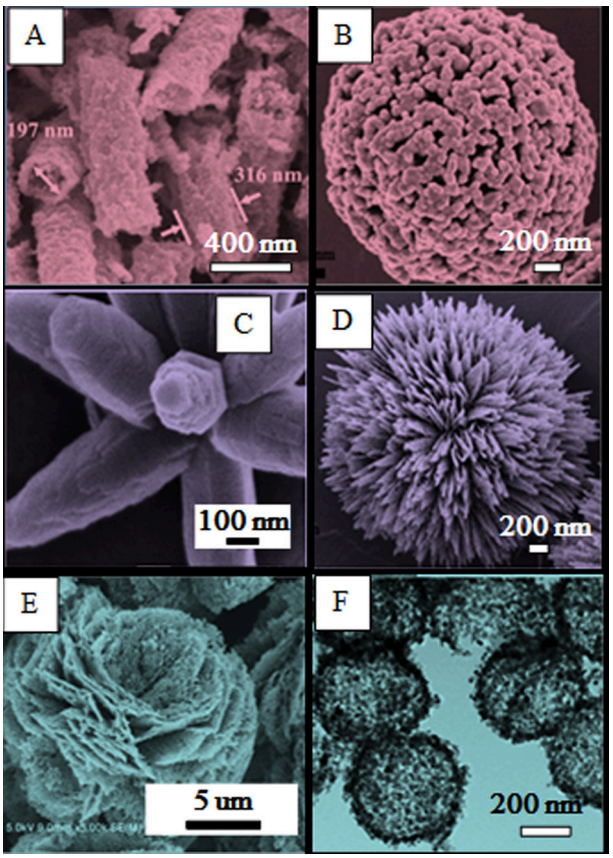

FIGURE 1 | ZnO with different 3D hierarchical structures: **(A)** Nanofibers assembly by 0D structures. Reprinted with permission from Li X. et al. (2015). Copyright (2015) Elsevier Science BV. **(B)** Nanospheres assembly by 0D structures. Reprinted with permission from Chen H. et al. (2016). Copyright (2016) Elsevier Science SA. **(C)** Flower-like microstructure assembly by 1D structures. Reprinted with permission from Lin et al. (2015). Copyright (2015) Elsevier Science SA. **(D)** Sea-urchin-like ZnO nanostructures assembly by 1D structures. Reprinted with permission from Chen H. et al. (2016). Copyright (2016) Elsevier Science SA. **(E)** Porous flower-like ZnO nanostructures assembly by 2D structures. Reprinted with permission from Gu et al. (2011). Copyright (2011) Elsevier Science SA. **(F)** Core-shell hollow spheres assembly by 2D structures. Reprinted with permission from Han et al. (2016). Copyright (2016) Elsevier Science SA.

Factors Affecting the Sensitivity of ZnO Hierarchical Structure Based Gas Sensor

Recently, numerous reports confirmed that ZnO-based nanomaterials are promising candidates for the fabrication of gas sensors (Gu et al., 2013; Wang et al., 2014). Given this, a number of strategies have been proposed for enhancing the gas sensitivity. It can be introduced from the following four aspects.

- Modulation of the dimensional and the exposed crystal facet of their constituting building blocks.

Zhang et al. (2009) synthesized brush-like hierarchical ZnO nanostructures. The FESEM image (**Supplementary Figure 1A**) shows that this structure is composed of 6-fold nanorod arrays grown on the side surface of core nanowires. The central stems provide its six prismatic facets as growth platforms for branching of multipod units. The sensor based on these structures shows high sensitivity and fast response.

- Enhance the porosity of hierarchical structures.

Lei et al. (2017) successfully synthesized hierarchical porous ZnO microspheres assembled from 2D nanosheets. The high specific surface area and hierarchical pore structure are beneficial to increase the adsorption capacity (**Supplementary Figure 1B**). Song et al. (2018) reported hierarchical porous ZnO microflowers which composed of ultrathin nanosheets. From the SEM image (**Supplementary Figure 1C**), we can see that the surface of nanosheet has lots of pores. The porous structure is favorable for gas sensor to promote the inward/outward gas diffusion and improve gas sensitivity.

- Modification by doping with noble metals and loading other n-type or p-type MOS materials.

It's known that noble metals, such as Pt (Rout et al., 2006), Pd (Yang et al., 2010) and Au (Vallejos et al., 2011) are frequently used in gas sensing materials due to doping can sensitize the ZnO electronic and structural properties. Lin et al. (2015) reported that Au nanoparticles were decorated on the surface of hierarchical flower-like ZnO microstructures, as shown in **Supplementary Figure 1D**. After Au nanoparticle-decoration,

TABLE 1 | A summary about factors affecting gas sensing performances of ZnO hierarchical structure based gas sensors and improvement approaches.

Main characteristic indexes which reflect the performances	Influencing factors and improvement approaches	References
Sensitivity	Modulation of the dimensional and the exposed crystal facet of their constituting building blocks	Zhang et al., 2009
	Enhance the porosity of hierarchical structures	Lei et al., 2017; Song et al., 2018
	Modification by doping with noble metals and loading other n-type or p-type MOS materials	Lin et al., 2015
	Control of grain size	Mirzaei et al., 2018
Selectivity	Dope with noble metals and p-type metal oxides	Li T. M. et al., 2015
	Lower the operating temperature by activating the sensing material under UV illumination	Chen Y. et al., 2016; Espid and Taghipour, 2017
Long-term stability	Calcination/annealing as the post-processing treatment	Gu et al., 2011
	Reduce the working temperature of gas sensing element	Chen Y. et al., 2016
	Dope noble metal or synthesis of mixed oxides	Dey, 2018

the specific surface area is much higher than that of the bare ZnO (**Figure 1C**). Au nanoparticles can act as catalysts to accelerate the chemisorption process and greatly improve the sensitivity. So far, heterostructure composites consisting of two metal oxides, such as (n-n type) SnO_2/ZnO (Park et al., 2013) and (n-p type) NiO/ZnO, AgO/ZnO (Gandomania et al., 2014) have been successfully prepared and have improved the sensitivity. Liu et al. (2017) reported the NiO nanoparticles which were decorated onto the surfaces of well-dispersed ZnO hollow spheres (**Supplementary Figures 1E,F**). Such hollow structures with rough surfaces endow the NiO/ ZnO composites high surface areas and abundant active sites, which could facilitate the gas diffusion toward the entire materials and an improvement of the sensitivity (Lee, 2009).

- Control of grain size.

Previous research found that sensors which consist of fine particles of MOS tend to exhibit high sensitivity. Thus, one of the most important factors affecting the sensitivity is grain size (D) of the sensor materials in conjunction with the thickness of the space charge layer (L). **Supplementary Figure 1G** illustrates three kinds of schematic models for grain-size effects (Shimizu and Egashira, 1999). When $D >> 2L$, the conductance is limited by Schottky barrier at grain boundaries (grain boundary control). If $D \geq 2L$, the conductance is limited by necks between grains (neck control). When $D < 2L$, the conductance is controlled by grains themselves (grain control). Among three models, grain control is the most sensitive condition (Mirzaei et al., 2018). The smaller the grain size, the higher the sensitivity of gas sensor. But, excessive decrease in grain size can reduce structural stability.

Factors Affecting the Selectivity of ZnO Hierarchical Structure Based Gas Sensor

Selectivity is the ability of gas sensor to recognize the target gas in a mixture of other gases. Generally, there are two approaches for enhancing the selectivity of gas sensor. The first one is to synthesize a material which is selective to the specific compound and has very low cross-sensitivity for other compounds. Moreover, the synergistic effect of two component system is greater than the production effect of the two elements. In fact, noble metals and p-type metal oxides have been extensively applied as good catalysts in the two component systems to promote selectivity of sensors (Li T. M. et al., 2015). Another approach to improve the selectivity is to combine with other methods. Recently, some reports have suggested that lowering the operating temperature can be realized by activating the sensing material under UV illumination (Helwig et al., 2009; Lu et al., 2012; Cui et al., 2015). The possible UV-activated selective photo catalysis plays an important role in the enhancement of the selectivity at low temperature (Li X. et al., 2015). It can be explained based on the selective photocatalytic oxidation. The adsorbed oxygen would be re-activated by the photon generated electron-hole pairs, which is conductive to enhancing their reactivity with target gas. After the target gas reacted with the adsorbed oxygen on ZnO surface, the donated electrons would thus decrease resistance of the sensor and finally reduce the operating temperature (Ho et al., 2015). Chen et al. reported that the mesoporous hollow ZnO microspheres were applied to detect volatile organic vapors (VOCs) with the help of UV LED illumination at lower temperatures (Chen Y. et al., 2016). The sensor with UV activation at 80°C shows a much higher response to ethanol (**Supplementary Figure 2A**). When the sensor was operated at 220°C, the UV illumination became ineffective. It shows almost same response to ethanol and acetone (**Supplementary Figure 2B**). This is because the difference about catalytic conversion of O^{2-} would have negligible toward them at 220°C. However, the O^{-} possibly indicated higher preference to ethanol at 80°C, resulting in the better selectivity. When metal doped-ZnO was illuminated by UV light, the sensor had an appreciable selectivity at low temperature, which was attributed to the heterostructure was in favor of chemical interactions, adsorption of gases and changes in electronic bind energies in the composite (Chen et al., 2008). Espid investigated the photo-responsive behavior of ZnO/ In_2O_3 composite sensors (Espid and Taghipour, 2017). When the semiconductor composites are irradiated with photons emitted from a UV source, the photo-generated electron/hole pairs will enhance the conductance of the sensing layer and improve the selectivity.

Factors Affecting the Long-Term Stability of ZnO Hierarchical Structure Based Gas Sensor

Stability is a key parameter for the long-term development of gas sensors, which determines its application state in the real market. Generally, the long-term stability refers to the attenuation degree of gas sensing performances (e.g., sensitivity, selectivity, response and recovery time) during a certain period of time. When the sensor is in working state, working conditions including high temperature and toxic gases can reduce the stability. When the sensor is in normal storage state, changes of humidity, fluctuations of temperature in the surrounding atmosphere may also interfere with the stability of sensor. At present, there is not a recognized method to improve stability of ZnO-based gas sensors. Stability can be increased to some extent by calcination/ annealing as the post-processing treatment (Gu et al., 2011) and reducing the working temperature of gas sensing element. Chen et al. tested the long-term stability of ZnO-based sensor working at 80°C with UV activitation (Chen Y. et al., 2016). The sensor test lasted 1 month (**Supplementary Figure 2C**). In the first 2 days, the response values dropped significantly, which might be related to the "pre-aging" effect. In the next few days, the sensor response became stabilized and showed a good long-term stability. It might be because the microstructure of the materials had little change under low temperature with low-powered UV activation. In addition, doping noble metal or synthesis of mixed oxides can also increase the stability of the sensors (Dey, 2018).

GAS SENSING MECHANISM OF ZnO HIERARCHICAL STRUCTURE BASED GAS SENSOR

By summarizing the methods to improve the gas sensing performances in section Gas Sensing Performances of ZnO-Based Gas Sensor, we find that metal doping is an excellent

method to promote sufficient reaction between sensing material and target gas.

The gas sensing mechanism of noble metals doped-ZnO hierarchical structures based gas sensors is explained as an example. This process mainly involves two effects: chemical effect and electronic effect (Zhu and Zeng, 2017). Firstly, the chemical effect is related to spillover process (Nakate et al., 2016). Oxygen molecules were adsorbed on the surface and grain boundary of ZnO, forming the oxygen ions. The sensitization of noble metals increases the quantity of oxygen species and accelerates the surface reaction, causing an expansion of charge depletion layer, which results in a higher baseline resistance (**Supplementary Figures 3A,B**). When the reducing gas is introduced, the catalysis of noble metals may give rise to the dissociation of target gas molecules. The trapped electrons are released and transmitted to the conduction band, resulting in a remarkable decrease in depletion layer with a lower resistance. Secondly**,** the electric effect is produced by contact resistance of noble metal modified ZnO gas sensors (Hosseini et al., 2015). Electrons from the conduction band of ZnO transfer into noble metals owing to their work functions are different, forming the Schottky barriers at noble metal-ZnO interface, which leading to generate the additional depletion region near ZnO surface (**Supplementary Figure 3C**).

Therefore, the enhanced sensing performance was ascribed to the spillover phenomenon, the formation of Schottky barriers at the interface between noble metals and ZnO, more introduced surface active sites and effective surface areas (Hosseini et al., 2015).

CONCLUSION

A study on gas sensing performances of ZnO hierarchical structures has been shortly summarized in this review. Firstly, unique 3D hierarchical architectures with high sensing capabilities are discussed by modifying surface morphologies. Small grain size, high effective specific surface area and porosity are favorable to the enhancement of gas sensing performances. Therefore, the preparation of the desired 3D hierarchical structure can lay a solid foundation for the development of gas sensor. Then, factors that affect the sensitivity, selectivity and stability of ZnO hierarchical structures based gas sensors and their improvement strategies are summarized separately. Among these methods, additive doping and UV-light irradiation are more effective methods to improve gas sensing performances. The former can increase charge carrier concentration and decrease activation energy. The latter can promote the catalytic oxidation reaction between target gases and oxygen ions, thus reduce the working temperature and power consumption. Numerous reports indicate that the integration of metal doped-oxide and UV excitation is one of the most effective and workable attempts to achieve high sensor performances. The composite oxides based sensors under UV illumination have better charge separation, which benefit for the gas performances enhancement of the sensors. We hope our work is helpful for further exploration on higher gas sensing performances of MOS sensing materials for detecting dissolved fault gases in transformer oil. Finally, gas sensing mechanism of noble metal sensitized ZnO is illuminated from the point of view of chemical effect and electronic effect. Nevertheless, the authors suggest only a few possible ways to improve the existed oxygen-absorbed model in recent researchers. Much effort should be made to hunt for an integration of different models which was used to explain the gas sensing reaction.

AUTHOR CONTRIBUTIONS

HZ and W-GC conceived and designed the experiments, HZ and Y-QL performed the experiments, HZ and Z-HS analyzed the data, HZ wrote the manuscript with input from all authors. All authors read and approved the manuscript.

ACKNOWLEDGMENTS

This work was supported by the Science Fund for Creative Research Groups of the National Natural Science Foundation of China (Grant No. 51321063), the Joint Fund of the National Natural Science Foundation of China and the Smart Grid of State Grid Corporation of China (Grant No. U1766217), and the Scientific Research Fund of Chongqing University of Arts and Sciences (2017RDQ38).

SUPPLEMENTARY MATERIAL

The Supplementary Material for this article can be found online at: https://www.frontiersin.org/articles/10.3389/fchem.2018.00508/full#supplementary-material

REFERENCES

Benounis, T. M., Ngnui, T. A., Jaffrezic, N., and Dutasta, J. P. (2008). NIR and optical fiber sensor for gases detection produced by transformation oil degradation. *Sens. Actuators A Phys.* 141, 76–83. doi: 10.1016/j.sna.2007.07.036

Bodzenta, J., Burak, B., Gacek, Z., Jakubik, W. P., Kochowski, S., and Urbanczyk, M. (2002). Thin palladium film as a sensor of hydrogen gas dissolved in transformer oil. *Sens. Actuators B Chem.* 87, 82–87. doi: 10.1016/S0925-4005(02)00221-6

Chen, H., Ma, S. Y., Jiao, H. Y., Yang, G. J., Xu, X. L., Wang, T. T., et al. (2016). The effect microstructure on the gas properties of Ag doped zinc oxide sensors: spheres and sea-urchin-like nanostructures. *J. Alloy Compd.* 687, 342–351. doi: 10.1016/j.jallcom.2016.06.153

Chen, L. Y., Bai, S. L., Zhou, G. J., Li, D. Q., Chen, A. F., and Chung, C. L. (2008). Synthesis of ZnO-SnO_2 nanocomposites by microemulsion and sensing properties for NO_2. *Sens. Actuators B Chem.* 134, 360–366. doi: 10.1016/j.snb.2008.04.040

Chen, Y., Li, X. G., Li, X. X., Wang, J., and Tang, Z. N. (2016). UV activated hollow ZnO microspheres for selective ethanol sensors at low temperatures. *Sens. Actuators B Chem.* 232, 158–164. doi: 10.1016/j.snb.2016.03.138

Cho, S., Kim, S., Jung, D. W., and Lee, K. H. (2011). Formation of quasi-single crystalline porous ZnO nanostructures with a single large cavity. *Nanoscale* 3, 3841–3848. doi: 10.1039/c1nr10609k

Christina, A. J., Salam, M. A., Rahman, Q. M., Wen, F. S., Ang, S. P., and Voon, W. (2018). Causes of transformer failures and diagnostic methods: a review. *Renew. Sust. Energ. Rev.* 82, 1442–1456. doi: 10.1016/j.rser.2017.05.165

Cui, J. B., Shi, L. Q., Xie, T. F., Wang, D. J., and Lin, Y. H. (2015). UV-light illumination room temperature HCHO gas-sensing mechanism of ZnO with different nanostructures. *Sens. Actuators B Chem.* 227, 220–226. doi: 10.1016/j.snb.2015.12.010

Das, M., and Sarkar, D. (2017). One-pot synthesis of zinc oxide-polyaniline nanocomposite for fabrication of efficient room temperature ammonia gas sensor. *Ceram. Int.* 43, 11123–11131. doi: 10.1016/j.ceramint.2017.05.159

Dey, A. (2018). Semiconductor metal oxide gas sensors: a review. *Mater. Sci. Eng. B* 229, 206–217. doi: 10.1016/j.mseb.2017.12.036

Ding, J., Li, X., Cao, J., Sheng, L., Yin, L., and Xu, X. (2014). New sensor for gases dissolved in transformer oil based on solid oxide fuel cell. *Sens. Actuators B Chem.* 202, 232–239. doi: 10.1016/j.snb.2014.05.061

Espid, E., and Taghipour, F. (2017). Development of highly sensitive ZnO/In_2O_3 composite gas sensor activated by UV-LED. *Sens. Actuators B Chem.* 241, 828–839. doi: 10.1016/j.snb.2016.10.129

Fan, J. M., Wang, F., Sun, Q. Q., Ye, H. S., and Jiang, Q. J. (2018). Application of polycrystalline SnO_2 sensor chromatographic system to detect dissolved gases in transformer oil. *Sens. Actuators B Chem.* 267, 636–646. doi: 10.1016/j.snb.2018.04.014

Gandomania, S. K., Yousefib, R., Sheinic, F. J., and Huang, N. M. (2014). Optical and electrical properties of p-type Ag-doped ZnO nanostructures. *Ceram. Int.* 40, 7957–7963. doi: 10.1016/j.ceramint.2013.12.145

Ganesh, R. S., Durgadevi, E., Navaneethan, M., Patil, V. L., Ponnusamy, S., Muthamizhchelvan, C., et al. (2017). Low temperature ammonia gas sensor based on Mn-doped ZnO nanoparticle decorated microspheres. *J. Alloys Compd.* 721, 182–190. doi: 10.1016/j.jallcom.2017.05.315

Gardon, M., and Guilemany, J. M. (2013). A review on fabrication, sensing mechanisms and performance of metal oxide gas sensors. *J. Mater. Sci. Mater. Electron.* 24, 1410–1421. doi: 10.1007/s10854-012-0974-4

Gu, C. P., Huang, J. R., Wu, Y. J., Zhai, M. H., Sun, Y. F., Liu, J. H., et al. (2011). Preparation of porous flower-like ZnO nanostructures and their gas-sensing property. *J. Alloy Compd.* 509, 4499–4504. doi: 10.1016/j.jallcom.2010.11.078

Gu, C. P., Li, S. S., Huang, J. R., Shi, C. C., and Liu, J. H. (2013). Preferential growth of long ZnO nanowires and its application in gas sensor. *Sens. Actuators B Chem.* 177, 453–459. doi: 10.1016/j.snb.2012.11.044

Guo, W. W. (2016). ZnO nanosheets assembled different hierarchical structures and their gas sensing properties. *J Mater Sci. Mater. Electron.* 27, 7302–7310. doi: 10.1007/s10854-016-4699-7

Guo, W. W., Liu, T. M., Sun, R., Chen, Y., Zeng, W., and Wang, Z. C. (2013). Hollow, porous, and yttrium functionalized ZnO nanospheres with enhanced gas-sensing performances. *Sens. Actuators B Chem.* 178, 53–62. doi: 10.1016/j.snb.2012.12.073

Guo, W. W., Liu, T. M., Zeng, W., Liu, D. J., Chen, Y., and Wang, Z. C. (2011). Gas-sensing property improvement of ZnO by hierarchical flower-like architectures. *Mater. Lett.* 65, 3384–3387. doi: 10.1016/j.matlet.2011.07.059

Guo, W. W., Liu, T. M., Zhang, H. J., Sun, R., Chen, Y., Zeng, W., et al. (2012). Gas-sensing performance enhancement in ZnO nanostructures by hierarchical morphology. *Sens. Actuators B Chem.* 166, 492–499. doi: 10.1016/j.snb.2012.02.093

Han, B. Q., Liu, X., Xing, X. X., Chen, N., Xiao, X. C., Liu, S. Y., et al. (2016). A high response butanol gas sensor based on ZnO hollow spheres. *Sens. Actuators B Chem.* 237, 423–430. doi: 10.1016/j.snb.2016.06.117

Helwig, A., Müller, G., Sberveglieri, G., and Eickhoff, M. (2009). On the low-temperature response of semiconductor gas sensors. *J. Sens.* 2009, 1–17. doi: 10.1155/2009/620720

Ho, Y. H., Huang, W. S., Chang, H. C., Wei, P. K., Sheen, H. J., and Tian, W. C. (2015). Ultraviolet-enhanced room-temperature gas sensing by using floccule-like zinc oxide nanostructures. *Appl. Phys. Lett.* 106, 1831031–1831034. doi: 10.1063/1.4919921

Hosseini, Z. S., Mortezaali, A., Iraji, A., and Fardindoost, S. (2015). Sensitive and selective room temperature H_2S gas sensor based on Au sensitized vertical ZnO nanorods with flower-like structures. *J. Alloys Compd.* 628, 222–229. doi: 10.1016/j.jallcom.2014.12.163

Lee, J. H. (2009). Gas sensors using hierarchical and hollow oxide nanostructures: overview. *Sens. Actuators B Chem.* 140, 319–336. doi: 10.1016/j.snb.2009.04.026

Lei, C. S., Pi, M., Jiang, C. J., Cheng, B., and Yu, J. G. (2017). Synthesis of hierarchical porous zinc oxide (ZnO) microspheres with highly efficient adsorption of Congo red. *J. Colloid Interrface Sci.* 490, 242–251. doi: 10.1016/j.jcis.2016.11.049

Li, T. M., Zeng, W., and Wang, Z. C. (2015). Quasi-one-dimensional metal-oxide-based heterostructural gas-sensing materials: a review. *Sens. Actuators B Chem.* 221, 1570–1585. doi: 10.1016/j.snb.2015.08.003

Li, W. Q., Ma, S. Y., Yang, G. J., Mao, Y. Z., Luo, J., Cheng, L., et al. (2015). Preparation, characterization and gas sensing properties of pure and Ce doped ZnO hollow nanofibers. *Mater. Lett.* 138, 188–191. doi: 10.1016/j.matlet.2014.09.130

Li, X., Li, X., Wang, J., and Lin, S. (2015). Highly sensitive and selective room-temperature formaldehyde sensors using hollow TiO_2 microspheres, *Sens. Actuators B Chem.* 219, 158–163. doi: 10.1016/j.snb.2015.05.031

Liao, L., Mai, H. X., Yuan, Q., Lu, H. B., Li, J. C., Liu, C., et al. (2008). Single CeO_2 nanowire gas sensor supported with Pt nanocrystals: gas sensitivity, surface bond states, and chemical mechanism. *J. Phys. Chem. C* 112, 9061–9065. doi: 10.1021/jp7117778

Lin, Y., Wei, W., Wang, Y., Zhou, J. R., Sun, D. M., Zhang, X. D., et al. (2015). Highly stabilized and rapid sensing acetone sensor based on Au nanoparticle-decorated flower-like ZnO microstructures. *J. Alloy Compd.* 650, 37–44. doi: 10.1016/j.jallcom.2015.07.242

Liu, C., Zhao, L. P., Wang, B. Q., Sun, P., Wang, Q. J., Gao, Y., et al. (2017). Acetone gas sensor based on NiO/ZnO hollow spheres: Fast response and recovery, and low (ppb) detection limit. *J. Colloid Interrface Sci.* 495, 207–215. doi: 10.1016/j.jcis.2017.01.106

Lu, G. Y., Xu, J., Sun, J. B., Yu, Y. S., Zhang, Y. Q., and Liu, F. M. (2012). UV-enhanced room temperature NO_2 sensor using ZnO nanorods modified with SnO_2 nanoparticles. *Sens. Actuators B Chem.* 162, 82–88. doi: 10.1016/j.snb.2011.12.039

Ma, G. M., Li, C. R., Luo, Y. T., Mu, R. D., and Wang, L. (2012). High sensitive and reliable fiber bragg grating hydrogen sensor for fault detection of power transformer. *Sens. Actuators B Chem.* 169, 195–198. doi: 10.1016/j.snb.2012.04.066

Mariprasath, T., and Kirubakaran, V. (2018). A real time study on condition monitoring of distribution transformer using thermal imager. *Infrared Phys. Technol.* 90, 78–86. doi: 10.1016/j.infrared.2018.02.009

Mirzaei, A., Kim, J. H., Kim, H. W., and Kim, S. S. (2018). How shell thickness can affect the gas sensing properties of nanostructured materials: Survey of literature. *Sens. Actuators B Chem.* 258, 270–294. doi: 10.1016/j.snb.2017.11.066

Mo, M. S., Lim, S. H., Mai, Y. W., Zheng, R. K., and Ringer, S. P. (2008). *In situ* self-assembly of thin ZnO nanoplatelets into hierarchical mesocrystal microtubules with surface grafting of nanorods: a general strategy towards hollow mesocrystal structures. *Adv. Mater.* 20, 339–342. doi: 10.1002/adma.200701137

Nakate, U. T., Patil, P., Bulakhe, R. N., Lokhande, C. D., Kale, S. N., Naushad, M., et al. (2016). Sprayed zinc oxide films: ultra-violet light-induced reversible surface wettability and platinum-sensitization-assisted improved liquefied petroleum gas response. *J. Colloid Interface Sci.* 480, 109–117. doi: 10.1016/j.jcis.2016.07.010

Park, S., An, S., Mun, Y., and Lee, C. (2013). UV-enhanced NO_2 gas sensing properties of SnO_2-core/ZnO-shell nanowire at room temperature. *ACS Appl. Mater. Interf.* 5, 4285–4292. doi: 10.1021/am400500a

Rout, C. S., Govindaraj, A., and Rao, C. (2006). High-sensitivity hydrocarbon sensors based on tungsten oxide nanowires. *J. Mater. Chem.* 16, 3936–3941. doi: 10.1039/B607012B

Seiyama, T., Kato, A., Fujiishi, K., and Nagatani, M. (1962). A new detector for gaseous components using semiconductive thin films. *Anal. Chem.* 34, 1502–1503. doi: 10.1021/ac60191a001

Shimizu, Y., and Egashira, M. (1999). Basic aspects and challenges of semiconductor gas sensors. *MRS Bull.* 24, 18–24. doi: 10.1557/S0883769400052465

Siada, A. A., and Hmood, S. (2015). A new fuzzy logic approach to identify power transformer criticality using dissolved gas-in-oil analysis. *Int. J. Electr. Power* 67, 401–408. doi: 10.1016/j.ijepes.2014.12.017

Song, L. M., Yue, H., Li, H. Y., Liu, L., Li, Y., Du, L. T., et al. (2018). Hierarchical porous ZnO microflowers with ultra-high ethanol gas sensing at low concentration. *Chem. Phys. Lett.* 699, 1–7. doi: 10.1016/j.cplett.2018.03.021

Sun, R., Wang, Z. C., Saito, M., Shibata, N., and Ikuhara, Y. (2015). Atomistic mechanisms of nonstoichiometry-induced twin boundary structural transformation in titanium dioxide. *Nat. Commun.*, 6, 7120–7126. doi: 10.1038/ncomms8120

Sun, Y. F., Liu, S. B., Meng, F. L., Liu, J. Y., Jin, Z., Kong, L. T., et al. (2012). Metal oxide nanostructures and their gas sensing properties: a review. *Sensors* 12, 2610–2631. doi: 10.3390/s120302610

Uddin, A., Yaqoob, U., and Chung, G. S. (2016). Dissolved hydrogen gas analysis in transformer oil using Pd catalyst decorated on ZnO nanorod array. *Sens. Actuators B Chem.* 226, 90–95. doi: 10.1016/j.snb.2015.11.110

Vallejos, S., Stoycheva, T., Umek, P., Navio, C., Snyders, R., Bittencourt, C., et al. (2011). Au nanoparticle-functionalised WO_3 nanoneedles and their application in high sensitivity gas sensor devices. *Chem. Commun.* 47, 565–567. doi: 10.1039/c0cc02398a

Wang, H., Qu, Y., Chen, H., Lin, Z. D., and Dai, K. (2014). Highly selective n-butanol gas sensor based on mesoporous SnO_2 prepared with hydrothermal treatment. *Sens. Actuators B Chem.* 201, 153–159. doi: 10.1016/j.snb.2014.04.049

Wang, X., Liu, W., Liu, J., Wang, F., Kong, J., Qiu, S., et al. (2012). Synthesis of nestlike ZnO hierarchically porous structures and analysis of their gas sensing properties. *ACS Appl. Mater. Interfaces* 4, 817–825. doi: 10.1021/am201476b

Xu, T. T., Xu, Y. M., Zhang, X. F., Deng, Z. P., Huo, L. H., and Gao, S. (2018). Enhanced H_2S Gas-Sensing Performance of Zn_2SnO_4 Lamellar Micro-Spheres. *Front. Chem.* 6:165. doi: 10.3389/fchem.2018.00165

Yang, D. J., Kamienchick, I., Youn, D. Y., Rothschild, A., and Kim, I. D. (2010). Ultrasensitive and highly selective gas sensors based on electrospun SnO_2 nanofibers modified by Pd loading. *Adv. Funct. Mater.* 20, 4258–4264. doi: 10.1002/adfm.201001251

Yang, F., Jung, D., and Penner, R. M. (2011). Trace detection of dissolved hydrogen gas in oil using a palladium nanowire array. *Anal. Chem.* 83, 9472–9477. doi: 10.1021/ac2021745

Zeng, W., Zhu, L. P., Zhang, Z. Y., and Ye, Z. Z. (2015). Fabrication of gas sensor based on mesoporous rhombus-shaped ZnO rod arrays. *Sens. Actuators B Chem.* 208, 112–121. doi: 10.1016/j.snb.2014.11.024

Zhang, Y., Xu, J. Q., Xiang, Q., Li, H., Pan, Q. Y., and Xu, P. C. (2009). Brush-Like hierarchical ZnO nanostructures: synthesis, photoluminescence and gas sensor properties. *J. Phys. Chem. C* 113, 3430–3435. doi: 10.1021/jp8092258

Zhao, T., Nguyen, N. T., Xie, Y., Sun, X. F., Li, Q., and Li, X. (2017). Inorganic Nanocrystals Functionalized Mesoporous Silica Nanoparticles: Fabrication and Enhanced Bio-applications. *Front. Chem.* 5:118. doi: 10.3389/fchem.2017.00118

Zhu, L., and Zeng, W. (2017). Room-temperature gas sensing of ZnO-based gas sensor: A review. *Sens. Actuators A Phys.* 267, 242–261. doi: 10.1016/j.sna.2017.10.021

Conflict of Interest Statement: The authors declare that the research was conducted in the absence of any commercial or financial relationships that could be construed as a potential conflict of interest.

frontiers in Chemistry

ORIGINAL RESEARCH
published: 18 October 2018
doi: 10.3389/fchem.2018.00493

Enhanced Sub-ppm NH_3 Gas Sensing Performance of PANI/TiO_2 Nanocomposites at Room Temperature

Chonghui Zhu, Xiaoli Cheng, Xin Dong and Ying ming Xu**

Key Laboratory of Functional Inorganic Material Chemistry, Ministry of Education, School of Chemistry and Materials Science, Heilongjiang University, Harbin, China

PANI/TiO_2 nanocomposites spheres were synthesized using a simple and efficient one-step hydrothermal process. The morphology and structure of PANI/TiO_2 nanocomposites spheres were investigated by X-ray diffraction (XRD), scanning electron microscopy (SEM), and transmission electron microscopy (TEM) techniques. The PANI/TiO_2 nanocomposite sphere-based sensor exhibits good selectivity, sensitivity (5.4 to 100 ppm), repeatability, long-term stability and low detection limit (0.5 ppm) to ammonia at room temperature (20 ± 5°C). It also shows a good linearity relationship in the range of 0.5–5 and 5–100 ppm. The excellent NH_3 sensing performance is mainly due to the formation of the p-n heterostructure in the nanocomposites.

Keywords: gas sensing, polyaniline, TiO_2, NH_3, nanocomposites

OPEN ACCESS

Edited by:
Wen Zeng,
Chongqing University, China

Reviewed by:
Jianping Yang,
Donghua University, China
Zhenmeng Peng,
University of Akron, United States

****Correspondence:***
Xin Dong
xdong92@yahoo.com
Ying ming Xu
xuyingming@hlju.edu.cn

Specialty section:
This article was submitted to Nanoscience, a section of the journal Frontiers in Chemistry

Received: *04 June 2018*
Accepted: *27 September 2018*
Published: *18 October 2018*

Citation:
Zhu C, Cheng X, Dong X and Xu Ym (2018) Enhanced Sub-ppm NH_3 Gas Sensing Performance of PANI/TiO_2 Nanocomposites at Room Temperature. Front. Chem. 6:493. doi: 10.3389/fchem.2018.00493

INTRODUCTION

Polyaniline (PANI), as an intrinsically conductive polymer, is the widely used material in anti-corrosion, anti-static electricity, stealth and so on. Since its low density, excellent processability, excellent flexibility, and good electrical conductivity, (Bhadra et al., 2009; Baker et al., 2017) polyaniline is also attracting more attention in the field of gas sensing. However, pure PANI sensors often show lower sensitivity or higher detection limit than semiconductor metal oxide sensors (Sutar et al., 2007; Kebiche et al., 2012). The addition of semiconducting metal oxides not only improves gas-sensing properties, but also avoids high operating temperatures. In recent years, SnO_2, ZnO, TiO_2, and In_2O_3 have been chosen as the addition of polyaniline to prepare ammonia sensors, which can used at room temperature (Guo et al., 2013; Chen et al., 2015; Dai et al., 2016; Zhang et al., 2018). Most of the materials reported so far have been prepared by electrospinning, interfacial synthesis, or mechanical mixing (Talwar et al., 2014; Li et al., 2015; Nie et al., 2016). Pawar et al. synthesized PANI and TiO_2 by chemical oxidative polymerization and sol-gel method, respectively. Then, they mixed PANI and TiO_2 by mechanical mixing method to prepare PANI-TiO_2 nanocomposites. The response of the sensor to 100 ppm NH_3 is 50% (Pawar et al., 2011a). Liu et al. prepared the PANI-TiO_2-Au ternary nanocomposite thin film by *in-situ* self-assembly method. The response of the sensor is 2.23 toward 50 ppm NH_3, and the detection limit is 1 ppm (Liu et al., 2017). Their synthetic methods basically need more than one-step reactions. And the recovery time, sensitivity and other properties of the sensors need to be further improved.

In this work, the PANI/TiO_2 nanocomposite was synthesized by one step hydrothermal method. The PANI/TiO_2 nanocomposite exhibits good selectivity, sensitivity (5.4 to 100 ppm), repeatability, long-term stability, and low detection limit (0.5 ppm) to ammonia at room temperature. Meanwhile, the sensor exhibits a good liner relationship in the range of 0.5–5 and 5-100 ppm.

EXPERIMENTAL

All reagents were of analytical grade, offered by Aladdin Reagent Company, and used without further purification.

Preparation of PANI/TiO_2 Nanocomposites and Pure PANI

1.147 g of ammonium persulfate (APS) was added to 10 mL of HCl (1 mol·L^{-1}) to obtain solution A. In 10 mL of anhydrous ethanol, tetrabutyl titanate (TBT), and 0.47 mL of aniline were added to obtain solution B. Solution C is the mixture of 10 mL absolute ethanol and 0.47 mL aniline. The mixture solution of A and B were poured into a 50 mL Teflon-lined stainless steel autoclave and kept at 100°C for 2 h. The mixtures of solution A and C were treated as the same. The PANI/TiO_2 nanocomposite and pure PANI was obtained after washing several times by deionized water and ethanol. With other conditions remaining constant, the amount of TBT added in solution B is 0.05, 0.1, 0.15, or 0.2 mol·L^{-1}, respectively, to make products PT1, PT2, PT3, PT4. The synthetic routes of the samples are shown in **Scheme S1**.

Characterization of PANI/TiO_2 Nanocomposites

The phase structure of the products were analyzed by X-ray powder diffractometer (XRD, Rigaku, D/MAX-3B) with Cu Kα1 radiation (λ = 1.54059 Å). Raman spectra of products were tested by a LabRAM HR800 laser confocal microscopic Raman spectrometer. The morphology and structure of products were investigated by scanning electron microscope (SEM, FEI/Philips, XL-30) and transmission electron microscope (TEM, Jeol, Jem-2100). Thermogravimetric analysis (TGA) was executed by a Perkin-Elmer instruments corporation thermogravimetric analyzer. The specific surface area and pore size distribution were detected by nitrogen adsorption-desorption measurement at 77 K using the TriStar II 3020 system.

Fabrication and Gas Sensing Measurement of the PANI/TiO_2 Nanocomposites Sensors

The products were made into a paste with ethanol and coated on the surface of Al_2O_3 tube whose length was 4 mm and internal diameter was 0.8 mm. The Al_2O_3 tube brought with two gold electrodes which spaced 1 mm and the distance between two gold electrodes was 1 mm. Two platinum wires were connected with each gold electrode. After a Ni/Cr wire passed through the Al_2O_3 tube, it was welded to the base together with the platinum wires.

The responses of sensors were recorded by JF02E type gas sensor measurement system (Kunming Guiyan Jinfeng Technology Co. Ltd., China). The static testing method was used to measure the property of sensors. After a certain amount of NH_3 was injected into a vacuum 10 L glass bottle, the pressure was returned to the atmospheric pressure. The gas sensor was placed in the glass bottle for testing. The sensor's response to NH_3 was defined as S = Rg/Ra. Rg and Ra were the resistance values of the sensor in NH_3 and air, respectively. The response time is 100s, the recovery time is defined as the time that the resistance changed 90%. The sensor response to humidity measured by the saturated solution of LiCl (11.3 RH%), CH_3COOK (23.4 RH%), $MgCl_2$ (32.8 RH%), K_2CO_3(43 RH%), $Mg(NO_3)_2$ (54.3 RH%), $CuCl_2$ (67 RH%), NaCl (75.3 RH%), KCl (85 RH%), and KNO_3 (93.5 RH%; Yang et al., 2017).

RESULTS AND DISCUSSION

The XRD peaks of the nanocomposites samples PT1, PT2, PT3, and PT4, shown in **Figure 1a** at 25°, is consistent with the XRD diffraction peak of pure PANI. As is shown in **Figure S1**, the diffraction peak of the pure PANI appears at about 25°. Other peaks at 25.3°, 37.8°, and 48.0° are corresponding to (101), (004), and (200) crystal planes of anatase crystal structure TiO_2 (JCPDS Card NO.21-1272). This reminds that TiO_2 is present in the nanocomposites. Further, the Raman spectrum of the nanocomposites was analyzed, as shown in **Figure S2**. The peaks at 164, 406, 635 cm^{-1} are the characteristic peaks of TiO_2, and 1,595 cm^{-1} is attributed to the C-C stretching vibration of benzenoid ring in PANI, which further proves the presence of TiO_2 in the nanocomposites (Chen and Mao, 2007). Through the thermogravimetric analysis (**Figure S3**) to determine the TiO_2 content of PT1, PT2, PT3 and PT4 is 3.04, 19.48, 21.09, and 38.75%, respectively. The response of the PT1, PT2, PT3, PT4 nanocomposites and pure PANI to 20–100 ppm NH_3 at room temperature is shown in **Figure S4**. As can be seen from the figure, the PT3 nanocomposites sensor has better response to NH_3 than the other four sensors. **Figure S5** exhibits the pore structure and specific surface area of the PT1, PT2, PT3, and PT4 nanocomposites, which were detected by N_2 adsorption-desorption measurement and Barrett-Joyner-Halenda (BJH) pore size distribution analysis. The BET specific surface area of the PT1, PT2, PT3, and PT4 nanocomposites are 26.76, 46.13, 47.73, and 55.80 $m^2 \cdot g^{-1}$, respectively. The result shows that the specific surface area increase as the TiO_2 content rises. The gas-sensing performance of the sensor is generally related to the micro-structure of sensing material, specific surface area and so on. Compared with other four sensors, the morphology of the PT3 nanocomposites is uniform (**Figure S6**), many TiO_2 nanoparticles are uniformly dispersed on the surface of the PANI nanospheres, which makes the nanocomposites have many p-n heterostructure and a large specific surface area. These will increase the contact area of PT3 nanocomposites, make the NH_3 molecules diffuse easily and provide more active sites for the efficient adsorption of NH_3, which is more conducive to the reaction of the nanocomposite with NH_3. Therefore, a more detailed characterization of the PT3 nanocomposites was performed.

The morphology and structure of the PT3 nanocomposites were tested by SEM and TEM. In **Figure 1b**, it is found that the PT3 nanocomposites were composed by the stacking of nanoparticles whose diameter is about 80 nm. **Figure 1c** indicates the same result that the PT3 nanocomposites is composed of nanoparticles, stacked on top of each other. In addition, the

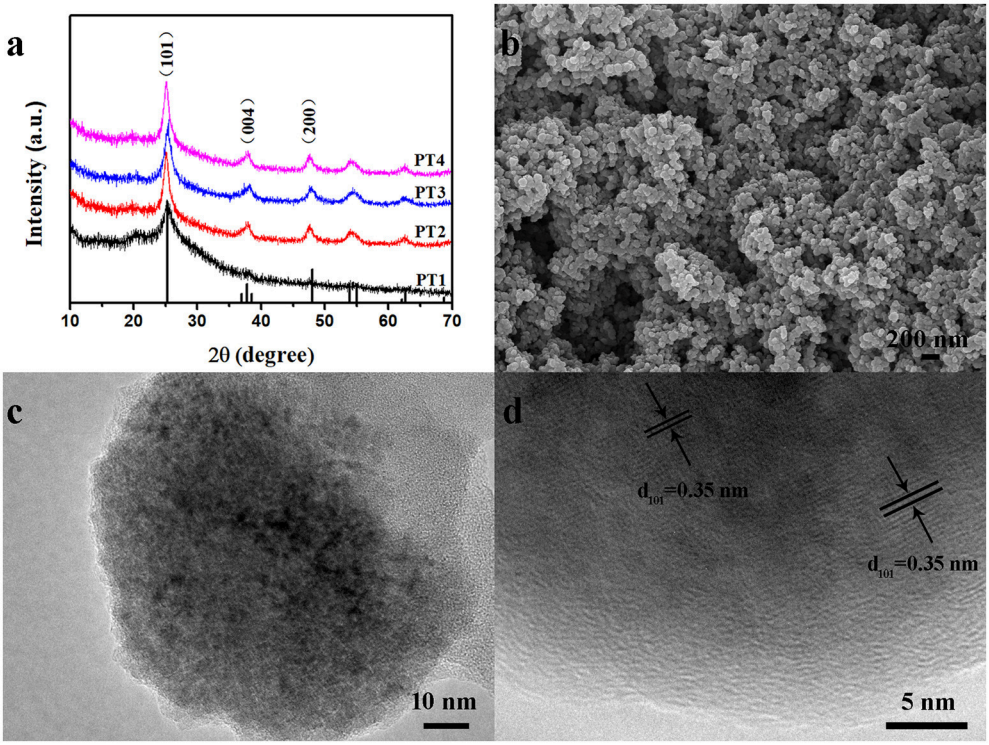

FIGURE 1 | XRD patterns of the PT1, PT2, PT3 and PT4 nanocomposites **(a)**; SEM **(b)**, TEM **(c),** and HRTEM **(d)** images of the PT3 nanocomposites.

HRTEM image of the PT3 nanocomposites (**Figure 1d**) shows characteristic lattice fringes of TiO_2 with a pitch of 0.35 nm, corresponding to the (101) crystal plane of TiO_2. This is consistent with the XRD result that there is TiO_2.

The gas sensing properties of the PT3 nanocomposites sensor was further studied. The response-recovery curves for 0.5–100 ppm NH_3 at room temperature are shown in **Figure 2A**. To 100 ppm NH_3, the sensitivity of PT3 nanocomposite sensor is 5.4, the response time is 100 s, and the recovery time is 232 s. Moreover, the sensitivity of the PT3 nanocomposite sensor presents a clear linear relationship with the NH_3 concentration between 0.5 and 5 ppm (R^2 = 0.9992) and 5 and 100 ppm (R^2 = 0.9945) (**Figure 2B**). The PT3 nanocomposite sensor performed four consecutive tests on 50 ppm of NH_3 at room temperature (**Figure 2C**). The corresponding sensitivities are 2.59, 2.6, 2.56, and 2.56, respectively. And the relative deviation is 1.75%. This shows that the PT3 nanocomposite sensor has a satisfactory reproducibility. The interference of other seven gases to the sensor was further researched (**Figure 2D**). The responds at room temperature to 100 ppm ethanol (C_2H_5OH), acetone (CH_3COCH_3), triethylamine (TEA), ethyne (C_2H_2), NO, H_2, styrene (C_8H_8), and NH_3 are 1.020, 1.034, 1.027, 1.006, 1.008, 1.007, 1.010, and 5.423, respectively. The result proves that the PT3 nanocomposite sensor is more sensitive to NH_3 at room temperature. The influence of humidity was studied in the humidity range of 11.3–93.5% at room temperature (**Figure S7a**). The maximum response of the sensor is 1.4. It means that the effect of humidity to the sensor is much small. In order to deeply investigate the long-term stability, the sensor responds to 50 ppm NH_3 every 5 days at room temperature. During the 2 months monitoring time (**Figure S7b**), the response of the sensor was reduced by <2% after 60 days. Our investigation leads us to conclude that the sensor has a good long-term stability.

Compared the gas sensing property between the PANI-TiO_2 nanocomposites sensor with the reported sensor in **Table 1**. The results show that the PT3 nanocomposites sensor exhibits excellent sensitivity and good response to NH_3 gas at room temperature. The detection limit of PANI-TiO_2 nanocomposites sensor is lower and sensitivity is better than the other reported sensors. The improvement of the NH_3 sensing property of PT3 sensor is might attributed to the following reasons. First, One-step synthesis is more conducive to the dispersion of titanium dioxide nanoparticles on the surface of PANI. Secondly, the p-n heterostructure formed between TiO_2 and PANI can provide a synergistic effect, which can effectively improve the ability to adsorb NH_3. Therefore, the PT3 nanocomposites has potential application value in detecting NH_3 at room temperature.

The possible sensing mechanism of the PT3 nanocomposites sensor for detecting NH_3 is as shown in **Figure S8**. TiO_2 is an n-type semiconductor with a 3.2 eV forbidden band width. And PANI is a p-type semiconductor with a 2.8 eV forbidden band width. At the contact interface, the TiO_2 and PANI interact to

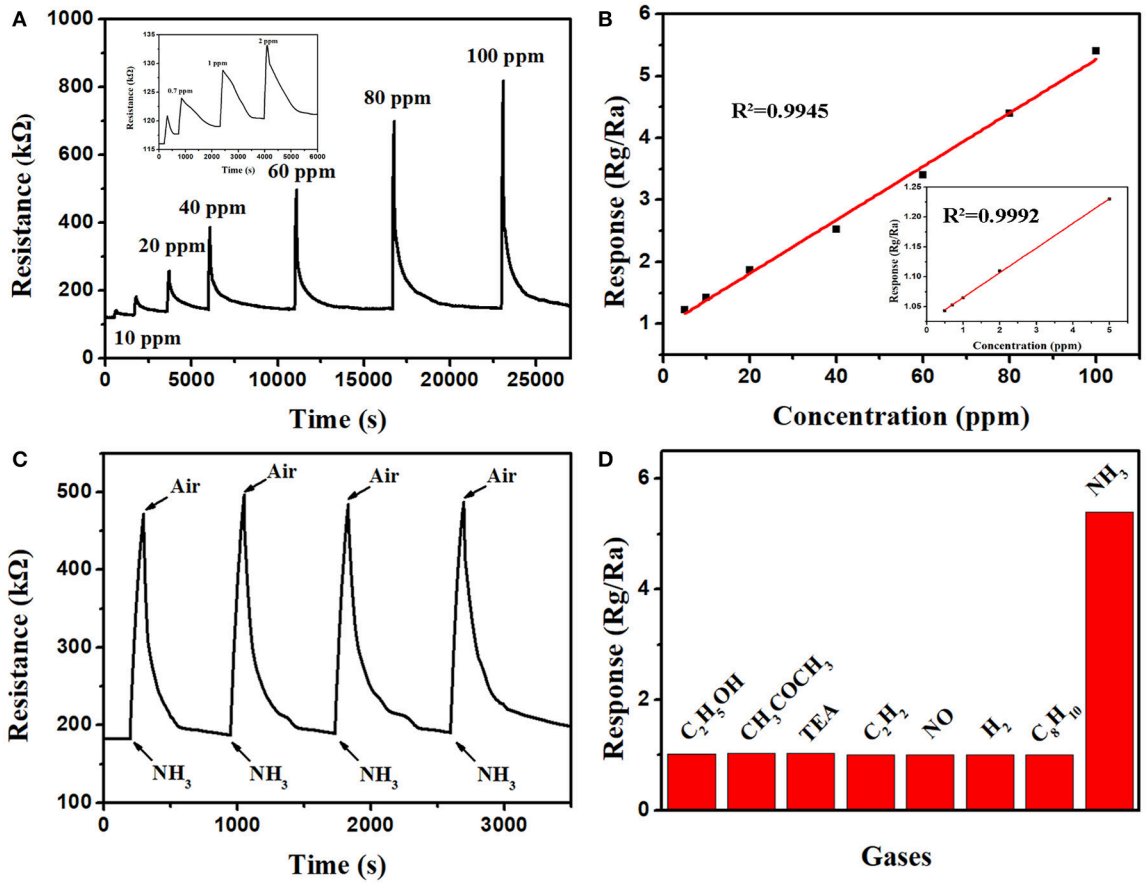

FIGURE 2 | The response-recovery curves **(A)** and the linear relationship **(B)** of the PT3 nancomposites sensor to different concentrations of NH_3; the reproducibility of the PT3 nancomposites sensor to 50 ppm NH_3 **(C)**; the selectivity of the PT3 nanocomposites sensor to 100 ppm of eight gases **(D)**.

TABLE 1 | Summary of recent publications of PANI-TiO_2 nanocomposities based NH_3 sensors.

Sensing materials	Detection limit	Response/NH_3 concentration	Response time (s)	Recovery time (s)	References
PANI/TiO_2	45 ppb	38.3/10.5 ppm	600	–	Li et al., 2015
PANI-TiO_2-Au	1 ppm	2.23/50 ppm	122	–	Liu et al., 2017
PANI/TiO_2	23 ppm	<6/94 ppm	2 s	25 s	Tai et al., 2008
PA6/TiO_2/PANI	–	2.6/250 ppm	150 s	450 s	Pang et al., 2014
cellulose/TiO_2/PANI	10 ppm	3.57/100 ppm	<150 s	800 s	Pang et al., 2016
PANI/TiO_2	25 ppb	>0.8/200 ppb	80 s	–	Li et al., 2011
PANI/TiO_2	–	48%/100 ppm	40 s	70 s	Pawar et al., 2012
CSA Doped PANi- TiO_2	20 ppm	0.75/100 ppm	49 s	413 s	Pawar et al., 2011b
PANi-TiO_2	20 ppm	50%/100 ppm	40 s	70 s	Pawar et al., 2011a
TiO_2-SiO_2/PANI	10 ppm	23/100 ppm	<500 s	–	Pang et al., 2018
TiO_2-PANI/PA6	–	18.3/250 ppm	250 s	–	Wang et al., 2012
PANi-TiO_2	–	3.9/60 ppm	35 s	140 s	Bairi et al., 2015
PANI/TiO_2	0.5 ppm	5.4/100 ppm	100 s	232 s	This work

form a p-n heterostructure. The p-n heterostructure will make a positively charged depletion layer. So, the activation energy and enthalpy of physisorption for NH_3 will reduce as a result to cause the enhancement of gas sensitivity (Costello et al., 1996; Tai et al., 2010). In addition, the LUMO level of PANI and the conduction band of TiO_2 are well helps charge transfer. It can also effectively improve the gas sensing performance (Li et al., 2006; Tai et al., 2008). When the sensor is exposed to NH_3, H^+

on -NH- site of PANI combines with NH_3, cause the electron hole concentration in the PANI to be low. The resistance of the sensor will increase. When the sensor is exposed to air after NH_3, PANI gets H^+ from NH_4^+, the electron hole concentration of PANI recovers. The resistance decreases to the initial value (**Figure S8b**).

CONCLUSION

In summary, the PANI/TiO_2 nanocomposites, which is consisted of uniform nanoparticles, are synthesized by one-step hydrothermal synthesis. At room temperature, the sensor based on PANI/TiO_2 nanocomposites has a good linear relationship (0.9945 to 5–100 ppm), high response to NH_3 (5.4 to 100 ppm), and the detection limit is 0.5 ppm. The response and recovery time to 100 ppm NH_3 is 100 and 232 s, respectively. With small humidity effects, the sensor exhibits excellent selectivity, good reproducibility and long-term stability to NH_3. Moreover, the excellent gas sensing property of PANI/TiO_2 nanocomposites can be rewarded to p-n heterostructure. The more charge transfer on the surfaces where PANI is in contact with TiO_2, the beter gas-sensing performance of PANI/TiO_2. These results illustrate that the PANI/TiO_2 nanocomposites sensor has great potential application for detecting NH_3 at room temperature.

AUTHOR CONTRIBUTIONS

CZ performed the experiments, analyzed the data with the help from YX and XC. XD wrote the manuscript with input from all authors. YX conceived the study. All authors read and approved the manuscript.

ACKNOWLEDGMENTS

This work is financial supported by International Science & Technology Cooperation Program of China (2016YFE0115100), National Natural Science Foundation of China (21771060, 21547012, and 21305033), the Project of Natural Science Foundation of Heilongjiang Province (No. B2015007), and the Project of Nitro Graduate Innovation Research of Heilongjiang University (YJSCX2018-062HLJU). We thank the Key Laboratory of Functional Inorganic Material Chemistry, Ministry of Education, Heilongjiang University for supporting this study.

SUPPLEMENTARY MATERIAL

The Supplementary Material for this article can be found online at: https://www.frontiersin.org/articles/10.3389/fchem.2018.00493/full#supplementary-material

REFERENCES

Bairi, V. G., Bourdo, S. E., Sacre, N., Nair, D., Berry, B. C., Biris, A. S., et al. (2015). Ammonia gas sensing behavior of tanninsulfonic acid doped polyaniline-TiO_2 composite. *Sensors* 15, 26415–26429. doi: 10.3390/s151026415

Baker, C., Huang, X., Nelsonc, W., and Kaner, R. B. (2017). Polyaniline nanofibers: broadening applications for conducting polymers. *Chem. Soc. Rev*6, 1510–1525. doi: 10.1039/C6CS00555A

Bhadra, S., Khastgir, D., Singha, N., and Lee, H. (2009). Progress in preparation, processing and applications of polyaniline. *Prog. Polym. Sci.* 34, 783–810. doi: 10.1016/j.progpolymsci.2009.04.003

Chen, T. Y., Chen, H. I., Hsu, C. S., Huang, C. C., Wu, J. S., Chou, P. C., et al. (2015). Characteristics of ZnO nanorods-based ammonia gas sensors with a cross-linked configuration. *Sens. Actuators B Chem.* 221, 491–498. doi: 10.1016/j.snb.2015.06.122

Chen, X., and Mao, S. (2007). Titanium dioxide nanomaterials: synthesis, properties, modifications, and applications. *Chem. Rev.* 107, 2891–2959. doi: 10.1021/cr0500535

Costello, L., Evans, P., Ewen, R. J., Honeybourne, C., and Ratcliffe, N. M. (1996). Novel composite organic-inorganic semiconductor sensors for the quantitative detection of target organic vapours. *J. Mater. Chem.* 6, 289–294. doi: 10.1039/JM9960600289

Dai, L., Liu, Y., Meng, W., Yang, G., Zhou, H., He, Z., et al. (2016). Ammonia sensing characteristics of $La_{10}Si_5MgO_{26}$-based sensors using In_2O_3 sensing electrode with different morphologies and CuO reference electrode. *Sens. Actuators B Chem.* 228, 716–724. doi: 10.1016/j.snb.2016.01.106

Guo, W., Duan, X., Shen, Y., Qi, K. Z., Wei, C. Y., and Zheng, W. J. (2013). Ionothermal synthesis of mesoporous SnO_2 nanomaterials and their gas sensitivity depending on the reducing ability of toxic gases. *Phys. Chem. Chem. Phys.* 15, 11221–11225. doi: 10.1039/c3cp51663f

Kebiche, H., Debarnota, D., Merzoukib, A., Poncin-Epaillard, F., and Haddaoui, N. (2012). Relationship between ammonia sensing properties of polyaniline nanostructures and their deposition and synthesis methods. *Anal. Chim. Acta* 737, 64–71. doi: 10.1016/j.aca.2012.06.003

Li, J., Zhu, L., Wu, Y., Harima, Y., Zhang, A., and Tang, H. (2006). Hybrid composites of conductive polyaniline and nanocrystalline titanium oxide prepared via self-assembling and graft polymerization. *Polymer* 47, 7361–7367. doi: 10.1016/j.polymer.2006.08.059

Li, Y., Ban, H. T., Zhao, H. J., and Yang, M. J. (2015). Facile preparation of a composite of TiO_2 nanosheets and polyaniline and its gas sensing properties. *RSC Adv.* 5, 106945–106952. doi: 10.1039/C5RA20879C

Li, Y., Gong, J., He, G., and Deng, Y. (2011). Fabrication of polyaniline/titanium dioxide composite nanofibers for gas sensing application. *Mater. Chem. Phys.* 129, 477–482. doi: 10.1016/j.matchemphys.2011.04.045

Liu, C., Tai, H. L., Zhang, P., Ye, Z. B., Su, Y. J., and Jiang, Y. D. (2017). Enhanced ammonia-sensing properties of PANI-TiO_2-Au ternary self-assembly nanocomposite thin film at room temperature. *Sens. Actuators B Chem.* 246, 85–95. doi: 10.1016/j.snb.2017.01.046

Nie, Q., Pang, Z., Lu, H., Cai, Y. B., and Wei, Q. F. (2016). Ammonia gas sensors based on In_2O_3/PANI hetero-nanofibers operating at room temperature. *Beilstein J. Nanotechnol.* 7, 1312–1321. doi: 10.3762/bjnano.7.122

Pang, Z., Fu, J., Luo, L., Huang, F., and Wei, Q. (2014). Fabrication of PA6/TiO_2/PANI composite nanofibers by electrospinning-electrospraying for ammonia sensor. *Colloids Surf. A* 461, 113–118. doi: 10.1016/j.colsurfa.2014.07.038

Pang, Z., Yang, Z., Chen, Y., Zhang, J., Wang, Q., Huang, F., et al. (2016). A room temperature ammonia gas sensor based on cellulose/TiO_2/PANI composite nanofibers, *Colloids Surf. A* 494, 248–255. doi: 10.1016/j.colsurfa.2016.01.024

Pang, Z., Yu, J., Li, D., Nie, Q., Zhang, J., and Wei, Q. (2018). Free-standing TiO_2-SiO_2/PANI composite nanofibers for ammonia sensors. *J. Mater. Sci. Mater. Electron.* 29, 3576–3583. doi: 10.1007/s10854-017-8287-2

Pawar, S. G., Chougule, M. A., Patil, S. L., Raut, B. T., Godse, P. R., Sen, S., et al. (2011a). Room temperature ammonia gas sensor based on polyaniline-TiO_2 nanocomposite. *IEEE Sens. J.* 11, 3417–3423. doi: 10.1109/JSEN.2011.2160392

Pawar, S. G., Chougule, M. A., Sen, S., and Patil, V. B. (2012). Development of nanostructured polyaniline-titanium dioxide gas sensors for ammonia recognition. *J. Appl. Polym. Sci.* 125, 1418–1424. doi: 10.1002/app.35468

Pawar, S. G., Patil, S. L., Chougule, M. A., Raut, B. T., Godase, P. R., Mulik, R. N., et al. (2011b). New method for fabrication of CSA doped PANi-TiO_2 thin-film ammonia sensor. *IEEE Sens. J.* 11, 2980–2985. doi: 10.1109/JSEN.2011.2152391

Sutar, D. S., Padma, N., Aswal, D. K., Deshpande, S. K., Gupta, S. K., and Yakhmi, J. V. (2007). Preparation of nanofibrous polyaniline films and their application as ammonia gas sensor. *Sens. Actuators B Chem.* 128, 286–292. doi: 10.1016/j.snb.2007.06.015

Tai, H., Jiang, Y., Xie, G., and Yu, J. (2010). Preparation, characterization and comparative NH_3-sensing characteristic studies of PANI/inorganic oxides nanocomposite thin films. *J. Mater. Sci. Technol.* 26, 605–613. doi: 10.1016/S1005-0302(10)60093-X

Tai, H. L., Jiang, Y., Xie, G., Yu, J., Chen, X., and Ying, Z. (2008). Influence of polymerization temperature on NH_3 response of PANI/TiO_2 thin film gas sensor. *Sens. Actuators B Chem.* 129, 319–326. doi: 10.1016/j.snb.2007.08.013

Talwar, V., Singh, O., and Singh, R. (2014). ZnO assisted polyaniline nanofibers and its application as ammonia gas sensor. *Sens. Actuators B Chem.* 191, 276–282. doi: 10.1016/j.snb.2013.09.106

Wang, Q., Dong, X., Pang, Z., Du, Y., Xia, X., Wei, Q., et al. (2012). Ammonia sensing behaviors of TiO_2-PANI/PA6 composite nanofibers, *Sensors* 12, 17046–17057. doi: 10.3390/s121217046

Yang, M., Zhang, X., Cheng, X., Xu, Y., Gao, S., Zhao, H., et al. (2017). Hierarchical NiO Cube/Nitrogen-doped reduced graphene oxide composite with enhanced H_2S sensing properties at low temperature. *ACS Appl. Mater. Interfaces* 9, 26293–26303. doi: 10.1021/acsami.7b04969

Zhang, Y., Zeng, W., Ye, H., and Li, Y. (2018). Enhanced carbon monoxide sensing properties of TiO_2 with exposed (001) facet: a combined first-principle and experimental study. *Appl. Surf. Sci.* 442, 507–516. doi: 10.1016/j.apsusc.2018.02.036

Conflict of Interest Statement: The authors declare that the research was conducted in the absence of any commercial or financial relationships that could be construed as a potential conflict of interest.

frontiers in Chemistry

ORIGINAL RESEARCH
published: 11 October 2018
doi: 10.3389/fchem.2018.00472

3D Flower-Like NiO Hierarchical Structures Assembled With Size-Controllable 1D Blocking Units: Gas Sensing Performances Towards Acetylene

He Zhang[1], *Wei-Gen Chen*[1]*, *Yan-Qiong Li*[2], *Ling-Feng Jin*[1], *Fang Cui*[1] *and Zi-Hao Song*[1]

[1] State Key Laboratory of Power Transmission Equipment & System Security and New Technology, School of Electrical Engineering, Chongqing University, Chongqing, China, [2] School of Electronic and Electrical Engineering, Chongqing University of Arts and Sciences, Chongqing, China

Acetylene gas (C_2H_2) is one of the main arc discharge characteristic gases dissolved in power transformer oil. It is of great potential to monitor the fault gas on-line by applying gas sensor technology. In this paper, gas sensors based on nanorods and nanoneedles assembled hierarchical NiO structures have been prepared. Herein, we focus on investigate the relationship between the sizes of the assembling blocking units and gas sensing properties. It can be found that the addition of CTAB/EG plays a vital role in controlling the sizes of blocking unit and assembly manner of 3D hierarchical structures. A comparison study reveals that an enhanced gas sensing performance toward C_2H_2 for the sensor based on nanoneedle-assembled NiO flowers occurs over that of nanorod-assembled NiO. This enhancement could be ascribed to the larger specific area of needle-flower, which provides more adsorption and desorption sites for chemical reaction as well as effective diffusion channels for C_2H_2. Besides, a method of calculating the specific surface area without BET testing was presented to verify the results of gas sensing measurement. The possible growth mechanism and gas sensing mechanism were discussed. Such a synthesis way may open up an avenue to tailor the morphologies and control the sizes of blocking units of some other metal oxides and enhance their gas sensing performances.

Keywords: NiO, hierarchical structures, blocking units, sensor, gas sensing performances

OPEN ACCESS

Edited by:
Zhenyu Li,
Deakin University, Australia

Reviewed by:
Ming-Guo Ma,
Beijing Forestry University, China
Hua Wang,
Beihang University, China
Wei Wang,
Harbin Institute of Technology, China

***Correspondence:**
Wei-Gen Chen
weigench@cqu.edu.cn

Specialty section:
This article was submitted to Nanoscience, a section of the journal Frontiers in Chemistry

Received: *12 May 2018*
Accepted: *18 September 2018*
Published: *11 October 2018*

Citation:
Zhang H, Chen W-G, Li Y-Q, Jin L-F, Cui F and Song Z-H (2018) 3D Flower-Like NiO Hierarchical Structures Assembled With Size-Controllable 1D Blocking Units: Gas Sensing Performances Towards Acetylene. Front. Chem. 6:472. doi: 10.3389/fchem.2018.00472

INTRODUCTION

As we all know, the stable and reliable operation of power transformers is particularly important for the safety and stability of power system. When the oil-immersed power transformers work for a long time, the insulating oil, and paper will gradually deteriorate and produce various trace characteristic gases, which actually dissolve in transformer insulation oil (Singh and Bandyopadhyay, 2010). When the power transformer has the spark of oil or arc discharge fault, it will generate the fault characteristic gas with acetylene gas (C_2H_2) as the main component. It is of great potential to monitor the fault gas on-line by applying gas sensor technology. The monitoring

of C_2H_2 gas content can predict the internal latent failure of the transformer (Chen et al., 2013; Jin et al., 2017). So, C_2H_2 gas is selected as the target gas in this paper.

A common method for detecting C_2H_2 gas dissolved in transformer oil is metal oxide semiconductor (MOS) based gas sensor (Zhu and Zeng, 2017). Among various MOS sensing materials, nickel oxide (NiO) as a wide band gap (Eg = 3.6–4.0 ev) p-type semiconductor has taken a dominated position due to its outstanding physical and chemical properties. Recently, NiO has been extensively applied in multifarious application fields such as electrode materials (Zhang et al., 2004), solar cells (Nakasa et al., 2005), catalysts (Kaminski et al., 2018), and gas sensors (Cao et al., 2015a; Yu et al., 2017).

It's believed that one-dimensional (1D) nanostructures with large surface to volume have great potential to improve the sensing properties. However, there are some shortcomings for 1D structure, i.e., inevitable serious stacking configuration and thermal/ chemical instability. Given this, the sensing materials can be designed into three–dimensional (3D) hierarchical structure assembled by 1D blocking units, which not only prevents the 1D blocking units from serious stacking but also inherits the merits of 1D nanomaterials (Duo et al., 2016; Zhu et al., 2018). The ability to control the assembly configuration, the morphology and size of building units in hierarchical architectures is of utmost importance for the realization of multifunctional nanodevices (Kim and Yong, 2011). Recently, assembly of 1D blocking units into hierarchical structures has been a hot topic in the research. But there are few explorations about the synthesis of hierarchical structures with size-controllable blocking units and studying the influence of the size of the assembling units on gas sensing performances.

In this paper, nanorods, and nanoneedles assembled 3D flower-like NiO hierarchical structures were successfully synthesized via hydrothermal synthesis. Herein, we focus on investigate the relationship between the sizes of the assembling blocking units and gas sensing properties. It can be found that the addition of CTAB/EG plays a vital role in controlling the sizes of blocking unit and assembly manner of 3D hierarchical structures. A comparison study reveals that an enhanced gas sensing performance toward C_2H_2 for the sensor based on nanoneedle-assembled NiO flowers occurs over that of nanorod-assembled NiO. In order to shed light on this phenomenon, a method of calculating the specific surface area without BET testing was presented to verify the results of gas sensing measurement. Based on our experimental results, the possible formation mechanism of two kinds of NiO nanoflowers is primarily discussed. It's expected that this study can promote the development of gas sensing materials via lower dimensional assembly.

EXPERIMENTAL

Synthesis of the Nanorods-Assembled Hierarchical NiO Nanoflowers

In a typical experiment of nanorods assembled NiO nanoflowers, 0.4 g of $Ni(NO_3)_2{\cdot}6H_2O$ was added to 40 ml of distilled water under vigorous stirring for 10 min. 0.18 g of cetyltrimethyl ammonium bromide (CTAB) was introduced into the above solution. Then, under continuous magnetic stirring, ammonia ($NH_3{\cdot}H_2O$, 25%) was dripped into the mixed solution to obtain the pH = 9. After thorough mixing, the resulting mixture was transferred to a 50 ml autoclave and maintained overnight at 180°C. After cooling naturally, the precipitates were washed sequentially and dried in air at 60°C. Finally, the powder was calcined at 500°C for 2 h. The sample was labeled as rod-flower.

Synthesis of the Nanoneedles-Assembled Hierarchical NiO Nanoflowers

Typically, 0.4 g of $NiCl_2{\cdot}6H_2O$ and 0.08 g of $Na_2C_2O_4$ were poured into 15 ml of distilled water. Then 25 ml ethylene glycol (EG) was added into the solution with sequentially stirring. The mixed solution was loaded into a 50 ml autoclave and heated to 160°C for 12 h. The subsequent process including centrifugation, washing, drying and calcining are the same as the above. The sample after annealing was designated as needle-flower.

Characterization

Crystal structure of as-prepared samples was examined through X-ray diffraction (XRD, D/Max-1200X, Rigaku). The surface morphologies and nanostructures of the samples were inspected by scanning electronic microscopy (SEM, JEM-6700F) and transmission electron microscopy (TEM, JEM-1200EX).

The detailed process about the fabrication of planar gas sensor and gas-sensing test is as follows Jin et al. (2017). Firstly, the appropriate amount of as-prepared NiO powders was fully ground and mixed with diethanolamine and ethanol to form a slurry suspension. The pastes were evenly coated onto the electrodes of sensor's substrate. Then, the sensor was placed in aging platform and maintained at 120°C for 100 h to improve the stability of the sensor. Gas sensing properties toward C_2H_2 were measured using a CGS-1TP (Chemical Gas Sensor-1 Temperature Pressure) intelligent gas sensing analysis system. The sensor was placed on the heating table of the gas chamber and two probes were adjusted to ensure good electrical signals of the sensing materials. Then, the working temperature was set and air was delivered into the chamber at a constant flow rate. When the resistance of the sensor was stable in the air, it's denoted as Ra. Then, a certain amount of target gas was injected into the chamber through the injection hole. The change of resistance curve in the software was observed until the resistance value was stable again, denoted as Rg. The target gas flow was vented and the sensor was exposed to air again. The concentration of target gas (C_2H_2) was controlled by the mass flow controllers (MFC) with the following equation (Equation 1):

$$\text{Gas concentration (ppm)} = \frac{\text{Flow rate (target gas)} \times \text{Gas cylinder (target gas)}}{\text{Flow rate (target gas)} + \text{Flow rate (air)}} \quad (1)$$

The response (S) of the sensor was defined as the ratio of Rg to Ra. And the response (recovery) time was regarded as the time required reach 90% of the total resistance change.

RESULTS AND DISCUSSION

Morphology and Structure

Figure 1A shows the XRD patterns of the obtained samples. The identified peaks in two curves can be well matched with the cubic crystalline structure of NiO (JCPDS Card no. 04-0835) without observable impurity peaks, demonstrating that high purity of NiO. Morphologies and structural features of the samples are characterized by SEM and TEM, as shown in **Figures 1B–E**. From **Figure 1B**, the NiO hierarchical nanoflowers are assembled from a bunch of well-defined nanorods. The roots of these nanorods come together while the tips are detached. **Figure 1C** illustrates that each individual nanorod from the flower shared the same geometric center. The average diameter of these nanorods is ∼900 nm and the length is ∼6 μm. Additionally, some rods are scattered around flower-like structures. As observed in the inset of **Figure 1C**, the size of nanorods was similar to what we had observed in SEM images. In **Figure 1D**, the nanoneedles are assembled into homogeneously distributed flower-like structures (AlHadeethi et al., 2017). The magnified SEM image in **Figure 1E** displays the nanoneedles are thicker at roots with sharper emanative ends. Each needle is ∼2.5 um in length and ∼80 nm in diameter at the middle, which is in consistence with the observation in TEM image (the inset of **Figure 1E**).

Formation Mechanism

Based on the above observations, we proposed a possible formation mechanism for the morphologies evolution of the nanorod-assembled NiO nanoflowers, as shown in **Figure 2A**. Firstly, ammonia aqueous acts as an alkaline reagent to release OH^- ions. CTAB is a surfactant with a hydrophobic part (Li Y. Q. et al., 2015; Liu et al., 2017). When the $Ni(OH)_2$ comes across CTAB, $Ni(OH)_2$ will be preferably absorbed on the CTA^+ heads. Subsequently, the grown $Ni(OH)_2$ nanoparticles are connected with each other by orientation attachment to form many nanorods. It's proposed that CTAB seemingly acts as an adhesive to gather the nanorods together (Li T. M. et al., 2015; Miao et al., 2017). Finally, the nanorods self-assemble into the ultimate flower-like architectures driven by the minimum surface energy theory.

For the formation of the nanoneedle-assembled hierarchical NiO nanoflowers (**Figure 2B**), firstly, Ni^{2+} and $C_2O_4^{2-}$ can be illustrated as a $NiC_2O_4{\cdot}2H_2O$ polymer type ribbon owing to the complexation of Ni^+ and $C_2O_4^{2-}$. EG is a surfactant with symmetrical structures and functional group-OH, which serves as a ligand to Ni and blocked the crystal surface paralleled to [0,1,1] direction (Cao et al., 2015b). And then the above microstructures are connected with each other along [0,1,1] direction fabricate the needle-like structures. With the reaction time goes by, $NiC_2O_4{\cdot}2H_2O$ nanoneedles aggregate with each other to assemble into hierarchical needle-flower. Finally, NiO nanoflowers are obtained by thermal calcination.

Gas Sensing Properties

To further study the connection between the size of the assembling units and gas sensing performances, we conduct gas sensing experiments. Firstly, we investigate gas response curves with temperature changing toward 200 ppm C_2H_2. In **Figure 2C**, there is a volcano-shaped trend for the changes in gas response of both kinds of nanoflowers. Apparently, the gas response of the needle-flower NiO is higher than that of rod-flower. The responses at peaks are 15.76 and 25.71 at 300°C, respectively (Long et al., 2018; Zhang et al., 2018). Herein, we determine the

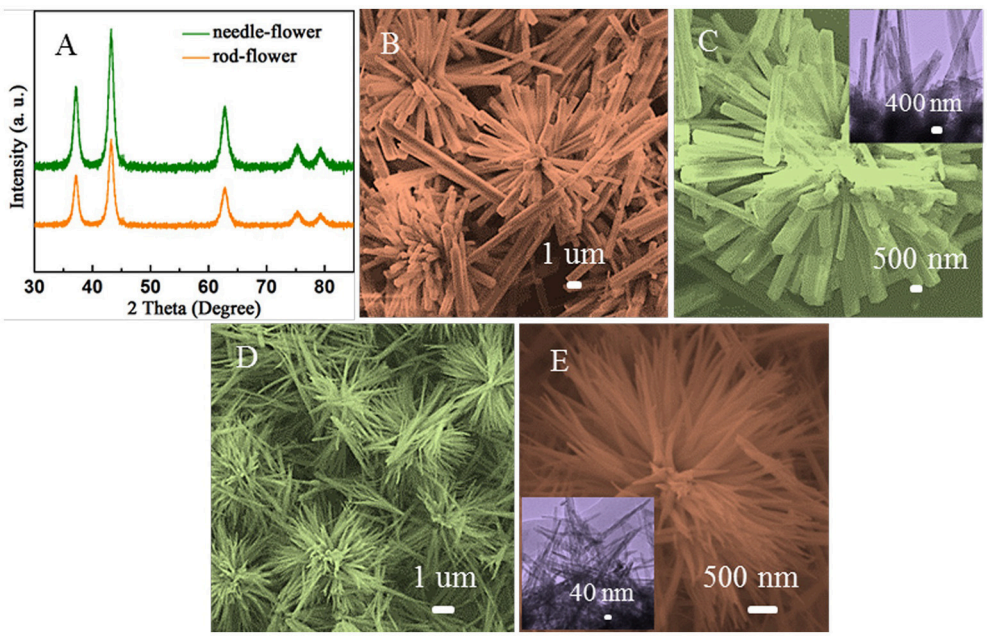

FIGURE 1 | (A) XRD patterns of the obtained samples. **(B,C)** SEM images of the rod-flower NiO and TEM image in the inset of **(C)**. **(D,E)** SEM images of the needle-flower NiO and TEM image in the inset of **(E)**.

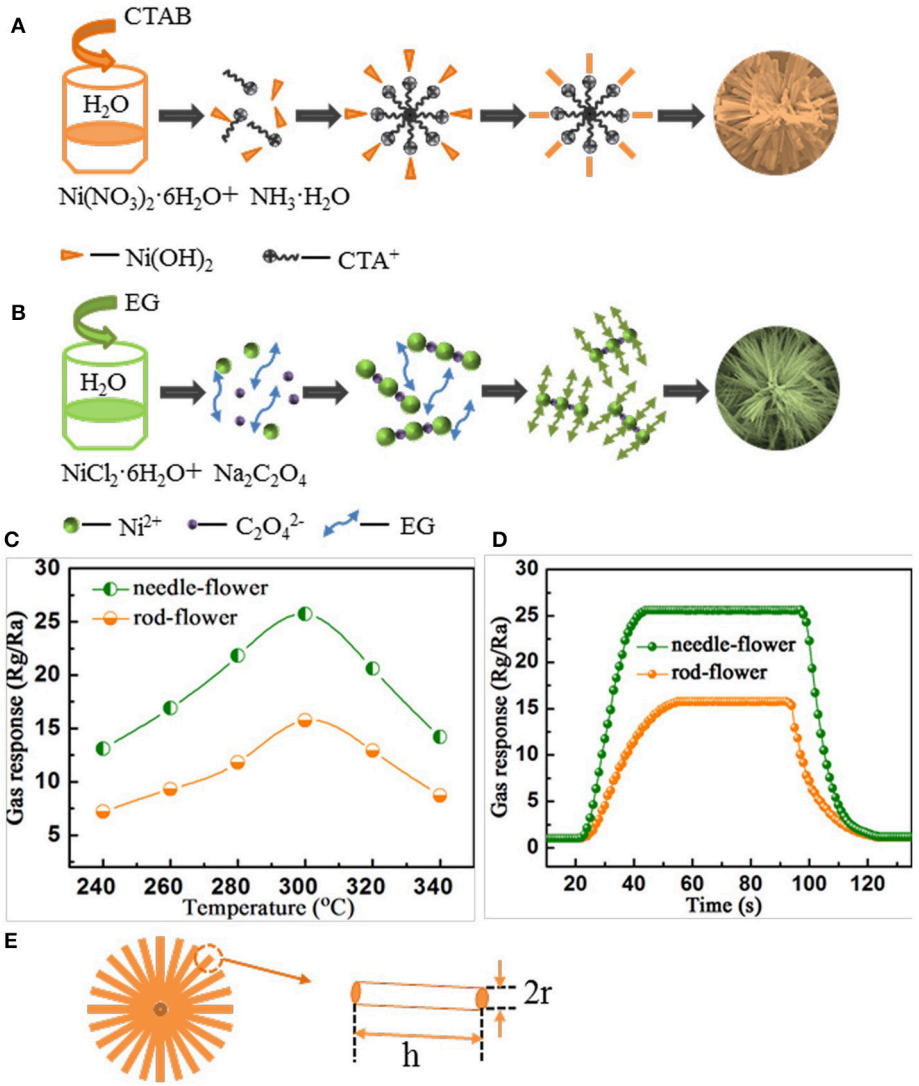

FIGURE 2 | (A,B) Schematic of the formation process. **(C)** Gas response as the function of operating temperature under C_2H_2 concentration of 200 ppm. **(D)** The response and recovery characteristics of rod-flower and needle-flower NiO under C_2H_2 concentration of 200 ppm at 300°C. **(E)** A simplified model to calculate the surface area of hierarchical NiO nanoflowers.

optimum working temperature to be 300°C for the later testing. **Figure 2D** demonstrates the response and recovery characteristic of hierarchical NiO nanoflowers toward 200 ppm C_2H_2 at 300°C. Both sensors exhibit excellent gas sensing performances. It's clearly seen that the response of the needle-flower NiO is higher than that of rod-flower. Besides, the needle-flower NiO exhibits a shorter response and recovery time (23 and 26 s) compared with that of the rod-flower NiO (34 and 32 s). In addition, a comparison about the sensing performances of NiO sensors in this work and other literature reports is summarized in **Table 1**. It is not difficult to find that the needle-flower NiO based gas sensor in this paper has excellent gas sensing characteristics and has great potential to be a promising candidate for gas-sensitive materials (Lin et al., 2015; Lu et al., 2016; Majhi et al., 2018; San et al., 2018).

Whether the working temperature vs. response or the response and recovery characteristic, sensor based on needle-flower NiO absolutely prevails over that of rod-flower. This may be attributed to the needle-flower's high surface area. In order to verify this hypothesis, we use a simple simplified model to calculate the surface area of the hierarchical NiO structures (**Figure 2E**) from associated literature (Lee, 2009; Zhang et al., 2012). We made a slight change according to our data based on the theory. Whether constituent blocking units are nanorods or naononeedles, this proposal has reasonable guiding significance to conduct qualitative analysis. In this modified model, the specific surface area (Equation 2) is

$$S \cong \frac{(\pi r^2 + 2\pi rh)n}{n\pi r^2 \rho} \sim \frac{1}{\rho}\left(1 + \frac{2h}{r}\right) \quad (2)$$

TABLE 1 | Comparison of NiO based gas sensor in this work and those literature reports.

Sensing materials	Target gas (ppm)	Temperature (°C)	Response	References
Needle-flower NiO	Acetylene 200 ppm	300	25.71	This work
Rod-flower NiO	Acetylene 200 ppm	300	15.76	This work
Hollow NiO/SnO_2 heterostructure	Acetylene 100 ppm	206	13.8	Lin et al., 2015
Porous cactus-like NiO	Acetone 100 ppm	260	13.51	Lu et al., 2016
NiO/ZnO heterojunction microflowers	Formaldehyde 100 ppm	200	13.1	San et al., 2018
Pristine NiO nanoparticles	Ethanol 100 ppm	300	1.88	Majhi et al., 2018
Core-shell Au@NiO	Ethanol 100 ppm	200	2.54	Majhi et al., 2018

Where S stands for the specific surface area, r is the equivalent radius of 1D unit, h is the length of 1D unit which can be also expressed as the radius of hierarchical structures, n is the number and ρ is the density of 1D unit. To a specific material, ρ can be considered as a constant. So S is proportional to h/r. Through the measurement and calculation, the h/r value (66.7) of the nanoneedles is ∼5 times that of the nanorods (13.4). So the S of the needle-flower is larger. It can explain why the needle-flower NiO shows higher gas response and rapid response/recovery behavior. The larger specific area will provide many adsorption and desorption sites for oxygen, leading to the increasement in the conductivity.

Gas Sensing Mechanism

The sensing mechanism of NiO-based gas sensors involves three serial reactions: adsorption-oxidation-desorption (Zhu et al., 2017). In the case of p-type semiconductor, its carrier is the hole with positive charge. Specifically, when the sensor is in the air, oxygen molecules react with NiO surface (Equations 3, 4). Due to the above reaction, electrons on the NiO surface combine with O_2 to form oxygen negative ions (O_2^-, O^-, and O^{2-}). This process cause the decrease of electrons and the increase of holes to form a hole accumulation layer, resulting in the resistance of the sensor decreases correspondingly. When NiO surface comes into contact with C_2H_2 gas, oxygen ions will oxidize gas molecules into CO_2 and H_2O, and releases electrons to recombine with holes (Equations 5, 6), leading to the decrease of carriers in hole accumulation layer and an increase in the resistance (Balamurugan et al., 2014; San et al., 2015).

$$O_2\ (gas) \rightarrow O_2\ (ads) \quad (3)$$

$$O_2\ (ads) + ne^- \rightarrow O^{n-}\ (ads) \quad (4)$$

$$C_2H_2\ (gas) \rightarrow C_2H_2\ (ads) \quad (5)$$

$$C_2H_2\ (ads) + O^{n-}(ads)^- \rightarrow CO_2 + H_2O + ne^- \quad (6)$$

CONCLUSION

In summary, nanorods and nanoneedles assembled NiO hierarchical structures have been successfully synthesized via a hydrothermal method and annealing process. Based on the comparative studies, we draw a conclusion that the size (length and diameter) of blocking units has a great influence on gas sensing properties of hierarchical structures. The integral morphologies and sizes of blocking units can be controlled by tuning the additives. Here, CTAB/EG was introduced as a structure-directing agent to regulate the aggregation and assembly. Compared with rod-flower NiO, the needle-flower NiO based sensor exhibits an enhanced gas sensing performance. This enhancement could be ascribed to the larger specific area of needle-flower, which provides more adsorption and desorption sites for chemical reaction as well as abundant effective diffusion channels for C_2H_2. The results hold a novel point in constructing highly efficient gas sensors. The detection capability of gas sensors determines the effectiveness of transformer on-line monitoring. Therefore, optimize the morphology and structure of gas sensitive materials is very meaningful work. Gas sensors with the advantages of miniaturization structure, high sensitivity, and fast response speed have very high practical value in power system security.

AUTHOR CONTRIBUTIONS

HZ and W-GC conceived and designed the experiments. HZ, Y-QL, and L-FJ performed the experiments. FC and Z-HS analyzed the data. HZ wrote the manuscript with input from all authors. All authors read and approved the manuscript.

FUNDING

This work was supported by the National 111 Project of the Ministry of Education of China (No. B08036), the Plan of Innovation Team Construction from Chongqing Universities (No. CXTDX201601001), and the Scientific Research Fund of Chongqing University of Arts and Sciences (2017RDQ38).

ACKNOWLEDGMENTS

We thank the State Key Laboratory of Power Transmission Equipment and System Security and New Technology, Chongqing University for supporting this study.

REFERENCES

AlHadeethi, Y., Umar, A., Ibrahim, A. A., AlHeniti, S. H., Kumar, R., and Baskoutas, S., et al. (2017). Synthesis, characterization and acetone gas sensing applications of Ag-doped ZnO nanoneedles. *Ceram. Int.* 43, 6765–6770. doi: 10.1016/j.ceramint.2017.02.088

Balamurugan, C., Maheswari, A. R., and Lee, D. W. (2014). Structural, optical, and selective ethanol sensing properties of p-type semiconducting $CoNb_2O_6$ nanopowder. *Sens. Actuators B Chem.* 205, 289–297. doi: 10.1016/j.snb.2014.08.076

Cao, S. K., Zeng, W., Li, T. M., Gong, J., and Zhu, Z. J. (2015a). Hydrothermal synthesis of NiO nanobelts and the effect of sodium oxalate. *Mater. Lett.* 156, 25–27. doi: 10.1016/j.matlet.2015.04.149

Cao, S. K., Zeng, W., Long, H. W., Gong, J., Zhu, Z. J., and Chen, L. (2015b). Synthesis and controlled growth of NiO hierarchical bundle-like nanoflowers with the assistance of ethylene glycol. *Mater. Lett.* 161, 275–277. doi: 10.1016/j.matlet.2015.08.129

Chen, W. G., Zhou, Q., Gao, T. Y., Su, X. P., and Wan, F. (2013). Pd-doped SnO_2-based sensor detecting characteristic fault hydrocarbon gases in transformer oil. *J. Nanomater.* 2013, 2527–2531. doi: 10.1155/2013/127345

Duo, S. D., Li, Y. Y., Zhang, H., Liu, T. Z., Wu, K., and Li, Z. Q. (2016). A facile salicylic acid assisted hydrothermal synthesis of different flower-like ZnO hierarchical architectures with optical and concentration-dependent photocatalytic properties. *Mater. Character.* 114, 185–196. doi: 10.1016/j.matchar.2016.02.021

Jin, L. F., Chen, W. G., Zhang, H., Xiao, G. W., Yu, C. T., and Zhou, Q. (2017). Characterization of reduced graphene oxide (rGO)-loaded SnO_2 nanocomposite and applications in C_2H_2 gas detection. *Appl. Sci.* 7, 19–33. doi: 10.3390/app7010019

Kaminski, T., Anis, S. F., Husein, M. M., and Hashaikeh, R. (2018). Hydrocracking of athabasca VR using NiO-WO_3 zeolite-Based catalysts. *Energ. Fuel.* 32, 2224–2233. doi: 10.1021/acs.energyfuels.7b03754

Kim, J. Y., and Yong, K. J. (2011). Mechanism study of ZnO nanorod-bundle sensors for H_2S gas sensing. *J. Phys. Chem. C* 115, 7218–7224. doi: 10.1021/jp110129f

Lee, J. H. (2009). Gas sensors using hierarchical and hollow oxide nanostructures: overview. *Sens. Actuators B Chem.* 140, 319–336. doi: 10.1016/j.snb.2009.04.026

Li, T. M., Zeng, W., Zhang, Y. Y., and Hussain, S. (2015). Nanobelt-assembled nest-like MoO_3 hierarchical structure: hydrothermal synthesis and gas-sensing properties. *Mater. Lett.* 160, 476–479. doi: 10.1016/j.matlet.2015.08.031

Li, Y. Q., Liu, T. M., Li, T. M., and Peng, X. H. (2015). Hydrothermal fabrication of controlled morphologies of MoO_3 with CTAB: structure and growth. *Mater. Lett.* 140, 48–50. doi: 10.1016/j.matlet.2014.10.153

Lin, Y., Li, C., Wei, W., Li, Y. J., Wen, S. P., Sun, D. M., et al. (2015). A new type acetylene gas sensor based on hollow heterostructure. *RSC Adv.* 5, 61521–61527. doi: 10.1039/c5ra10327d

Liu, S. L., Zeng, W., and Chen, T. (2017). Synthesis of hierarchical flower-like NiO and the influence of surfactant. *Phys. E* 85, 13–18. doi: 10.1016/j.physe.2016.08.016

Long, H. W., Zeng, W., Wang, H., Qian, M. M., Liang, Y. H., and Wang, Z. (2018). Self-Assembled biomolecular 1D nanostructures for aqueous sodium-Ion battery. *Adv. Sci.* 5, 1700634–1700637. doi: 10.1002/advs.201700634

Lu, Y., Ma, Y. H., Ma, S. Y., Jin, W. X., Yan, S. H., Xu, X. L., et al. (2016). Synthesis of cactus-like NiO nanostructure and their gas-sensing properties. *Mater. Lett.* 164, 48–51. doi: 10.1016/j.matlet.2015.10.117

Majhi, S. M., Naik, G. K., Lee, H. J., Song, H. G., Lee, C. R., Lee, I. H., et al. (2018). Au@NiO core-shell nanoparticles as a p-type gas sensor: novel synthesis, characterization, and their gas sensing properties with sensing mechanism. *Sens. Actuators B Chem.* 268, 223–231. doi: 10.1016/j.snb.2018.04.119

Miao, R. Y., Zeng, W., and Gao, Q. I. (2017). Hydrothermal synthesis of novel NiO nanoflowers assisted with CTAB and SDS respectively and their gas-sensing properties. *Mater. Lett.* 186, 175–177. doi: 10.1016/j.matlet.2016.09.127

Nakasa, A., Usami, H., Sumikura, S., Hasegawa, S., Koyama, T., and Suzuki, E. (2005). A high voltage dye-sensitized solar cell using a nanoporous NiO photocathode. *Chem. Lett.* 34, 500–501. doi: 10.1246/cl.2005.500

San, X. G., Li, M., Liu, D. Y., Wang, G. S., Shen, Y. B., Meng, D., et al. (2018). A facile one-step hydrothermal synthesis of NiO/ZnO heterojunction microflowers for the enhanced formaldehyde sensing properties. *J. Alloy. Compd.* 739, 260–269. doi: 10.1016/j.jallcom.2017.12.168

San, X. G., Wang, G. S., Liang, B., Ma, J., Meng, D., and Shen, Y. (2015). Flower-like NiO hierarchical microspheres self-assembled with nanosheets: surfactant-free solvothermal synthesis and their gas sensing properties. *J. Alloy. Compd.* 636, 357–362. doi: 10.1016/j.jallcom.2015.02.191

Singh, S., and Bandyopadhyay, M. (2010). Dissolved gas analysis technique for incipient fault diagnosis in power transformers: a bibliographic survey. *IEEE Electr. Insul. Mag.* 26, 41–46. doi: 10.1109/MEI.2010.5599978

Yu, Y., Xia, Y., Zeng, W., and Liu, R. (2017). Synthesis of multiple networked NiO nanostructures for enhanced gas sensing performance. *Mater. Lett.* 206, 80–83. doi: 10.1016/j.matlet.2017.06.119

Zhang, F. B., Zhou, Y. K., and Li, H. L. (2004). Nanocrystalline NiO as an electrode material for electrochemical capacitor. *Mater. Chem. Phys.* 83, 260–264. doi: 10.1016/j.matchemphys.2003.09.046

Zhang, L. X., Zhao, J. H., Lu, H. Q., Li, L., Zheng, J. F., Li, H., et al. (2012). Facile synthesis and ultrahigh ethanol response of hierarchically porous ZnO nanosheets. *Sens. Actuators B Chem.* 161, 209–215. doi: 10.1016/j.snb.2011.10.021

Zhang, Y., Zeng, W., Ye, H., and Li, Y. (2018). Enhanced carbon monoxide sensing properties of TiO_2 with exposed {001} facet: a combined first-principle and experimental study. *Appl. Surf. Sci.* 442, 507–516. doi: 10.1016/j.apsusc.2018.02.036

Zhu, L., Li, Y., and Zeng, W. (2018). Hydrothermal synthesis of hierarchical flower-like ZnO nanostructure and its enhanced ethanol gas-sensing properties. *Appl. Surf. Sci.* 427, 281–287. doi: 10.1016/j.apsusc.2017.08.229

Zhu, L., Li, Y. Q., and Zeng, W. (2017). Enhanced ethanol sensing and mechanism of Cr-doped ZnO nanorods: experimental and computational study. *Ceram. Int.* 43, 14873–14879. doi: 10.1016/j.ceramint.2017.08.003

Zhu, L., and Zeng, W. (2017). Room-temperature gas sensing of ZnO-based gas sensor: a review. *Sens. Actuators A Phys.* 267, 242–261. doi: 10.1016/j.sna.2017.10.021

Conflict of Interest Statement: The authors declare that the research was conducted in the absence of any commercial or financial relationships that could be construed as a potential conflict of interest.

frontiers in Chemistry

ORIGINAL RESEARCH
published: 05 October 2018
doi: 10.3389/fchem.2018.00452

Synthesis and Gas-Sensing Property of Highly Self-assembled Tungsten Oxide Nanosheets

Liangbin Hu, Pengfei Hu, Yong Chen, Zehui Lin and Changjun Qiu**

School of Mechanical Engineering, University of South China, Hengyang, China

We report the synthesis of tungsten oxide (WO_3) nanosheets using a simple yet efficient hydrothermal technique free of surfactantand template. The WO_3 nano-sheets are self-assembled as well to form ordered one-dimensional chain nanostructure. A comprehensive microscopic characterization reveals that the nano-sheets have triangular and circular two different shape edges, dislocation and stacking faults are also observed, which should have implications for our understanding of catalytic activity of ceria. We also propose a growth mechanism for the nano-sheets. As a result of this unique morphology, this WO_3 nano-sheets are found to show excellent gas-sensing properties which can use as promising sensor materials detecting ethanol with low concentration.

Keywords: crystal structure, defects, nanosheets, highly self-assembled, gas-sensitivity

OPEN ACCESS

Edited by:
Zhongchang Wang,
Laboratório Ibérico Internacional de Nanotecnologia (INL), Portugal

Reviewed by:
Jun Wang,
Shenzhen University, China
Xin Wang,
Shenzhen University, China

****Correspondence:***
Yong Chen
chenyongjsnt@163.com
Changjun Qiu
qiuchangjun@hotmail.com

Specialty section:
This article was submitted to Nanoscience, a section of the journal Frontiers in Chemistry

Received: *02 June 2018*
Accepted: *12 September 2018*
Published: *05 October 2018*

Citation:
Hu L, Hu P, Chen Y, Lin Z and Qiu C (2018) Synthesis and Gas-Sensing Property of Highly Self-assembled Tungsten Oxide Nanosheets. Front. Chem. 6:452. doi: 10.3389/fchem.2018.00452

INTRODUCTION

Tungsten trioxide WO_3 nanomaterials are extensively applied in electrochromic device, gas sensor and photocatalysts filed (Hai et al., 2016; Zhang et al., 2018). Great effort has been devoted to the control the specific size and shape of WO_3 nanoparticles which can significantly impact properties of materials. Up to now, the WO_3 nanoparticles with avariety of morphologies (such as nano-wires, nano-rods, nano-plate, nano-spheres and so on) have been syhthesized successfully via high-intensity ultrasound, rapid microwave, hydrothermal synthesis and other methods (Chai et al., 2016, Hu et al., 2017a, Xu et al., 2017; Chen et al., 2018; Parthibavarman et al., 2018; Zhan et al., 2018). Among all of those applied methods, hydrothermal synthesis technique has been concerned due to the merits of simple operation, low energy consumption, the possibility for large-scale industrialization and so on.

Here,we report the WO_3 nano-sheets with highly self-assembled architecture synthesized via the hydrothermal synthesis process. Defects are observed in the nano-sheets, which may play a key role in affecting properties of WO_3 nano-sheets. In addtion,we also test the response and selectivity of the sensor fabricated from the WO_3 nano-sheets.

MATERIALS AND METHODS

All the reagents were analytical grade and without further purification. We adopted a facile hydrothermal method to synthesize the nanostructures. First of all, 32 ml of deionized water and 8 ml glycerol ($C_3H_8O_3$) were mixed into a mixture, then 1.6 nmol of sodium tungstate dihydrate ($Na_2WO_4{\cdot}2H_2O$) and 3 nmol oleic acid ($C_{18}H_{34}O_2$) were dispersed into the mixture, and stirred for 15 min with a magnetic stirrer. Secondly, the pH of the mixture was adjusted to 1.25 by HCl. After stirring for 15 min, the solution was transferred into the Teflon-lined stainless steel autoclave and treated at 120°C during 12 h under autogenously pressure.

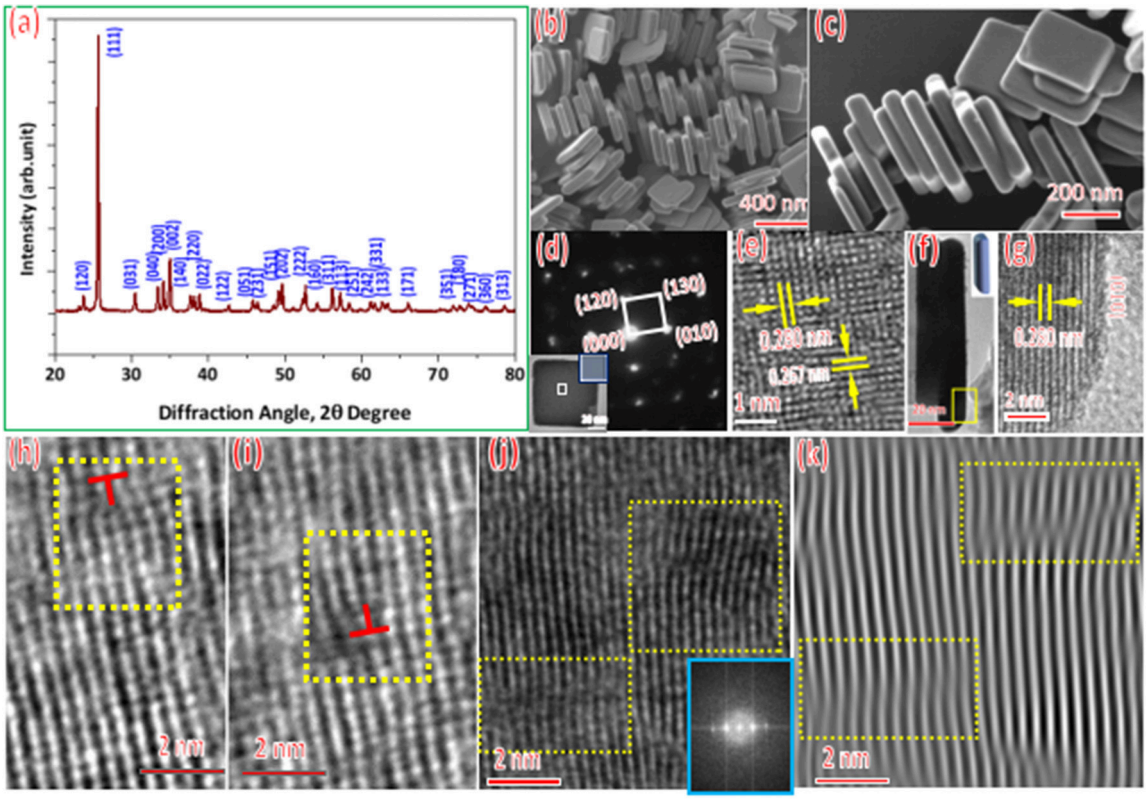

FIGURE 1 | Characterization of the samples prepared by hydrothermal method:**(a)** XRD spectrum, **(b–c)** SEM images, **(d–g)**TEM images, insert of **(d)** shows the TEM image of a WO3 nanoparticle, insert of **(f)** shows the model of the side of the nanosheet, **(h–k)** defects of samples, insert of **(j)** shows the Fast Fourier transform of the HRTEM image.

Finally, the obtained particles were washed by deionized and alcohol to remove the unexpected ions by high-speed centrifugation and then dried at 60°C for 10 h in air.

The characterization of speciemen as our previous work (Chen et al., 2013, 2014; Hu et al., 2017b). The process of measuring the gas sensitivity of the prepared nanomaterials is described in the literature (Guo and Wang, 2016). Response of the sensors was defined as the ratio of Ra (resistances in air) to Rg (resistances in target gases).

RESULTS

Figure 1a shows a typical XRD spectrum of the products, the diffraction peaks match well with those of a standard $WO_3 \cdot H_2O$ with orthorhombic structure (JCPDS No. 84-0886). The $WO_3 \cdot H_2O$ nano-particles exhibit rectangle shape with an average size of ∼400 nm and thickness of 30nm (**Figure 1b**). In addtion, one-dimensional chain nanostructure is self-assembled by the quadrilateral faces on the both sides of the nano-sheets. The face of nano-sheet are flat (**Figures 1b,c**). The corresponding SADP identifies that the structure of WO_3 nano-sheets is orthorhombic (**Figures 1d**). **Figure 1e** shows a high-resolution TEM (HRTEM) image taken around the corner of a nano-sheet. We determined the lattice spacing of the perpendicular lattice fringes to be ∼0.280 and ∼0.267 nm which are belong to the WO_3 (010) and (120) planes respectively. **Figure 1g** shows a HRTEM image taken from the corner area of the nano-sheet **Figure 1f** from which lattice spacing is determined to be ∼0.280 nm, in line with the distance between {010} planes of WO_3. In addtion, the edges of the nano-sheets are in an arc shape (insert of **Figure 1f**). Two different direction edge dislocations: positive edge dislocation (**Figure 1h**) and negative edge dislocation (**Figure 1i**) are deteced by the HR-TEM, which should be critical for the properties of WO_3. Apart from the defects on the surface, we also observed the stacking faults in nano-sheet (**Figure 1j**), which should impact the properties of WO_3 nanoparticles as well. The stacking fault was observed obviously by the one-dimensionally filtered HR-TEM images of the WO_3 nano-sheet (**Figure 1k**). Those dislocations and stacking faults may affect the catalytic activity or other properties of nano material (Wang et al., 2011, 2014, 2016; Sun et al., 2015).

Figure 2 shows the gases (NH_3, CH_3OH, C_6H_6) response of the sensor based on WO_3 nanosheets. All of the gases were tested at an operating temperature of 300°C with a concentration of 30 ppm. In **Figure 2**, the results indicate that the sensor exhibited little responses to NH_3, C_6H_6, to indicated that it was insensitive to NH_3, C_6H_6. For ethanol, the highest response of the sensor was 25.6, while the responses to NH_3 and C_6H_6 were no >1.

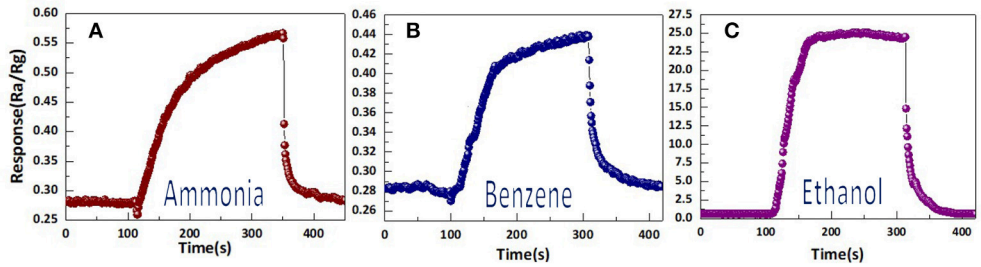

FIGURE 2 | The response of highly self-assembled tungsten oxide nanosheets sensor toward 30 ppm of different testing gases: **(a)** ammonia, **(b)** benzene, **(c)** ethanol.

DISCUSSION

In light of the aforementioned microstructural characterization, we propose a likely growth mechanism for the nanosheet. First, the $Na_2WO_4{\cdot}2H_2O$ is ionized to WO_4^-. Then, the WO_4^- ion react with H^+ which ionized by HCl, forming the H_2WO_4 suspension. The H_2WO_4 suspension decomposes, at the high temperature and pressure during hydrothermal process, resulting in to the nucleation of WO_3. The oleic acid acts as a soft template and controls the growth rate of different crystal plane owing to its selective absorption and desorption behavior. Then most of WO_3 nano-sheets with {010} exposure planes are self-assembled, forming one-dimensional chain nanostructures, due to the addition of oleic acid. The formation process can be described as follows:

$$Na_2WO_4{\cdot}2H_2O \rightarrow 2Na^+ + WO_4^- + 2H_2O \quad (1)$$

$$HCl \rightarrow H^+ + Cl^- \quad (2)$$

$$2H^+ + WO_4^- \rightarrow H_2WO_4 \quad (3)$$

$$H_2WO_4 \rightarrow WO_3 + H_2 \quad (4)$$

We imply that the WO_3 nano-sheets can act as an efficient gas-sensing material for selective detection of ethanol. Such the sensing performance due to the fact that the diffusion of ethanol and its oxidation with O^- or O^{2-} are very rapidly in nanoplates structures (Xiao et al., 2017). When sensor prepared by the WO_3 nanosheets is exposed in air, the resistance of the WO_3 nanosheets is increased by oxygen molecules which adsorbed on the surfaces of the WO_3 nanosheets, trapping electrons in the conduction band and forming oxygen species (O^-, O^{2-}). As ethanol is introduced to the sensor, the oxygen species (O^-, O^{2-}) react with ethanol molecules on the surface of the WO_3 nanosheets, which will release trapped electrons to conduction band and resistance of the WO_3 nanosheets is decreased (Ahmad et al., 2013).

CONCLUSIONS

We have adopted the hydrothermal technique to synthesize highly self-assembled WO_3 nano-sheets using the tungsten resource $Na_2WO_4{\cdot}2H_2O$ and the soft template oleic acid. We demonstrated that the WO_3 nano-sheets are mainly exposed with {010} planes and crystal defects such as edge dislocations and stacking faults exist in single crystalline nano WO_3 by microscopic investigations, which may be important for the catalytic activity of WO_3. We indicate that the WO_3 nano-sheets could be used as promising sensor material for detecting CH_3OH with low concentration.

AUTHOR CONTRIBUTIONS

LH synthesized and characterized the microstructure of highly self-assembled tungsten oxide nanosheets and wrote the manuscript. PH and ZL tested the response and selectivity of the sensor fabricated from the WO_3 nano-sheets. YC and CQ directed the experiment. All authors read and approved the manuscript.

ACKNOWLEDGMENTS

YC thanks the financial support by the Construct Program of the Key Discipline of Hunan province (Education Department of Hunan Province Bulletin grant no.[2014]85). ZL thanks the financial support by the Project of Research Study and Creativity Experiment Plan for College Students of the Hunan province (Education Department of Hunan Province Bulletin grant no.[2016]283).

REFERENCES

Ahmad, M. Z., Sadek, A. Z., Ou, J. Z., Yaacob, M. H., Latham, K., and Wlodarski, W. (2013). Facile synthesis of nanostructured WO_3 thin films and their characterization for ethanol sensing. *Mater. Chem. Phys.* 141, 912–919. doi: 10.1016/j.matchemphys.2013.06.022

Chai, Y., Ha, F. Y., Yam, F. K., and Hassan, Z. (2016). Fabrication of tungsten oxide nanostructure by sol-gel method. *Proc. Chem.* 19, 113–118. doi: 10.1016/j.proche.2016.03.123

Chen, G. C., Chua, X. F., Qiao, H. B., Ye, M. F., Chen, J., Gao, C., et al. (2018). Thickness controllable single-crystal WO_3 nanosheets: highly selective sensor for triethylamine detection at room temperature. *Mater. Lett.* 226, 59–62. doi: 10.1016/j.matlet.2018.05.022

Chen,Y., Liu, T. M., Chen, C. L., Guo, W. W., Sun, R., Lv, S., et al. (2013). Synthesis and characterization of CeO_2 Nano-rods. *Ceram. Int.* 39, 6607–6610. doi: 10.1016/j.ceramint.2013.01.096

Chen,Y., Lv, S. H., Chen, C. L., Qiu, C. J., Fan, X. F., and Wang, Z. C. (2014). Controllable synthesis of ceria nanoparticles with uniform reactive {100} exposure planes. *J. Phys. Chem. C* 118, 4437–4443. doi: 10.1021/jp410625n

Guo, W. W., and Wang, Z. C. (2016). Composite of ZnO spheres and functionalized SnO_2 nanofibers with an enhanced ethanol gas sensing properties. *Mater. Lett.* 169, 246–249. doi: 10.1016/j.matlet.2016.01.118

Hai, G., Huang, J., Jie, Y., Li, J., Cao, L., Zhang, G., et al. (2016). Influence of octadecylamine on the phase composition and the photocatalytic property of the tungsten oxide. *Mater. Lett.* 174, 134–137. doi: 10.1016/j.matlet.2016.03.049

Hu, P. F., Chen, Y., Chen, Y., Lin, Z. H., and Wang, Z. C., (2017a). Hydrothermal synthesis and photocatalytic properties of WO_3 nanorods by using capping agent $SnCl_4{\cdot}5H_2O$. *Phys. E* 92, 12–16. doi: 10.1016/j.physe.2017.05.004

Hu, P. F., Chen, Y., Sun, R., Chen, Y., Yin, Y. R., Wang, Z. C., et al. (2017b). Synthesis, characterization and frictional wear behavior of ceria hybrid architectures with {111} exposure planes. *Appl. Surf. Sci.* 401, 100–105. doi: 10.1016/j.apsusc.2017.01.005

Parthibavarman, M., Karthik, M., and Prabhakaran, S. (2018). Facile and one step synthesis of WO_3 nanorods and nanosheets as an efficient photocatalyst and humidity sensing material. *Vacuum* 155, 224–232. doi: 10.1016/j.vacuum.2018.06.021

Sun, R., Wang, Z. C., Saito, M., Shibata, N., and Ikuhara, Y. (2015). Atomistic mechanisms of nonstoichiometry-induced twin boundary structural transformation in titanium dioxide. *Nat. Commun.* 6:7120. doi: 10.1038/ncomms8120

Wang, Z. C., Saito, M., McKenna, K. P., Fukami, S., Sato, H., Ikeda, S., et al. (2016). Atomic-scale structure and local chemistry of CoFeB-MgO magnetic tunnel junctions. *Nano Lett.* 16, 1530–1536. doi: 10.1021/acs.nanolett.5b03627

Wang, Z. C., Saito, M., McKenna, K. P., Gu, L., Tsukimoto, S., Shluger, A. L., et al. (2011). Atom-resolved imaging of ordered defect superstructures at individual grain boundaries. *Nature* 479, 380–383. doi: 10.1038/nature10593

Wang, Z. C., Saito, M., McKenna, K. P., and Ikuhara, Y. (2014). Polymorphism of dislocation core structures at the atomic scale. *Nate Commun*. 5:3239 doi: 10.1038/ncomms4239

Xiao, J., Song, C. W., Dong, W., Chen, L., and Yanyan, Y. (2017). Synthesis, characterization, and gas sensing properties of WO_3 nanoplates. *Rare Metal Mater. Eng.* 46, 1241–1244. doi: 10.1016/S1875-5372(17)30144-3

Xu, L., Gu, D. X., Chang, X. T., Chai, L. G., Li, Z., Jin, X., et al. (2017). Rare-earth-doped tungsten oxide microspheres with highly enhanced photocatalytic activites. *Ceram. Int.* 43, 10263–10269. doi: 10.1016/j.ceramint.2017.05.055

Zhan,Y., Liu, Y. L., Liu, Q. Q., Liu, Z. M., Yang, H., Lei, B., et al. (2018). Size-controlled synthesis of fluorescent tungsten oxide quantum dots via one-pot ethanol-thermal strategy for ferric ions detection and bioimaging. *Sens. Actuats B Chem.* 255, 290–298. doi: 10.1016/j.snb.2017.08.043

Zhang, J., Fu, X., Hao, H., and Gan, W. (2018). Facile synthesis 3D flower-like $Ag@WO_3$ nanostructures and applications in solar-light photocatalysis. *J. Alloys Compd.* 757,134–141. doi: 10.1016/j.jallcom.2018.05.068

Conflict of Interest Statement: The authors declare that the research was conducted in the absence of any commercial or financial relationships that could be construed as a potential conflict of interest.

frontiers in Chemistry

ORIGINAL RESEARCH
published: 26 September 2018
doi: 10.3389/fchem.2018.00430

Functionalization of α-In_2Se_3 Monolayer via Adsorption of Small Molecule for Gas Sensing

Zhi Xie[1]*, *Fugui Yang*[2], *Xuee Xu*[1], *Rui Lin*[1] and *Limin Chen*[1]

[1] College of Mechanical and Electronic Engineering, Fujian Agriculture and Forestry University, Fuzhou, China, [2] School of Electronic Information Science, Fujian Jiangxia University, Fuzhou, China

Based on first-principles calculations, the adsorption of NO and NO_2 gas molecules on the α-In_2Se_3 monolayer have been studied. The adsorption configuration, adsorption energy, electronic structure and charge transfer properties are investigated. It is found that the charge transfer processes of NO and NO_2 adsorbed on the surface of α-In_2Se_3 monolayer exhibit electron donor and acceptor characteristics, respectively. After the adsorption of the molecules, the α-In_2Se_3 monolayers have new states near the Fermi level induced by NO and NO_2, which can trigger some new effects on the conducting and optical properties of the materials, with potential benefits to gas selectivity. The present work provides new valuable results and theoretical foundation for potential applications of the In_2Se_3-based gas sensor.

Keywords: 2D materials, first-principles calculation, In_2Se_3, charge transfer, gas sensor

OPEN ACCESS

Edited by:
Zhongchang Wang,
Laboratório Ibérico Internacional de Nanotecnologia (INL), Portugal

Reviewed by:
Shuping Huang,
Fuzhou University, China
Youzhao Lan,
Zhejiang Normal University, China

***Correspondence:**
Zhi Xie
xzfjau@126.com

Specialty section:
This article was submitted to Nanoscience, a section of the journal Frontiers in Chemistry

Received: *17 July 2018*
Accepted: *30 August 2018*
Published: *26 September 2018*

Citation:
Xie Z, Yang F, Xu X, Lin R and Chen L (2018) Functionalization of α-In_2Se_3 Monolayer via Adsorption of Small Molecule for Gas Sensing. Front. Chem. 6:430. doi: 10.3389/fchem.2018.00430

INTRODUCTION

In recent years, Layered two-dimensional (2D) materials have received tremendous research attention due to their unique physical and chemical properties (Miró et al., 2014; Bhimanapati et al., 2015; Xie et al., 2018). Because of their ultrahigh flexibility, strength and thickness-dependent electronic properties (Wang et al., 2012; Novoselov et al., 2016), the nanodevices based on 2D materials and tuning the properties of their heterostructures via defects engineering (Cervenka et al., 2009; Wang et al., 2011; Park et al., 2014; Sun et al., 2015) hold great promise for potential applications in nanoscale electronics, optoelectronics and spintronics (Wang et al., 2008, 2016; Geim and Grigorieva, 2013; Lan, 2018). Additionally, the high surface/volume ratio, weak electronic screening and ultrathin thickness of 2D materials induce that their structural stability and electronic properties are very sensitive to environmental molecules, and the relevant effects make them efficient for gas molecules sensing, catalysis, and energy storage technologies (Lightcap and Kamat, 2013; Yang et al., 2016; Zhang et al., 2018). Graphene has exhibited good performance in the field of gas sensor (Kemp et al., 2013). Previous reports have also shown that MoS_2-based nanosensors possess excellent sensing ability with high response value, and their molecule adsorption properties can be modulated by applying light, strain, and external electric field (Late et al., 2013; Ma et al., 2016). Recently, InSe monolayer has been found having tunable electronic properties via the molecule adsorption and promising for gas sensing application (Ma et al., 2017). All these studies clearly reveal that external factors can modulate the properties of 2D materials effectively and extend their application fields.

Indium selenide (In_2Se_3) is an interesting III-VI group layered chalcogenide compound with multiple phases and excellent properties (Shi et al., 2013), and have attracted extensive research interest for the applications in phase change memory (Yu et al., 2007), lithium batteries (Feng et al., 2016), optoelectronic and photovoltaic devices (Zhai et al., 2010; Jacobs-Gedrim et al., 2014). Among all the phases, 2D materials based on α-In_2Se_3 exhibit obvious thickness-dependent shift of band gap and promising prospects for tunable wavelength photodetection (Quereda et al., 2016). It is also reported that the strain sensor fabricated from 2D α-In_2Se_3 films possesses good stability, excellent sensitivity, and high spatial resolution in strain distribution, showing attractive properties for e-skin applications in wearable electronics (Feng et al., 2016). However, to best of our knowledge, the investigations on the adsorption of small gas molecules on atomically thin 2D In_2Se_3 materials and the related modification of their properties are still lacking so far. It is well-known that NO_2 and NO are common air pollutants and harmful to human health. The detection and control of them are very important for the environmental protection. Hence, in this work, we have made first-principles studies on the α-In_2Se_3 monolayers adsorbed by NO and NO_2, respectively. The adsorption configuration, structural stability, electronic structure and charge transfer properties have been investigated and discussed in detail.

COMPUTATIONAL METHODS

All calculations are carried out using the Vienna *ab initio* simulation package (VASP)(Kresse and Furthmüller, 1996), with the core electrons described by the projected augmented wave (PAW) method. For the exchange-correlation term, the generalized gradient approximation (GGA) with Perdew-Burke-Ernzerhof (PBE) scheme is employed. The cutoff energy for plane-wave basis is set as 450 eV. For simulating the adsorption of the molecules, a $4 \times 4 \times 1$ supercell of the α-In_2Se_3 monolayer is built with one NO or NO_2 molecule adsorbed on its surface, and a vacuum space of more than 15 Å is set up to prevent the interactions between the repeated monolayers. The Monkhorst-Pack of $2 \times 2 \times 1$ ($4 \times 4 \times 2$) *k*-point grid is adopted for the Brillion zone sampling in geometry optimization (total energy calculation). The convergence criterion of energy is taken as 10^{-5} eV. Structure relaxation is performed until the force on each atom is smaller than 0.02 eV/Å. To estimate the adsorption stability of gas molecules on the surface of α-In_2Se_3 monolayer, the adsorption energy (E_{ad}) is calculated by the formula: $E_{ad} = E_M + E_G - E_{M+G}$, where E_M, E_G, and E_{M+G} denote the total energy of the α-In_2Se_3 monolayer, the free gas molecule, and the α-In_2Se_3 monolayer adsorbed by gas molecules, respectively. According to this definition, a positive value of E_{ad} represents the adsorption is energetically favorable.

RESULTS AND DISCUSSION

Firstly, the geometry optimizations of free gas molecules were performed. The obtained bond lengths of NO and NO_2 are 1.17 and 1.21 Å, respectively, and the O-N-O bond angle of NO_2 is 133.39°. The band gap of the clean α-In_2Se_3 monolayer has been calculated to be 0.77 eV (see **Figure 3A**). All these results are in line with the data of previous reports (Debbichi et al., 2015; Ma et al., 2017). In order to find the most stable adsorption configuration, four typical adsorbing sites on the Se atom plane of one side have been considered including the top of Se atom, the center of a Se-In bridge and two centers of the hexagonal void (see **Figure 1A**). Because of the different coordination structures of the Se atom plane on the other side, four similar adsorbing sites were also investigated on the other side (see **Figure 1B**).

For the adsorption of NO molecule, besides the eight adsorbing sites mentioned above, we also considered two different orientations of the molecule with the N-O bond perpendicular or parallel to the surface of α-In_2Se_3 monolayer. Therefore, 16 configurations have been examined. **Figure 2A** presents the top and side views of the most stable configuration obtained, where the O atom of NO molecule points away from the α-In_2Se_3 surface and the N atom of NO molecule points toward the surface with the smallest distance between the adsorbed NO and the surface atom is 2.65 Å. The N-O bond is a little shortened to 1.16 Å compared with that (1.17 Å) of free NO molecule. The adsorption energy was calculated

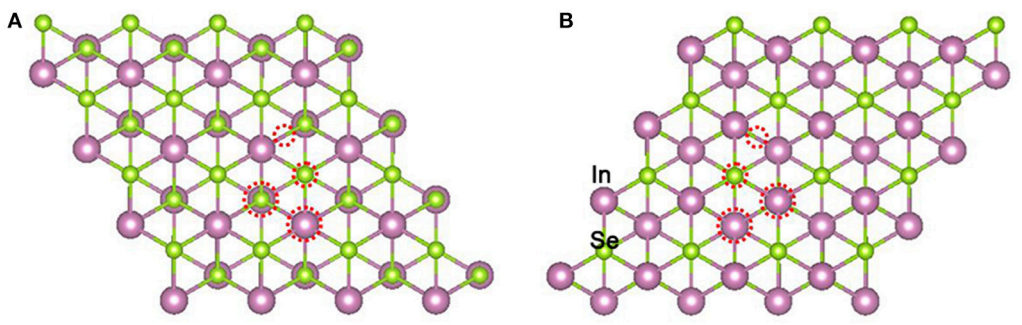

FIGURE 1 | Top views of typical adsorbing sites on the Se atom planes of one side **(A)** and the other side **(B)** of the α-In_2Se_3 monolayer. The adsorbing sites are denoted by red dotted circles.

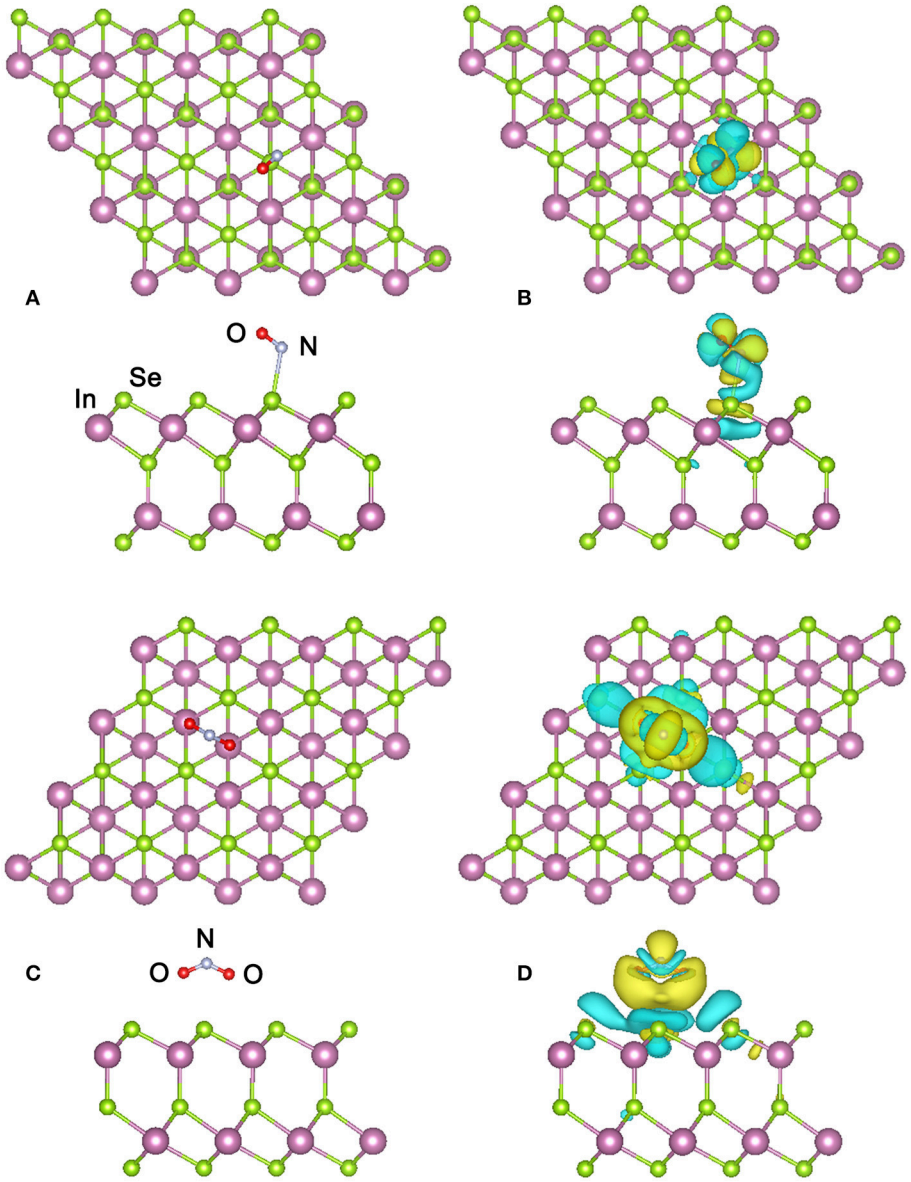

FIGURE 2 | (A) Top and side views of the most stable configuration of the α-In_2Se_3 monolayer adsorbed by NO and **(B)** its charge density difference. **(C)** Top and side views of the most stable configuration of the α-In_2Se_3 monolayer adsorbed by NO_2 and **(D)** its charge density difference. The cyan and yellow isosurfaces denote the electron depletion and accumulation, respectively. The isosurface value is set as 0.0001 e/$bohr^3$.

to be 208 meV, which is comparable to those of NO adsorptions on the monolayers of InSe, GaSe, and MoS_2 (Yue et al., 2013; Ma et al., 2017; Zhou et al., 2017). This low adsorption energy indicates the NO adsorption capability of α-In_2Se_3 monolayer is not very strong, which is applicable for the gas detection since the adsorption-desorption of NO molecule on α-In_2Se_3 monolayer can be easily achieved.

For further investigating the interactions and electron transfers between the adsorbed NO molecule and the α-In_2Se_3 monolayer, the charge density difference (CDD) is calculated from the formula: $\Delta\rho = \rho_{M+G} - \rho_M - \rho_G$, where ρ_{M+G}, ρ_M and ρ_G represent the total charge densities of the α-In_2Se_3 monolayer adsorbed by gas molecules, the α-In_2Se_3 monolayer, and the isolated gas molecule, respectively. The ρ_M and ρ_G are obtained with each atom at the same position as the adsorption configuration. In the NO_2 adsorption case, the similar calculation has also been performed. As shown in **Figure 2B**, it can be seen that the adsorption make the redistribution of charges around the NO molecule. In the space between the adsorbed NO and the α-In_2Se_3 surface, the depletion of electrons is dominant. Based on the Bader charge analysis, the charge transfer has been quantitatively calculated. It is demonstrated that the NO

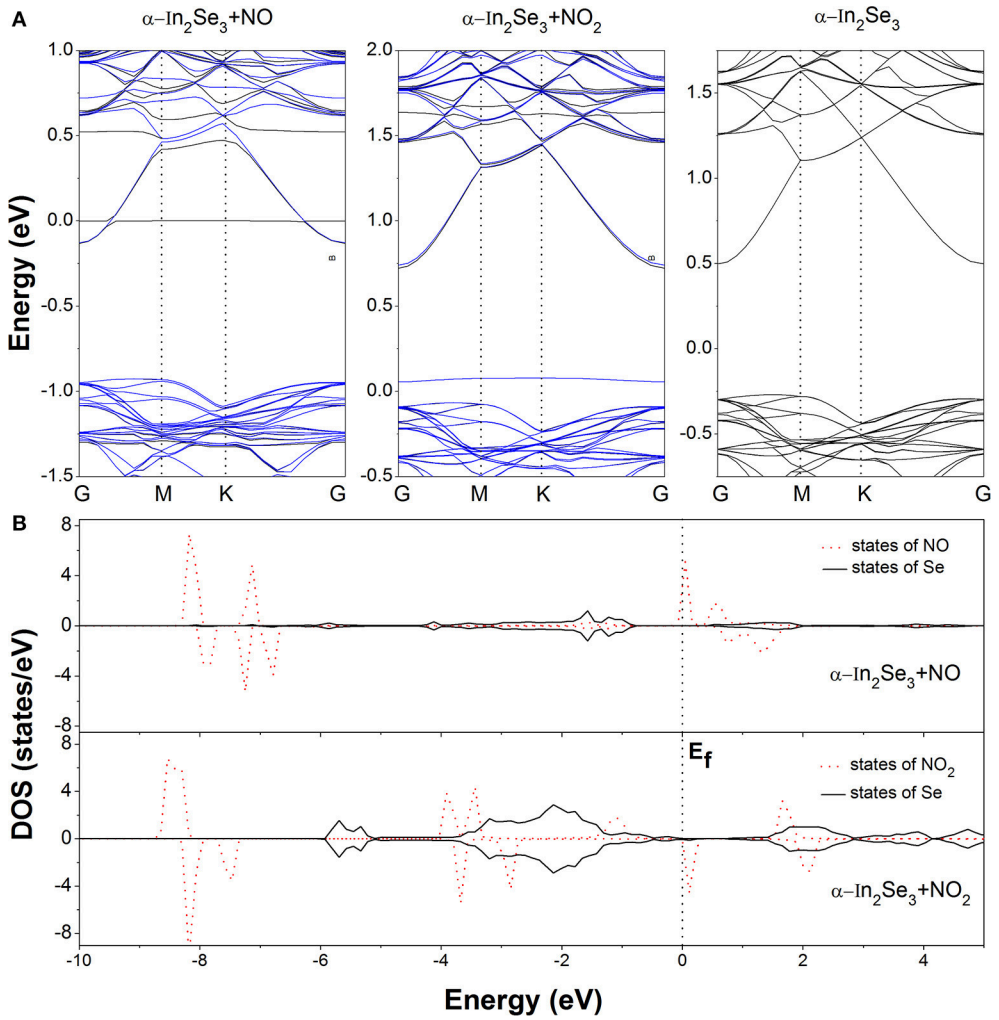

FIGURE 3 | (A) The band structures of the clean α-In_2Se_3 monolayer and the most stable configurations of the α-In_2Se_3 monolayer adsorbed by NO and NO_2. For the two adsorption cases, the black and blue curves represent the spin up and spin down bands, respectively. **(B)** The local density of states (DOS) of the adsorbed molecules and the Se atoms near them. The Fermi level is set as 0 eV.

molecule provides 0.054 *e* electrons to the α-In_2Se_3 surface and acts as an electron donor. This behavior is different from the situation of the NO adsorption on InSe monolayer, where the NO molecule acts as an electron acceptor with the amount (0.018 *e*) of transferred charges (Ma et al., 2017) smaller than that (0.054 *e*) between NO and α-In_2Se_3 monolayer. The band structure of the most stable configuration is depicted in **Figure 3A**, it is shown that after the NO adsorption the Fermi level (E_f) of the system moves upwards to the bottom of the conduction bands compared with that of the clean α-In_2Se_3 monolayer (see **Figure 3A**), demonstrating an n-type conducting property of the materials with NO adsorption, which is similar to the situation of property modification in the NO-adsorbed MoS_2 monolayer (Shokri and Salami, 2016). This property changes can be useful to the detection of NO molecule. In addition, some new states are found to be located at the E_f. To better understand the adsorption effect of NO molecule on the α-In_2Se_3 monolayer, the local density of states (DOS) of the adsorbed NO and its nearest Se atom are illustrated in **Figure 3B**. It is clearly shown the new states at the E_f are from the adsorbed NO, and there is little hybridization between the states of NO molecule and the states of the surface Se atom near it, which is similar to the NO adsorption behavior on InSe monolayer, further confirming that the interaction between the adsorbed NO molecule and the α-In_2Se_3 monolayer is not strong.

In the NO_2 adsorption case, two orientations of NO_2 molecule have been considered. One is the two O atoms point toward the α-In_2Se_3 surface, and the other is that they point away from the α-In_2Se_3 surface. The obtained most stable adsorption configuration is displayed in **Figure 2C**, in which the NO_2 is adsorbed on the Se atom plane of the other side different from that of the NO adsorption case and the two O atoms of NO_2 molecule point toward the α-In_2Se_3 surface. The smallest distance between the NO_2 molecule and the α-In_2Se_3 surface is

3.57 Å, and the N-O bond is a little elongated to 1.22 Å with the O-N-O angle reduced to 131.89°. The adsorption energy was calculated to be 59 meV, suggesting the adsorption of NO_2 on α-In_2Se_3 monolayer is weak, which is comparable to that of the NO_2 adsorption on graphene (Leenaerts et al., 2008).

The CDD of the most stable configuration for NO_2 adsorption is displayed in **Figure 2D**. It is shown that the charge redistribution of NO_2 molecule is apparent. The electrons accumulate in the vicinity of the adsorbed NO_2 with a little electron depletion in its core region. The depletion of electrons mainly occurs for the Se atoms around the NO_2 molecule. From the Bader analysis, it is indicated that the NO_2 molecule is an electron acceptor and obtains 0.081 *e* electrons from the α-In_2Se_3 monolayer, which is similar to the situation of NO_2 adsorption on InSe monolayer, and their amounts of transferred charges are comparable (Ma et al., 2017). The band structure of the discussed configuration is shown in **Figure 3A**. It can be seen that there is a new impurity band lying just above the top of the valence bands and the E_f, which can modify the optical and conducting properties of the materials, benefiting the detection of NO_2 molecule. As shown in **Figure 3B**, the local DOS distributions demonstrate that the impurity states just above the E_f are from the adsorbed NO_2 molecule, and there are some overlaps of states between the NO_2 molecule and the Se atoms near it.

CONCLUSION

To explore the gas sensing applications of 2D materials based on In_2Se_3, the effects of the adsorbed NO and NO_2 molecules on α-In_2Se_3 monolayer have been studied using first-principles calculations. When the NO and NO_2 are adsorbed on the surface of the α-In_2Se_3 monolayer, the calculated adsorption energies of positive value indicate their adsorption processes are exothermic and energetically favorable. Their low adsorption energies demonstrate the α-In_2Se_3 monolayer is applicable for the gas molecules detection. In the most stable configurations, the gas molecules are adsorbed on different Se atom planes for NO and NO_2, respectively, and the smallest distance (3.57 Å) between the adsorbed NO_2 and the α-In_2Se_3 monolayer is larger than that (2.65 Å) of NO adsorption case. NO provides 0.054 *e* electrons to the α-In_2Se_3 monolayer as the donor gas molecule, while NO_2 acts as the acceptor gas molecule and gains 0.081 *e* electrons from the α-In_2Se_3 monolayer. Both of the adsorbed molecules induce new electronic states near the Fermi level compared with the electronic structure of clean α-In_2Se_3 monolayer. These changes of electronic properties can modify the conducting and optical properties of the materials and benefit gas sensing. The theoretical findings of this work suggest the 2D α-In_2Se_3 materials hold great promise for the application of gas sensor.

AUTHOR CONTRIBUTIONS

ZX and FY performed the calculations and analyzed the data with the help of XX, RL, and LC. ZX and FY wrote the manuscript with input from all authors. All authors read and approved the manuscript.

FUNDING

This study is financially supported by the Natural Science Foundation of Fujian Province (2018J01587) and the Scientific Research Development Funds (107/KF2015096) of Fujian Agriculture and Forestry University.

REFERENCES

Bhimanapati, G. R., Lin, Z., Meunier, V., Jung, Y., Cha, J., Das, S., et al. (2015). Recent advances in two-dimensional materials beyond graphene. *ACS Nano* 9, 11509–11539. doi: 10.1021/acsnano.5b05556

Cervenka, J., Katsnelson, M. I., and Flipse C, F. J. (2009). Room-temperature ferromagnetism in graphite driven by two-dimensional networks of point defects. *Nat. Phys*. 5, 840–844. doi: 10.1038/nphys1399

Debbichi, L., Eriksson, O., and Lebègue, S. (2015). Two-dimensional indium selenides compounds: an *ab initio* study. *J. Phys. Chem. Lett*. 6, 3098–3103. doi: 10.1021/acs.jpclett.5b01356

Feng, W., Zheng, W., Gao, F., Chen, X., Liu, G., Hasan, T., et al. (2016). Sensitive electronic-skin strain sensor array based on the patterned two-dimensional α In_2Se_3. *Chem. Mater*. 28, 4278–4283. doi: 10.1021/acs.chemmater.6b01073

Geim, A. K., and Grigorieva, I. V. (2013). Van der waals heterostructures. *Nature* 499, 419–425. doi: 10.1038/nature12385

Jacobs-Gedrim, R. B., Shanmugam, M., Jain, N., Durcan, C. A., Murphy, M. T., Murray, T. M., et al. (2014). Extraordinary photoresponse in two-dimensional In_2Se_3 nanosheets. *ACS Nano* 8, 514–521. doi: 10.1021/nn405037s

Kemp, K. C., Seema, H., Saleh, M., Le, N. H., Mahesh, K., Chandraa, V., et al. (2013). Environmental applications using graphene composites: water remediation and gas adsorption. *Nanoscale* 5, 3149–3171. doi: 10.1039/c3nr33708a

Kresse, G., and Furthmüller, J. (1996). Efficiency of ab-initio total energy calculations for metals and semiconductors using a plane-wave basis set. *Comput. Mater. Sci*. 6, 15–50. doi: 10.1016/0927-0256(96)00008-0

Lan, Y. Z. (2018). First-principles studies of effects of layer stacking, opposite atoms, and stacking order on two-photon absorption of two-dimensional layered silicon carbide. *Comp. Mater. Sci*. 151, 231–239. doi: 10.1016/j.commatsci.2018.04.058

Late, D. J., Huang, Y. K., Liu, B., Acharya, J., Shirodkar, S. N., Luo, J., et al. (2013). Sensing behavior of atomically thin-layered MoS_2 transistors, *ACS Nano* 7, 4879–4891. doi: 10.1021/nn400026u

Leenaerts, O., Partoens, B., and Peeters, F. M. (2008). Adsorption of H_2O, NH_3, CO, NO_2, and NO on graphene: a first-principles study. *Phys. Rev. B* 77:125416. doi: 10.1103/PhysRevB.77.125416

Lightcap, I. V., and Kamat, P. V. (2013). Graphitic design prospects of graphene-based nanocomposites for solar energy conversion, storage, and sensing. *Acc. Chem. Res*. 46, 2235–2243. doi: 10.1021/ar300248f

Ma, D., Ju, W., Li, T., Zhang, X., He, C., Ma, B., et al. (2016). The adsorption of CO and NO on the MoS_2 monolayer doped with Au, Pt, Pd, or Ni: a first-principles study. *Appl. Surf. Sci*. 383, 98–105. doi: 10.1016/j.apsusc.2016.04.171

Ma, D., Ju, W., Tang, Y., and Chen, Y. (2017). First-principles study of the small molecule adsorption on the InSe monolayer. *Appl. Surf. Sci*. 426, 244–252. doi: 10.1016/j.apsusc.2017.07.198

Miró P., Audiffred, M., and Heine, T. (2014). An atlas of two-dimensional materials. *Chem. Soc. Rev*. 43, 6537–6554. doi: 10.1039/C4CS00102H

Novoselov, K. S., Mishchenko, A., Carvalho, A., and Castro Neto, A. H. (2016). 2D materials and van der Waals heterostructures. *Science* 353:aac9439. doi: 10.1126/science.aac9439

Park, S., Park, C., and Kim, G. (2014). Interlayer coupling enhancement in graphene/hexagonal boron nitride heterostructures by intercalated defects or vacancies. *J. Chem. Phys*. 140:134706. doi: 10.1063/1.4870097

Quereda, J., Biele, R., Rubio-Bollinger, G., Agraït, N., Agosta, R. D., and Castellanos-Gomez, A. (2016). Strong quantum confinement effect in the optical properties of ultrathin α-In_2Se_3. *Adv. Optical Mater*. 4, 1939–1943. doi: 10.1002/adom.201600365

Shi, W., Yu, S., Liu, P., Fan, W., Luo, H., and Song, S. (2013). Near-infrared photoluminescent flowerlike a-In_2Se_3 nanostructures from a solvothermal treatment. *Chem. Eng. J*. 225, 474–480. doi: 10.1016/j.cej.2013.03.066

Shokri, A., and Salami, N. (2016). Gas sensor based on MoS_2 monolayer. *Sens. Actuat. B-Chem*. 236, 378–385. doi: 10.1016/j.snb.2016.06.033

Sun, R., Wang, Z., Saito, M., Shibata, N., and Ikuhara, Y. (2015). Atomistic mechanisms of nonstoichiometry-induced twin boundary structural transformation in titanium dioxide. *Nat. Commun*. 6:7120. doi: 10.1038/ncomms8120

Wang, Q. H., Kalantar-Zadeh, K., Kis, A., Coleman, J. N., and Strano, M. S. (2012). Electronics and optoelectronics of two-dimensional transition metal dichalcogenides. *Nat. Nanotechnol*. 7, 699–712. doi: 10.1038/nnano.2012.193

Wang, Z., Gu, T., Tada, T., and Watanabe, S. (2008). Excess-silver-induced bridge formation in a silver sulfide atomic switch. *Appl. Phys. Lett*. 93:152106. doi: 10.1063/1.2963197

Wang, Z., Saito, M., McKenna, K. P., Fukami, S., Sato, H., Ikeda, S., et al. (2016). Atomic-Scale structure and local chemistry of CoFeB–MgO magnetic tunnel junctions. *Nano Lett*. 16, 1530–1536. doi: 10.1021/acs.nanolett.5b03627

Wang, Z., Saito, M., McKenna, K. P., Gu, L., Tsukimoto, S., Shluger, A. L., et al. (2011). Atom-resolved imaging of ordered defect superstructures at individual grain boundaries. *Nature* 479, 380–383. doi: 10.1038/nature10593

Xie, Z., Lin, S., and Wang, Z. (2018). Electronic structure and magnetism in transition metal doped InSe monolayer: a GGA + U study. *Ceram. Int*. 44, 15912–15917. doi: 10.1016/j.ceramint.2018.06.008

Yang, W., Gan, L., Li, H., and Zhai, T. (2016). Two-dimensional layered nanomaterials for gas-sensing applications. *Inorg. Chem. Front*. 3, 433–451. doi: 10.1039/C5QI00251F

Yu, B., Ju, S., Sun, X., Ng, G., Nguyen, T. D., Meyyappan, M., et al. (2007). Indium selenide nanowire phase-change memory. *Appl. Phys. Lett*. 91:133119. doi: 10.1063/1.2793505

Yue, Q., Shao, Z., Chang, S., and Li, J. (2013). Adsorption of gas molecules on monolayer MoS_2 and effect of applied electric field. *Nanoscale Res. Lett*. 8:425. doi: 10.1186/1556-276X-8-425

Zhai, T., Fang, X., Liao, M., Xu, X., Li, L., Liu, B., et al. (2010). Fabrication of high-quality In_2Se_3 nanowire arrays toward high-performance visible-light photodetectors. *ACS Nano* 4, 1596–1602. doi: 10.1021/nn9012466

Zhang, Z., Zhang, Y., Li, Y., Lin, J., Truhlar, D. G., and Huang, S. (2018). $MnSb_2S_4$ monolayer as an anode material for metal-ion batteries. *Chem. Mater*. 30, 3208–3214. doi: 10.1021/acs.chemmater.7b05311

Zhou, C., Zhu, H., Wu, Y., Lin, W., Yang, W., and Dong, L. (2017). Effect of external strain on the charge transfer: adsorption of gas molecules on monolayer GaSe. *Mater. Chem. Phys*. 198, 49–56. doi: 10.1016/j.matchemphys.2017.05.046

Conflict of Interest Statement: The authors declare that the research was conducted in the absence of any commercial or financial relationships that could be construed as a potential conflict of interest.

frontiers in Chemistry

ORIGINAL RESEARCH
published: 24 September 2018
doi: 10.3389/fchem.2018.00416

Optical Temperature Sensing With Infrared Excited Upconversion Nanoparticles

*Kory Green[1], Kai Huang[2], Hai Pan[1], Gang Han[2] and Shuang Fang Lim[1]**

[1] Department of Physics, North Carolina State University, Raleigh, NC, United States, [2] Department of Biochemistry and Molecular Pharmacology, University of Massachusetts Medical School, Worcester, MA, United States

Upconversion Nanoparticles (UCNPs) enable direct measurement of the local temperature with high temporal and thermal resolution and sensitivity. Current studies focusing on small animals and cellular systems, based on continuous wave (CW) infrared excitation sources, typically lead to localized thermal heating. However, the effects of upconversion bioimaging at the molecular scale, where higher infrared intensities under a tightly focused excitation beam, coupled with pulsed excitation to provide higher peak powers, is not well understood. We report on the feasibility of 800 and 980 nm excited UCNPs in thermal sensing under pulsed excitation. The UCNPs report temperature ratiometrically with sensitivities in the 1×10^{-4} K^{-1} range under both excitation wavelengths. Our optical measurements show a $\ln(I_{525}/I_{545})$ vs. 1/T dependence for both 800 nm and 980 nm excitations. Despite widespread evidence promoting the benefits of 800 nm over 980 nm CW excitation in avoiding thermal heating in biological imaging, in contrary, we find that given the pulsed laser intensities appropriate for single particle imaging, at both 800 and 980 nm, that there is no significant local heating in air and in water. Finally, in order to confirm the applicability of infrared imaging at excitation intensities compatible with single nanoparticle tracking, DNA tightropes were exposed to pulsed infrared excitations at 800 and 980 nm. Our results show no appreciable change in the viability of DNA over time when exposed to either wavelengths. Our studies provide evidence for the feasibility of exploring protein-DNA interactions at the single molecule scale, using UCNPs as a reporter.

Keywords: upconversion thermal sensing, pulsed excitation, 800 nm, 980 nm, local thermal heating, DNA denaturation

OPEN ACCESS

Edited by:
Wen Zeng,
Chongqing University, China

Reviewed by:
Ruoxue Yan,
University of California, Riverside, United States
Daqin Chen,
Hangzhou Dianzi University, China

****Correspondence:***
Shuang Fang Lim
sflim@ncsu.edu

Specialty section:
This article was submitted to Nanoscience, a section of the journal Frontiers in Chemistry

Received: *04 June 2018*
Accepted: *23 August 2018*
Published: *24 September 2018*

Citation:
Green K, Huang K, Pan H, Han G and Lim SF (2018) Optical Temperature Sensing With Infrared Excited Upconversion Nanoparticles. Front. Chem. 6:416. doi: 10.3389/fchem.2018.00416

INTRODUCTION

Many biological processes occurring within intracellular structures may result in changes in the pH, temperature and electrical potential, to name a few. Exploring thermal changes at the cellular level provides insight into biochemical reactions taking place in a cell. Fluorescent thermometry relies on changes of relative fluorescent intensities, lifetimes and wavelengths to local temperature (Engeser et al., 1999; Sakakibara and Adrian, 1999; Ross et al., 2001; Wang et al., 2002; Löw et al., 2008; Binnemans, 2009; Vetrone et al., 2010a). Conventional fluorescence microscopy uses short-wavelength (UV-blue) excitation, and detection of a longer-wavelength, Stokes-shifted fluorescence (Stokes, 1852; Lichtman and Conchello, 2005). However, this use of short-wavelength excitation leads to autofluorescence, photobleaching, and photodamage to biological specimens

(Giloh and Sedat, 1982). Molecular dyes bleach under intense illumination (Shaner et al., 2008). Semiconductor nanoparticles (i.e., Qdots) (Tessmer et al., 2013) are stable, but display blinking and toxic behavior (Yao et al., 2005). In contrast, our method is based on rare-earth ion doped, upconversion nanoparticles (UCNPs) (Lim et al., 2006, 2009, 2010; Austin and Lim, 2008; Ungun et al., 2009). UCNPs absorb at 800 and 980 nm in the near infrared (NIR), exhibit no bleaching, are non-toxic, and are not affected by blinking (Chen et al., 2006; Schubert et al., 2006). Due to this lack of bleaching, UCNPs are well suited for long term monitoring of biological events at the high laser intensity levels employed in single cell imaging, as opposed to a dye that may bleach over time. The demonstration of UCNPs as nanothermometers in water has been shown by Vetrone et al. (2010a) and others (Chen et al., 2016; Zhu et al., 2016). The electrons in the 4f shell of rare earths are shielded from the surroundings by the filled 5s and 5p shells, and therefore the influence of the surrounding matrix on the optical transitions within the 4f shell is small, whether in crystals or in solution. Therefore, UCNPs show reduced sensitivity to physiological changes such as salt concentration (Gota et al., 2009) and pH while monitoring cellular temperatures (Vetrone et al., 2010a,b). UCNPs have also been used to measure the temperature of the interior nanoenvironment of magnetically heated iron oxide nanoparticles (Dong and Zink, 2014) and have been shown to enable direct measurement of the local temperature with high temporal (millisecond) and thermal resolution (0.3–2.0 K) (Debasu et al., 2013) and (10^{-5} K^{-1}) sensitivity (Xu et al., 2012) with simple equipment requirements. The emission of the dopant ions is sensitive to temperature in some configurations due to closely spaced energy levels being thermally coupled (Bai et al., 2007; Lü et al., 2011; Xu et al., 2012; Debasu et al., 2013). Moreover, these thermally coupled energy levels are not sensitive to other environmental factors such as scattering or tissue autofluorescence. Thermally coupled emissions, such as for the Er^{3+} rare earth ion, can be in the visible, such as in the intensity ratio (RHS) of the $^2H_{11/2}$ to $^4I_{15/2}$ (525 nm) over $^4S_{3/2}$ to $^4I_{15/2}$ (545 nm) transitions (Bai et al., 2007; Lü et al., 2011; **Figure 1**), or in the red to near infrared, with the Tm^{3+} rare earth ion, such as in the intensity ratio (RHS) of the $^3F_{2,3}$ to $^3H_6$ (700 nm) over the $^3H_4$ to $^3H_6$ (800 nm) transitions (Xu et al., 2012). In the aforementioned emissions, the energy separation between the nearest excited states Er: $^2H_{11/2}$ and Er: $^4S_{3/2}$, is only several hundred wavenumbers. Thus, the population distribution of Er: $^2H_{11/2}$ and Er: $^4S_{3/2}$ is influenced by both thermal distribution and nonradiative relaxation. As a consequence, the population of the Er: $^2H_{11/2}$ level varies as a function of the Boltzmann's distribution between the two states (Lei et al., 2005). Similarly, the small energy separation between the thermally coupled Tm^{3+} levels of about 1,850 cm^{-1}, gives rise to the same phenomenon (Xu et al., 2012). Measurements of the Boltzmann distribution between the two closely spaced states with varying temperatures show that the natural log of this ratio is inversely proportional to the temperature in the range relevant to most biological systems (Vetrone et al., 2010a).

However, primary excitation of the UCNPs occurs in the near infrared, where the absorption coefficient of the water abundant in biological tissue varies, resulting in some reservations regarding the use of these nanoparticles as a temperature sensor. Those reservations arise from the fact that the absorption coefficient of water at 980 nm is about 20 times larger than that at 800 nm (Weber, 1971; Wang et al., 2013). Specifically, at 980 nm CW excitation, thermal heating of the biological environment, may hamper the measurement process, as seen in small animals, and in cellular systems (Vetrone et al., 2010a; Wang et al., 2013). The more widely used sensitizer, the Yb^{3+} rare earth ion absorbs primarily at 980 nm, corresponding to the $^2F_{7/2}$ to $^2F_{5/2}$ transition, whereas the Nd^{3+} rare earth ion sensitizer absorbs at 800 nm, corresponding to the $^4I_{9/2}$ to $^4F_{5/2}$ transition. The Nd^{3+} ion has an absorption cross section an order of magnitude greater at 800 nm than the Yb^{3+} sensitizer(Kushida et al., 1968; Wang et al., 2013; Chen et al., 2015). Most studies focus on small animals and cellular systems, where the infrared excitation source is a continuous wave (CW) laser operating at low intensities. This has led to the prevailing belief that the benefits of bioimaging with CW infrared excitation at 980 nm, with low scattering background, is offset by the thermal cost of cellular heating. At this scale, 800 nm CW excitation has been shown to alleviate some of the issues with heating(Wang et al., 2013). However, given the emergent application of infrared imaging at the single molecule level, efforts to examine the thermal effects of pulsed excitation at 800 and 980 nm have never been made. Infrared upconversion bioimaging at the molecular scale, occurs at a much higher intensity under a tightly focused excitation beam, and is normally coupled with pulsed excitation to provide higher peak powers, for sharper discrimination along the Z axis. Therefore, in this work, particular emphasis is paid to the potential thermal effects of upconversion bioimaging at the molecular scale, under pulsed infrared excitation. An example of single upconversion nanoparticle imaging is shown in **Supplementary Video 1**. Furthermore, we address the proposed potential benefits of pulsed excitation infrared imaging at the single molecule scale, first through spectroscopic studies, and then in single molecule viability studies using DNA tightrope, under pulsed laser excitation at high magnification and intensities. A long-term single molecule imaging technology that is resistant to photobleaching and is excited at longer wavelengths can be a powerful tool to study physiological processes that take time to unfold, such as disease progression.

To that end, comparisons are made between excitations at 980 nm (β-$NaYF_4$:20%Yb, 2%Er UCNPs) and 800 nm (β-$NaYF_4$:40%Yb, 2%Er@$NaYF_4$:20%Yb@$NaNdF_4$:10%Yb core-shell-shell UCNPs), where the thermal response of the UCNP is recorded as a thermally responsive intensity ratio variation in the spectra, with no fluorescence intensity quenching, and with simple equipment requirements. In contrast to other researchers, where both I_{525} and I_{545} emission lines are derived from a spectral scan over the appropriate wavelength range, we collect both lines simultaneously, in order to avoid heat dissipation effects. Our optical measurements show a $\ln(I_{525}/I_{545})$ vs. 1/T dependence for both 800 nm and 980 nm excitations, in the Yb^{3+}/Er^{3+} codoped and triply doped $Yb^{3+}/Er^{3+}@Yb^{3+}/Nd^{3+}$ samples. We also observe a strong influence of the laser intensity on the relative spectroscopic ratio of I_{525}/I_{545}. Additionally, we

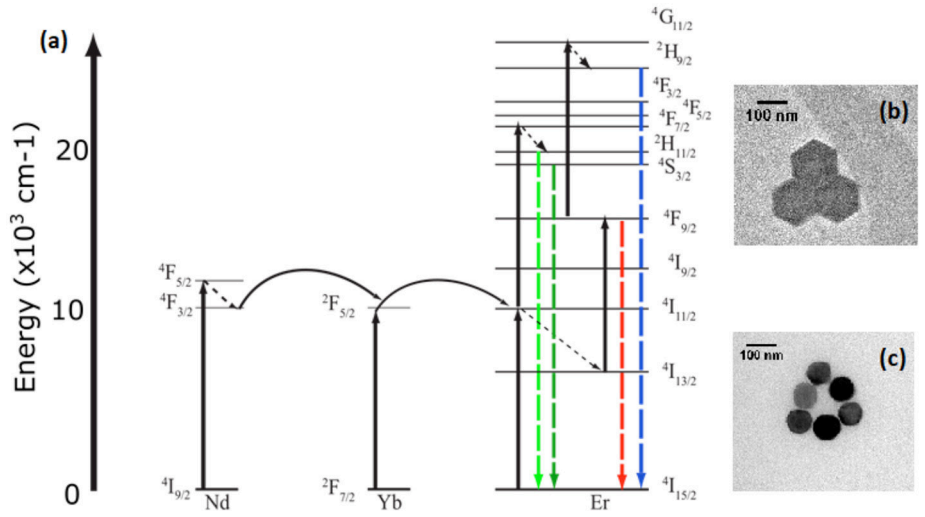

FIGURE 1 | Energy level diagram **(a)** of the sensitization of Erbium by Neodymium and Ytterbium at 806 nm and 976 nm excitation respectively. Insets of transmission electron microscopy of both **(b)** β-$NaYF_4$:20%Yb, 2% Er and **(c)** β-$NaYF_4$:40%Yb, 2%Er@$NaYF_4$:20%Yb@$NaNdF_4$:10%Yb particles.

find that given the pulsed laser intensities appropriate for single particle imaging, at both 800 and 980 nm, that there are no significant differences in the local heating effects. This result is in contrast with that obtained when comparing excitation at both wavelengths under CW excitation. We further demonstrate our observations by comparing the differences in a DNA tightrope denaturation experiment at 800 and 980 nm pulsed irradiation respectively, and find no significant change in denaturation at excitation fluences that have previously been shown to support upconversion imaging utilizing 976 nm excitation at the single particle level at diameters of 10 nm with an intensity of 3e4 W/cm^2 and diameter of 25 nm at an intensity of 4e4 W/cm^2 as demonstrated by Gargas et al. (2014) and Green et al. (2016).

EXPERIMENTAL

Synthesis of β-$NaYF_4$: 20% Yb^{3+}, 2% Er^{3+}

The β-$NaYF_4$:20%Yb, 2%Er UCNPs were prepared by combining 2.1 mmol of sodium trifluoroacetate, 0.78 mmol of yttrium trifluoroacetate, 0.2 mmol of ytterbium trifluoroacetate, and 0.02 mmol of erbium trifluoroacetate in 6 mL of oleic acid and 6.1 mL of octadecene. The solution was degassed at 120°C for 2 h with argon purging. Temperature was then increased to 330°C under argon and allowed to maintain this temperature for 25 min. The particles were then cooled, precipitated, washed in excess ethanol with centrifuging, and dried under vacuum.

Synthesis of β-$NaYF_4$:40%Yb, 2%Er@$NaYF_4$:20%Yb@$NaNdF_4$:10%Yb Core-Shell-Shell UCNPs

The β-$NaYF_4$:40%Yb, 2%Er Core UCNPs were prepared by a two-step thermolysis method. In the first step, CF_3COONa (0.50 mmol), $Y(CF_3COO)_3$ (0.29 mmol), $Yb(CF_3COO)_3$ (0.20 mmol) and $Er(CF_3COO)_3$ (0.01 mmol) precursors were mixed with oleic acid (5 mmol), oleyamine (5 mmol), and 1-octadecene (10 mmol) in a two-neck round bottom flask. The mixture was heated to 110°C to form a transparent solution followed by 10 min of degassing. Then the mixture was heated to 300°C at a rate of 15°C/min under dry argon flow, and maintained at 300°C for 30 min to form the α-$NaYF_4$:40%Yb, 2%Er intermediate UCNPs. After the mixture cooled to room temperature, the α-$NaYF_4$:40%Yb, 2%Er intermediate UCNPs were collected by centrifugal washing with excessive ethanol (7,500 g, 30 min). In the second step, the α-$NaYF_4$:40%Yb, 2%Er intermediate UCNPs were redispersed into oleic acid (10 mmol) and 1-octadecene (10 mmol) together with CF_3COONa (0.5 mmol) in a new two-neck round bottom flask. After degassing at 110°C for 10 min, this flask was heated to 325°C at a rate of 15°C/min under dry argon flow, and maintained at 325°C for 30 min to complete the phase transfer from α to β. After the mixture cooled to room temperature, the β-$NaYF_4$:40%Yb, 2%Er UCNPs were collected by precipitated with equal volume of ethanol and centrifugation afterwards (7,500 g, 30 min). The β-$NaYF_4$:40%Yb, 2%Er UCNPs were stored in hexane (10 mL).

Next, the as-synthesized β-$NaYF_4$:40%Yb, 2%Er core UCNPs served as cores for the epitaxial growth of core-shell UCNPs. A hexane stock solution of β-$NaYF_4$:40%Yb, 2% Er core UCNPs was transferred into a two-neck round bottom flask, and the hexane was sequentially evaporated by heating. CF_3COONa (0.50 mmol), $Y(CF_3COO)_3$ (0.40 mmol) and $Yb(CF_3COO)_3$ (0.10 mmol) were introduced as UCNP shell precursors with oleic acid (10 mmol) and 1-octadecene (10 mmol). After 10 min of degassing at 110°C, the flask was heated to 325°C at a rate of 15°C/min under dry argon flow and maintained at 325°C for 30 min to complete the shell crystal growth. After the mixture cooled to room temperature, the β-$NaYF_4$:40%Yb, 2%Er@$NaYF_4$:20%Yb core-shell UCNPs were collected by precipitated with equal volume

of ethanol and centrifugation afterwards (7,500 g, 30 min). The β-$NaYF_4$:40%Yb, 2%Er@$NaYF_4$:20%Yb core-shell UCNPs were stored in hexane (10 mL).

Afterwards, the as-synthesized β-$NaYF_4$:40%Yb, 2%Er@$NaYF_4$:20%Yb core-shell UCNPs served as cores for the epitaxial growth of shell crystal. A hexane stock solution of β-$NaYF_4$:40%Yb, 2%Er@$NaYF_4$:20%Yb core-shell UCNPs was transferred into a two-neck round bottom flask, and the hexane was sequentially evaporated by heating. CF_3COONa (0.50 mmol), $Nd(CF_3COO)_3$ (0.45 mmol) and $Yb(CF_3COO)_3$ (0.05 mmol) were introduced as UCNP shell precursors with oleic acid (10 mmol) and 1-octadecene (10 mmol). After 10 min of degassing at 110°C, the flask was heated to 325°C at a rate of 15°C/min under dry argon flow and maintained at 325°C for 30 min to complete the shell crystal growth. After the mixture cooled to room temperature, the β-$NaYF_4$:40%Yb, 2%Er@$NaYF_4$:20%Yb@$NaNdF_4$:10%Yb core-shell-shell UCNPs were collected by precipitated with equal volume of ethanol and centrifugation afterwards (7,500 g, 30 min). The β-$NaYF_4$:40%Yb, 2%Er@$NaYF_4$:20%Yb@$NaNdF_4$:10%Yb core-shell-shell UCNPs were stored in hexane (10 mL).

Characterization and Sample Preparation

UCNP were characterized with Transmission Electron Microscopy (TEM) to determine average diameter. The β-$NaYF_4$:20%Yb, 2%Er (Wirth et al., 2017; **Figure 1b**) and β-$NaYF_4$:40%Yb, 2%Er@$NaYF_4$:20%Yb@$NaNdF_4$:10%Yb core-shell-shell (**Figure 1c**) UCNPs were imaged using a JEOL 2000FX TEM at the Analytical Instrumentation Facility on North Carolina State University's campus. Samples used for spectroscopic experimentation were created by diluting the concentration of UCNPs to 10 ng/mL in ethanol and pipetting 100 uL of solution onto the sample surface. The solution was shaken on the sample surface for 20 min before washing with ethanol and drying under nitrogen.

Time-Resolved Spectroscopy Measurements

Objects resolved on an optical microscope (40x, 0.9 N.A. air objective) imaged by a Andor NEO sCMOS camera with excitation from a 1,000 hz, tunable Nd: YAG laser with a 4.5 ns pulse width were selected by size, ensuring that imaged objects were less than the size of the diffraction limited spot of the wavelength of collection. Spectral distributions were separated using a half-meter monochromator with a custom exit with two slits. The gap between the slits correspond to a 10 nm wavelength difference centered at the monochromator's single slit location. By setting the monochromator to 535 nm, the 525 nm peak and 545 nm peak were effectively separated at the exit slits and further separated by a prism and coupled into separate SPCM-AQRH avalanche photodiodes. Controlled heating was performed using a peltier heater fixed to the back of the sample slide by epoxy. A thermistor attached to a PTC2.5K-CH temperature controller was embedded in the epoxy to ensure a constant set temperature during operation, and a K-type thermocouple was used to monitor the temperature at the sample surface.

DNA Tightrope Measurements

The DNA substrates (CpG-free-rich, 7,163 bp) were ligated using the Quick Ligation Kit (New England BioLabs) at room temperature for overnight and then purified by phenol-chloroform extraction to remove the ligase (Pan et al., 2017). Coverslips were PEGylated prior to use Flow cells were assembled by using double-sided tape to attach PEGylated coverslips to microscope slides with drilled input holes. After assembling the flow cell, poly-L-lysine (Wako Chemicals) treated silica beads (D∼5 um) were immobilized on the coverslips at a proper density and incubated for 5 min to ensure attachment. Afterwards, 100 uL of 5 ng/uL ligated DNA in a 7.4 pH buffer containing 50 mM HEPES, 100 mM NaCl, and 1 mM $MgCl_2$ was injected into the flow cell and pushed back and forth for 10 min using a syringe pump at a flow rate of 300 uL/min (Pan et al., 2017). After the DNA was stretched between the beads, the DNA was stained with a YOYO-1 dye. Following that, the DNA tightropes were centered in the laser focal area and imaged for 10 s with a Xenon lamp at 70 mW/cm^2. The DNA is then exposed to 976 nm at 7 × 10^4 W/cm^2 or 806 nm at 5 × 10^4 W/cm^2, for 2 min, followed by Xenon lamp imaging again for 10 s. A control DNA tightrope experiment without near infrared exposure was also performed alongside the near infrared exposed DNA tightropes.

RESULT AND DISCUSSION

To establish the temperature sensing abilities of each type of UCNP under each excitation condition, controlled heating was used to bring the samples to set temperatures as described in the methods section. Spectroscopic measurements were performed at each temperature after a period of equilibration of 10 min. **Figure 2** shows a plot of $\ln(I_{525}/I_{545})$ vs. 1/T measured for the both the β-$NaYF_4$:20%Yb, 2%Er UCNPs and β-$NaYF_4$:40%Yb, 2%Er@$NaYF_4$:20%Yb@$NaNdF_4$:10%Yb core-shell-shell UCNPs at 976 and 806 nm respectively. Since the population of the Er: $^2H_{11/2}$ and Er: $^4S_{3/2}$ levels fluctuates as a function of the Boltzmann's distribution (Lei et al., 2005),

$$R = \frac{I_{525}}{I_{545}} = \Lambda e^{\frac{-\Delta E}{kT}}$$

where by taking the slope of the $\ln(I_{525}/I_{545})$ vs. 1/T plot, a ΔE of 887.170 cm^{-1} (806 nm, core-shell-shell with Nd) and 966.176 cm^{-1} (976 nm core only) is obtained. The calculated difference between 545 and 525 nm peaks is 700 cm^{-1}. The sensitivity S is defined as,

$$S = \frac{d(R)}{dT} = \Lambda \frac{\Delta E}{kT^2} e^{\frac{-\Delta E}{kT}}$$

where the higher the temperature, the greater the sensitivity. Given the calculated ΔE, a plot of the sensitivity against temperature is shown in **Figure 2B**. Our sensitivity values are comparable to other researchers (León-Luis et al., 2012; **Table 1**). The higher sensitivity expands the applicability to environmental and electronics sensing where typical critical operating temperatures are higher.

Local temperature rise with continuous laser irradiation at high pump power intensity and duration has been observed

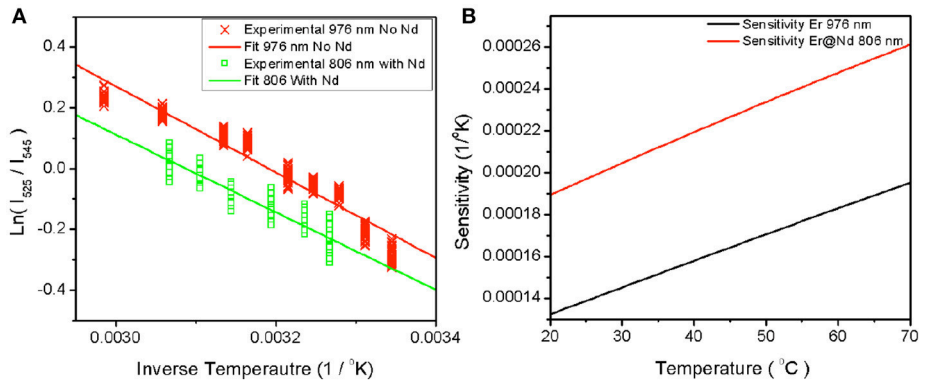

FIGURE 2 | Plot of experimentally measured ratio against inverse temperature **(A)** for β-$NaYF_4$:20%Yb, 2% Er excited at 976 nm and β-$NaYF_4$:40%Yb, 2%Er@$NaYF_4$:20%Yb@$NaNdF_4$:10%Yb excited at 806 nm. The fit lines represent the slope between the natural log of the measured ratios and the inverse temperature. The sensitivity over the range of interest is plotted in **(B)** against temperature.

TABLE 1 | The natural log of the ratio between emissive states was plotted against inverse temperature as seen in **Figure 2**.

Parameter	No Nd 976	No Nd 800	With Nd 976	With Nd 800
Delta E (cm^{-1})	966	1,492	1,288	887
Slope	−1,413	−2,147	−1,768	−913
Intercept	4.51	6.485	4.984	2.971
Sensitivity at 25°C	1.4*E*−04	1.8*E*−05	5.28*E*−05	4.8*E*−04
Sensitivity at 60°C	1.8*E*−04	3.07*E*−05	7.88*E*−05	5.3*E*−04

This table is the result of fitting the resulting curve. The slope is directly equivalent to Delta E over k.

(Wang et al., 2013), which can potentially impact *in vivo* applications. To address these concerns, we investigated the influence of the irradiation pump intensity and duration. To investigate the feasibility of experiments utilizing high laser fluence combined with pulsed excitation, we investigate the change in the spectroscopic ratio, with laser intensity and time duration in air and water.

Figure 3 shows the dependence of the spectroscopic ratio, R, on the pump power intensity. There is a marked difference in the optical response of the particles with respect to near infrared excitation wavelength. In the β-$NaYF_4$:20%Yb, 2%Er UCNPs (**Figure 3A**), R is observed to decrease with increasing pump power intensity at 976 nm excitation. This decrease in ratio apparently contradicts an expected rise in R in the presence of potential local heating. This is expected as a higher pump power intensity enables transition from 2 photon to 3 photon upconversion, where increasing pump power intensity leads to population of the $^4G_{11/2}$, after which phonon relaxation to the $^2H_{9/2}$ level occurs. Subsequently radiative relaxation from the $^2H_{9/2}$ to $^4I_{15/2}$ level results in blue emission, as shown in **Figure 4B**. Thereby, due to preferential population of the $^4G_{11/2}$ level, we expect to observe a lower photon population of the $^2H_{11/2}$ (525 nm) level, at high pump power intensities. As the pump power is increased, the increase in phonon coupling to the lattice, and subsequent non-radiative energy transfer from the $^2H_{9/2}$ to $^2H_{11/2}$ and the $^4S_{3/2}$ level to the $^4F_{9/2}$ level occurs. Since the energy gap for the $^4S_{3/2}$ to $^4F_{9/2}$ transition of 3117 cm^{-1} coincides with the typical value of 3,000–3,600 cm^{-1} for OH vibrations(Kim et al., 2017), a higher pump power results in greater non-radiative relaxation via this pathway, as seen by the decrease in the rise and decay time of the Er^{3+}: $^4F_{9/2}$ to $^4I_{15/2}$ transition (**Figures 2–4** and **Table 2**). In comparison, the energy gap for the Er^{3+}: $^2H_{9/2}$ to $^2H_{11/2}$ transition of around 6000 cm^{-1}, is much larger than that of the OH absorption energy. The resulting effect of a higher pump power is to promote greater blue and red emissions at the expense of green emission. A similar, but less dramatic, decrease in R is also seen at 806 nm excitation, where the absorption of two photons populates the $^2H_{9/2}$ and subsequent radiative relaxation to the $^4I_{15/2}$ level results in blue emission. We note that the absorption cross-section at 806 nm is comparatively low for this sample. However, increased pump power intensity at 806 nm did further increase blue emission, while also increasing rates of non-radiative transfer, leading to population of the $^4F_{9/2}$ state. Therefore, in the β-$NaYF_4$:20%Yb, 2%Er UCNPs, if used as a temperature sensor at either 806 nm or 976 nm excitation, blue emission is triggered at pump power intensities, which affects the $^2H_{11/2}$ (525 nm) level population significantly and the ratio decrease should be accounted for.

In **Figure 3B**, the β-$NaYF_4$:40%Yb, 2%Er@$NaYF_4$:20%Yb@$NaNdF_4$:10%Yb core-shell-shell UCNPs, at 976 nm excitation, shows a drop in R, but to a smaller degree, with increasing pump power intensity. This is attributed similarly to the β-$NaYF_4$:20%Yb, 2%Er UCNPs as shown earlier. The smaller drop may be due to the protective nature of the core-shell-shell configuration, which limits the effect of lattice vibration effects. In contrast, at 806 nm excitation, an increase in R is seen with increasing pump power. The immediate assumption is that of an increase in local temperature, but results shown later will demonstrate that this is not the case. The increase in R appears to be an optical effect only. Under 806 nm excitation, the Nd^{3+}: $^4F_{5/2}$ and Nd^{3+}: $^2H_{9/2}$ levels are populated due to transitions from the Nd^{3+}:$^4I_{9/2}$ ground state. Subsequent non-radiative relaxation from these two states occur,

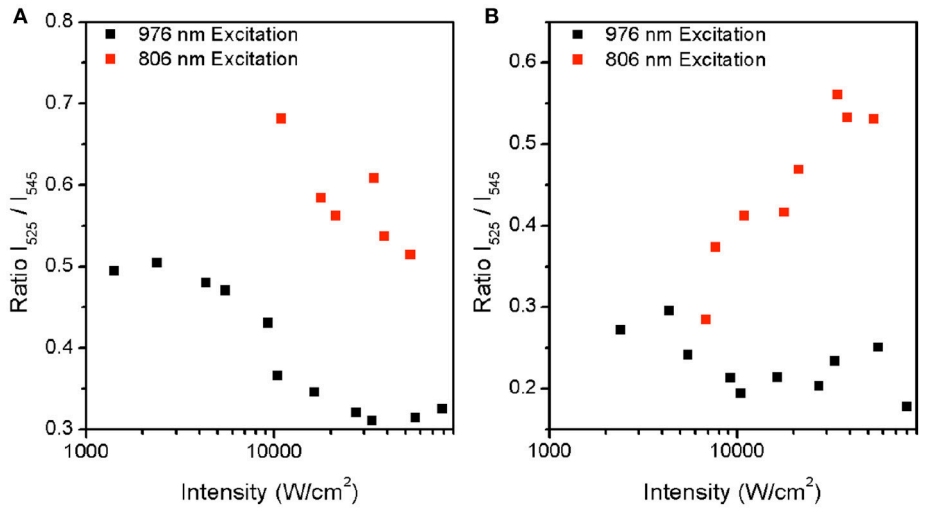

FIGURE 3 | Plot of measured ratio between $^2H_{11/2}$ and $^4S_{3/2}$ at increasing intensity for both 806 nm and 976 nm excitation for **(A)** β-$NaYF_4$:20%Yb, 2% Er **(A)** and **(B)** β-$NaYF_4$:40%Yb, 2%Er@$NaYF_4$:20%Yb@$NaNdF_4$:10%Yb.

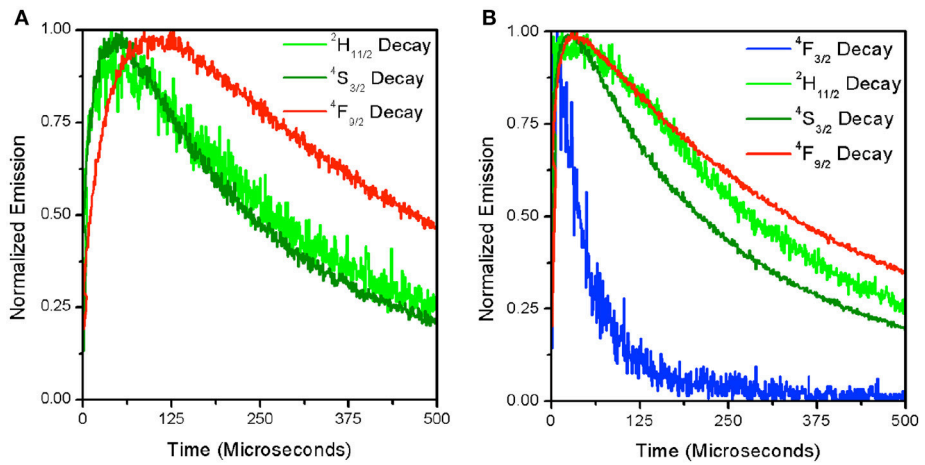

FIGURE 4 | Time-resolved decay for each of the visible emitting levels for β-$NaYF_4$:20%Yb, 2% Er at 1.0 × 10^4 W/cm^2 **(A)** and 5.6 × 10^4 W/cm^2 **(B)**. The $^4F_{3/2}$ decay is only shown in the right panel where signal intensity was sufficient to produce a readable curve.

leading to population of the Nd^{3+}: $^4F_{3/2}$ state. The resonant energy levels of Nd^{3+}: $^4F_{3/2}$ and Yb^{3+}: $^2F_{5/2}$ ensures a very high efficiency energy transfer (ET) between Nd^{3+} ions and Yb^{3+} ions(Wang et al., 2013; Tian et al., 2014; Zhong et al., 2014; Chen et al., 2015). Thereafter, two consecutive energy transfers from the Yb^{3+}: $^2F_{5/2}$ state to the neighboring Er^{3+} ions, result in population of the $^4F_{7/2}$ state. Relaxation from the $^4F_{7/2}$ state to the lower $^2H_{11/2}$, $^4S_{3/2}$ and $^4F_{9/2}$ states, followed by radiation relaxation from all three of states to the $^4I_{15/2}$ ground state, give rise to emission at 525 nm, 545 nm, and 655 nm, respectively. Since the highly absorbing Nd^{3+} ion promotes more efficient energy transfer to the Yb^{3+} ion, a higher pump power intensity also leads to a more efficient population of the $^4F_{7/2}$ level, where further non-radiative relaxation to the $^2H_{11/2}$ state occurs, giving rise to preferential emission at 520 nm. Therefore, the Nd^{3+} dopant, due to the larger absorption cross-section, and more efficient energy transfer to the Yb^{3+} ion, clearly favors upconversion over linear decay. As a result, an increase in laser intensity, leads to greater upconversion.

To further understand the source of the decrease in R with increasing excitation intensity for the β-$NaYF_4$:20%Yb, 2%Er UCNPs, time-resolved decay spectra were measured. **Figures 4A,B** displays the decay spectra for $^4F_{3/2}$(blue), $^2H_{11/2}$(green), $^4S_{3/2}$(green), and $^4F_{9/2}$(red) emissions at two different excitation intensities. It can be seen that at a higher excitation intensity (5.6 × 10^4 W/cm^2) in **Figure 4B**, that the $^4F_{9/2}$ and $^4S_{3/2}$ states excitation pathways are more strongly coupled as evidenced by the narrowing of the gap between

their rise times (See **Table 2**). This has been attributed to the increase in phonon coupling to the lattice OH vibrations at higher laser intensity. At lower laser intensity, the $^4F_{9/2}$ rise time is significantly longer in comparison to that of the $^4S_{3/2}$ state. **Supporting Figure S1** shows normalized time-resolved decay at 545 nm of the β-$NaYF_4$:20%Yb, 2%Er UCNPs and β-$NaYF_4$:40%Yb, 2%Er@$NaYF_4$:20%Yb@$NaNdF_4$:10%Yb core-shell-shell UCNPs. **Supporting Figures S1A,B** show the 545 nm decay of the Yb/Er co-doped sample from excitation at 976 nm and 806 nm respectively. In **Supporting Figure S1A**, the slow rise times and long decay times are indicative of the ETU upconversion process. As the pump power intensity is increased, the rise times and mean lifetimes are both reduced. The corresponding emission at 806 nm excitation is dim, due to the low absorption cross-section at this excitation wavelength, hence the decay curves are noisy, and convey less information. **Supporting Figures S1C,D** shows the decay curves at 545 nm for the core-shell-shell UCNPs for excitation at 976 nm and 806 nm respectively. Both figures clearly show faster rise times and decay,

TABLE 2 | Lifetime and rise times fitted from the time-resolved decay for β-$NaYF_4$:20% Yb^{3+}, 2% Er^{3+} from **Figure 4**.

	Blue	H	S	Red
5.6 × 10^4 W/cm^2				
Lifetime	53.792	352.113	267.308	432.339
Rise Time	13.125	20.125	35.000	35.000
1.0 × 10^4 W/cm^2				
Lifetime	N/A	344.471	272.405	558.971
Risetime	N/A	45.500	59.500	91.875

The lifetime was fitted as a single exponential for the emission's decay and the rise time was defined as the time between the laser excitation and the maximum point of the decay curve.

which we attribute, for the 976 nm excitation, to the presence of core-shell-shell nanostructure, which reduces phonon coupling to the host matrix. At 800 nm excitation, the highly absorbing Nd^{3+} ion further increases the decay rate for the Er^{3+}: $^4S_{3/2}$ to $^4I_{15/2}$ transition.

Since it is unclear as to the impact of pump power intensity on local heating due to the increased probability of higher energy level transitions, we investigated the effect of time duration of excitation on the local temperature rise. **Figures 5A,B** show the dependence of the local temperature with time duration of irradiation in air (**Figure 5A**) and water (**Figure 5B**), respectively. Neither 976 nm, nor 806 nm excitation introduces a local temperature rise over time at laser intensities in the range of 10^4 W/cm^2. Our results are significantly different from other researchers primarily because our experiments are conducted with pulsed excitation, unlike the effects seen using continuous irradiation as observed by other researchers (Wang et al., 2013). Therefore, the laser mode of operation should be carefully considered regarding the use of upconversion nanocrystals in thermal sensing. While continuous wave lasers are affordable and highly adaptable to many laboratories, the probability of local heating is high. In contrast, pulsed wave excitation under a tightly focused beam, which is typical in single-molecule imaging does not cause appreciable local temperature rise in the sample.

As a demonstration of the effects of 976 vs. 806 nm irradiation at the single-molecule level, we compared DNA tightropes exposed to both wavelengths at intensities shown previously to support single particle imaging (Gargas et al., 2014; Green et al., 2016). In order to clearly identify effects of near infrared exposure, we first stretch DNA on silica beads by flowing the DNA across the beads in an aqueous environment. After the DNA are stretched out and stained with YOYO-1 dye, the laser spot is localized on the DNA tightrope. The tightropes are then exposed to 806 nm or 976 nm excitation separately

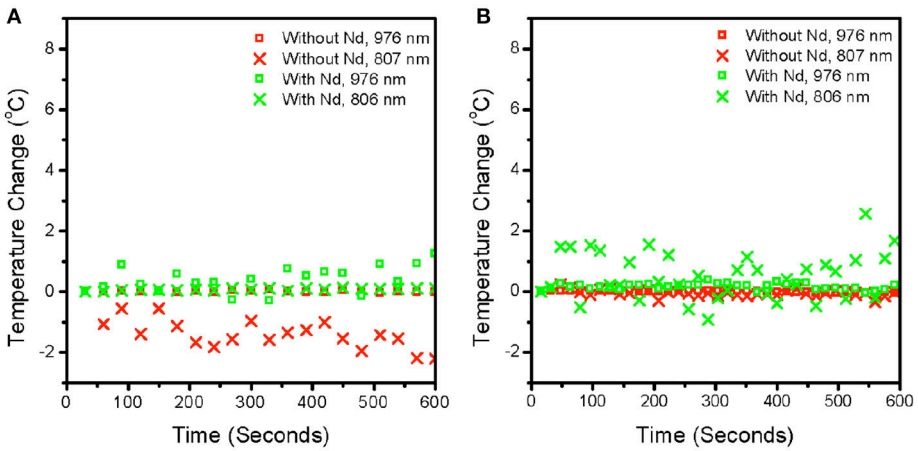

FIGURE 5 | Plot of measured temperature converted from spectroscopic ratio against time at a fixed power for particles without Nd (β-$NaYF_4$: 20% Yb^{3+}, 2% Er^{3+}) and with Nd (β-$NaYF_4$: 40%Yb^{3+}, 2% Er^{3+}@$NaYF_4$: 20% Yb^{3+}@NaNdF4: 10% Yb^{3+}) in air **(A)** and in water **(B)**. The laser was blocked for 10 min before the beginning of the measurement and unblocked at around 20 s to collect any changes in temperature after the sample was exposed. The powers used were 8.0 × 10^4 W/cm^2 and 5.3 × 10^4 W/cm^2 for 976 and 806 nm respectively. Both power intensities were maintained at comparable orders of magnitude as much as possible. The pulse width is ~4.5 ns and pulse frequency is at 1,000 hz. Each point is at 16 s intervals, so each point is the sum of 16 k pulses.

at power intensities compatible with single UCNP imaging as demonstrated in previous studies (Gargas et al., 2014; Green et al., 2016). **Figure 6** shows that exposure to 800 nm (5×10^4 W/cm$^{2)}$ and 976 nm (7×10^4 W/cm^2) excitation for 2-min durations only cause dsDNA breaks 10% of the time. For a control DNA tightrope experiment where there was no exposure to near infrared excitation, the rate of occurrence of dsDNA breaks were also around 10%. Therefore, any damage observed is consistent with 10 s of UV or blue light nicking of the DNA, from the Xenon Arc Lamp source used to detect YOYO-1 emission. Clearly, from our measurements, the lack of DNA damage under infrared exposure leads us to infer that thermal heating is not significant at the current pump power intensities used in our measurements especially when considered alongside the lack of heating in water, as shown in **Figure 5**.

CONCLUSION

UCNPs with and without Nd^{3+} sensitization may be good candidates for application as nanothermometers in single biological molecule experimental situations. It was demonstrated that each type of UCNP was able to report temperature ratiometrically with sensitivities in the 1×10^{-4} K^{-1} range. In addition, it was determined that excitation intensity is a parameter of nanothermometry that must be strongly controlled in the single particle level to avoid ratio suppression due to alteration of the optical pathways involved in ratio reporting. Finally, the excitation intensities previously used to image single nanoparticles were shown to be applicable to DNA tightrope experiments without appreciable change in the viability of DNA over time windows appropriate for the study of protein-DNA interactions.

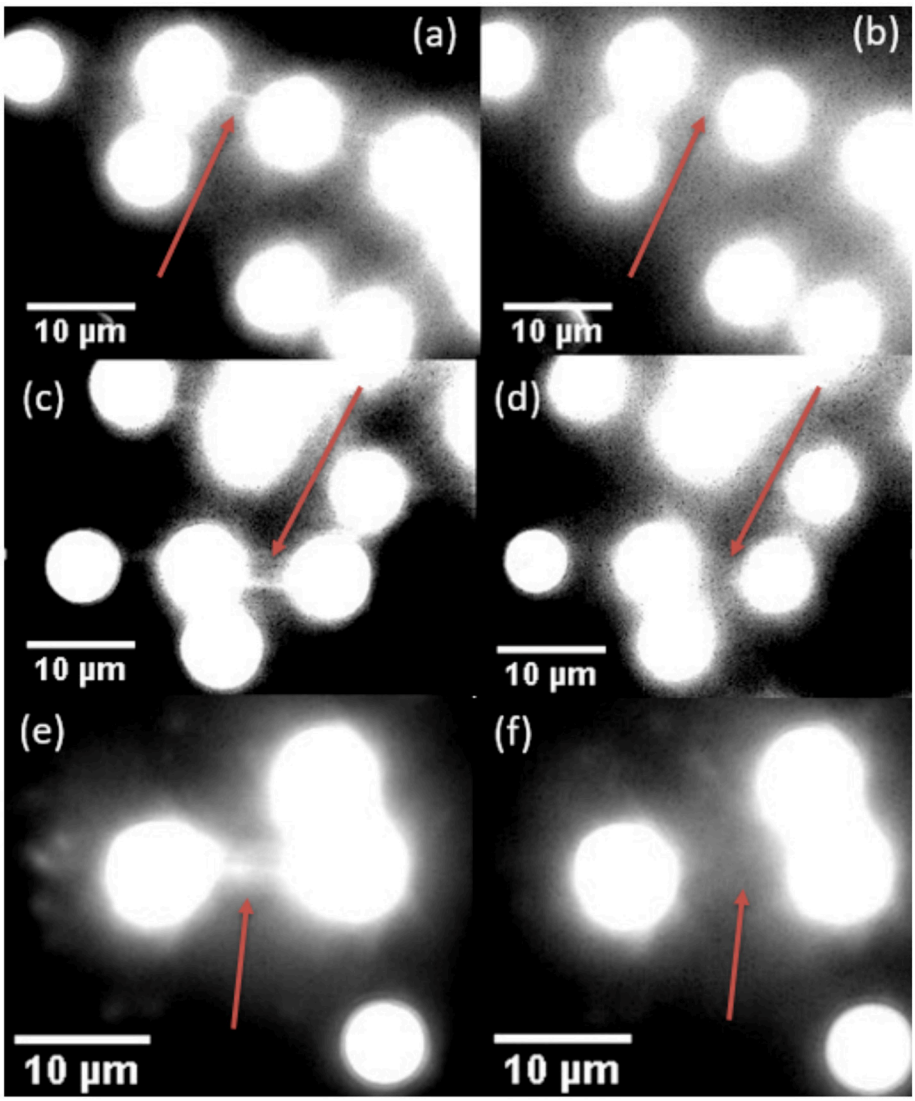

FIGURE 6 | Examples of DNA tightropes before and after breaking under 806 nm fluence **(a,b)**, 976 nm fluence **(c,d)**, and with no applied fluence **(e,f)**. In all three cases, the left image was taken upon the initial location of the DNA tightrope. The lamp was then blocked, and the right image was taken after exposure to 806 nm **(b)**, 976 nm **(d)**, or no laser fluence **(f)** for 2 min.

AUTHOR CONTRIBUTIONS

The study aims were proposed by SL. KH synthesized the UCNPs. KG designed and performed the spectroscopic experiments. HP prepared the biologicals for the DNA tightrope experiments. Data interpretation and analysis were performed by KG, KH, GH, and SL.

FUNDING

This work was financially supported by the National Institutes of Health 1R21ES027641-01 grant and the National Science Foundation NSF1706651 grant.

SUPPLEMENTARY MATERIAL

The Supplementary Material for this article can be found online at: https://www.frontiersin.org/articles/10.3389/fchem.2018.00416/full#supplementary-material

Supplementary Video 1 | Intensity varies as nanoparticles tumble in the laser spot due to polarization sensitivity. Seen here, single nanoplasmonic UCNPs tumble in 50% sucrose solution, recorded at a frame rate of 10 Hz.

Supporting Figure S1 | Time-resolved decay curves at 545 nm for β-$NaYF_4$:20%Yb, 2%Er at **(A)** 976 nm, and **(B)** 807 nm excitation respectively, and β-$NaYF_4$:40%Yb, 2%Er@$NaYF_4$:20%Yb@$NaNdF_4$:10%Yb at **(C)** 976 nm, and **(D)** 806 nm excitation respectively. In frame **(D)** the sample was partially removed from the collection area, resulting in lower signal, noisy collection.

REFERENCES

Austin, R. H., and Lim, S. F. (2008). The Sackler Colloquium on promises and perils in nanotechnology for medicine. *Proc. Natl. Acad. Sci. U.S.A.* 105, 17217–17221. doi: 10.1073/pnas.0709499105

Bai, X., Song, H., Pan, G., Lei, Y., Wang, T., Ren, X., et al. (2007). Size-dependent upconversion luminescence in Er^{3+}/Yb^{3+}-codoped nanocrystalline yttria: saturation and thermal effects. *J. Phys. Chem. C* 111, 13611–13617. doi: 10.1021/jp070122e

Binnemans, K. (2009). Lanthanide-based luminescent hybrid materials. *Chem. Rev.* 109, 4283–4374. doi: 10.1021/cr8003983

Chen, D., Liu, L., Huang, P., Ding, M., Zhong, J., and Ji, Z. (2015). Nd^{3+}-Sensitized Ho^{3+} single-band red upconversion luminescence in core–shell nanoarchitecture. *J. Phys. Chem. Lett.* 6, 2833–2840. doi: 10.1021/acs.jpclett.5b01180

Chen, D., Xu, M., and Huang, P. (2016). Core@shell upconverting nanoarchitectures for luminescent sensing of temperature. *Sens. Actuators B Chem.* 231, 576–583. doi: 10.1016/j.snb.2016.03.070

Chen, J. P., Patil, S., Seal, S., and McGinnis, J. F. (2006). Rare earth nanoparticles prevent retinal degeneration induced by intracellular peroxides. *Nat. Nanotechnol.* 1, 142–150. doi: 10.1038/nnano.2006.91

Debasu, M. L., Ananias, D., Pastoriza-Santos, I., Liz-Marzán, L. M., Rocha, J., and Carlos, L. D. (2013). Nanothermometry: all-in-one optical heater-thermometer nanoplatform operative from 300 to 2000 K based on Er^{3+} emission and blackbody radiation (Adv. Mater. 35/2013). *Adv. Mater.* 25, 4817–4817. doi: 10.1002/adma.201370219

Dong, J., and Zink, J. I. (2014). Taking the temperature of the interiors of magnetically heated nanoparticles. *ACS Nano* 8, 5199–5207. doi: 10.1021/nn501250e

Engeser, M., Fabbrizzi, L., Licchelli, M., and Sacchi, D. (1999). A fluorescent molecular thermometer based on the nickel(II) high-spin/low-spin interconversion. *Chem. Commun.* 1191–1192. doi: 10.1039/A901931F

Gargas, D. J., Chan, E. M., Ostrowski, A. D., Aloni, S., Altoe, M. V., Barnard, E. S., et al. (2014). Engineering bright sub-10-nm upconverting nanocrystals for single-molecule imaging. *Nat Nano* 9, 300–305. doi: 10.1038/nnano.2014.29

Giloh, H., and Sedat, J. (1982). Fluorescence microscopy: reduced photobleaching of rhodamine and fluorescein protein conjugates by n-propyl gallate. *Science* 217, 1252–1255. doi: 10.1126/science.7112126

Gota, C., Okabe, K., Funatsu, T., Harada, Y., and Uchiyama, S. (2009). Hydrophilic fluorescent nanogel thermometer for intracellular thermometry. *J. Am. Chem. Soc.* 131, 2766–2767. doi: 10.1021/ja807714j

Green, K., Wirth, J., and Lim, S. F. (2016). Optical investigation of gold shell enhanced 25 nm diameter upconverted fluorescence emission. *Nanotechnology* 27:135201 doi: 10.1088/0957-4484/27/13/135201

Kim, B. J., Lim, S. Y., Cho, Y., Nam, S. H., Suh, Y. D., Park, C. R., et al. (2017). Tuning 2D light upconversion emission by modulating phonon relaxation. *Chem. Asian J.* 12, 2038–2043. doi: 10.1002/asia.201700782

Kushida, T., Marcos, H. M., and Geusic, J. E. (1968). Laser transition cross section and fluorescence branching ratio for Nd^{3+} in yttrium aluminum garnet. *Phys. Rev.* 167, 289–291

Lei, Y., Song, H., Yang, L., Yu, L., Liu, Z., Pan, G., et al. (2005). Upconversion luminescence, intensity saturation effect, and thermal effect in Gd2O3:Er3,Yb3+ nanowires. *J. Chem. Phys.* 123, 174710. doi: 10.1063/1.2087487

León-Luis, S. F., Rodríguez-Mendoza, U. R., Haro-González, P., Martín, I. R., and Lavín, V. (2012). Role of the host matrix on the thermal sensitivity of Er^{3+} luminescence in optical temperature sensors. *Sens. Actuators B Chem.* 174, 176–186. doi: 10.1016/j.snb.2012.08.019

Lichtman, J. W., and Conchello, J. A. (2005). Fluorescence microscopy. *Nat. Methods* 2, 910–919. doi: 10.1038/nmeth817

Lim, S. F., Riehn, R., Ryu, W. S., Khanarian, N., Tung, C. K., Tank, D., et al. (2006). *In vivo* and scanning electron microscopy imaging of upconverting nanophosphors in *Caenorhabditis elegans*. *Nano Lett.* 6, 169–174. doi: 10.1021/nl0519175

Lim, S. F., Riehn, R., Tung, C. K., Ryu, W. S., Zhuo, R., Dalland, J., et al. (2009). Upconverting nanophosphors for bioimaging. *Nanotechnology* 20:405701. doi: 10.1088/0957-4484/20/40/405701

Lim, S. F., Ryu, W. S., and Austin, R. H. (2010). Particle size dependence of the dynamic photophysical properties of NaYF4:Yb, Er nanocrystals. *Opt. Express* 18, 2309–2316. doi: 10.1364/OE.18.002309

Löw, P., Kim, B., Takama, N., and Bergaud, C. (2008). High-spatial-resolution surface-temperature mapping using fluorescent thermometry. *Small* 4, 908–914. doi: 10.1002/smll.200700581

Lü, Q., Wu, Y., Li, A., Wang, Y., Gao, Y., and Peng, H. (2011). Local thermal effect at luminescent spot on upconversion luminescence in Y_2O_3:Er^{3+},Yb^{3+} nanoparticles. *Mater. Sci. Eng. B* 176, 1041–1046. doi: 10.1016/j.mseb.2011.05.039

Pan, H., Bilinovich, S. M., Kaur, P., Riehn, R., Wang, H., and Williams, D. C. (2017). CpG and methylation-dependent DNA binding and dynamics of the methylcytosine binding domain 2 protein at the single-molecule level. *Nucleic Acids Res.* 45, 9164–9177. doi: 10.1093/nar/gkx548

Ross, D., Gaitan, M., and Locascio, L. E. (2001). Temperature measurement in microfluidic systems using a temperature-dependent fluorescent dye. *Anal. Chem.* 73, 4117–4123. doi: 10.1021/ac010370l

Sakakibara, J., and Adrian, R. J. (1999). Whole field measurement of temperature in water using two-color laser induced fluorescence. *Exp. Fluids* 26, 7–15. doi: 10.1007/s003480050260

Schubert, D., Dargusch, R., Raitano, J., and Chan, S. W. (2006). Cerium and yttrium oxide nanoparticles are neuroprotective. *Biochem. Biophys. Res. Commun.* 342, 86–91. doi: 10.1016/j.bbrc.2006.01.129

Shaner, N. C., Lin, M. Z., McKeown, M. R., Steinbach, P. A., Hazelwood, K. L., Davidson, M. W., et al. (2008). Improving the photostability of bright monomeric orange and red fluorescent proteins. *Nat. Methods* 5, 545–551. doi: 10.1038/nmeth.1209

Stokes, G. G. (1852). On the change of refrangibility of light. *Philos. Trans. R. Soc. Lond.* 142, 463–562. doi: 10.1098/rstl.1852.0022

Tessmer, I., Kaur, P., Lin, J., and Wang, H. (2013). Investigating bioconjugation by atomic force microscopy. *J Nanobiotechnol.* 11:25. doi: 10.1186/1477-3155-11-25

Tian, L. J., Xu, Z., Zhao, S. L., Cui, Y., Liang, Z. Q., Zhang, J. J., et al. (2014). The upconversion luminescence of Er^{3+}/Yb^{3+}/Nd^{3+} triply-doped beta-NaYF4 nanocrystals under 808-nm excitation. *Materials* 7, 7289–7303. doi: 10.3390/ma7117289

Ungun, B., Prud'homme, R. K., Budijon, S. J., Shan, J., Lim, S. F., Ju, Y., et al. (2009). Nanofabricated upconversion nanoparticles for photodynamic therapy. *Opt. Express* 17, 80–86. doi: 10.1364/OE.17.000080

Vetrone, F., Naccache, R., Juarranz de la Fuente, A., Sanz-Rodríguez, F., Blazquez-Castro, A., Rodriguez, E. M., et al. (2010a). Intracellular imaging of HeLa cells by non-functionalized NaYF4: Er^{3+}, Yb^{3+} upconverting nanoparticles. *Nanoscale* 2, 495–498. doi: 10.1039/b9nr00236g

Vetrone, F., Naccache, R., Zamarrón, A., Juarranz de la Fuente, A., Sanz-Rodríguez, F., Martinez Maestro, L., et al. (2010b). Temperature sensing using fluorescent nanothermometers. *ACS Nano* 4, 3254–3258. doi: 10.1021/nn100244a

Wang, S., Westcott, S., and Chen, W. (2002). Nanoparticle luminescence thermometry. *J. Phys. Chem. B* 106, 11203–11209. doi: 10.1021/jp026445m

Wang, Y. F., Liu, G. Y., Sun, L. D., Xiao, J. W., Zhou, J. C., and Yan, C. H. (2013). Nd3+-sensitized upconversion nanophosphors: efficient *in vivo* bioimaging probes with minimized heating effect. *ACS Nano* 7, 7200–7206. doi: 10.1021/nn402601d

Weber, M. J. (1971). Optical properties of Yb^{3+} and Nd^{3+}-Yb^{3+} energy transfer in $YAlO_3$. *Phys. Rev. B* 4, 3153–3159

Wirth, J., Green, K. K., O'Connor, M., and Lim, S. F. (2017). Enhancement of upconverted fluorescence by interference layers. *Small* 13:1602846. doi: 10.1002/smll.201602846

Xu, W., Gao, X., Zheng, L., Zhang, Z., and Cao, W. (2012). An optical temperature sensor based on the upconversion luminescence from Tm^{3+}/Yb^{3+} codoped oxyfluoride glass ceramic. *Sens. Actuators B Chem.* 173, 250–253. doi: 10.1016/j.snb.2012.07.009

Yao, J., Larson, D. R., Vishwasrao, H. D., Zipfel, W. R., and Webb, W. W. (2005). Blinking and nonradiant dark fraction of water-soluble quantum dots in aqueous solution. *Proc. Natl. Acad. Sci. U.S.A.* 102, 14284–14289. doi: 10.1073/pnas.0506523102

Zhong, Y., Tian, G., Gu, Z., Yang, Y., Gu, L., Zhao, Y., et al. (2014). Elimination of photon quenching by a transition layer to fabricate a quenching-shield sandwich structure for 800 nm excited upconversion luminescence of Nd^{3+} sensitized nanoparticles. *Adv. Mater.* 26, 2831–2837. doi: 10.1002/adma.201304903

Zhu, X., Feng, W., Chang, J., Tan, Y. W., Li, J., Chen, M., et al. (2016). Temperature-feedback upconversion nanocomposite for accurate photothermal therapy at facile temperature. *Nat. Commun.* 7:10437. doi: 10.1038/ncomms 10437

Conflict of Interest Statement: The authors declare that the research was conducted in the absence of any commercial or financial relationships that could be construed as a potential conflict of interest.

frontiers in Chemistry

ORIGINAL RESEARCH
published: 11 September 2018
doi: 10.3389/fchem.2018.00385

Acetone Sensing Properties and Mechanism of Rh-Loaded WO_3 Nanosheets

Zhilei Qiu[1], Zhongqiu Hua[1], Yan Li[1], Mengjun Wang[1]*, Dan Huang[1], Chen Tian[1], Chensheng Zhang[1], Xuemin Tian[1] and Erping Li[2]*

[1] Tianjin Key Laboratory of Electronic Materials and Devices, School of Electronics and Information Engineering, Hebei University of Technology, Tianjin, China, [2] Key Laboratory of Micro-Nano Electronics and Smart System of Zhejiang Province, Department of Information Science & Electronic Engineering, Zhejiang University, Hangzhou, China

WO_3 nanosheets was prepared by an acidification method and the Rh catalyst was dispersed on the surface of the nanosheets with a wet impregnation method. The morphology of pristine WO_3 and Rh modified WO_3 nanosheets and their responses to acetone gas were studied. According to oxygen adsorption combined with TPR results, the sensing and sensitization mechanism of acetone were discussed. It was found that no visible changes in nanostructures or morphologies were observed in WO_3 nanosheets with Rh, however, the sensor resistance and sensor response were greatly promoted. The basic sensitization mechanism could be caused by the electronic interaction between oxidized Rh and WO_3 surface.

Keywords: WO_3, Rh, acetone, surface modification, gas sensors

OPEN ACCESS

Edited by:
Wen Zeng,
Chongqing University, China

Reviewed by:
Dachi Yang,
Nankai University, China
Guotao Duan,
Institute of Solid State Physics, Hefei Institutes of Physical Science (CAS), China

***Correspondence:**
Zhongqiu Hua
zhongqiuhua@hebut.edu.cn
Mengjun Wang
wangmengjun@hebut.edu.cn

Specialty section:
This article was submitted to Nanoscience, a section of the journal Frontiers in Chemistry

Received: *12 July 2018*
Accepted: *09 August 2018*
Published: *11 September 2018*

Citation:
Qiu Z, Hua Z, Li Y, Wang M, Huang D, Tian C, Zhang C, Tian X and Li E (2018) Acetone Sensing Properties and Mechanism of Rh-Loaded WO_3 Nanosheets Front. Chem. 6:385. doi: 10.3389/fchem.2018.00385

INTRODUCTION

Acetone gas is closely related to people with diabetes. Medical research has shown that there is a significant difference of acetone concentration in the breath for diabetics and healthy people, the former being higher than 1.8 ppm and the latter being below 0.8 ppm (Owen et al., 1982; Natale et al., 2014). Therefore, through the quantitative detection of the acetone concentration in human exhaled gases, it could achieve the purpose of diagnosis and monitoring to the disease condition. Metal oxide semiconductors (MOS) have been widely reported for gas sensors with the significant advantages, such as low cost, simple process and small size (Hübner et al., 2010; Choi et al., 2014). Tungsten trioxide (WO_3) as an n-type semiconductor has become a research hotspot in the detection of VOC gases in recent years (Kanda and Maekawa, 2005; Kadir et al., 2015; Li et al., 2017). The adsorption and reaction of VOC gas on WO_3 surface could change the semiconductor resistance, so the gas response can be improved by adding highly efficient catalytic elements. The introduction of ruthenium (Ru) and silicon (Si) improve the sensitivity of WO_3 to acetone (Righettoni et al., 2010; Li et al., 2018). Further, Rh is known as a highly efficient catalyst to the catalytic reaction of acetone gas (Houtman and Barteau, 1991). It has been reported that Rh loaded SnO_2 and In_2O_3 significantly improve the response of acetone (Kim et al., 2011; Kou et al., 2018). Therefore, this highly efficient catalyst could be also loaded onto WO_3 surface to increase the response to acetone. In this study, the Rh element was uniformly loaded onto the surface of WO_3 nanosheets based on an impregnation approach. This method has been frequently used in our previous work (Li et al., 2018). The experimental results show that the Rh nanoparticles can significantly enhance the response of WO_3 nanosheets to acetone without changing the surface morphology of WO_3 nanosheets. The basic sensitization mechanism of Rh was also analyzed based on experimental results.

EXPERIMENTAL

WO_3 nanosheets was obtained by dropping Na_2WO_4 solution into H_2SO_4 solution (Kida et al., 2009). Aqueous solution of $RhCl_3$ was impregnated with WO_3 (Rh-WO_3) powders and formed a suspension slurry, which was washed by distilled water and dried. Subsequently, the powders were annealed at 500°C in air. Sensor devices were made by the screen-printing technique. The crystal structures were measured by X-ray diffractometer (XRD; D8FOCUS, Germany). The morphology of sample was analyzed using scanning electron microscopy (FE-SEM; Nova Nano SEM 450, FEI, U. S). Nanosheets were also characterized by a transmission electron microscopy (TEM; Tecnai-F20, FEI, U.S). Energy spectrum analysis of materials uses X-ray photoelectron spectroscopy (XPS, Thermo escalab 250Xi, U. S). The catalyst activity was characterized by H_2 temperature programmed reduction (H_2-TPR; TP-5076, China). The experimental procedure of the TPR was descripted in **Figure S1**. Gas sensing tests were carried out by a conventional gas flow apparatus (see **Figure S2**). The gas sample was kept at a constant flow rate of 100 ml/min by mass flow controllers (MFC). The humidity of gas was <20 ppm and temperature of the chamber was about 50°C. The sensor response (S) was defined as $S = R_a/R_g$, where R_a and R_g are the sensor resistance in air and in the presence of target gases.

RESULTS AND DISCUSSION

The morphology of WO_3 nanosheets was characterized by SEM and TEM. **Figures 1A,B** show SEM images of pristine and 1wt.% Rh-WO_3 nanosheets. One can see that the sample powders consisted of a large amount of nanoparticles with a lateral size from dozens to several hundred nanometers. According to SEM images, there were no visible changes observed in pristine WO_3 and Rh modified one. For the results of specific surface area, pristine WO_3 was ∼12 m^2/g and 1wt. %Rh-WO_3 is about 13 m^2/g, which indicts no significant change. **Figure 2** shows TEM images of the pure WO_3 and 1wt.%Rh-WO_3 nanosheets. It was obvious that the sample powder is actually composed of highly irregular plate-like nanosheets. The insert image of **Figure 2A** presents a selected area diffraction (SAD) pattern of pristine WO_3 nanosheets, suggesting that the nanosheets have a good crystal quality. In addition, some white particles with dozens of nm in size were observed in WO_3 surface, as shown in **Figure 2B**. With the help of SAD in **Figure 2C**, these particles were identified as Rh_2O_3 with lattice spacing of 0.26 nm, corresponding to the (110) plane (JCPDS: 25-0707). It was thought that these large particles of Rh_2O_3 could be due to the aggregation of Rh during washing and drying process, which were not effectively removed during the washing process. While the lattice spacing of 0.38 nm in the HRTEM image was belong to monoclinic WO_3 (JCPDS: 43-1035), which was in a good agreement of XRD results (in **Figure S3**).

The chemical state of Rh on WO_3 surface was also analyzed by XPS. **Figure 3A** presents the XPS spectra of W, detection results of binding energy for $W4f_{7/2}$ and $W4f_{5/2}$ being 35.7eV and 37.9eV, respectively, which is in good agreement with W^{6+} (Dupin et al., 2000). **Figure 3B** shows the XPS spectra of Rh3d obtained from 1wt%Rh-WO_3. Among them, the $Rh2d_{5/2}$ peaked at 309.45eV is a typical oxide centered on Rh^{3+}. In addition, the $Rh2d_{3/2}$ located at 314.5eV is also an oxide centered on Rh^{3+} (Kim et al., 2011). Thus, it could be concluded that Rh was present as an oxidized state of Rh_2O_3 on WO_3 surface. Additional with XPS results, the oxidized state of Rh could be also evidenced by H_2-TPR. **Figure 3C** shows the H_2-TPR results of pristine and 1wt%Rh-WO_3 nanosheets. As expected, there was one weak peak around 370°C observed in pristine WO_3 nanosheets indicating a weak consumption of H_2, which may be due to the weak reduction behavior of WO_3 surface at a high temperature (Li et al., 2018). In contrast, large consumptions of H_2 were observed in 1wt%Rh-WO_3, suggesting a strong reduction behavior. There were two overlapped peaks of H_2 consumption at a low temperature around 110°C and the intensities of peaks were relatively high. It was believed that the consumption of H_2 observed at low temperatures could be due to the reduction of Rh_2O_3 and peaks located different temperature

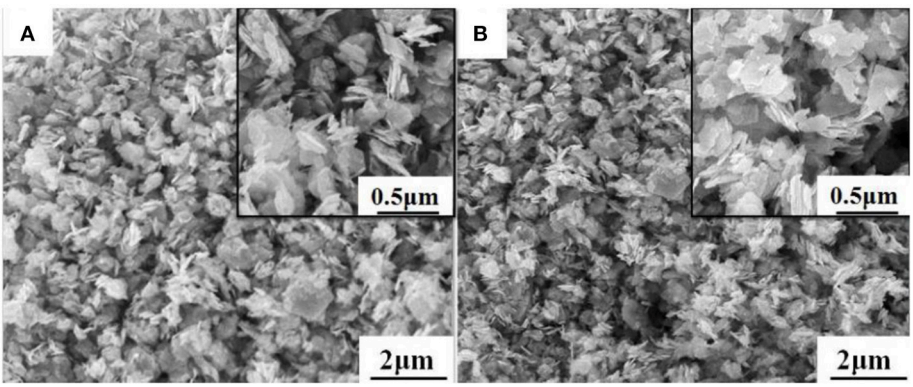

FIGURE 1 | SEM images of **(A)** pure WO_3 nanosheets and **(B)** 1wt%Rh-WO_3 nanosheets.

may be ascribed to different dispersion states of Rh species. There was a broad but weak peak of H_2 consumption at around 450°C, which could be attributable to the weak reduction of WO_3 surface, i.e., surface lattice oxygen (O_L) reacting with H_2 at a high temperature. The reduction behavior of Rh-WO_3 was much stronger than pristine WO_3 indicating that the reactivity of lattice oxygens is slightly promoted by Rh_2O_3 on the surface. We can see significant differences, comparing this reduction behavior with our previous study of Pt-WO_3 nanosheets (in **Figure S4**). At low temperature, Pt-WO_3 produces a negative peak of H_2 desorption. Based on the results of TPR and the resistance behavior under P_{O2}, it is concluded that the main sensitization of Pt-WO_3 may be caused by redox of Pt. nanoparticles (Li et al., 2017). This phenomenon of Rh may cause different sensitization mechanisms.

The sensing properties of pristineWO_3 and Rh-WO_3 nanosheets were characterized with acetone ranging from 0.5 to 10 ppm. **Figure 4A** shows the time dependence of sensor

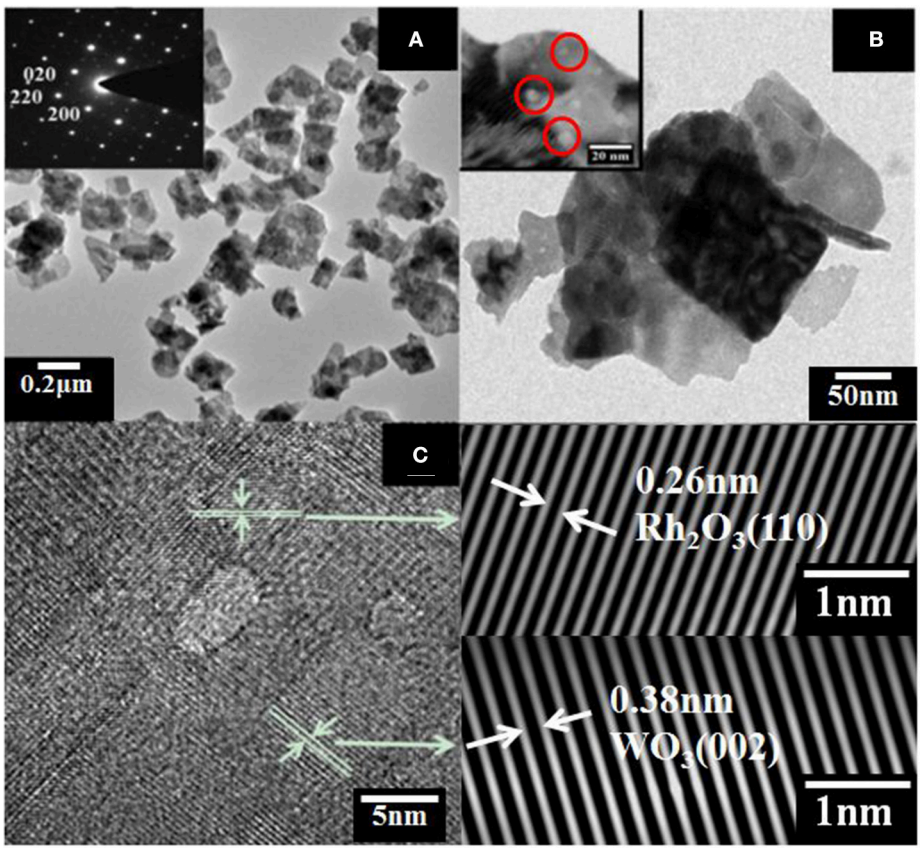

FIGURE 2 | TEM images of **(A)** WO_3 nanosheets insert with selected area diffraction (SAD) pattern, **(B)** 1wt%Rh-WO_3 nanosheets, **(C)** HRTEM image of 1wt%Rh-WO_3 nanosheets and SAD pattern of Rh_2O_3 and WO_3.

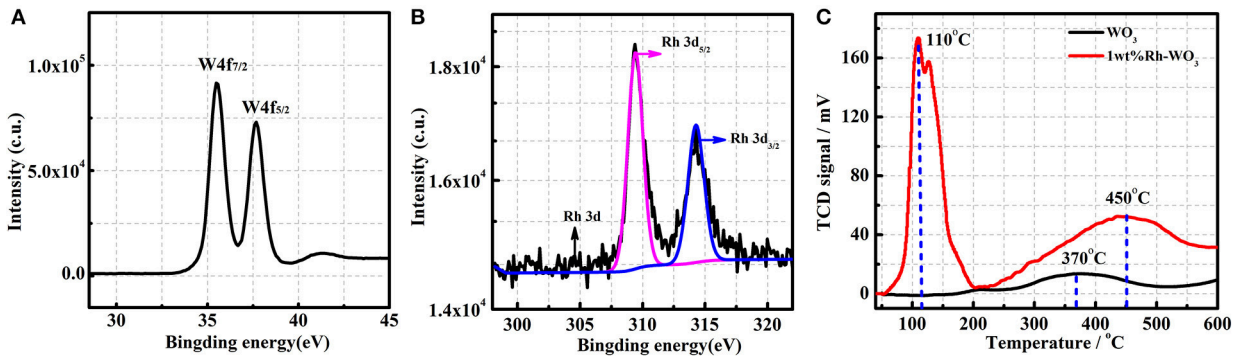

FIGURE 3 | The XPS of 1wt%Rh-WO_3: **(A)** W4f, **(B)** Rh3d, and **(C)** the H_2-TPR patterns of pure WO_3 and 1wt%Rh-WO_3.

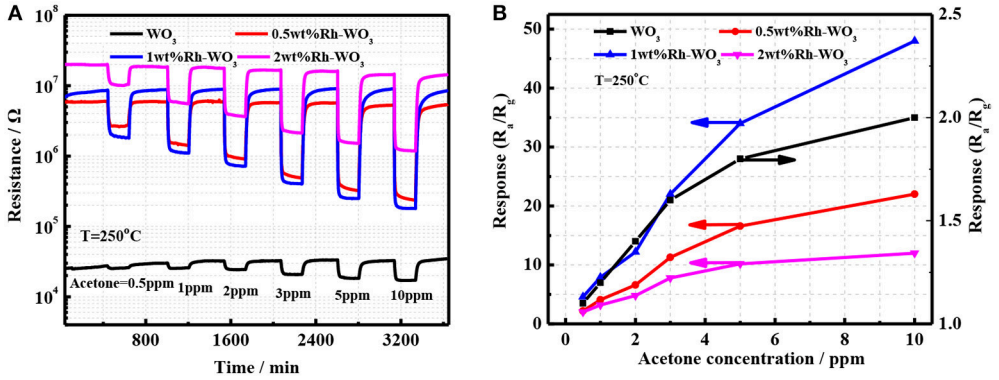

FIGURE 4 | (A) The transient response of four different sensor devices and **(B)** the sensor response as a function of acetone concentration.

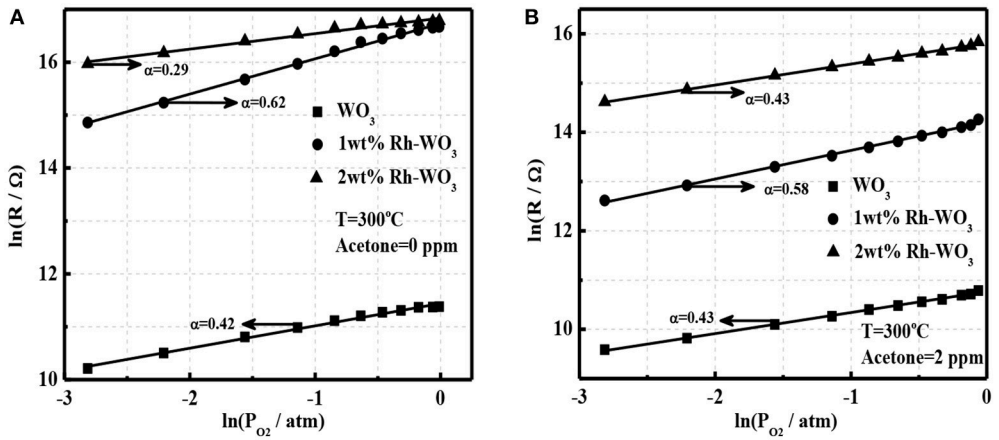

FIGURE 5 | The power-law response to oxygen for pristine WO_3 and Rh-WO_3 **(A)** in the absence of acetone and **(B)** in the presence of 2 ppm acetone at 300°C.

resistance. It was worth noting that the introduction of Rh greatly increased the sensor resistance of WO_3. For 2wt.% Rh-WO_3, the sensor resistance was almost three orders of pristine one. This indicated a strong electronic interaction between Rh_2O_3 and WO_3 surface, forming the well-known P-N junction or fermi-level control sensitization mechanism. Due to the electronic junction of Rh_2O_3 with WO_3, the sensors response and responding speed were significantly promoted. **Figure 4B** shows the calibration line of sensors resistance with concentration of acetone at an operation temperature of 250°C. It was found that sensor based on 1wt.%Rh-WO_3 also responded to 0.5 ppm acetone. One can see that sensor response was increased by 3 times compared with the neat WO_3. However, an excess of Rh did not effectively to promote the sensor response. This observation was in conflict with the great enhancement in sensor resistance. In order to explain the reduction in sensor response for 2wt.%Rh-WO_3, there were two factors should be considered. Firstly, an excessive amount of Rh could lead to agglomeration of Rh_2O_3 and poor dispersion on the surface of WO_3 nanoparticles. Consequently, some electronic interaction of Rh_2O_3 with WO_3 leading to the high resistance were not effective to the sensitization. Secondly, with increasing the amount of Rh the surface activity of WO_3 could be enhanced and then leaded to a catalytic reaction of acetone, which inhibit the diffusion of acetone molecule into inside of sensor films. As a result, the sensor response was reduced by a high loading amount of Rh. This reduction in sensor response could be also observed when increasing operation temperatures. This was evidenced by the strong dependence of sensor response on the operation temperatures for Rh-WO_3 as shown in **Figure S5a**. It was thought that increasing the operating temperature leaded to an enhancement in catalytic activity, which reduces the gas diffusion and sensor response to acetone. When operating at a temperature larger than 250°C, one can note the sensor response greatly decreased with temperatures. It was also found that sensors resistance also obviously decreased with temperature, as shown in **Figure S5b**. For pristine WO_3, the sensor response did not change significantly with temperature and exhibited a lower response at different temperatures. This poor response is associated with a weaker oxygen adsorption on WO_3 surface (Zeng et al., 2017). At the same time, the stability of the sensor was also evaluated as shown in **Figures S5c,d**.

It can be seen that Rh-WO_3 nanoparticles can work for a long time at 350°C and has favorable response recovery performance.

It is well-known that oxygen adsorption in the form of O_2^-, O^-, or O^{2-} on the surface serves as the receptor function and determines the sensing ability and mechanism of MOS gas sensors (Hua et al., 2018a). In order to explore the sensitization effect of Rh-WO_3 nanosheets, we analyzed the oxygen adsorption behavior. **Figure 5A** shows a linear plot of sensor resistance (R_g) with the partial pressure of oxygen (P_{O2}) at a double logarithm-scale for pristine and 1wt.% Rh-WO_3 sensors. It was observed that a linear relationship indicating a power-law response within all P_{O2} ranging from 0.06 to 0.99 atm (1 atm = 100% in volume) and the linear fitting coefficients were 0.42 and 0.62 for pristine and Rh-WO_3, respectively. This indicated that the main type of oxygen adsorption was in the form of O^- for both sensors (Hua et al., 2018a,b) at working temperature of 300°C through:

$$O_2 + 2e^- \rightleftarrows 2O^- \quad (1)$$

In case of 2 wt.% Rh-WO_3, the linear plot of $\ln R_g$ with $\ln P_{O2}$ was also valid. Remarkably, the slope, i.e., fitting coefficient was just 0.29, considerably <0.5. However, it was unlikely that a large amount of Rh on the surface could tailor the form of oxygen ionisorption on the surface. The most probably explanation was that with increasing P_{O2} the oxidized state of Rh, which has been limited to be exposed to atmosphere due to the aggregation of particles, was enhanced and then the electronic interaction between Rh_2O_3 and WO_3 surface was promoted. Consequently, new depletion regions formed, leading to an increase in sensor resistance with P_{O2} and a reduction in the fitting coefficient. This has also been observed in our previous Pt-WO_3 sensor (Li et al., 2017).

According to our recent study, it was found that the power-law response of oxygen in the presence of reducing gas such as H_2, CO, and acetone can be used to clarify the basic sensing mechanism of gas sensors (Hua et al., 2018c). **Figure 5B** shows the power-law response of oxygen in the presence of acetone (2 ppm) for pure and Rh-WO_3 sensors. A very good linearity was observed for all sensors indicating that the basic sensing mechanism of acetone could be explained by the oxidation of acetone with oxygen adsorbates by:

$$CH_3COCH_3 + 8O^- \rightarrow 3CO_2 + 3H_2O + 8e^- \quad (2)$$

For simplicity, it was assumed that acetone catalytic reaction was a complete reaction only producing CO_2 and H_2O. However, in fact the oxidation of acetone was rather complex. In addition, it was also found that linear coefficients of the power-law response were all around 0.5, which was consistent with **Figure 5A** and Equation (1). Importantly, for 2wt.%Rh-WO_3, the fitting coefficient significantly raised up compared with that in the absence of acetone. This clearly supported our explanation for the degradation of sensitization effect with large loading amount of Rh and the reduction in the exponent of the power-law response to oxygen. In this respect, we believe that the basic sensitization mechanism of Rh on WO_3 could be ascribed to the electronic interaction between Rh_2O_3 and WO_3 (p-n junction), which was very similar with the fermi-level control model, popular for Pd-SnO_2 sensors (Tang et al., 2015). The key factor to achieve a good sensitization effect highly relies on an elegant dispersion of Rh_2O_3 on WO_3 surface, which can enhance the electronic interaction with WO_3 surface as schematically drawn in **Figure S6**. This finding was similar with the case of Pt and Ru loaded WO_3 nanosheets, however, it was significantly different with Pd and Fe loaded WO_3. For the later one, the chemical sensitization effect of Pd and Fe plays a vital role through the reaction of surface lattice oxygens with reducing gases.

CONCLUSION

In summary, Rh as a noble catalyst was dispersed onto the surface of WO_3 nanosheets through a wet impregnation method. Experimental results indicated that Rh was in a form of oxidized state Rh_2O_3 on WO_3 surface and an excessive amount of Rh can lead to an aggregation of Rh_2O_3 and poor sensitization effect as well. An electronic interaction between Rh_2O_3 and WO_3 surface was evidenced by an extremely high argument in sensor resistance and it was thought that such an electronic was responsible for the observed sensitization effect of Rh loading. To achieve a good sensitization effect, an elegant dispersion of Rh_2O_3 is required, which highly relies on an effective dispersion method and a proper loading amount. Additionally, a power-law response to oxygen was observed for both pristine and Rh-WO_3 in the presence of acetone, which indicts that oxygen adsorption on the surface of WO_3 serves as a basic receptor function.

AUTHOR CONTRIBUTIONS

YL performed the experiments and analyzed the data with help from DH, CT, CZ, and XT. ZH, MW and EL conceived and guided the study. ZQ wrote the manuscript based on experimental data.

FUNDING

This study was supported by the National Natural Science Foundation of China (Grant NO. 61501167) and Natural Science Foundation of Tianjin (Grant NO. 15JCYBJC52100).

SUPPLEMENTARY MATERIAL

The Supplementary Material for this article can be found online at: https://www.frontiersin.org/articles/10.3389/fchem.2018.00385/full#supplementary-material

REFERENCES

Choi, K. I., Hwang, S. J., Dai, Z., Kang, Y. C., and Lee, J. H. (2014). Rh-catalyzed WO_3 with anomalous humidity dependence of gas sensing characteristics. *RSC Adv.* 4, 53130–53136. doi: 10.1039/C4RA06654E

Dupin, J. C., Gonbeau, D., Vinatier, P., and Levasseur, A. (2000). Systematic XPS studies of metal oxides, hydroxides and peroxides. *Phys. Chem. Chem. Phys.* 2, 1319–1324. doi: 10.1039/a908800h

Houtman, C., and Barteau, M. A. (1991). Adsorbed states of acetone and their reactions on rhodium(111) and rhodium(111)-(2.times.2)oxygen surfaces. *J. Phys. Chem.* 95, 3755–3764.

Hua, Z., Li, Y., Zeng, Y., and Wu, Y. (2018a). A theoretical investigation of the power-law response of metal oxide semiconductor gas sensors ?: schottky barrier control. *Sens. Actuators B Chem.* 255, 1911–1919. doi: 10.1016/j.snb.2017.08.206

Hua, Z., Qiu, Z., Li, Y., Zeng, Y., Wu, Y., Tian, X., et al. (2018b). A theoretical investigation of the power-law response of metal oxide semiconductor gas sensors ??: size and shape effects. *Sens. Actuators B Chem.* 255, 3541–3549. doi: 10.1016/j.snb.2017.09.189

Hua, Z., Tian, C., Huang, D., Yuan, W., Zhang, C., Tian, X., et al. (2018c). Power-law response of metal oxide semiconductor gas sensors to oxygen in presence of reducing gases. *Sens. Actuators B Chem.* 267, 510–518. doi: 10.1016/j.snb.2018.04.002

Hübner, M., Simion, C. E., Haensch, A., Barsan, N., and Weimar, U. (2010). CO sensing mechanism with WO_3, based gas sensors. *Sens. Actuators B Chem.* 151, 103–106. doi: 10.3-106.10.1016/j.snb.2010.09.040

Kadir, R. A., Zhang, W., Wang, Y., Ou, J. Z., Wlodarski, W., and O'Mullane, A. P., et al. (2015). Anodized nanoporous WO_3 schottky contact structure for hydrogen and ethanol sensing. *J. Mater. Chem. A* 3, 7994–8001. doi: 10.1039/C4TA06286H

Kanda, K., and Maekawa, T. (2005). Development of a WO_3, thick-film-based sensor for the detection of VOC. *Sens. Actuators B Chem.* 108, 97–101. doi: 10.1016/j.snb.2005.01.038

Kida, T., Nishiyama, A., Yuasa, M., Shimanoe, K., and Yamazoe, N. (2009). Highly sensitive NO_2 sensors using lamellar-structured WO_3 particles prepared by an acidification method. *Sens. Actuators B Chem.* 135, 568–574. doi: 10.1016/j.snb.2008.09.056

Kim, S. J., Hwang, I. S., Na, C. W., Kim, I. D., Kang, Y. C., and Lee, J. H. (2011). Ultrasensitive and selective C_2H_5OH sensors using Rh-loaded In_2O_3 hollow spheres. *J. Mater. Chem.* 21, 18560–18567. doi: 10.1039/C1JM14252F

Kou, X., Xie, N., Chen, F., Wang, T., Guo, L., Wang, C., et al. (2018). Superior acetone gas sensor based on electrospun SnO_2 nanofibers by Rh doping. *Sens. Actuators B Chem.* 256, 861–869. doi: 10.1016/j.snb.2017.10.011

Li, Y., Hua, Z., Wu, Y., Zeng, Y., Qiu, Z., and Tian, X., et al. (2017). Surface modification of Pt-loaded WO_3 nanosheets for acetone sensing application. *Chem. Lett.* 47, 167–170. doi: 10.1246/cl.170990

Li, Y., Hua, Z., Wu, Y., Zeng, Y., Qiu, Z., and Tian, X., et al. (2018). Modified impregnation synthesis of Ru-loaded WO_3, nanoparticles for acetone sensing. *Sens. Actuators B Chem.* 265, 249–256. doi: 10.1016/j.snb.2018.03.037

Natale, C. D., Paolesse, R., Martinelli, E., and Capuano, R. (2014). Solid-state gas sensors for breath analysis: a review. *Anal. Chim. Acta* 824, 1–17. doi: 10.1016/j.aca.2014.03.014

Owen, O. E., Trapp, V. E., Skutches, C. L., Mozzoli, M. A., Hoeldtke, R. D., and Boden,G. A. (1982). Acetone metabolism during diabetic ketoacidosis. *Diabetes* 31, 242–248. doi: 10.2337/diabetes.31.3.242

Righettoni, M., Tricoli, A., and Pratsinis, S. E. (2010). Si: WO_3 sensors for highly selective detection of acetone for easy diagnosis of diabetes by breath analysis. *Anal. Chem.* 82, 3581–3587. doi: 10.1021/ac902695n

Tang, W., Wang, J., Qiao, Q., Liu, Z., and Li, X. (2015). Mechanism for acetone sensing property of Pd-loaded SnO_2, nanofibers prepared by electrospinning: fermi-level effects. *J. Mater. Sci.* 50, 2605–2615. doi: 10.1007/s10853-015-8836-0

Zeng, Y., Hua, Z., Tian, X., Li, Y., Qiu, Z., and Wang, T. (2017). Modified impregnation synthesis of Fe-loaded WO_3 nanosheets and the gas-sensing properties. *Chem. Lett.* 46, 1353–1356. doi: 10.1246/cl.170555

Conflict of Interest Statement: The authors declare that the research was conducted in the absence of any commercial or financial relationships that could be construed as a potential conflict of interest.

frontiers in Chemistry

MINI REVIEW
published: 11 September 2018
doi: 10.3389/fchem.2018.00399

Application of Graphene Hybrid Materials in Fault Characteristic Gas Detection of Oil-Immersed Equipment

Lingfeng Jin[1,2,3], *Weigen Chen*[1,2]* *and Ying Zhang*[3]*

[1] State Key Laboratory of Power Transmission Equipment & System Security and New Technology, Chongqing University, Chongqing, China, [2] School of Electrical Engineering, Chongqing University, Chongqing, China, [3] School of Electrical and Computer Engineering, Georgia Institute of Technology, Atlanta, GA, United States

Graphene and its hybrid materials, due to their unique structures and properties, have attracted enormous attention for both fundamental and applied research in the gas sensing field. This review highlights the recent advances in the application of graphene-based gas sensors in fault characteristic gas detection of oil-immersed equipment, which can effectively achieve condition monitoring of the oil-immersed power equipment. In this review, the synthetic methods of graphene hybrid materials with noble metals, metal oxides and their combination are presented. Then, the basic sensing mechanisms of graphene hybrid materials and gas sensing properties of graphene hybrid materials sensors to hydrogen (H_2), carbon monoxide (CO), carbon dioxide (CO_2), methane (CH_4), acetylene (C_2H_2), ethylene (C_2H_4), and ethane (C_2H_6), which are the fault characteristic gas in oil-immersed power equipment, are summarized. Finally, the future challenges and prospects of graphene hybrid materials gas sensors in this field are discussed.

Keywords: graphene, gas sensor, oil-immersed equipment, sensing mechanism, fault characteristic gas

OPEN ACCESS

Edited by:
Zhongchang Wang,
Laboratório Ibérico Internacional de Nanotecnologia (INL), Portugal

Reviewed by:
Ming-Guo Ma,
Beijing Forestry University, China
Chunli Zhang,
Zhejiang University, China

***Correspondence:**
Weigen Chen
weigench@cqu.edu.cn
Ying Zhang
yzhang@gatech.edu

Specialty section:
This article was submitted to Nanoscience, a section of the journal Frontiers in Chemistry

Received: *22 June 2018*
Accepted: *20 August 2018*
Published: *11 September 2018*

Citation:
Jin L, Chen W and Zhang Y (2018) Application of Graphene Hybrid Materials in Fault Characteristic Gas Detection of Oil-Immersed Equipment. Front. Chem. 6:399. doi: 10.3389/fchem.2018.00399

INTRODUCTION

Graphene is an allotrope of carbon consisting of a single layer of carbon atoms arranged in a hexagonal lattice, which was rediscovered, isolated, and characterized by Geim and Novoselov in 2004 (Novoselov et al., 2004; Geim and Novoselov, 2007). Owing to the unique structure, graphene exhibits excellent physical and chemical properties, and has opened a new and very promising scientific area with a lot of focus on material science and potential applications (Aïssa et al., 2015; Higgins et al., 2016; Long et al., 2018). Among these outstanding properties of graphene, the high electron mobility of up to 200,000 cm^2/Vs and superior specific surface area of 2,630 m^2/g make graphene an extremely sensitive material for gas detection (Akturk and Goldsman, 2008; Chen et al., 2008; Bonaccorso et al., 2015). However, pristine graphene, which lacks dangling bonds, is unfavorable for the adsorption of gas molecules on its surface. Therefore, the modification of graphene and its derivatives via physicochemical methods, such as covalent, non-covalent and doping functionalization, has been investigated. Usually, graphene hybrid materials, which are composed of graphene and typical sensing materials (e.g., noble metals, metal oxides, or their ternary hybrids), have significantly improved performance due to the synergistic interaction between graphene and the typical sensing material (Meng et al., 2015). There have been numerous works published on the basic research and the sensing applications of graphene and graphene hybrid materials.

One such application is condition monitoring of oil-immersed equipment. Insulating oil with high specific heat and dielectric strength is widely used in the high voltage power equipment. However, the insulating oil can be cracked into small related gas molecules due to the long-term electrothermal effect, which reduces the insulation strength and leads to the malfunction of the power equipment. According to previous studies, effective detection of seven typical fault characteristic gases, including H_2, CO, CO_2, CH_4, C_2H_2, C_2H_4, and C_2H_6, can reflect the operation state of oil immersed power equipment (Bakar et al., 2014). Recently, a lot of research has been carried out on using graphene hybrid materials to detect these gases for rapid and accurate fault detection of oil-immersed equipment (Acharyya and Bhattacharyya, 2016; Zhou et al., 2016; Nasresfahani et al., 2017; Zhang et al., 2017b).

Although there are many reviews on the applications of gas sensing using graphene materials (Wang T. et al., 2016; Singhal et al., 2017; Dai et al., 2018), few has focused on detecting the typical gases reflecting the characteristics of faults in oil-immersed equipment. The objective of this review is to provide researchers a systematic understanding of the development of graphene hybrid materials in this application field. The main synthesis method and properties of graphene hybrid materials are introduced in section Synthesis, Properties, and Experimental Testing. Then, the gas sensing mechanism of graphene hybrid materials is discussed in section Sensing Mechanism. In section Application of Gas Sensor, the gas sensing properties of graphene hybrid materials to typical fault characteristic gases of oil-immersed equipment are summarized and compared. Finally, we analyze the challenges of gas sensing application in this field and present the suggestions of the future development trend.

SYNTHESIS, PROPERTIES, AND EXPERIMENTAL TESTING

Synthesis and Properties

Since the discovery of graphene in 2004, a lot of research has been conducted on how to synthesize graphene with high quality and large scale. To this date, the preparation of graphene can be mainly divided into top-down routes and bottom-up routes. Top-down routes use graphite as raw materials, and graphene is mainly obtained through separating the carbon atom layer by mechanical exfoliation, chemical oxidation-reduction reaction, and electrochemical methods. In contrast, bottom-up routes use small carbon-based molecules as raw materials, and graphene is obtained by silicon carbide pyrolysis, chemical vapor deposition (CVD), and solvothermal methods. Paton et al. (2014) developed a simple model that shows exfoliation occurs once the local shear rate exceeds 10^4/s and demonstrated a scalable method for producing relatively large quantities of defect-free graphene. Rathnayake et al. (Yola et al., 2015) presented the methods for preparing graphene oxide (GO) and reduced graphene oxides (rGO) using chemical oxidation and reduction processes, respectively, which are based on needle platy variety of natural vein graphite that has high purity and crystallinity and low cost. Hofmann et al. (2015) investigated the process of electrochemical exfoliation and the impact of its parameters on the produced graphene, and achieved the synthesis of graphene with controllable electronic and mechanical characteristics. Son et al. (2015) reported direct graphene growth over silicon nanoparticles without silicon carbide formation, and the volumetric energy densities are 972 and 700 Wh/L at the first and 200th cycles, respectively. Banszerus et al. (2015) showed that the quality of CVD-grown graphene depends critically on the used transfer process and reported an advanced transfer technique that allows both reusing the copper substrate of the CVD growth and making devices with mobilities as high as 350,000 cm^2/Vs. Quan et al. (2014) successfully synthesized sulfur-doped and nitrogen-doped graphene by using a solvothermal method, and these heteroatom-doped graphene materials exhibited high surface areas and high contents of heteroatoms. With the synthetic routes mentioned above, controllable preparation of graphene can be achieved.

Graphene as an ideal base material can be combined with noble metals, metal oxides, or their ternary hybrids to form graphene hybrid materials with outstanding gas sensing properties. Metal nanoparticles combine the excellent properties of metal and characteristics of nanomaterials, and show great potential in catalysis, sensing and electronics fields. Up to now, nanoparticles of many different metals, such as Au, Ag, Pd, Pt, Cu, Ni, Co, have been successfully combined with graphene. Phan et al. (in press) synthesized Pt nanoparticle-loaded 3D graphene for H_2 sensing using a polymer-assisted hydrothermal method and the H_2 sensor had a response value of 16% and response/recovery times of 9/10 s with a 1% H_2 concentration at 200 °C. Semiconductor metal oxide such as SnO_2 (Wang et al., 2015), ZnO (Zhu and Zeng, 2017), TiO_2 (Zhang et al., 2018), etc. are used widely in gas detection. The hybrids of graphene and metal oxides are mainly prepared by *in-situ* synthesis, liquid phase method and hydrothermal method. Ye et al. (2015) developed porous graphene embedded with various types of metal oxide nanoparticles through direct laser scribing on the metal-complex-containing polyimide film. Zhang B. et al. (2017) prepared rGO/α-Fe_2O_3 hybrids with different rGO contents, which were composed of the round-edged cubic α-Fe_2O_3 particles adhering uniformly on both sides of the crumpled and rippled rGO sheets. The local p-n heterojunctions between n-type α-Fe_2O_3 and p-type rGO caused an extension of electron depletion layer and potential barriers, which in turn led to significant resistance variation. Zhou et al. (2017) synthesized rGO and rGO/ZnO thin films and the performances of sensing organic vapor molecules are enhanced. In order to combe the advantages of noble metal and metal oxide, the ternary graphene hybrid materials have been developed. Uddin et al. (2015a) synthesized an Ag/ZnO/rGO hybrid via photochemical method and the 5 wt% hybrid enhanced the C_2H_2 sensing performance. Wei et al. (2017) synthesized the composite of Ag/SnO_2/rGO via a hydrothermal reaction process with a high surface area of 191.583 m^2/g and showed enhanced sensing properties to ethanol. Esfandiar et al. (2014) synthesized Pd/WO_3/ rGO as hybrid sensing material via the facile hydrothermal method and an improvement in H_2 sensing at low temperatures was observed.

Sensor Fabrication and Testing

Graphene hybrid materials can be used to fabricate gas sensors. Based on the operating mode, the device structure of gas sensor can be classified into directly heated and indirectly heated types. For a directly heated sensor, the sensing materials are in direct contact with the heater, which may make the sensor lose its stability and anti-interference ability. Therefore, the indirectly heated sensors are most widely used in scientific research and commerce, as shown in **Figure 1B**. The planar gas sensor is usually composed of three layers: sensing materials, detection electrodes and substrate (Nguyen et al., 2014). The synthesized sensing materials are covered by the detection electrodes. The interdigital electrodes are used to measure the resistance of the sensing materials. The substrate, made of silicon or alumina, has a good compatibility with integrated circuits and can support the sensing materials.

The responses of the sensor to different gases are carried out by using the gas sensing experimental platform, which composed of gas sources, MFCs (mass flow controllers), testing chamber and computer-controlled data acquisition and analysis system, as presented in **Figure 1A**. The experimental procedure is as follows: firstly, the sensor is placed in the center of the heating stage with two adjustable probes. Then, the heater starts to work and the background gas is delivered into the sealed chamber with a constant speed. When the resistance of the sensor no longer changes, the test chamber is filled with a different concentration of the gas being tested. At last, the background gas will be delivered again after the response of the sensor becomes stable. The response of sensor can be defined as a function of the change of resistance value of sensor (Barsan and Weimar, 2003). All the experiments need to be carried out under the same ambient temperature and relative humidity.

SENSING MECHANISM

Schedin et al. reported that the graphene gas sensor can effectively detect the adsorption or dissociation behavior of a single gas molecule on the surface of graphene, due to the fact that the change of carrier concentration of graphene leads to the change in electrical conductivity (Schedin et al., 2007). Meanwhile, due to the existence of oxygen functional groups, GO and rGO usually show better sensing properties than graphene. When GO or rGO are exposed to the air, the oxygen functional groups of them mainly combine H_2O molecules with hydrogen bonds and the adsorbed H_2O molecules are transferred to H_3O^+, further promoting the formation of ion channels on the surface of the sample. When they are in contact with adsorbed molecules, the hydrogen bonds will be destroyed, which inhibits the ionization reaction between oxygen functional groups and H_2O molecules and leads to step-like changes in resistance (Ozcan et al., 2018). Prezioso et al. (2013) prepared a p-type gas sensor through GO drop-cast on standard interdigitated Pt electrodes and its sensing properties to NO_2 was analyzed. They also presented the sensing mechanism of the gas sensor: when NO_2 molecules adsorbed on the oxygen functional groups, the electrons of the adsorption sites are transferred to NO_2 molecules, which leads to the decrease of electron concentration in the surface of the sensing materials, giving a reason for the p-type behavior.

In general, the sensing mechanisms of graphene hybrid are analyzed from the following three aspects. First, the introduction of nanoparticles can effectively prevent the aggregation of graphene sheets, thereby the graphene hybrid material is more favorable to form a 3D porous nanostructure with higher specific surface area, and more adsorption sites, vacancies, defects, and sp^2-bonded carbon, which are beneficial to the adsorption of gas molecules (Russo et al., 2012; Zhang et al., 2015a). Secondly, the formation of p-n heterojunctions between graphene and metal/metal oxide enhances the gas sensing properties. Once the target gas molecules are in contact with these interfaces, the depletion layers at the heterojunctions will be modulated, the electron state will be changed, and the phenomenon of charge transfer is more active, which lead to a larger relative change of resistance of graphene hybrid material (Tran et al., 2014). Thirdly, when hybrid materials contain metal oxide (e.g., SnO_2, ZnO, CuO, Co_3O_4), the sensing behavior can be explained by the surface-adsorbed oxygen (Bai et al., 2015). For n-type metal oxide material, the oxygen molecules $O_{2(gas)}$ will capture electrons from the surface of metal oxide to form chemisorbed oxygen species (O_2^-, O^-, or O^{2-}), which leads to a high resistance of the sensor, as observed in the experiments (Jin et al., 2016). As shown in **Figure 1C**, when the sensor is exposed to reducing gas such as methane, the target gas molecules will react with chemisorbed oxygen species and obtain electrons from them, which reduces the concentration of electron on the surface of the sensing materials. Obviously, the gas sensing reaction is a ticklish issue associated with the intricate nanostructure and complicated sensing mechanism (Wang et al., 2011; Sun et al., 2015; Wang Z. et al., 2016). The research on the characterization methods and simulation analysis from atomic level provide a new perspective and starting point for the study on the sensing mechanism of nanomaterials.

APPLICATION OF GAS SENSOR

Graphene hybrid materials exhibit excellent sensing properties to H_2, CO, CO_2, and small hydrocarbon gas (e.g., CH_4, C_2H_2, C_2H_4, C_2H_6). In this section, we summarize and discuss the related works based on the recently published papers (**Table 1**).

Hydrogen

The amount of H_2 in the insulating oil will increase significantly before the electrical fault or thermal failure occurs. Therefore, online monitoring of the H_2 content can ensure the security and stability of operation of oil immersed equipment. Noble metal is known for its high superior selectivity for the adsorption of H_2 due to its catalytic activity for H_2 molecules. The gas sensor based on Pd (Alfano et al., 2017) or Pt (Harley-Trochimczyk et al., 2015) nanoparticles loaded graphene demonstrated high sensitivity to H_2 with short response and recovery time. Sharma and Kim (2018) fabricated a MEMS H_2 sensor based on Pd-Ag/graphene, which showed a detection limit of 500 μL/L due to the phase transition of Pd-Ag. In addition, as metal oxide exhibits excellent gas sensing properties for H_2, the graphene-metal oxide

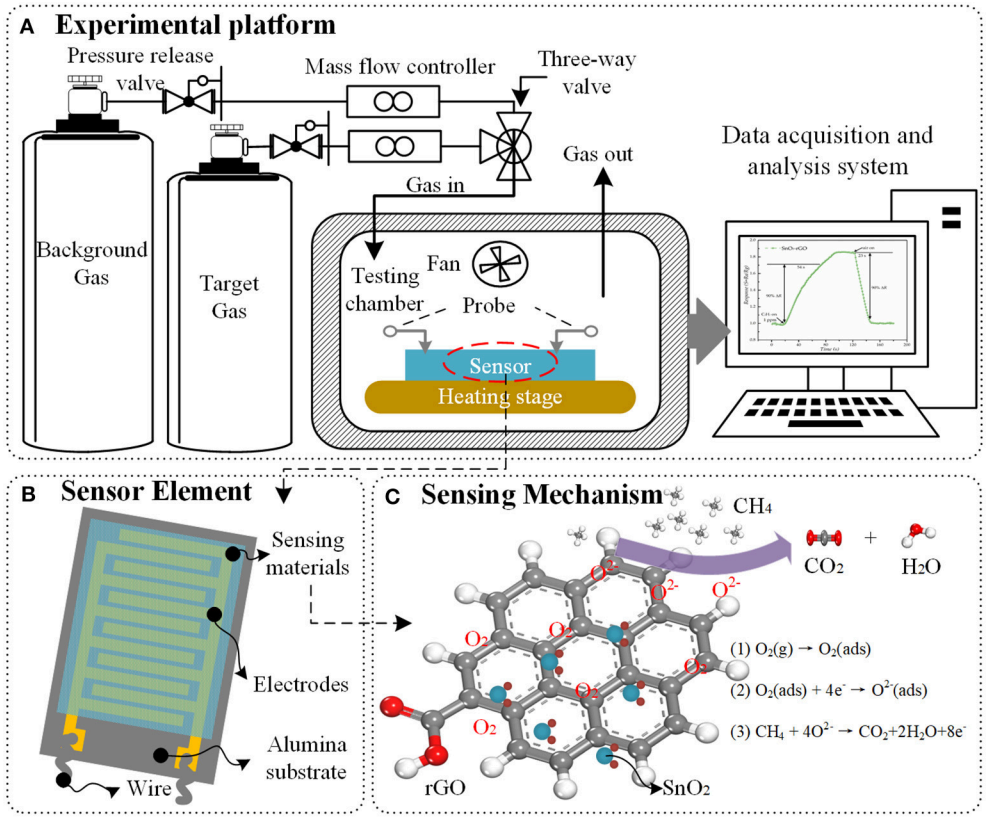

FIGURE 1 | Schematic illustration of **(A)** gas sensing experimental platform, **(B)** structure of planar sensor element, and **(C)** sensing mechanism between SnO_2/rGO hybrid materials and methane.

hybrid materials are usually used to detect H_2 with low limit of detection (LOD) at room temperature. Wang et al. synthesized MoO_3 nanoribbon/graphene hybrid for H_2 sensing with ultralow LOD of 0.5 μL/L (Yang et al., 2017). Zhang et al. (2017c) reported a high-performance H_2 gas sensor based on CuO/rGO/CuO sandwiched nanostructure. Chen and co-workers successfully fabricated a device based on gasochromic-Pd/WO_3/graphene/Si tandem structure with fast response and recovery time for H_2 (Chen et al., 2018).

Carbon Monoxide and Carbon Dioxide

CO and CO_2 are mainly associated with the presence of overheating fault, which are decomposed from the cellulose of insulating oil paper. Consequently, development of high-performance CO and CO_2 gas sensors is an effective way to monitor the insulation performance of oil-immersed equipment. The gas sensors based on rGO (Hafiz et al., 2014; Panda et al., 2016; Wu et al., 2016) can lower the operating temperature to room temperature. The graphene metal oxide hybrid materials such as NiO/graphene (Khaleed et al., 2017), CuO/rGO (Zhang et al., 2017a) ZnO (Ha et al., 2018), can detect CO with low LOD (as low as 1 μL/L), and quick response and recovery time (9 s/10 s). Balamurugan et al. (2016) demonstrated a selective CO sensor based on rGO decorated mesoporous hierarchical $GaInO_3$, which exhibited a high response rate of 48% to 20 μL/L CO and appreciably fast response (∼14 s) and recovery (∼15 s) at 90°C. Shojaee and co-workers synthesized Pd-loaded SnO_2/rGO hybrid materials by a hydrothermal method for CO sensing application (Shojaee et al., 2018). Additionally, much research on CO_2 sensor based on graphene hybrid materials have been carried out by Nemade's group. They have fabricated sensors with excellent stability, low LOD and short response and recovery time within 30 s based on Sb_2O_3 quantum dots (QDs)/graphene (Nemade and Waghuley, 2014b), Al_2O_3 QDs/graphene (Nemade and Waghuley, 2014a), and Y_2O_3 QDs/graphene (Nemade and Waghuley, 2013).

Hydrocarbon Gas

The hydrocarbon gas (CH_4, C_2H_2, C_2H_4, and C_2H_6) may be generated when electrical or thermal failures occur, such as oil or high-temperature overheating, partial discharge, spark discharge, or arc discharge. These four hydrocarbon gases have a small difference in molecular structure and chemical composition, and the sensing materials usually have the similar response to them. According to the relationship between principle gases and associated fault types (Bakar et al., 2014), when the oil-immersed equipment is suffering an electric or heating fault under any condition, the produced hydrocarbon fault characteristics gas

TABLE 1 | Summary of recent researches on graphene hybrid materials sensor for sensing of fault characteristic gases in oil-immersed equipment.

Gas	Hybrid material	Temp. (°C)	Detection range (μL/L)	Conc. (μL/L)	Response type	Sensor response	τ_{res}/τ_{rec} (s/s)	References
H_2	Pd/G	RT	1,000	1,000	$\Delta G/G_{air}$	26%	40/490	Alfano et al., 2017
	Pt/G	320	1,000–20,000	10,000	$\Delta R/R_{air}$	1.6%	~1/0.72	Harley-Trochimczyk et al., 2015
	Pd/Ag/G	105	100-5,000	500	$\Delta R/R_{air}$	9.96%	102/–	Sharma and Kim, 2018
	MoO_3/G	RT	0.5–1,000	1,000	R_{air}/R_{gas}	20.5	~10/30	Yang et al., 2017
	CuO/rGO/CuO	RT	50–1,500	100	$\Delta R/R_{air}$	4.2%	<80/60	Zhang et al., 2017c
	Pd/WO_3/G	RT	1,000–5,0000	1,000	ΔI	12 μA	~17/–	Chen et al., 2018
CO	rGO	RT	10–30	30	$\Delta R/R_{air}$	~71%	<30/–	Panda et al., 2016
	NiO/G	100	5–100	100	$\Delta R/R_{air}$	~120%	20/152	Khaleed et al., 2017
	CuO/rGO	RT	0.25–1,000	1	$\Delta R/R_{air}$	2.56%	70/160	Zhang et al., 2017a
	ZnO/rGO	200	1–1,000	1,000	$\Delta R/R_{air}$	85.2%	9/10	Ha et al., 2018
	$GdInO_3$/rGO	90	20–100	20	$\Delta R/R_{gas}$	48%	14/15	Balamurugan et al., 2016
	Pd/SnO_2/rGO	RT	50–1,600	1,500	$\Delta R/R_{air}$	4%	70/80	Shojaee et al., 2018
CO_2	rGO	RT	100–1,000	1000	$\Delta R/R_{air}$	1.65%	–	Nemade and Waghuley, 2014b
	rGO	RT	0–1,500	1,500	$\Delta R/R_{air}$	71%	~4 min	Nemade and Waghuley, 2014a
	Sb_2O_3/G	RT	0–50	50	$\Delta R/R_{air}$	~22%	16/22	Wu et al., 2016
	Al_2O_3/G	125	0–200	100	$\Delta R/R_{air}$	~8.1%	14/22	Hafiz et al., 2014
	Y_2O_3/G	RT	0–35	35	$\Delta R/R_{air}$	1.08%	–	Nemade and Waghuley, 2013
CH_4	PANI/rG	RT	10–3,200	100	R_{air}/R_{gas}	~3	85/45	Wu et al., 2013
	NiO/rGO	260	100–6,000	100	$\Delta R/R_{air}$	~2.2%	6/16	Zhang et al., 2016
	ZnO/rGO	190	100–4,000	1000	$\Delta R/R_{air}$	~12%	~200	Zhang et al., 2015b
	SnO_2/rGO	150	1,000–10,000	1000	$\Delta R/R_{air}$	47.6%	61/330	Navazani et al., 2018
	Pd/SnO_2/rGO	RT	800–16,000	14,000	$\Delta R/R_{air}$	9.8%	5/7 min	Nasresfahani et al., 2017
C_2H_2	SnO_2/rGO	180	0.5–500	50	R_{air}/R_{gas}	12.4	54/23	Jin et al., 2016
	Ag/ZnO/rGO	150	1–1,000	100	R_{air}/R_{gas}	21.2	25/80	Uddin et al., 2015b
	Ag/SnO_2/rGO	90	5–500	50	$\Delta R/R_{air}$	15.44	235/160	Jiang et al., 2017

G, graphene; rGO, reduced graphene oxide; PANI, polyaniline; RT, room temperature; ΔI, which is calculated as the current change of gas sensitive response; $\Delta G=|G_{air} - G_{gas}|$, where G_{gas} is the conductance exposure to target gas concentration and G_{air} is the conductance exposure to air or nitrogen; $\Delta R=|R_{air} - R_{gas}|$, where R_{gas} is the resistance exposure to target gas concentration and R_{air} is the resistance exposure to air or nitrogen.

is mainly CH_4 or C_2H_2, and the amount of each of them is larger than high molecular weight gases (C_2H_4 and C_2H_6) (Sun et al., 2017). Moreover, the detection of CH_4 or C_2H_2 is becoming more and more important in many fields as the mining industry, environment monitoring and petrochemical industry. Therefore, the research on the detection of hydrocarbon gas in oil-immersed equipment is mainly focused on CH_4 and C_2H_2. Wu et al. reported a CH_4 sensor based on polyaniline (PANI)/graphene. Due to the existence of the π-π* conjugation system within the PANI/graphene, this sensor showed a high sensitivity of 10–3,200 μL/L at room temperature (Wu et al., 2013). Zhang et al. (2016) prepared NiO/rGO hybrid materials and demonstrated a high selectivity toward CH_4 against H_2, CO, and CO_2. The response to 100 μL/L CH_4 was 2.2% at 260°C. Graphene hybrid with ZnO (Zhang et al., 2015b) and SnO_2 (Navazani et al., 2018) also exhibited unique sensing properties to CH_4 around 190 and 150°C. Nasresfahani et al. (2017) synthesized Pd-doped SnO_2/rGO via hydrothermal route, and the sensing performance to 800–16,000 μL/L CH_4 were carried out at room temperature. Gas sensing characteristics of C_2H_2 sensor based on SnO_2/rGO were carried out for 0.5–500 μL/L C_2H_2 at 180°C. The *p-n* heterojunctions between SnO_2 and rGO, oxygen functional groups and high specific surface area of SnO_2/rGO hybrid materials contribute to the high performance of sensor (Jin et al., 2016). Furthermore, Ag/ZnO/rGO (Uddin et al., 2015b) and Ag/SnO_2/rGO (Jiang et al., 2017) hybrid materials were synthesized, and the sensors were developed for low-temperature C_2H_2 sensing. However, with the decrease of operating temperature, the sensitivity of the sensor was reduced with longer response-recovery time.

CONCLUSIONS

Graphene hybrids are distinctive and promising sensing materials for detection of various gases, due to their ultrahigh electron mobility and large specific surface area. Compared to other types of sensor, the graphene-based sensors exhibit

excellent properties and provide a new idea for high sensitivity detection of the oil-immersed power equipment at low temperature.

Although great progress has been made in this field, there are still many challenges that need to be addressed. First, lower LOD and faster response-recovery time are needed. Graphene-based sensors provide a possible approach to detect gases at room temperature, but the reaction activities between gas molecules and sensing materials may be reduced, especially during the desorption, making it difficult to meet the engineering requirements. Ultraviolet light assisted excitation technology and novel multi-dimensional hierarchical nanostructure of graphene hybrid materials are useful ways to solve this problem. Secondly, avoiding the cross-sensitivity in the detection of mixed gas. Gas sensors usually exhibit similar responses toward different gases of different concentrations. The functionalization of graphene, operating temperature modulation and design of filter layer are workable methods to overcome this challenge. Moreover, gas sensor arrays, composed of group of sensors and signal processing algorithms, can realize the qualitative identification and quantitative detection of mixed gas. Thirdly, developing more stable materials and sensors. In practical application, the condition of detection environment, such as vibration, temperature, humidity, and other contaminants, may affect the sensitivity of sensors. The improvement of sensing materials, coating method, and fabrication techniques can avoid or reduce the impact of these factors. Finally, the development in this field is inseparable from the research of new materials as well as the corresponding sensing mechanism.

AUTHOR CONTRIBUTIONS

WC and LJ summarized and analyzed the related literature. LJ wrote the manuscript under the guidance of YZ and WC. All authors read and approved the manuscript.

ACKNOWLEDGMENTS

This study was supported by the Science Fund for Creative Research Groups of the National Natural Science Foundation of China (Grant No. 51321063) and the Joint Fund of the National Natural Science Foundation of China and the Smart Grid of State Grid Corporation of China (Grant No. U1766217). LJ thanks the China Scholarship Council (CSC) project (201706050039) for financial support.

REFERENCES

Acharyya, D., and Bhattacharyya, P. (2016). Highly efficient room-temperature gas sensor based on TiO_2 nanotube-reduced graphene-oxide hybrid device. *IEEE Electron Device Lett.* 37, 656–659. doi: 10.1109/LED.2016.2544954

Aïssa, B., Memon, N. K., Ali, A., and Khraisheh, M. K. (2015). Recent progress in the growth and applications of graphene as a smart material: a review. *Front. Mater* 2:58. doi: 10.3389/fmats.2015.00058

Akturk, A., and Goldsman, N. (2008). Electron transport and full-band electron-phonon interactions in graphene. *J. Appl. Phys.* 103:053702. doi: 10.1063/1.2890147

Alfano, B., Massera, E., Polichetti, T., Miglietta, M. L., and Di Francia, G. (2017). Effect of palladium nanoparticle functionalization on the hydrogen gas sensing of graphene based chemi-resistive devices. *Sensors Actuat. B Chem.* 253, 1163–1169. doi: 10.1016/j.snb.2017.07.146

Bai, S., Chen, C., Luo, R., Chen, A., and Li, D. (2015). Synthesis of MoO3/reduced graphene oxide hybrids and mechanism of enhancing H2S sensing performances. *Sensors Actuat. B Chem.* 216, 113–120. doi: 10.1016/j.snb.2015.04.036

Bakar, N., Abu-Siada, A., and Islam, S. (2014). A review of dissolved gas analysis measurement and interpretation techniques. *IEEE Electric. Insulation Magaz.* 30, 39–49. doi: 10.1109/MEI.2014.6804740

Balamurugan, C., Arunkumar, S., and Lee, D.-W. (2016). Hierarchical 3D nanostructure of GdInO3 and reduced-graphene-decorated GdInO3 nanocomposite for CO sensing applications. *Sensors Actuat. B Chem.* 234, 155–166. doi: 10.1016/j.snb.2016.04.043

Banszerus, L., Schmitz, M., Engels, S., Dauber, J., Oellers, M., Haupt, F., et al. (2015). Ultrahigh-mobility graphene devices from chemical vapor deposition on reusable copper. *Sci. Adv.* 1:e1500222. doi: 10.1126/sciadv.1500222

Barsan, N., and Weimar, U. (2003). Understanding the fundamental principles of metal oxide based gas sensors; the example of CO sensing with SnO_2 sensors in the presence of humidity. *J. Phys. Condens. Matter* 15, R813. doi: 10.1088/0953-8984/15/20/201

Bonaccorso, F., Colombo, L., Yu, G., Stoller, M., Tozzini, V., Ferrari, A. C., et al. (2015). Graphene, related two-dimensional crystals, and hybrid systems for energy conversion and storage. *Science* 347:1246501. doi: 10.1126/science.1246501

Chen, J.-H., Jang, C., Xiao, S., Ishigami, M., and Fuhrer, M. S. (2008). Intrinsic and extrinsic performance limits of graphene devices on SiO_2. *Nat. Nanotechnol.* 3, 206. doi: 10.1038/nnano.2008.58

Chen, M., Zou, L., Zhang, Z., Shen, J., Li, D., Zong, Q., et al. (2018). Tandem gasochromic-Pd-WO_3/graphene/Si device for room-temperature high-performance optoelectronic hydrogen sensors. *Carbon* 130, 281–287. doi: 10.1016/j.carbon.2018.01.013

Dai, Y., Liu, Y., Ding, K., and Yang, J. (2018). A short review of nanographenes: structures, properties and applications. *Mol. Phys.* 116, 987–1002. doi: 10.1080/00268976.2018.1433881

Esfandiar, A., Irajizad, A., Akhavan, O., Ghasemi, S., and Gholami, M. R. (2014). Pd–WO3/reduced graphene oxide hierarchical nanostructures as efficient hydrogen gas sensors. *Int. J. Hydrogen Energy* 39, 8169–8179. doi: 10.1016/j.ijhydene.2014.03.117

Geim, A. K., and Novoselov, K. S. (2007). The rise of graphene. *Nat. Mater.* 6, 183. doi: 10.1038/nmat1849

Ha, N. H., Thinh, D. D., Huong, N. T., Phuong, N. H., Thach, P. D., and Hong, H. S. (2018). Fast response of carbon monoxide gas sensors using a highly porous network of ZnO nanoparticles decorated on 3D reduced graphene oxide. *Appl. Surf. Sci.* 434, 1048–1054. doi: 10.1016/j.apsusc.2017.11.047

Hafiz, S. M., Ritikos, R., Whitcher, T. J., Razib, N. M., Bien, D. C. S., Chanlek, N., et al. (2014). A practical carbon dioxide gas sensor using room-temperature hydrogen plasma reduced graphene oxide. *Sensors Actuat. B Chem.* 193, 692–700. doi: 10.1016/j.snb.2013.12.017

Harley-Trochimczyk, A., Chang, J., Zhou, Q., Dong, J., Pham, T., Worsley, M. A., et al. (2015). Catalytic hydrogen sensing using microheated platinum nanoparticle-loaded graphene aerogel. *Sensors Actuat B Chem.* 206, 399–406. doi: 10.1016/j.snb.2014.09.057

Higgins, D., Zamani, P., Yu, A., and Chen, Z. (2016). The application of graphene and its composites in oxygen reduction electrocatalysis: a perspective and review of recent progress. *Energy Environ. Sci.* 9, 357–390. doi: 10.1039/C5EE02474A

Hofmann, M., Chiang, W.-Y., Nguyễn, T. D., and Hsieh, Y.-P. (2015). Controlling the properties of graphene produced by electrochemical exfoliation. *Nanotechnology* 26:335607. doi: 10.1088/0957-4484/26/33/335607

Jiang, C., Zhang, D., Yin, N., Yao, Y., Shaymurat, T., and Zhou, X. (2017). Acetylene gas-sensing properties of layer-by-layer self-assembled

Ag-decorated tin dioxide/graphene nanocomposite film. *Nanomaterials* 7, 278. doi: 10.3390/nano7090278

Jin, L., Chen, W., Zhang, H., Xiao, G., Yu, C., and Zhou, Q. (2016). Characterization of Reduced Graphene Oxide (rGO)-loaded SnO_2 nanocomposite and applications in C_2H_2 gas detection. *Appl. Sci.* 7, 19. doi: 10.3390/app7010019

Khaleed, A., Bello, A., Dangbegnon, J., Madito, M., Ugbo, F., Akande, A., et al. (2017). Gas sensing study of hydrothermal reflux synthesized NiO/graphene foam electrode for CO sensing. *J. Mater. Sci.* 52, 2035–2044. doi: 10.1007/s10853-016-0491-6

Long, H., Zeng, W., Wang, H., Qian, M., Liang, Y., and Wang, Z. (2018). Self-assembled biomolecular 1D nanostructures for aqueous sodium-ion battery. *Adv. Sci.* 5:1700634. doi: 10.1002/advs.201700634

Meng, F.-L., Guo, Z., and Huang, X.-J. (2015). Graphene-based hybrids for chemiresistive gas sensors. *TrAC Trends Anal. Chem.* 68, 37–47. doi: 10.1016/j.trac.2015.02.008

Nasresfahani, S., Sheikhi, M., Tohidi, M., and Zarifkar, A. (2017). Methane gas sensing properties of Pd-doped SnO2/reduced graphene oxide synthesized by a facile hydrothermal route. *Mater. Res. Bull.* 89, 161–169. doi: 10.1016/j.materresbull.2017.01.032

Navazani, S., Shokuhfar, A., Hassanisadi, M., Askarieh, M., Di Carlo, A., and Agresti, A. (2018). Facile synthesis of a SnO_2@ rGO nanohybrid and optimization of its methane-sensing parameters. *Talanta* 181, 422–430. doi: 10.1016/j.talanta.2018.01.015

Nemade, K., and Waghuley, S. (2013). "Carbon dioxide gas sensing application of graphene/Y_2O_3 quantum dots composite," *Paper presented at the International Journal of Modern Physics: Conference Series* (Bikaner).

Nemade, K., and Waghuley, S. (2014a). Highly responsive carbon dioxide sensing by graphene/Al_2O_3 quantum dots composites at low operable temperature. *Indian J. Phys.* 88, 577–583. doi: 10.1007/s12648-014-0454-1

Nemade, K., and Waghuley, S. (2014b). Role of defects concentration on optical and carbon dioxide gas sensing properties of Sb_2O_3/graphene composites. *Opt. Mater.* 36, 712–716. doi: 10.1016/j.optmat.2013.11.024

Nguyen, H., Quy, C. T., Hoa, N. D., Van Duy, N., Van Quang, V., and Van Hieu, N. (2014). Controllable growth of ZnO nanowires grown on discrete islands of Au catalyst for realization of planar-type micro gas sensors. *Sensors Actuat. B Chem.* 193, 888–894. doi: 10.1016/j.snb.2013.11.043

Novoselov, K. S., Geim, A. K., Morozov, S. V., Jiang, D., Zhang, Y., Dubonos, S. V., et al. (2004). Electric field effect in atomically thin carbon films. *Science,* 306, 666–669. doi: 10.1126/science.1102896

Ozcan, S., Vempati, S., Çirpan, A., and Uyar, T. (2018). Associative behaviour and effect of functional groups on the fluorescence of graphene oxide. *Phys. Chem. Chem. Phys.* 20, 7559–7569. doi: 10.1039/C7CP08334C

Panda, D., Nandi, A., Datta, S. K., Saha, H., and Majumdar, S. (2016). Selective detection of carbon monoxide (CO) gas by reduced graphene oxide (rGO) at room temperature. *RSC Adv.* 6, 47337–47348. doi: 10.1039/C6RA06058G

Paton, K. R., Varrla, E., Backes, C., Smith, R. J., Khan, U., O'Neill, A., et al. (2014). Scalable production of large quantities of defect-free few-layer graphene by shear exfoliation in liquids. *Nat. Mater.* 13, 624. doi: 10.1038/nmat3944

Phan, D.-T., Youn, J.-S., and Jeon, K.-J. (in press). High-sensitivity and fast-response hydrogen sensor for safety application using Pt nanoparticle-decorated 3D graphene. *Renewable Energy*. doi: 10.1016/j.renene.2018.05.033.

Prezioso, S., Perrozzi, F., Giancaterini, L., Cantalini, C., Treossi, E., Palermo, V., et al. (2013). Graphene oxide as a practical solution to high sensitivity gas sensing. *J. Phys. Chem. C* 117, 10683–10690. doi: 10.1021/jp3085759

Quan, B., Yu, S.-H., Chung, D. Y., Jin, A., Park, J. H., Sung, Y.-E., et al. (2014). Single source precursor-based solvothermal synthesis of heteroatom-doped graphene and its energy storage and conversion applications. *Sci. Rep.* 4:5639. doi: 10.1038/srep05639

Russo, P. A., Donato, N., Leonardi, S. G., Baek, S., Conte, D. E., Neri, G., et al. (2012). Room-temperature hydrogen sensing with heteronanostructures based on reduced graphene oxide and tin oxide. *Angewand. Chem. Int. Ed.* 51, 11053–11057. doi: 10.1002/anie.201204373

Schedin, F., Geim, A., Morozov, S., Hill, E., Blake, P., Katsnelson, M., et al. (2007). Detection of individual gas molecules adsorbed on graphene. *Nat. Mater.* 6, 652. doi: 10.1038/nmat1967

Sharma, B., and Kim, J.-S. (2018). Graphene decorated Pd-Ag nanoparticles for H_2 sensing. *Int. J. Hydrogen Energy* 43, 11397–11402. doi: 10.1016/j.ijhydene.2018.03.026

Shojaee, M., Nasresfahani, S., and Sheikhi, M. (2018). Hydrothermally synthesized Pd-loaded SnO_2/partially reduced graphene oxide nanocomposite for effective detection of carbon monoxide at room temperature. *Sensors Actuat. B Chem.* 254, 457–467. doi: 10.1016/j.snb.2017.07.083

Singhal, A. V., Charaya, H., and Lahiri, I. (2017). Noble metal decorated graphene-based gas sensors and their fabrication: a review. *Crit. Rev. Solid State Mater. Sci.* 42, 499–526. doi: 10.1080/10408436.2016.1244656

Son, I. H., Park, J. H., Kwon, S., Park, S., Rümmeli, M. H., Bachmatiuk, A., et al. (2015). Silicon carbide-free graphene growth on silicon for lithium-ion battery with high volumetric energy density. *Nat. Commun.* 6:8393. doi: 10.1038/ncomms8393

Sun, C., Ohodnicki, P. R., and Stewart, E. M. (2017). Chemical sensing strategies for real-time monitoring of transformer oil: a review. *IEEE Sensors J.* 17, 5786–5806. doi: 10.1109/JSEN.2017.2735193

Sun, R., Wang, Z., Saito, M., Shibata, N., and Ikuhara, Y. (2015). Atomistic mechanisms of nonstoichiometry-induced twin boundary structural transformation in titanium dioxide. *Nat. Commun.* 6, 7120. doi: 10.1038/ncomms8120

Tran, Q. T., Hoa, H. T. M., Yoo, D.-H., Cuong, T. V., Hur, S. H., Chung, J. S., et al. (2014). Reduced graphene oxide as an over-coating layer on silver nanostructures for detecting NH_3 gas at room temperature. *Sensors Actuat. B Chem.* 194, 45–50. doi: 10.1016/j.snb.2013.12.062

Uddin, A. I., Lee, K.-W., and Chung, G.-S. (2015a). Acetylene gas sensing properties of an Ag-loaded hierarchical ZnO nanostructure-decorated reduced graphene oxide hybrid. *Sensors Actuat. B Chem.* 216, 33–40. doi: 10.1016/j.snb.2015.04.028

Uddin, A. I., Phan, D.-T., and Chung, G.-S. (2015b). Low temperature acetylene gas sensor based on Ag nanoparticles-loaded ZnO-reduced graphene oxide hybrid. *Sensors Actuat. B Chem.* 207, 362–369. doi: 10.1016/j.snb.2014.10.091

Wang, S., Yang, J., Zhang, H., Wang, Y., Gao, X., Wang, L., et al. (2015). One-pot synthesis of 3D hierarchical SnO_2 nanostructures and their application for gas sensor. *Sensors Actuat. B Chem.* 207, 83–89. doi: 10.1016/j.snb.2014.10.032

Wang, T., Huang, D., Yang, Z., Xu, S., He, G., Li, X., et al. (2016). A review on graphene-based gas/vapor sensors with unique properties and potential applications. *Nano Micro Lett.* 8, 95–119. doi: 10.1007/s40820-015-0073-1

Wang, Z., Saito, M., McKenna, K. P., Fukami, S., Sato, H., Ikeda, S., et al. (2016). Atomic-Scale structure and local chemistry of COFeB–MgO magnetic tunnel junctions. *Nano Lett.* 16, 1530–1536. doi: 10.1021/acs.nanolett.5b03627

Wang, Z., Saito, M., McKenna, K. P., Gu, L., Tsukimoto, S., Shluger, A. L., et al. (2011). Atom-resolved imaging of ordered defect superstructures at individual grain boundaries. *Nature* 479, 380. doi: 10.1038/nature10593

Wei, Y., Yi, G., Xu, Y., Zhou, L., Wang, X., Cao, J., et al. (2017). Synthesis, characterization, and gas-sensing properties of Ag/SnO_2/rGO composite by a hydrothermal method. *J. Mater. Sci. Mater. Electron.* 28, 17049–17057. doi: 10.1007/s10854-017-7630-y

Wu, J., Tao, K., Zhang, J., Guo, Y., Miao, J., and Norford, L. K. (2016). Chemically functionalized 3D graphene hydrogel for high performance gas sensing. *J. Mater. Chem. A* 4, 8130–8140. doi: 10.1039/C6TA01426G

Wu, Z., Chen, X., Zhu, S., Zhou, Z., Yao, Y., Quan, W., et al. (2013). Room temperature methane sensor based on graphene nanosheets/polyaniline nanocomposite thin film. *IEEE Sensors J.* 13, 777–782. doi: 10.1109/JSEN.2012.2227597

Yang, S., Wang, Z., Zou, Y., Luo, X., Pan, X., Zhang, X., et al. (2017). Remarkably accelerated room-temperature hydrogen sensing of MoO 3 nanoribbon/graphene composites by suppressing the nanojunction effects. *Sensors Actuat. B Chem.* 248, 160–168. doi: 10.1016/j.snb.2017.03.106

Ye, R., Peng, Z., Wang, T., Xu, Y., Zhang, J., Li, Y., et al. (2015). *In situ* formation of metal oxide nanocrystals embedded in laser-induced graphene. *Acs Nano* 9, 9244–9251. doi: 10.1021/acsnano.5b04138

Yola, M. L., Atar, N., Eren, T., Karimi-Maleh, H., and Wang, S. (2015). Sensitive and selective determination of aqueous triclosan based on gold nanoparticles on polyoxometalate/reduced graphene oxide nanohybrid. *RSC Adv.* 5, 65953–65962. doi: 10.1039/C5RA07443F

Zhang, B., Liu, J., Cui, X., Wang, Y., Gao, Y., Sun, P., et al. (2017). Enhanced gas sensing properties to acetone vapor achieved by α-Fe2O3 particles ameliorated with reduced graphene oxide sheets. *Sensors Actuat. B Chem.* 241, 904–914. doi: 10.1016/j.snb.2016.11.023

Zhang, D., Chang, H., Li, P., and Liu, R. (2016). Characterization of nickel oxide decorated-reduced graphene oxide nanocomposite and its sensing properties toward methane gas detection. *J. Mater. Sci. Mater. Electron.* 27, 3723–3730. doi: 10.1007/s10854-015-4214-6

Zhang, D., Jiang, C., Liu, J., and Cao, Y. (2017a). Carbon monoxide gas sensing at room temperature using copper oxide-decorated graphene hybrid nanocomposite prepared by layer-by-layer self-assembly. *Sensors Actuat. B Chem.* 247, 875–882. doi: 10.1016/j.snb.2017.03.108

Zhang, D., Jiang, C., Yin, N., and Xia, B. (2017b). Sensing characteristics of acetylene gas in transformer oil of nano-modified graphene-based film sensor. *High Voltage Eng.* 11, 029. doi: 10.13336/j.1003-6520.hve.20171031029

Zhang, D., Liu, A., Chang, H., and Xia, B. (2015a). Room-temperature high-performance acetone gas sensor based on hydrothermal synthesized SnO 2-reduced graphene oxide hybrid composite. *RSC Adv.* 5, 3016–3022. doi: 10.1039/C4RA10942B

Zhang, D., Yin, N., Jiang, C., and Xia, B. (2017c). Characterization of CuO–reduced graphene oxide sandwiched nanostructure and its hydrogen sensing characteristics. *J. Mater. Sci. Mater. Electron.* 28, 2763–2768. doi: 10.1007/s10854-016-5856-8

Zhang, D., Yin, N., and Xia, B. (2015b). Facile fabrication of ZnO nanocrystalline-modified graphene hybrid nanocomposite toward methane gas sensing application. *J. Mater. Sci. Mater. Electron.* 26, 5937–5945. doi: 10.1007/s10854-015-3165-2

Zhang, Y., Zeng, W., Ye, H., and Li, Y. (2018). Enhanced carbon monoxide sensing properties of TiO2 with exposed (0 0 1) facet: a combined first-principle and experimental study. *Appl. Surf. Sci.* 442, 507–516. doi: 10.1016/j.apsusc.2018.02.036

Zhou, Q., Jin, L., Chen, W., Li, J., and Zeng, W. (2016). Detection of hydrogen at room temperature based on Au@ rGO composites chemical sensor. *Sensor Lett.* 14, 961–966. doi: 10.1166/sl.2016.3719

Zhou, Y., Lin, X., Wang, Y., Liu, G., Zhu, X., Huang, Y., et al. (2017). Study on gas sensing of reduced graphene oxide/ZnO thin film at room temperature. *Sensors Actuat B Chem.* 240, 870–880. doi: 10.1016/j.snb.2016.09.064

Zhu, L., and Zeng, W. (2017). A novel coral rock-like ZnO and its gas sensing. *Mater. Lett.* 209, 244–246. doi: 10.1016/j.matlet.2017.08.020

Conflict of Interest Statement: The authors declare that the research was conducted in the absence of any commercial or financial relationships that could be construed as a potential conflict of interest.

frontiers in Chemistry

MINI REVIEW
published: 29 August 2018
doi: 10.3389/fchem.2018.00364

Recent Advances of SnO_2-Based Sensors for Detecting Fault Characteristic Gases Extracted From Power Transformer Oil

Qingyan Zhang[1], *Qu Zhou*[1,2]*, *Zhaorui Lu*[1], *Zhijie Wei*[1], *Lingna Xu*[1] *and Yingang Gui*[1]

[1] College of Engineering and Technology, Southwest University, Chongqing, China, [2] Electrical and Computer Engineering Department, Wayne State University, Detroit, MI, United States

Tin oxide SnO_2-based gas sensors have been widely used for detecting typical fault characteristic gases extracted from power transformer oil, namely, H_2, CO, CO_2, CH_4, C_2H_2, C_2H_4, and C_2H_6, due to the remarkable advantages of high sensitivity, fast response, long-term stability, and so on. Herein, we present an overview of the recent significant improvement in fabrication and application of high performance SnO_2-based sensors for detecting these fault characteristic gases. Promising materials for the sensitive and selective detection of each kind of fault characteristic gas have been identified. Meanwhile, the corresponding sensing mechanisms of SnO_2-based gas sensors of these fault characteristic gases are comprehensively discussed. In the final section of this review, the major challenges and promising developments in this domain are also given.

Keywords: tin oxide, gas sensors, fault characteristic gases, power transformer oil, sensing properties, sensing mechanism

OPEN ACCESS

Edited by:
Zhongchang Wang,
Laboratório Ibérico Internacional de Nanotecnologia (INL), Portugal

Reviewed by:
Yiyi Zhang,
Guangxi University, China
Song Xiao,
Wuhan University, China

***Correspondence:**
Qu Zhou
zhouqu@swu.edu.cn

Specialty section:
This article was submitted to Nanoscience, a section of the journal Frontiers in Chemistry

Received: *22 June 2018*
Accepted: *30 July 2018*
Published: *29 August 2018*

Citation:
Zhang Q, Zhou Q, Lu Z, Wei Z, Xu L and Gui Y (2018) Recent Advances of SnO_2-Based Sensors for Detecting Fault Characteristic Gases Extracted From Power Transformer Oil. Front. Chem. 6:364. doi: 10.3389/fchem.2018.00364

INTRODUCTION

Power transformers are one of the most important apparatuses in power systems, and their reliability is extremely vital to ensure the stable system operation (Zheng et al., 2018). Thermal and electrical faults in oil-filled power transformers may produce typical fault characteristic gases including hydrogen H_2 (David et al., 2018), carbon monoxide CO (Joseph, 1980; Uddin et al., 2016; Zhou et al., 2018b), carbon dioxide CO_2 (2015; Dan et al., 2016; Iwata et al., 2017; Zhang et al., 2017), methane CH_4 (Sedghi et al., 2010), acetylene C_2H_2 (Qi et al., 2008), ethylene C_2H_4, and ethane C_2H_6. These typical fault characteristic gases could be dissolved in transformer oil or accumulate as free gases if produced rapidly in large quantities. Therefore, detection and analysis of the species, quantities and generation rates of these fault gases presented in the fluid allow for the identification of power transformer fault types such as corona, sparking, overheating, and arcing.

During the past few decades, dissolved gas analysis has been developed to detect the latent faults of oil-immersed power transformers (Morais and Rolim, 2006; Zhan et al., 2015; Uddin et al., 2016; Gong et al., 2018). Gas sensing detection technology is the core of dissolved gas analysis. Different types of sensing technologies have been reported in previous studies for detecting typical fault characteristic gases extracted from transformer oil, such as metal oxide semiconductor gas sensors (Zhu and Zeng, 2017a; Chen et al., 2018), catalytic combustion sensors (Liu et al., 2011),

fuel cell sensors (Modjtahedi et al., 2016; Tonezzer et al., 2017), and optical sensors (Trieu-Vuong et al., 2016; Paliwal et al., 2017). Given the remarkable advantages of simple fabrication process, low maintenance cost, fast response and recovery, long service life, and so on, metal oxide semiconductor materials like SnO_2 (Choi et al., 2014; Zeng et al., 2014), ZnO (Zhou et al., 2017; Zhu and Zeng, 2017b; Zhu et al., 2017), TiO_2 (Zeng and Liu, 2010; Zhang et al., 2018b) and In_2O_3 (Cao et al., 2015) have received scientific and technological importance for many years and are widely used to detect these gases. Among them, as the most widely used gas-sensitive material, SnO_2 is currently the main sensing materials used in experimental research and commercial application for detecting typical fault characteristic gases extracted from power transformer oil (Zhang et al., 2010; Zhou et al., 2018a).

Herein, the first section of this review will briefly outline the preparation of the currently used SnO_2 sensing materials, the microstructure morphology, and doping modification of SnO_2 sensing materials for detecting typical fault characteristic gases extracted from power transformer oil. The second section addresses the main gas sensing mechanisms of SnO_2 gas sensors for these gases. The third section presents the conclusions, focusing on future challenges and potentialities associated with SnO_2-based gas sensors for detecting these typical fault characteristic gases.

SENSING PERFORMANCES OF SNO_2-BASED SENSORS TO FAULT CHARACTERISTIC GASES EXTRACTED FROM POWER TRANSFORMER OIL

For detecting and analyzing typical fault characteristic gases extracted from power transformer oil with SnO_2-based gas sensors, the most important concerns are the sensor sensitivity, selectivity, and repeatability (Fan et al., 2017). Combined with the research concerns mentioned above, this section briefly summarizes recent progress in the application of SnO_2 sensing materials to detect typical fault characteristic gases dissolved in transformer oil. The gas sensing performance of some modified SnO_2 gas sensors are listed in **Table 1**.

T_{oper}, temperature at which the best sensor performance, usually in terms of the highest response toward target gas, could be obtained.

S, gas sensing response of a SnO_2-based sensor to target gas, which is defined as S =Ra/Rg for reducing gas and S = Rg/Ra for oxidizing gas (where Ra and Rg are the resistance of the sensor in air and in the test gas, respectively).

It is known that the metal oxide semiconductor SnO_2 is a promising material for sensing the typical fault characteristic gases extracted from power transformer oil. Nevertheless, the sensing performance of the proposed sensors considerably depends on the preparation method and surface structure of the sensing materials and the dopants. The structure of modern SnO_2 gas sensors could be classified into two main types including thick/thin films and nanoparticles. The preparation methods of the sensing materials mainly include the hydrothermal method, the sol-gel method, the electrospinning technique, chemical vapor deposition and so on. Different preparation methods could affect the morphology of the sensing materials and further change their gas sensing properties (Long et al., 2018; Zhang et al., 2018a; Zhou et al., 2018c). Noble metals or metal oxide doped on SnO_2-based sensors can play an important role in accelerating the sensing process and improving the gas sensor performances.

In power transformers, H_2 is generated from the thermal decomposition of oil at high temperatures, which is a serious problem for transformer oil (Uddin et al., 2016). Various high-efficacy and workable SnO_2-based sensors have been recently introduced for detecting H_2. It can be seen from the data in **Table 1** that various metal particles such as Co (Liu et al., 2010), Au (Yin and Tao, 2017), and Pd (Nguyen et al., 2017) have been added to SnO_2-based sensors to enhance H_2 gas sensing performance. Among them, the Au-loaded SnO_2 sensor can detect H_2 down to 1 ppm, which is a good property for detecting low concentrations of H_2 dissolved in transformer oil (Yin and Tao, 2017). K. Inyawilert reported that a SnO_2 sensing film with an optimal Rh-doping level of 0.2 wt% exhibited an ultra-high response of 22,170 and a short response time of 6 s toward 30,000 ppm H_2 at an optimum operating temperature of 300°C. In addition, the proposed Rh-doped SnO_2 sensor displayed good H_2 selectivity against NO_2, SO_2, C_2H_4, C_3H_6O, CH_4, H_2S, and CO (Inyawilert et al., 2017). Except for nanoparticles embedded in the metal oxide matrix, the morphology of the SnO_2 materials could be applied to improve the H_2 sensing properties, and low dimensional nanostructures have attracted increasing attention. Nguyen Kien et al. introduced the on-chip growth of SnO_2 nanowire-based gas sensors to detect low concentrations of H_2 gas, which responded with 2.6 for 20 ppm H_2 gas at 400°C (Nguyen et al., 2017). Taken together, these findings suggest that the Au-loaded SnO_2 gas sensor is the most promising candidate for detecting low concentration H_2 extracted from power transformer oil.

The insulating paper, pressboard and wood blocks in power transformers contain a large number of anhydroglucose rings as well as weak C-O molecular bonds and glycosidic bonds that are thermally less stable than the hydrocarbon bonds in oil. These bonds could decompose to CO and CO_2 at lower temperatures when potential faults occur. As shown in **Table 1**, Pt-doped SnO_2 thick film (Chen et al., 2018), ZnO-SnO_2 nanoparticles (Chen et al., 2015), and Au-doped SnO_2 yolk-shell nanospheres (Wang et al., 2013) could be potential candidates for CO sensors. Among them, Wang et al. compared the gas sensing properties of Au@SnO_2 yolk-shell nanospheres with that of hollow SnO_2 nanospheres. The sensor fabricated with the Au@SnO_2 yolk-shell nanospheres showed lower operating temperature (210°C), lower detection limit (5 ppm), faster response (0.3 s), and better selectivity to CO gas (Wang et al., 2013), which could be attributed to the catalytic effect of Au and enhanced electron depletion at the surface of the Au@SnO_2 yolk–shell nanospheres. Moreover, SnO_2 loaded with Pd nanoparticles may be another kind of promising material for CO gas sensing (Zhou et al., 2018d). Yuasa et al. prepared PdO-loaded SnO_2 nanoparticles by the reverse micelle method and reported that the 0.1 mol% PdO-loaded SnO_2 sensor exhibited a high gas response value of 320

TABLE 1 | Comparison of the representative SnO_2 based sensors for fault characteristic gases extracted from power transformer oil.

Target gas	Sensing material	Synthesis method	Morphology	Detection range (ppm)	$T_{oper.}$ (°C)	S/ppm	Selectivity	References
H_2	1 wt% Co-doped SnO_2	Electrospinning	Nanofibers	100–25,000	330	24/100	H_2 > CO	Liu et al., 2010
	1 mol% Au-doped SnO_2	Sol-gel	Nanoparticles	1–5,000	400	48/5,000	H_2 >CO	Yin and Tao, 2017
	Pd-decorated SnO_2	Chemical vapor deposition	Nanowires	10–100	350	7.1/100	H_2 >CO_2	Nguyen et al., 2017
CO	1.5% Pd-doped SnO_2	Co-precipitation	Thick-film	100–1,000	260	6.59/400	–	Chen et al., 2018
	ZnO–SnO_2 nanoparticles	Typical hydrothermal	Nanoparticles	40–160	300	13/100	–	Chen et al., 2015
	Au@SnO_2	Hydrothermal deposition	Yolk–shell nanospheres	5–100	210	30/50	CO>H_2 >C_2H_4 > CO_2	Wang et al., 2013
CO_2	$LaFeO_3$/SnO_2	Sol-gel	Thick film	–	250	2.72/4,000	–	Zhang et al., 2017
	LaOCl-doped SnO_2	One-step electrospinning	Nanofibers	100–20,000	300	3.7/1,000	–	Xiong et al., 2017
CH_4	20 mol% Pt-SnO_2	Electrospinning	Nanofibers	1–1,000	350	1.11/1	–	Lu et al., 2018
	Pt-SnO_2	Wet chemical	Thin film	1000–10,000	400	1.55/1,000	–	Min and Choi, 2005
C_2H_2	Sm_2O_3-doped SnO_2	Sol–gel	Nanoparticles	1–5,000	180	63.8/1,000	C_2H_2 >CO>CH_4 >H_2	Qi et al., 2008
	rGO-Loaded SnO_2	Hydrothermal	Nanoparticles	0.5–500	180	12.4/50	C_2H_2 >CH_4 >H_2 > CO>CO_2	Jin et al., 2017
C_2H_4	silicalite-1 layer coated on SnO_2	Ultrasonic spray pyrolysis technique	Thin film	2–70	350	2.21/8	–	Jadsadapattarakul et al., 2010
	SnO_2	R.F. magnetron sputtering	Thin film	10–100	300	10.43/100	–	Ahn et al., 2010
C_2H_6	5 wt% Pd-doped SnO_2	Hydrothermal	Nanoparticles	5–100	400	5.89/100	–	Chen et al., 2013a

to 200 ppm CO gas (Yuasa et al., 2009). Chen et al. synthesized Pd-doped SnO_2 nanoparticles using a co-precipitation method, and the 1.5 wt% PdO decorated SnO_2 presented the largest gas-sensitive response of 6.59 at 260°C in 400 ppm CO atmosphere (Chen et al., 2018). Another study reported that Pd-modified nanocrystalline SnO_2 displayed a fairly high and reversible CO response (2–100 ppm) at room temperature (Marikutsa et al., 2010). Yin et al. prepared Pd-loaded and Fe-doped SnO_2 by the sol-gel method. The composite with 10 mol% Fe and 0.2 mol% Pd had the highest sensitivity and selectivity to CO in the range of 200–3,000 ppm at 350°C, and the response value to 2,000 ppm CO was increased 13 times compared with pure SnO_2 (Yin and Guo, 2014). Therefore, Pd is a highly effective catalyst for improving the sensing performance of SnO_2-based sensors to CO gas (Xiong et al., 2017).

Due to their high chemical stability, conventional binary metal oxides have very low sensitivity to chemically inert gases such as CO_2 (Korotcenkov and Cho, 2017). However, it was reported that La-doped SnO_2 nanocomposites can be used for CO_2 sensing (Kim et al., 2000). And the 8% LaOCl-SnO_2 nanofibers exhibited an optimal response of 3.7 toward 1,000 ppm CO_2 at 300°C with response/recovery times of 24/92 s (Xiong et al., 2017). Karthik et al. reported the sensing properties of tin oxide (SnO_2) and zinc oxide (ZnO) thin films deposited onto macroporous silicon (PS) substrates to CO_2 and found that the obtained SnO_2/PS films showed the highest sensing response of 19 to 15 ppm CO_2 gas (Karthik et al., 2018).

For hydrocarbons, namely, CH_4, C_2H_2, C_2H_4, and C_2H_6, when high energy discharge occurs, such as arcing, in transformer oil, the content of C_2H_2 is relatively high. At low temperature thermal faults (T < 300°C), the contents of CH_4 and C_2H_6 tend to be high. C_2H_4 is the main content of hydrocarbon while at high temperature thermal faults (T > 300°C) (Fan et al., 2017). For detecting these hydrocarbons, an online monitoring system based on a SnO_2-based gas chromatographic detector for assessing the running condition of a power transformer was developed (Fan et al., 2017). Qi et al. fabricated a C_2H_2 sensor based on 6 wt% Sm_2O_3-doped SnO_2, whose gas response to 1,000 ppm C_2H_2 could reach 63.8, 16.8 times larger than that of pure SnO_2 (Qi et al., 2008).

Moreover, Jin et al. reported that reduced graphene oxide (rGO)-loaded SnO_2 hybrid nanocomposite showed high sensor response (12.4 toward 50 ppm), fast response-recovery time (54 and 23 s), low detection limit (1.3 ppm), good linearity, excellent selectivity and long-term stability to C_2H_2 (Jin et al., 2017). These results indicated that rGO would be an effective addition to enhance the sensing properties of SnO_2-based sensors to C_2H_2 and make a contribution to developing a ppm-level gas sensor for on-line monitoring of C_2H_2 gas extracted from transformer oil.

Sensors for CH_4 detection have also been widely studied and are partly summarized in **Table 1**. The 20 mol% Pt-SnO_2 nanofibers exhibited excellent CH_4 sensing properties over a temperature range of 100–350°C, and an obvious response of 1.11 to 1 ppm CH_4 was measured at 350°C (Lu et al., 2018). Koeck et al. found a device prepared by ultra-long single crystalline SnO_2-nanowires, which was able to detect a few ppm of CO and CH_4 at the operating temperature of 200–250°C (Koeck et al., 2009). Chen et al. successfully synthesized Co-doped SnO_2 nanofibers via an electrospinning method and reported that the Co-doped SnO_2 nanofiber sensor exhibited a high response of 30.28 toward 50 ppm CH_4 at 300°C (Chen et al., 2013b). For C_2H_4 and C_2H_6 detection, only a few sensors including SnO_2 thin films and Pd-doped SnO_2 nanoparticles are found to be effective. Jadsadapattarakul et al. reported that the sensing response, response and recovery time of SnO_2 thin film sensors for selective detecting of C_2H_4 gas could be improved by coating a layer of [010] highly preferred-orientation silicalite-1 polycrystals (Jadsadapattarakul et al., 2010). Ahn et al. obtained SnO_2 thin films by R.F. magnetron sputtering to fabricate high performance C_2H_4 gas sensors (Ahn et al., 2010). Chen et al. discovered that the 5 wt% Pd-doped SnO_2 sensor could detect C_2H_6 at 400°C, and the sensor exhibited the largest gas-sensitive response of 5.89 toward 100 ppm C_2H_6 (Chen et al., 2013a).

SENSING MECHANISMS OF SNO_2-BASED SENSORS TO FAULT CHARACTERISTIC GASES EXTRACTED FROM POWER TRANSFORMER OIL

It is well agreed that the sensing mechanism of SnO_2 gas sensors is the change in conductivity of the metal oxide layer caused by the interaction with the surrounding atmosphere (Ducéré et al., 2012; Zeng et al., 2013; Korotcenkov and Cho, 2017). When exposed to air, oxygen molecules would be adsorbed on the surface of the SnO_2 nanostructures and capture electrons from the conduction band of SnO_2 to generate chemisorbed oxygen species (O^-, O^{2-}, and O_2^-, depending on temperatures) (Shahabuddin et al., 2017). At low temperatures (below 150°C), oxygen molecules exist in the form of molecular ions O_2^-, which would change to atomic ions O^- (150–400°C) and O^{2-} (more than 400°C) as temperatures rising (Punginsang et al., 2017). The chemical adsorption process can be explained by the following reactions:

$$O_{2(\text{gas})} \Leftrightarrow O_{2(\text{abs})} \tag{1}$$

$$O_{2(\text{abs})}+e^- \Leftrightarrow {O_2}^-{}_{(\text{abs})} \tag{2}$$

$${O_2}^-{}_{(\text{abs})} + e^- \Leftrightarrow 2{O}^-{}_{(\text{abs})} \tag{3}$$

$${O}^-{}_{(\text{abs})} + e^- \Leftrightarrow {O}^{2-}{}_{(\text{abs})} \tag{4}$$

As the electrons transfer from the conduction band of SnO_2 to the chemisorbed oxygen, the electron concentration and electrical conductivity of the SnO_2 film decrease. When the SnO_2 film is exposed to typical fault characteristic gases, the reducing gas would react with the chemisorbed oxygen species, thereby releasing electrons back to the conduction band with increasing electrical conductivity. The sensing mechanisms of the SnO_2 sensor sensing these fault gases can be explained from the following reaction paths, where O^- is taken as an example (Samerjai et al., 2012).

$$H_2+{O}^-{}_{(\text{ads})} \rightarrow H_2O+e^- \tag{5}$$

$$CO+{O}^-{}_{(\text{ads})} \rightarrow CO_2+e^- \tag{6}$$

$$C_2H_2+{O}^-{}_{(\text{ads})} \rightarrow 2C+H_2O+e^-+\text{heat} \tag{7}$$

$$CH_4+2{O}^-{}_{(\text{ads})} \rightarrow 2H_2O + CO_2+2e^- \tag{8}$$

$$C_2H_4+2{O}^-{}_{(\text{ads})} \rightarrow 2H_2O + 2C + 2e^- \tag{9}$$

$$C_2H_6+3{O}^-{}_{(\text{ads})} \rightarrow 3H_2O + 2C + 3e^- \tag{10}$$

Dopants added to SnO_2-based gas sensors can accelerate the reaction process mentioned above and improve the sensing performance of gas sensors. The doped catalysts can enhance the sensing performance of a sensor in two ways, namely, chemical sensitization and electronic sensitization (Lin et al., 2017). The high surface area structures such as porous structures and hollow structures could accelerate gas diffusion on the material surface and then shorten the response time.

On the other hand, to understand the sensing mechanism of SnO_2-based materials at the atomic and quantum levels, based on the framework of Density Function Theory (DFT), Li et al. established a SnO_2 surface model, gas molecular models and adsorption models. A first principles calculation using the Cambridge Sequential Total Energy Package (CASTEP) program was performed, and the total energies, electronic structures and adsorption properties were investigated in detail. Theoretical calculations provided a qualitative explanation of the sensing properties of the fabricated SnO_2-based sensor to various fault characteristic gases (CH_4, C_2H_6, C_2H_4, and C_2H_2) extracted from power transformers (Li et al., 2017). Zeng et al. performed a first principles calculation to investigate how H_2 gas interacts with the SnO_2 (110) surface and the effect of metallic ions on the gas response of SnO_2. Based on the theoretical calculation, it was reported that the Pd-doped SnO_2 (110) surface could adsorb more H_2 gas and receive larger electrons from adsorbed H_2 molecules (Zeng et al., 2011). Other research involving a

possible CO sensing mechanism for Pd-doped SnO_2 sensors was investigated with first principles calculations (Chen et al., 2018), and the theoretical results demonstrated that CO molecules can grab O from the pre-adsorbed oxygen on the Pd^4 cluster or the PdO cluster on the SnO_2 (110) surface. These processes may play an important role in CO sensing for Pd-doped SnO_2 (Chen et al., 2018). In particular, theoretical calculations indicated that CO_2 molecules cannot be adsorbed onto the stoichiometric SnO_2 (110) surface or SnO_2 (110) surface pre-adsorbed by O_2^- and O^- in dry air. However in wet air, CO_2 could react with O of pre-adsorbed OH^-, bringing about the formation of carbonates containing $(CO_3)^{2-}$ and the dissociation/movement of surface OH^- groups, accompanying the release of electrons from CO_2 to the SnO_2 surface (Wang et al., 2016).

CONCLUSION AND PERSPECTIVE

In this mini-review, SnO_2-based gas sensors for detecting typical fault characteristic gases extracted from power transformer oil have been briefly summarized. The analysis shows that the detection performances of SnO_2-based gas sensors can be obviously enhanced with dopant addition or increasing the surface area of the sensing materials. Despite achieving good results, there is still much room for further development. First of all, due to the cross-sensitivity between these fault characteristic gases, selectivity is a large challenge for developing high performance SnO_2-based sensors to detect these gases independently. In the future, to promote engineering applications, a combination of SnO_2-based gas sensors and gas chromatography should be further studied for multi-component detection of these gases. For further development of the gas-sensing performances, the high surface area structures such as hollow and hierarchical nanostructures could be prepared to obtain more active sites for gas diffusion, and different types of dopant elements should be examined. Furthermore, the gas sensing mechanisms are still imperfect and controversial, which cannot effectively guide development of novel SnO_2-based sensors and limit the prevailing application of these sensors to fault characteristic gases extracted from power transformer oil. Further research should focus on determining a satisfying mechanism model of SnO_2-based sensors to provide a guide for future work.

AUTHOR CONTRIBUTIONS

All authors listed have made substantial, direct and intellectual contributions to the work and approved it for publication.

ACKNOWLEDGMENTS

This work has been supported in part by the National Natural Science Foundation of China (Nos. 51507144, 5127785), the China Postdoctoral Science Foundation Project (Nos. 2015M580771, 2016T90832), and the Chongqing Science and Technology Commission (CSTC) (No. cstc2016jcyjA0400).

REFERENCES

Ahn, H., Noh, J. H., Kim, S.-B., Overfelt, R. A., Yoon, Y. S., and Kim, D.-J. (2010). Effect of annealing and argon-to-oxygen ratio on sputtered SnO_2 thin film sensor for ethylene gas detection. *Mater. Chem. Phys.* 124, 563–568. doi: 10.1016/j.matchemphys.2010.07.012

Cao, Y., Zhao, J., Zou, X., Jin, P.-P., Chen, H., Gao, R., et al. (2015). Synthesis of porous In_2O_3 microspheres as a sensitive material for early warning of hydrocarbon explosions. *RSC Adv.* 5, 5424–5431. doi: 10.1039/C4RA13763A

Chen, W., Li, Q., Xu, L., and Zeng, W. (2015). Gas sensing properties of ZnO-SnO_2 nanostructures. *J. Nanosci. Nanotechnol.* 15, 1245–1252. doi: 10.1166/jnn.2015.9061

Chen, W., Zhou, Q., Gao, T., Su, X., and Wan, F. (2013a). Pd-doped SnO_2-based sensor detecting characteristic fault hydrocarbon gases in transformer oil. *J. Nanomater.* 2013:127345. doi: 10.1155/2013/127345

Chen, W., Zhou, Q., Xu, L., Wan, F., Peng, S., and Zeng, W. (2013b). Improved methane sensing properties of Co-doped SnO_2 electrospun nanofibers. *J. Nanomater.* 2013:173232. doi: 10.1155/2013/173232

Chen, Y., Qin, H., and Hu, J. (2018). CO sensing properties and mechanism of Pd doped SnO_2 thick-films. *Appl. Surf. Sci.* 428, 207–217. doi: 10.1016/j.apsusc.2017.08.205

Choi, S. W., Katoch, A., Kim, J. H., and Kim, S. S. (2014). Prominent reducing gas-sensing performances of n-SnO_2 nanowires by local creation of p-n heterojunctions by functionalization with p-Cr_2O_3 nanoparticles. *ACS Appl. Mater. Inter.* 6, 17723–17729. doi: 10.1021/am504164j

Dan, D. W., Yan, P. C., Zhong, X. L., Ling, L., Chang, M. S., Hong, W. Q., et al. (2016). CO_2-sensing properties and mechanism of nano-SnO_2 thick-film sensor. *Sens. Actuat. B* 227, 73–84. doi: 10.1016/j.snb.2015.12.025.

David, E. M., Gugu, H. M., Peter, R. M., Baban, P. D., Franscious, R. C., Hendrik, C. S., et al. (2018). Ultra-high sensitive and selective H_2 gas sensor manifested by interface of n-n heterostructure of CeO_2-SnO_2 nanoparticles. *Sens. Actuat. B* 254, 984–995. doi: 10.1016/j.snb.2017.07.093

Ducéré, J.-M., Hemeryck, A., Esteve, A., Rouhani, M. D., Landa, G., Menini, P., et al. (2012). A computational chemist approach to gas sensors: modeling the response of SnO_2 to CO, O_2, and H_2O Gases. *J. Comput. Chem.* 33, 247–258. doi: 10.1002/jcc.21959

Fan, J., Wang, F., Sun, Q., Bin, F., Ye, H., and Liu, Y. (2017). An online monitoring system for oil immersed power transformer based on SnO_2 GC detector with a new quantification approach. *IEEE Sens. J.* 17, 6662–6671. doi: 10.1109/JSEN.2017.2734072

Gong, Z., Chen, K., Yang, Y., Zhou, X., and Yu, Q. (2018). Photoacoustic spectroscopy based multi-gas detection using high-sensitivity fiber-optic low-frequency acoustic sensor. *Sens. Actuat. B* 260, 357–363. doi: 10.1016/j.snb.2018.01.005

Inyawilert, K., Wisitsoraat, A., Tuantranont, A., Phanichphant, S., and Liewhiran, C. (2017). Ultra-sensitive and highly selective H_2 sensors based on FSP-made Rh-substituted SnO_2 sensing films. *Sens. Actuat. B* 240, 1141–1152. doi: 10.1016/j.snb.2016.09.094

Iwata, T., Matsuda, K., Takahashi, K., and Sawada, K. (2017). CO_2 sensing characteristics of a La_2O_3/SnO_2 stacked structure with micromachined hotplates. *Sensors* 17:2156. doi: 10.3390/s17092156

Jadsadapattarakul, D., Thanachayanont, C., Nukeaw, J., and Sooknoi, T. (2010). Improved selectivity, response time and recovery time by 010 highly preferred-orientation silicalite-1 layer coated on SnO_2 thin film sensor for selective ethylene gas detection. *Sens. Actuat. B* 144, 73–80. doi: 10.1016/j.snb.2009.10.035

Jin, L., Chen, W., Zhang, H., Xiao, G., Yu, C., and Zhou, Q. (2017). Characterization of reduced graphene oxide (rGO)-loaded SnO_2 nanocomposite and applications in C_2H_2 gas detection. *Appl. Sci.* 7:19. doi: 10.3390/app7010019

Joseph, J. K. (1980). Transformer fault diagnosis by dissolved-gas analysis. *IEEE Trans. Ind. Appl.* IA−16, 777–782. doi: 10.1109/TIA.1980.4503871

Karthik, T. V. K., Martinez, L., and Agarwal, V. (2018). Porous silicon ZnO/SnO_2 structures for CO_2 detection. *J. Alloy Compd.* 731, 853–863. doi: 10.1016/j.jallcom.2017.10.070

Kim, D. H., Yoon, J. Y., Park, H. C., and Kim, K. H. (2000). CO_2-sensing characteristics of SnO_2 thick film by coating lanthanum oxide. *Sens. Actuat. B* 62, 61–66. doi: 10.1016/S0925-4005(99)00305-6

Koeck, A., Tischner, A., Maier, T., Kast, M., Edtmaier, C., Gspan, C., et al. (2009). Atmospheric pressure fabrication of SnO_2-nanowires for highly sensitive CO and CH_4 detection. *Sens. Actuat. B* 138, 160–167. doi: 10.1016/j.snb.2009.02.055

Korotcenkov, G., and Cho, B. K. (2017). Metal oxide composites in conductometric gas sensors: achievements and challenges. *Sens. Actuat. B* 244, 182–210. doi: 10.1016/j.snb.2016.12.117

Li, Z., Jin, L., Liu, B., Shen, Z., Peng, S., and Zhou, Q. (2017). Experiment and simulation study of nano-SnO_2 for dissolved fault gases analysis of power transformer. *Sci. Adv. Mater.* 9, 1888–1894. doi: 10.1166/sam.2017.3243

Lin, T., Lv, X., Li, S., and Wang, Q. (2017). The morphologies of the semiconductor oxides and their gas-sensing properties. *Sensors* 17:2779. doi: 10.3390/s17122779

Liu, F., Zhang, Y., Yu, Y., Xu, J., Sun, J., and Lu, G. (2011). Enhanced sensing performance of catalytic combustion methane sensor by using Pd nanorod/gamma-Al_2O_3. *Sens. Actuat. B* 160, 1091–1097. doi: 10.1016/j.snb.2011.09.032

Liu, L., Guo, C., Li, S., Wang, L., Dong, Q., and Li, W. (2010). Improved H_2 sensing properties of Co-doped SnO_2 nanofibers. *Sens. Actuat. B* 150, 806–810. doi: 10.1016/j.snb.2010.07.022

Long, H. W., Zeng, W., Wang, H., Qian, M. M., Liang, Y. H., and Wang, Z. C. (2018). Self-assembled biomolecular 1D nanostructures for aqueous sodium-ion battery. *Adv. Sci.* 5:1700634. doi: 10.1002/advs.201700634

Lu, W., Ding, D., Xue, Q., Du, Y., Xiong, Y., Zhang, J., et al. (2018). Great enhancement of CH_4 sensitivity of SnO_2 based nanofibers by heterogeneous sensitization and catalytic effect. *Sens. Actuat. B* 254, 393–401. doi: 10.1016/j.snb.2017.07.128

Marikutsa, A. V., Rumyantseva, M. N., Yashina, L. V., and Gaskov, A. M. (2010). Role of surface hydroxyl groups in promoting room temperature CO sensing by Pd-modified nanocrystalline SnO_2. *J. Solid State Chem.* 183, 2389–2399. doi: 10.1016/j.jssc.2010.07.017

Min, B.-K., and Choi, S.-D. (2005). Undoped and 0.1wt.% Ca-doped Pt-catalyzed SnO_2 sensors for CH_4 detection. *Sens. Actuat. B* 108, 119–124. doi: 10.1016/j.snb.2004.12.112

Modjtahedi, A., Amirfazli, A., and Farhad, S. (2016). Low catalyst loaded ethanol gas fuel cell sensor. *Sens. Actuat. B* 234, 70–79. doi: 10.1016/j.snb.2016.04.108

Morais, D. R., and Rolim, J. G. (2006). A hybrid tool for detection of incipient faults in transformers based on the dissolved gas analysis of insulating oil. *IEEE Trans. Power. Deliv.* 21, 673–680. doi: 10.1109/TPWRD.2005.864044

Nguyen, K., Hung, C. M., Ngoc, T. M., Thanh Le, D. T., Nguyen, D. H., Nguyen Van, D., et al. (2017). Low-temperature prototype hydrogen sensors using Pd-decorated SnO_2 nanowires for exhaled breath applications. *Sens. Actuat. B* 253, 156–163. doi: 10.1016/j.snb.2017.06.141

Paliwal, A., Sharma, A., Tomar, M., and Gupta, V. (2017). Carbon monoxide (CO) optical gas sensor based on ZnO thin films. *Sens. Actuat. B* 250, 679–685. doi: 10.1016/j.snb.2017.05.064

Punginsang, M., Wisitsoraat, A., Sriprachuabwong, C., Phokharatkul, D., Tuantranont, A., Phanichphant, S., et al. (2017). Roles of cobalt doping on ethanol-sensing mechanisms of flame-spray-made SnO_2 nanoparticles–electrolytically exfoliated graphene interfaces. *Appl. Surf. Sci.* 425, 351–366. doi: 10.1016/j.apsusc.2017.06.265

Qi, Q., Tong, Z., Xue, J. Z., Hui, T. F., Li, L., Rui, W., et al. (2008). Electrical response of Sm_2O_3-doped SnO_2 to C_2H_2 and effect of humidity interference. *Sens. Actuat. B* 134, 36–42. doi: 10.1016/j.snb.2008.04.011

Samerjai, T., Tamaekong, N., Wetchakun, K., Kruefu, V., Liewhiran, C., Siriwong, C., et al. (2012). Flame-spray-made metal-loaded semiconducting metal oxides thick films for flammable gas sensing. *Sens. Actuat. B* 171, 43–61. doi: 10.1016/j.snb.2012.05.052

Sedghi, S. M., Mortazavi, Y., and Khodadadi, A. (2010). Low temperature CO and CH_4 dual selective gas sensor using SnO_2 quantum dots prepared by sonochemical method. *Sens. Actuat. B* 145, 7–12. doi: 10.1016/j.snb.2009.11.002

Shahabuddin, M., Umar, A., Tomar, M., and Gupta, V. (2017). Custom designed metal anchored SnO_2 sensor for H_2 detection. *Int. J. Hydrogen Energ.* 42, 4597–4609. doi: 10.1016/j.ijhydene.2016.12.054

Tonezzer, M., Thi Thanh Le, D., Quang Huy, T., Van Hieu, N., and Iannotta, S. (2017). Selective hydrogen sensor for liquefied petroleum gas steam reforming fuel cell systems. *Int. J. Hydrogen Energ.* 42, 740–748. doi: 10.1016/j.ijhydene.2016.11.102

Trieu-Vuong, D., Choi, I.-Y., Son, Y.-S., and Kim, J.-C. (2016). A review on non-dispersive infrared gas sensors: improvement of sensor detection limit and interference correction. *Sens. Actuat. B* 231, 529–538. doi: 10.1016/j.snb.2016.03.040

Uddin, A. S. M. I., Yaqoob, U., and Chung, G.-S. (2016). Dissolved hydrogen gas analysis in transformer oil using Pd catalyst decorated on ZnO nanorod array. *Sens. Actuat. B* 226, 90–95. doi: 10.1016/j.snb.2015.11.110

Wang, D., Chen, Y., Liu, Z., Li, L., Shi, C., Qin, H., et al. (2016). CO_2-sensing properties and mechanism of nano-SnO_2 thick-film sensor. *Sens. Actuat. B* 227, 73–84. doi: 10.1016/j.snb.2015.12.025

Wang, L., Dou, H., Lou, Z., and Zhang, T. (2013). Encapsuled nanoreactors (Au@SnO_2): a new sensing material for chemical sensors. *Nanoscale* 5, 2686–2691. doi: 10.1039/c2nr33088a

Xiong, Y., Xue, Q., Ling, C., Lu, W., Ding, D., Zhu, L., et al. (2017). Effective CO_2 detection based on LaOCl-doped SnO_2 nanofibers: insight into the role of oxygen in carrier gas. *Sens. Actuat. B.* 241, 725–734. doi: 10.1016/j.snb.2016.10.143

Yin, X.-T., and Guo, X.-M. (2014). Selectivity and sensitivity of Pd-loaded and Fe-doped SnO_2 sensor for CO detection. *Sens. Actuat. B* 200, 213–218. doi: 10.1016/j.snb.2014.04.026

Yin, X.-T., and Tao, L. (2017). Fabrication and gas sensing properties of Au-loaded SnO_2 composite nanoparticles for low concentration hydrogen. *J. Alloy Compd.* 727, 254–259. doi: 10.1016/j.jallcom.2017.08.122

Yuasa, M., Masaki, T., Kida, T., Shimanoe, K., and Yamazoe, N. (2009). Nano-sized PdO loaded SnO_2 nanoparticles by reverse micelle method for highly sensitive CO gas sensor. *Sens. Actuat. B* 136, 99–104. doi: 10.1016/j.snb.2008.11.022

Zeng, W., He, Q., Pan, K., and Wang, Y. (2013). Synthesis of multifarious hierarchical flower-like SnO_2 and their gas-sensing properties. *Phys. E* 54, 313–318. doi: 10.1016/j.physe.2013.07.014

Zeng, W., Li, Y., Miao, B., Lin, L., and Wang, Z. (2014). Recognition of carbon monoxide with SnO_2/Ti thick-film sensor and its gas-sensing mechanism. *Sens. Actuat. B* 191, 1–8. doi: 10.1016/j.snb.2013.09.092

Zeng, W., Liu, T., Liu, D., and Han, E. (2011). Hydrogen sensing and mechanism of M-doped SnO_2 (M=Cr^{3+}, Cu^{2+} and Pd^{2+}) nanocomposite. *Sens. Actuat. B* 160, 455–462. doi: 10.1016/j.snb.2011.08.008

Zeng, W., and Liu, T. M. (2010). Hydrogen sensing characteristics and mechanism of nanosize TiO_2 dope with metallic ions. *Phys. B* 405, 564–568. doi: 10.1016/j.physb.2009.09.066

Zhan, W., Goulart, A. E., Falahi, M., and Rondla, P. (2015). Development of a low-cost self-diagnostic module for oil-immerse forced-air cooling transformers. *IEEE Trans. Power.Deliv.* 30, 129–137. doi: 10.1109/TPWRD.2014.2341454

Zhang, H., Li, Z., Liu, L., Xu, X., Wang, Z., and Wang, W. (2010). Enhancement of hydrogen monitoring properties based on Pd–SnO_2 composite nanofibers. *Sens. Actuat. B* 147, 111–115. doi: 10.1016/j.snb.2010.01.056

Zhang, W., Xie, C., Zhang, G., Zhang, J., Zhang, S., and Zeng, D. (2017). Porous $LaFeO_3$/SnO_2 nanocomposite film for CO_2 detection with high sensitivity. *Mater. Chem. Phys.* 186, 228–236. doi: 10.1016/j.matchemphys.2016.10.048

Zhang, Y. X., Zeng, W., and Li, Y. Q. (2018a). The hydrothermal synthesis of 3D hierarchical porous MoS_2 microspheres assembled by nanosheets with excellent gas sensing properties. *J. Alloy Compd.* 749, 355–362. doi: 10.1016/j.jallcom.2018.03.307

Zhang, Y. X., Zeng, W., Ye, H., and Li, Y. Q. (2018b). Enhanced carbon monoxide sensing properties of TiO_2 with exposed (001) facet: a combined first-principle and experimental study. *Appl. Surf. Sci.* 442, 507–516. doi: 10.1016/j.apsusc.2018.02.036

Zheng, H., Zhang, Y., Liu, J., Wei, H., Zhao, J., and Liao, R. (2018). A novel model based on wavelet LS-SVM integrated improved PSO algorithm for forecasting

of dissolved gas contents in power transformers. *Electr. Power Syst. Res.* 155, 196–205. doi: 10.1016/j.epsr.2017.10.010

Zhou, Q., Chen, W., Xu, L., Kumar, R., Gui, Y., Zhao, Z., et al. (2018a). Highly sensitive carbon monoxide (CO) gas sensors based on Ni and Zn doped SnO_2 nanomaterials. *Ceram. Int.* 44, 4392–4399. doi: 10.1016/j.ceramint.2017.12.038

Zhou, Q., Hong, C. X., Yao, Y., Ibrahim, A. M., Xu, L. N., Kumar, R., et al. (2017). Fabrication and characterization of highly sensitive acetone chemical sensor based on ZnO nanoballs. *Materials* 10:E799. doi: 10.3390/ma10070799

Zhou, Q., Lu, Z., Wei, Z., Xu, L., Gui, Y., and Chen, W. (2018b). Hydrothermal synthesis of hierarchical ultrathin NiO nanoflakes for high-performance CH_4 sensing. *Front. Chem.* 6:194. doi: 10.3389/fchem.2018.00194

Zhou, Q., Umar, A., Sodki, E. M., Amine, A., Xu, L., Gui, Y., et al. (2018c). Fabrication and characterization of highly sensitive and selective sensors based on porous NiO nanodisks. *Sens. Actuat. B* 259, 604–615. doi: 10.1016/j.snb.2017.12.050

Zhou, Q., Xu, L. N., Umar, A., Chen, W. G., and Kumar, R. (2018d). Pt nanoparticles decorated SnO_2 nanoneedles for efficient CO gas sensing applications. *Sens. Actuat. B* 256, 656–664. doi: 10.1016/j.snb.2017.09.206

Zhu, L., Li, Y., and Zeng, W. (2017). Enhanced ethanol sensing and mechanism of Cr-doped ZnO nanorods: experimental and computational study. *Ceram. Int.* 43, 14873–14879. doi: 10.1016/j.ceramint.2017.08.003

Zhu, L., and Zeng, W. (2017a). A novel coral rock-like ZnO and its gas sensing. *Mater. Lett.* 209, 244–246. doi: 10.1016/j.matlet.2017.08.020

Zhu, L., and Zeng, W. (2017b). Room-temperature gas sensing of ZnO-based gas sensor: a review. *Sens. Actuat. A* 267, 242–261. doi: 10.1016/j.sna.2017.10.021

Conflict of Interest Statement: The authors declare that the research was conducted in the absence of any commercial or financial relationships that could be construed as a potential conflict of interest.

frontiers in Chemistry

DATA REPORT
published: 09 August 2018
doi: 10.3389/fchem.2018.00337

SnO_2/Graphene Nanoplatelet Nanocomposites: Solid-State Method Synthesis With High Ethanol Gas-Sensing Performance

Run Zhang [1,2], Jian-Bo Jia [1,2], Jian-Liang Cao [1,2] and Yan Wang [1,3]**

[1] The Collaboration Innovation Center of Coal Safety Production of Henan Province, Henan Polytechnic University, Jiaozuo, China, [2] Department of Chemical Engineering and Technology, College of Chemistry and Chemical Engineering, Henan Polytechnic University, Jiaozuo, China, [3] School of Safety Science and Engineering, State Key Laboratory Cultivation Base for Gas Geology and Gas Control, Henan Polytechnic University, Jiaozuo, China

Keywords: Graphene nanoplatelet, SnO_2 nanoparticles, nanocomposites, ethanol, sensitivity

OPEN ACCESS

Edited by:
Wen Zeng,
Chongqing University, China

Reviewed by:
Akihiro Kushima,
University of Central Florida, United States
Arshad Saleem Bhatti,
COMSATS Institute of Information Technology, Pakistan

***Correspondence:**
Jian-Bo Jia
jiajianbo@hpu.edu.cn
Yan Wang
yanwang@hpu.edu.cn

Specialty section:
This article was submitted to Nanoscience, a section of the journal Frontiers in Chemistry

Received: *29 May 2018*
Accepted: *19 July 2018*
Published: *09 August 2018*

Citation:
Zhang R, Jia J-B, Cao J-L and Wang Y (2018) SnO_2/Graphene Nanoplatelet Nanocomposites: Solid-State Method Synthesis With High Ethanol Gas-Sensing Performance. Front. Chem. 6:337. doi: 10.3389/fchem.2018.00337

INTRODUCTION

Graphene nanoplatelet (GNP) is a well-known 2D carbon nanomaterial composed of network structure of sp^2-hybridized carbon atoms. So far, two main strategies (exfoliation and chemical oxidation-reduction) have been used for the preparation of GNP from graphite. Unfortunately, a lot of defects are caused by the strong oxidizing reagents on the GNP produced by chemical oxidation-reduction method, and such GNP lost the remarkable electrical and mechanical properties (Coleman, 2013). Exfoliation method could be adopted to product high-quality GNP from graphite, but the yield of GNP is quite low (∼1 wt.%) (Hernandez et al., 2008). Hence, the requisite large scale production of high-quality GNP remains a challenging task.

Even so, GNP is expected as a promising material for gas sensing due to its unrivaled physiochemical and electronic properties such as excellent flexibility, large specific surface area and high conductivity. Nevertheless, owing to the poor gas-sensing selectivity, GNP exhibited responses to several kinds of gas (Yoon et al., 2012; Nemade and Waghuley, 2013). But when GNP was incorporated with other sensor materials, like metal oxide semiconductors (MOSs), it could remarkably improve the sensing performance of the sensor materials (Eom et al., 2017; Thu et al., 2018). The MOSs phase facilitates the adsorption/desorption process of tested gas, thereby activating the reactions occurring on the carbon surface, which in turn increases the response speed and response/recovery time. In addition, n-p junctions can be formed by GNP with n-type metal oxides, and the resulting novel nanostructures perform much better gas sensing performance than single materials (Neri et al., 2013).

As an n-type metal oxide semiconductor, tin dioxide (SnO_2) has a wide band gap of Eg = 3.6 eV and excellent optical and electrical properties. SnO_2 have been one of the most extensive studied materials due to its wide applications including in transparent conductive electrodes and transistors (Liu et al., 2018; Satoh et al., 2018), lithium-ion batteries (Zhao et al., 2016; Shi et al., 2017), dye-sensitized solar cells (Hagfeldt et al., 2010), photocatalysis (Aslam et al., 2018; Praus et al., 2018) and gas sensors (Narjinary et al., 2017; Long et al., 2018; Xu et al., 2018). For gas sensing application, SnO_2 and SnO_2 based composites also show admirable gas sensing properties like low-cost, low detection limit, fast response and recovery, high response and good stability (Yan et al., 2015; Cao et al., 2017; Kim et al., 2017).

Herein, we put forward a simple and potentially scalable method to obtaining massive high-quality GNP from exfoliation of flake graphite in K_2FeO_4/H_2SO_4, and use the solid-state method to synthesize SnO_2 decorated graphene nanoplatelet nanocomposites

(SnO_2/GNP) with different mass ratio of SnO_2 and GNP. The as-prepared SnO_2/GNP nanocomposites possess the two-dimensional (2D) structure, and the 2D GNP accelerating the preferential growth and preventing the agglomeration of the SnO_2 nanoparticles. The gas sensing tests indicated that the sensors based on GNP/SnO_2 nanocomposites possess high sensitivity and excellent characteristic of response and recovery toward ethanol vapor. The sensor response was found to be dependent on the mass ratio of GNP in the composites and it reaches the maximum response when the mass percentage of GNP in the composites is 5%.

EXPERIMENTAL

Preparation of the GNP/SnO_2 Nanocomposites

All the reagents were of analytical grade (AR) and used as received without further purification. The preparation of GNP was listed in the **Supplementary Material**. A typical synthesis process of GNP/SnO_2 nanocomposites with 5 wt.% GNP content can be described as follows: 7 g of $SnCl_4 \cdot 5H_2O$, 0.15 g of GNP and 6 ml of PEG-400 were mixed adequately and ground together in an agate mortar. Subsequently, 3.2 g of NaOH was slowly added to the mixtures and ground together for about 30 min. The reaction started readily during the addition process of NaOH, accompanied by release of heat. As the reaction proceeded, the mixture became mushy. Then samples were collected, washed several times with distilled water and absolute ethanol, and dried at 60°C overnight in a drying oven. Finally, the product was ground to powder, marked as GNP/SnO_2-5. 2.5 and 7.5 wt.% GNP of GNP/SnO_2 nanocomposites were prepared using the aforementioned method, and marked as GNP/SnO_2-2.5 and GNP/SnO_2-7.5, respectively. For comparison, the same method was used to synthesize SnO_2 nanoparticles without GNP.

The characterization, sensor fabrication and measurement (**Figure S1**) were listed in the Supplementary Material.

RESULTS AND DISCUSSION

The XRD diffraction pattern of GNP is almost identical to that of pristine graphite (**Figure 1A**), revealing that no structural change occurred during the exfoliating process. The intensity of (002) peak centered at 26.5° of GNP decreases obviously compared with that of pristine graphite due to the ultrathin thickness of GNP (Zhang et al., 2016). The XRD diffraction patterns of pure SnO_2 nanoparticles and GNP/SnO_2 nanocomposites are shown in **Figure 1B**. We can see that four distinct diffraction peaks of SnO_2 centered at 2θ of 26.6°, 33.9°, 51.7°, and 65.9°, which are corresponding to the reflection from the (110), (101), (211), and (301) planes of the tetragonal rutile SnO_2 (JCPDS Card No. 41-1445), respectively. This confirmed that the synthesis method that SnO_2 was successfully prepared by solid-state reaction is feasible and complete. However, as seen from **Figure 1B**, there are no diffraction peak around 26.6° of SnO_2 observed in the curves, because the diffraction peaks of 26.5° of GNP is so high that the peak around 26.6° of SnO_2 is covered.

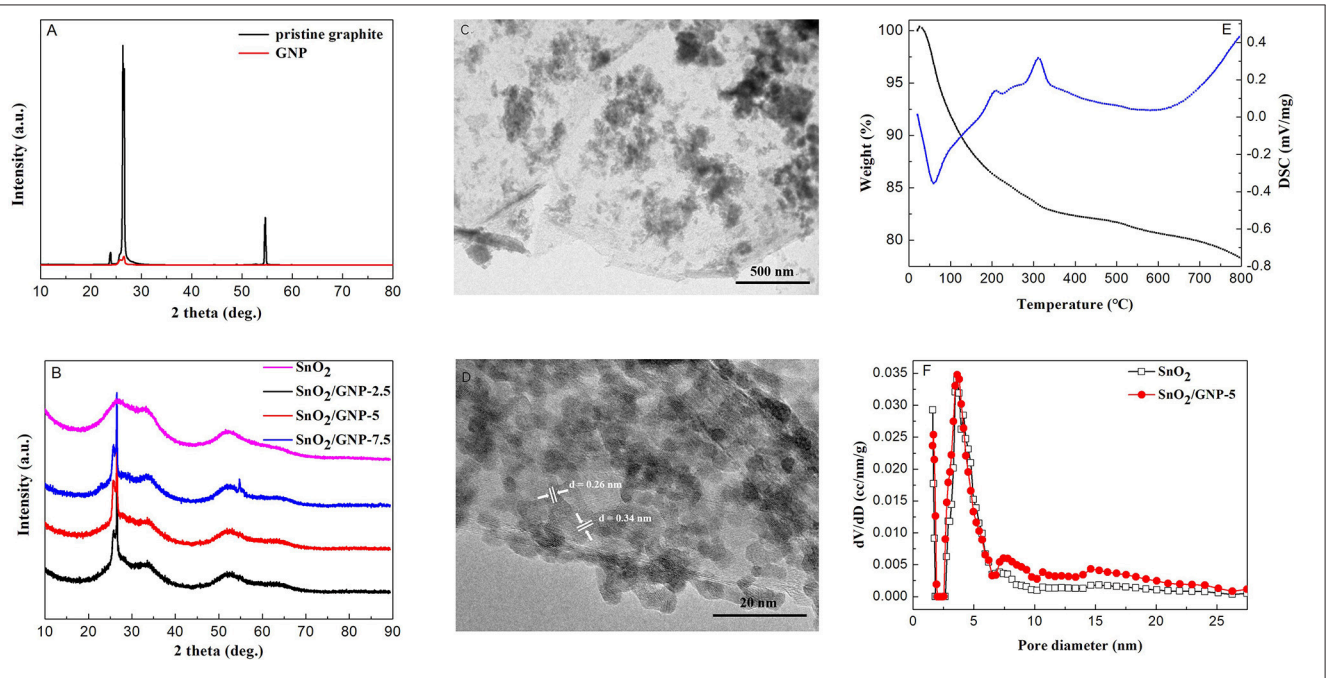

FIGURE 1 | (A) XRD patterns of pristine graphite and GNP. **(B)** XRD patterns of SnO_2 and the SnO_2/GNP nanocomposites with different GNP contents. **(C,D)** TEM and HRTEM images of the SnO_2/GNP-5 nanocomposite. **(E)** TG-DSC profiles of the SnO_2/GNP-5 nanocomposites. **(F)** The pore size distribution curves of the SnO_2 and SnO_2/GNP-5 nanocomposite.

Figure S2a shows the representative FESEM image of pristine graphite. In **Figure S2b** (FESEM image of GNP), two-dimensional (2D) structure of the thin layers can be seen clearly. As shown in **Figure S2c**, the FESEM image of the pure SnO_2 exhibits particles with the size of 100–200 nm. The FESEM and TEM images of the GNP/SnO_2-5 nanocomposite are presented in **Figure S2d** and **Figure 1C**, respectively, and which show that numerous particles are dispersed on the surface of 2D sheets of GNP. Meanwhile, as can be seen from **Figure 1D**, two phases of GNP and SnO_2 are clearly observed and closely in contact to form an intimate interface. And, the lattice fringes with interplanar spacings of 0.26 nm and 0.34 nm can be corresponding to the (101) and (110) planes of SnO_2 nanoparticles. It can be concluded that the GNP/SnO_2 composites were synthesized successfully using the solid-state method.

TG-DSC analysis revealed the weight change situation of GNP/SnO_2-5 nanocomposites from room temperature to 800°C with the heating rate of $10^{\circ}\cdot min^{-1}$. As is shown in **Figure 1E**, there are two stages of weight loss in the TG curve according to the peaks of DSC curve. The first stage in temperature before 300°C is due to desorption of moisture and solvent. The second stage of weight loss is due to the combustion of GNP in air. This result proves that the GNP/SnO_2-5 nanocomposite was not decomposed at the operating temperature of 280°C in the procedure of measuring gas-sensing properties.

Figure 1F displays the pore diameter distribution of the SnO_2 and GNP/SnO_2-5 samples. It can be clearly seen that the pore diameters of pure SnO_2 and GNP/SnO_2-5 are relatively small, which both the majority concentrate on about 2 nm and 4 nm. The specific surface areas of GNP/SnO_2-5 sample is 167.01 $m^2\cdot g^{-1}$, which is higher than SnO_2 (119.67 $m^2\cdot g^{-1}$). Increasing specific surface area could be in favor of enhancing gas-sensing properties.

Figure 2A shows the response values of pure SnO_2 nanoparticles-based sensor and GNP/SnO_2-based sensors to 500 ppm of ethanol at different temperatures. From the curves of GNP/SnO_2-2.5, GNP/SnO_2-5, and GNP/SnO_2-7.5, it can be clearly observed that the response values increased with the increase of the temperature. However, the response values decrease when the temperature is above 280°C. As a result, the best operating temperature of GNP/SnO_2-based sensors is 280°C. Similarly, the best operating temperature of pure SnO_2 sensors is 300°C. We can get a conclusion that the best operating temperature is lowered 20°C because of the joining of GNP. Compared between the different curves, it reaches the maximum response when the mass percentage of GNP in the composites is 5%. The response value of GNP/SnO_2-7.5 sample is lower than that of the GNP/SnO_2-5 sample. It is because that activation center still focuses on the SnO_2 nanoparticle, and the high content of GNP may lead to the decrease of SnO_2 nanoparticle on the unit specific surface area. Some SnO_2-based materials of ethanol sensing from the literature are summarized in **Table S1**. It can be observed that the GNP/SnO_2 composite exhibits superior performances compared with other SnO_2-based materials.

Figure S3 displays the response values of sensors based on pure SnO_2 and GNP/SnO_2-5 to different concentrations of ethanol at 280°C. As shown in the curves, the response values of the two sensors increased with the increasing of ethanol concentrations in the range of 50–2,000 ppm. We can find its regularity through a large number of relevant experiments to establish the relationship between response value and concentration of ethanol. From comparison of two curves, a gradual enhancement in response amplitude was observed for both sensors, and the response amplitudes of GNP/SnO_2-5 based sensor are always higher than that of pure SnO_2, demonstrating its better sensitivity to ethanol.

It is well known that selectivity is another key criterion for measuring the quality of gas sensors. **Figure 2B** shows the selectivity test results of the pure SnO_2 and GNP/SnO_2-5 sensors to five different gases of 500 ppm, including methanol, ethanol, methylbenzene, glycerine and methanal. It can be observed that the GNP/SnO_2-5-based sensor has good selectivity to ethanol compared to that of pure SnO_2 sensor at 280°C. The higher response to ethanol may be because ethanol is more likely to lose electrons in the process of a redox reaction with the absorbed oxygen, and the hydroxyl group (–OH) is much easier to oxidize at the optimum operating temperature.

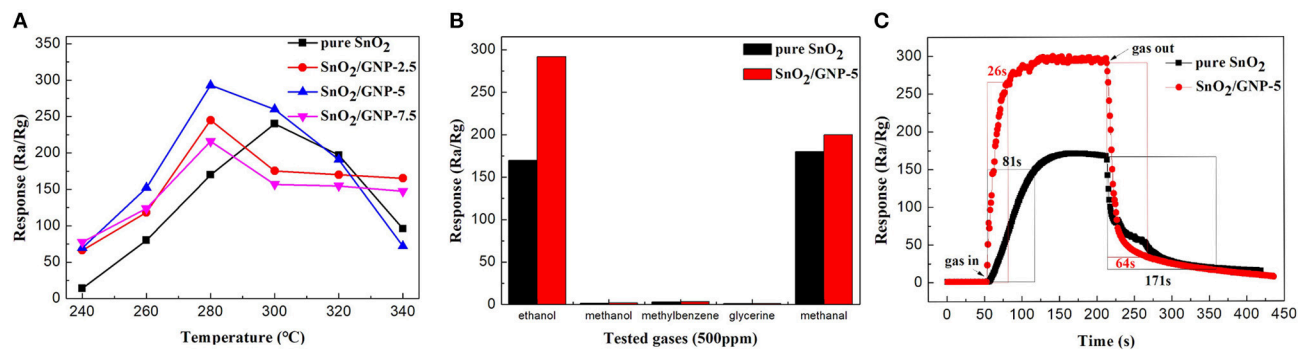

FIGURE 2 | (A) The response values of SnO_2, SnO_2/GNP-2.5, SnO_2/GNP-5, and SnO_2/GNP-7.5 sensors toward 500 ppm of ethanol at different working temperatures. **(B)** The responses of sensors (SnO_2 and SnO_2/GNP-5) operated at 280°C in 500 ppm of different gases. **(C)** The response-recovery curve of SnO_2 and SnO_2/GNP-5 toward 500 ppm of ethanol at 280°C.

The response–recovery time curve of GNP/SnO_2-5-based sensor to 500 ppm of ethanol is shown in **Figure 2C**. Response and recovery time are defined as change in the resistances from Ra to [Ra−90% × (Ra – Rg)] for gas-in and [Ra + 90% × (Ra – Rg)] to gas-out, respectively (Zhang S.S. et al., 2018; Zhang Y.J. et al., 2018). It can be clearly observed that the response increased and decreased quickly when the GNP/SnO_2-5-based sensor was exposed to and separated from ethanol, respectively. The response time and the recovery time of GNP/SnO_2-5-based sensor are 26 and 64 s, respectively, which are much shorter than of the pure SnO_2-based sensor that are 81 and 171 s. The relatively rapid response and recovery time could be due to the unique structure, which is the SnO_2 nanoparticles are decorated on the 2D sheet of GNP. This indicates that the large specific surface area is favorable to the adsorption of ethanol, which verifies the above conjecture. **Figure S4** depicts the response values of GNP/SnO_2-5-based sensor to 500 ppm of ethanol for every 3 days in 30 days at 280°C, which fall slightly but are maintained around 295. Therefore, the conclusion could be obtained that the GNP/SnO_2-5-based gas sensor to ethanol has a satisfactory stability, which confirms that the sensor might have a practical application.

CONCLUSION

In conclusion, we reported an easy method to successfully prepare massive high-quality GNP from exfoliation of flake graphite, and GNP/SnO_2 nanocomposites were successfully synthesized by a facile solid-state method. The 2D GNP has no structural change during the exfoliating process from flake graphite, and the SnO_2 nanoparticles were highly distributed on the surface of GNP. The GNP/SnO_2 based sensor showed excellent gas sensing performance toward ethanol, and the ameliorative gas-sensing properties may be due to the accrescent specific surface area and the interaction between 2D GNP and SnO_2 nanoparticles. Due to the procedure is convenient and environment-friendly, and good gas sensing property of the SnO_2/GNP nanocomposite, it could be a promising candidate for ethanol detection.

AUTHOR CONTRIBUTIONS

RZ performed the experiments and analyzed the data with the help from J-LC. J-BJ and YW conceived the study. All authors discussed the results and wrote the manuscript.

FUNDING

This work was supported by the National Natural Science Foundation of China (U1704146, U1704255), Program for Science & Technology Innovation Talents in Universities of Henan Province (19HASTIT042), the Research Foundation for Youth Scholars of Higher Education of Henan Province (2016GGJS-040, 2017GGJS-053), the Fundamental Research Funds for the Universities of Henan Province (NSFRF1606, NSFRF170201) and Program for Innovative Research Team of Henan Polytechnic University (T2018-2).

SUPPLEMENTARY MATERIAL

The Supplementary Material for this article can be found online at: https://www.frontiersin.org/articles/10.3389/fchem.2018.00337/full#supplementary-material

REFERENCES

Aslam, M., Qamar, M. T., Ali, S., Rehman, A. U., Soomro, M. T., Ahmed, I., et al. (2018). Evaluation of SnO_2 for sunlight photocatalytic decontamination of water. *J. Environ. Manage.* 217, 805–814. doi: 10.1016/j.jenvman.2018.04.042

Cao, J., Qin, C., Wang, Y., Zhang, B., Gong, Y., and Zhang, H. L. (2017). Calcination method synthesis of SnO_2/g-C_3N_4 Composites for a high-performance ethanol gas sensing application. *Nanomaterials* 7:98. doi: 10.3390/nano7050098

Coleman, J. N. (2013). Liquid exfoliation of defect-free graphene. *Acc. Chem. Res.* 46, 14–22. doi: 10.1021/ar300009f

Eom, N., Cho, H. B., Song, Y., Lee, W., Sekino, T., and Choa, Y. H. (2017). Room-Temperature H2 gas sensing characterization of graphene-doped porous silicon via a facile solution dropping method. *Sensors* 17:2750. doi: 10.3390/s17122750

Hagfeldt, A., Boschloo, G., Sun, L. C., Kloo, L., and Pettersson, H. (2010). Dye-sensitized solar cells. *Chem. Rev.* 110, 6595–6663. doi: 10.1021/cr900356p

Hernandez, Y., Nicolosi, V., Lotya, M., Blighe, F. M., Sun, Z., De, S., et al. (2008). High-yield production of graphene by liquid-phase exfoliation of graphite. *Nat. Nanotechnol.* 3, 563–568. doi: 10.1038/nnano.2008.215

Kim, H. W., Na, H. G., Kwon, Y. J., Kang, S. Y., Choi, M. S., Bang, J. H., et al. (2017). Microwave-Assisted synthesis of graphene–SnO_2 Nanocomposites and their applications in gas sensors. *ACS Appl. Mater. Interf.* 9, 31667–31682. doi: 10.1021/acsami.7b02533

Liu, X., Ning, H., Chen, W., Fang, Z., Yao, R., Wang, X., et al. (2018). Effect of Source/Drain Electrodes on the Electrical Properties of Silicon-Tin Oxide Thin-Film Transistors. *Nanomaterials* 8, 293–300. doi: 10.3390/nano8050293

Long, H., Zeng, W., Wang, H., Qian, M., Liang, Y., and Wang, Z. (2018). Self-Assembled Biomolecular 1D Nanostructures for Aqueous Sodium-Ion Battery. *Adv. Sci.* 5, 1700634–1700637. doi: 10.1002/advs.201700634

Narjinary, M., Rana, P., Sen, A., and Pal, M. (2017). Enhanced and selective acetone sensing properties of SnO_2-MWCNT nanocomposites: Promising materials for diabetes sensor. *Mater. Des.* 115, 158–164. doi: 10.1016/j.matdes.2016.11.042

Nemade, K. R., and Waghuley, S. A. (2013). Chemiresistive Gas Sensing by Few-Layered Graphene. *J. Electron. Mater.* 42, 2857–2866. doi: 10.1007/s11664-013-2699-4

Neri, G., Leonardi, S. G., Latino, M., Donato, N., Baek, S., Conte, D. E., et al. (2013). Sensing behavior of SnO_2/reduced graphene oxide nanocomposites toward NO_2. *Sens. Actuators B* 179, 61–68. doi: 10.1016/j.snb.2012.10.031

Praus, L., Svoboda, L., Dvorský, R., and Reli, M. (2018). Nanocomposites of SnO_2 and g-C_3N_4: preparation, characterization and photocatalysis under visible LED irradiation. *Ceram. Int.* 44, 3837–3846. doi: 10.1016/j.ceramint.2017.11.170

Satoh, K., Murakami, S., Kanaoka, Y., Yoshiharu, Y., Kakehi, Y., Sakurai, Y., et al. (2018). Effect of postannealing on properties of ZnO-SnO_2 thin film transistors. *J. Vac. Sci. Technol. A* 36:02C105. doi: 10.1116/1.5003283

Shi, Y., Ma, D., Wang, W., Zhang, L., and Xu, X. (2017). A supramolecular self-assembly hydrogel binder enables enhanced cycling of SnO_2-based anode for high-performance lithium-ion batteries. *J. Mater. Sci.* 52, 3545–3555. doi: 10.1007/s10853-016-0623-z

Thu, N. T. A., Cuong, N. D., Le, C. N., Khieu, D. Q., Nam, P. C., Toan, N. V., et al. (2018). Fe_2O_3 nanoporous network fabricated from Fe_3O_4/reduced

graphene oxide for high-performance ethanol gas sensor. *Sens. Actuators B* 255, 3275–3283. doi: 10.1016/j.snb.2017.09.154

Xu, S., Zhao, H., Xu, Y., Xu, R., and Lei, Y. (2018). Carrier Mobility-Dominated Gas Sensing: A Room-Temperature Gas-Sensing Mode for SnO_2 Nanorod Array Sensors. *ACS Appl. Mater. Interfaces*. 10, 13895–13902. doi: 10.1021/acsami.8b03953

Yan, H., Song, P., Zhang, S., Yang, Z., and Wang, Q. (2015). Dispersed SnO_2 nanoparticles on MoS_2 nanosheets for superior gas-sensing performances to ethanol. *RSC Adv.* 5, 79593–79599. doi: 10.1039/C5RA15019A

Yoon, H. J., Jun, D. H., Yang, J. H., Zhou, Z., Yang, S. S., and Cheng, M. C. (2012). Carbon dioxide gas sensor using a graphene sheet. *Sens. Actuators B* 157, 310–313. doi: 10.1016/j.snb.2011.03.035

Zhang, M., Liu, L., He, T., Wu, G., and Chen, P. (2016). Melamine assisted solid exfoliation approach for the synthesis of few-layered fluorinated graphene nanosheets. *Mater. Lett.* 171, 191–194. doi: 10.1016/j.matlet.2016.02.042

Zhang, S. S., Sun, G., Li, Y., Zhang, B., Lin, L., Wang, Y., et al. (2018). Continuously improved gas-sensing performance of SnO_2/Zn_2SnO_4 porous cubes by structure evolution and further NiO decoration. *Sens. Actuators B* 255, 2936–2943. doi: 10.1016/j.snb.2017.09.114

Zhang, Y. J., Zeng, W., and Lin, Y. Q. (2018). Hydrothermal synthesis and controlled growth of hierarchical 3D flower-like MoS_2 nanospheres assisted with CTAB and their NO_2 gas sensing properties.*Appl. Surf. Sci.* 455, 276–282. doi: 10.1016/j.apsusc.2018.05.224

Zhao, K., Zhang, L., Xia, R., Dong, Y., Xu, W., Niu, C., et al. (2016). SnO_2 Quantum Dots@Graphene Oxide as a High-Rate and Long-Life Anode Material for Lithium-Ion Batteries. *Small* 2, 588–594. doi: 10.1002/smll.201502183

Conflict of Interest Statement: The authors declare that the research was conducted in the absence of any commercial or financial relationships that could be construed as a potential conflict of interest.

frontiers in Chemistry

DATA REPORT
published: 30 May 2018
doi: 10.3389/fchem.2018.00194

Hydrothermal Synthesis of Hierarchical Ultrathin NiO Nanoflakes for High-Performance CH_4 Sensing

Qu Zhou [1,2], Zhaorui Lu [1], Zhijie Wei [1], Lingna Xu [1], Yingang Gui [1] and Weigen Chen [2]*

[1] College of Engineering and Technology, Southwest University, Chongqing, China, [2] State Key Laboratory of Power Transmission Equipment & System Security and New Technology, Chongqing University, Chongqing, China

Keywords: hydrothermal synthesis, ultrathin NiO nanoflakes, methane, gas sensor, sensing performances

OPEN ACCESS

Edited by:
Zhenyu Li,
Deakin University, Australia

Reviewed by:
Fuping Zeng,
Wuhan University, China
Peng Li,
King Abdullah University of Science and Technology, Saudi Arabia

****Correspondence:***
Qu Zhou
zhouqu@swu.edu.cn

Specialty section:
This article was submitted to Nanoscience, a section of the journal Frontiers in Chemistry

Received: *19 April 2018*
Accepted: *14 May 2018*
Published: *30 May 2018*

Citation:
Zhou Q, Lu Z, Wei Z, Xu L, Gui Y and Chen W (2018) Hydrothermal Synthesis of Hierarchical Ultrathin NiO Nanoflakes for High-Performance CH_4 Sensing. Front. Chem. 6:194. doi: 10.3389/fchem.2018.00194

INTRODUCTION

Methane (CH_4), as a colorless and odorless gas, is the main component of natural gas and widely used in various industries and human daily life (Schoonbaert et al., 2015). However, the leakage of natural gas, oil and gas storage, transportation and distribution systems increase atmospheric CH_4 concentration levels and lead to serious climate changes, which must be addressed (Zheng et al., 2017). Additionally, CH_4 will be easy to explode in a range of concentration (5–15%). Therefore, it is necessary to develop rapid and accurate gas sensors for CH_4 detection.

Nickel oxide NiO (Sun et al., 2014) is a significant p-type semiconductor, and has been widely used as catalyst (Yu et al., 2015), lithium-ion battery (Gu et al., 2016; Long et al., 2018), gas sensor (Wang et al., 2016; Zhou et al., 2018b), magnetic material (Cui et al., 2011), and so on. In recent years, many researchers have reported that NiO can be applied to fabricate high performance gas sensors for detecting some special gases such as hydrogen (Sta et al., 2016), NO_2 (Hoa and El-Safty, 2011), ethanol (Miao et al., 2017), etc. Zhang et al. studied a methane gas sensor based on nickel oxide (NiO)/reduced graphene oxide (rGO) nanocomposite film, which exhibited a response of 15% toward 1000 ppm CH_4 gas at 260°C (Zhang et al., 2016), and the sensing response of the pure NiO film sensor only was 2.5% under the same condition. Moreover, few reports about the synthesis of hierarchical NiO nanostructures and its application for CH_4 detection was reported recently.

Thus, in this study we reported the successful synthesis of hierarchical ultrathin NiO nanoflakes and systematically researched their gas sensing properties to CH_4. Interestingly, the proposed sensor exhibited high sensitivity, low optimal operating temperature, good linear relationship and excellent selectivity to CH_4.

EXPERIMENTAL DESIGN, MATERIALS, AND METHODS

Sample Synthesis

All raw chemicals used for the synthesis of hierarchical ultrathin NiO nanoflakes were analytical graded and used as received without further purifications. In a typical hydrothermal procedure, 3 mmol of nickel nitrate hexahydrate $Ni(NO_3)_2 \bullet 6H_2O$ and 0.200 g of polyvinylpyrrolidone (PVP) were dissolved in 100 mL DI deionized water under continuous stirring. After 15 min

of rigorous stirring, a few drops of NH4OH solution were added to the resultant solution to maintain the pH = 11. The mixture was stirred vigorously for 30 min and then transferred into a Teflon-lined stainless steel autoclave, sealed and heated to 180°C for 6 h. After cooling to room temperature naturally, the product was collected by centrifugation and washed with DI water and ethanol several times, respectively, and dried at 60°C overnight. Finally, the dried power was calcined at 400°C for 2 h.

Sample Characterization

The phase structure of the prepared products were characterized by X-ray diffraction (XRD) using a Rigaku D/Max-1200X diffractometry with Cu-Kα radiation operated at 30 KV and 100 mA. The morphologies, microstructures and elemental compositions of the synthesized samples were investigated with a Nova 400 Nano field emission scanning electronic microscopy (FE-SEM), equipped with an energy dispersive X-ray spectroscopy (EDS). Gas sensors were fabricated with the side heated structure (Zhou et al., 2018c) and gas sensing properties of the obtained sensors were performed with the CGS-8 (Chemical gas sensor-8) intelligent gas sensing analysis system (Beijing Elite Tech Co., Ltd., Beijing, China).

RESULTS

Materials Characterization

Figure 1A shows the XRD pattern of the synthesized NiO sample. As shown, all the primary diffraction peaks observed at 37.30°, 43.25°, 62.85°, 75.45°, and 79.20° could be well assigned to (111), (200), (220), (311), and (222) planes of the cubic form of NiO (JCPDS Card No. 47-1049). **Figure 1B** depicts the EDS spectrum of the prepared NiO sample. As demonstrated, only nickel (Ni) and oxygen (O) peaks are observed with O/Ni molar ratio of nearly 1:1. No other diffraction peaks from impurities and dispersive peaks related with any element were observed, indicating a high purity of the as-prepared hierarchical ultrathin NiO nanoflakes sample.

Figures 1C,D demonstrate the FESEM image of the synthesized hierarchical NiO nanostructures, which are constructed by many ultrathin nanoflakes with smooth surface. The diameter of the NiO nanoflakes is in the scope of 300 to 400 nm with thickness ranging from 10 to 15 nm.

Sensing Performances

The gas response of the fabricated side-heated sensor is defined as Rg/Ra, where Ra and Rg are the resistance values of the sensor in air and in the tested gas, respectively (Zeng et al., 2012; Zhou et al., 2018b). **Figure 2A** shows the relationship between the operating temperature and the gas response of the sensor to 30 ppm of CH_4 with working temperature ranging from 100 to 350°C. As can be seen, with the increase of the temperature, the sensing response increases at first and attains its maximum value, and then decreases rapidly with further increasing temperature. The optimum operating temperature of the sensor to CH_4 is measured to be about 225°C, lower than some already reported results (Zhang et al., 2016), and the corresponding response is 46.53.

Figure 2B illustrates the gas response of the sensor to various concentration of CH_4 ranging from 0.2 to 50 ppm at 225°C. It is apparent that the sensing response increases rapidly with increasing gas concentration and a good linear relationship

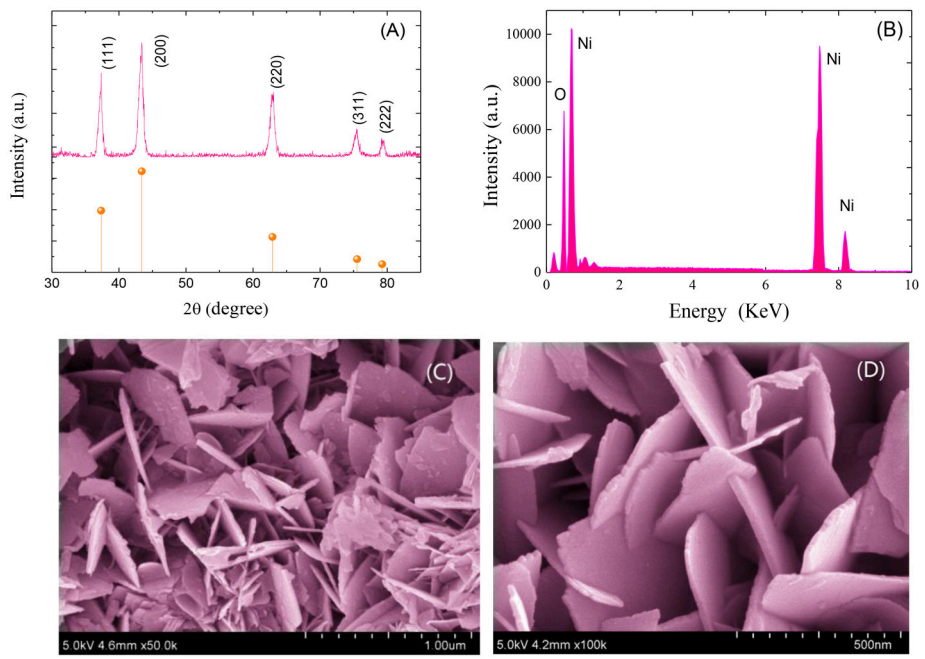

FIGURE 1 | XRD patterns **(A)**, EDS patterns **(B)** and FESEM images **(C,D)** of the synthesized hierarchical ultrathin NiO nanoflakes.

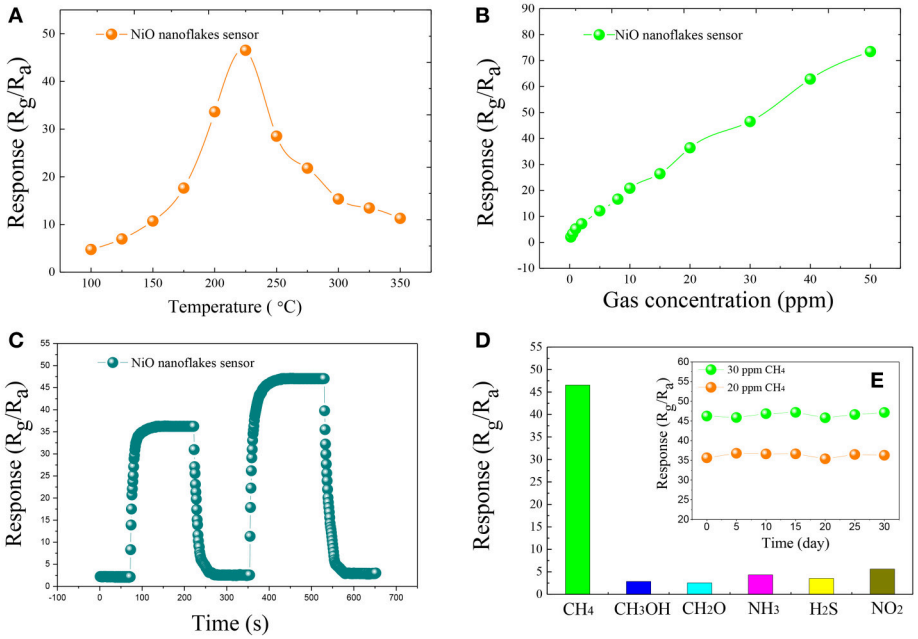

FIGURE 2 | The gas response of the synthesized NiO nanoflakes sensor toward 30 ppm of CH_4 at different working temperatures (100–350°C) **(A)**, gas response of the synthesized ultrathin NiO nanoflakes sensor to various concentration CH_4 in the range from 0.2 to 50 ppm at 225°C **(B)**, the response and recovery curves of the synthesized ultrathin NiO nanoflakes sensor to 20 and 30 ppm CH_4 at 225°C **(C)**, the response of NiO nanoflakes sensor toward 30 ppm of different testing gases at 225°C **(D)**, and the long-term stability of NiO nanoflakes sensor to 20 and 30 ppm CH_4 at 225°C **(E)**.

between the sensing response and gas concentration can be obtained, implying an effective candidate for low concentration CH_4 detection.

Figure 2C demonstrates the dynamic response and recovery curve of the as-prepared sensor to 20, 30 ppm CH_4 at 225°C. As illustrated, the sensor response increases dramatically when CH_4 gas was injected into the test chamber, and rapidly turns back to its initial state when subjected to air for sensor recovering. The time taken by the sensor to reach 90% of the total resistance change was defined as the response (recovery) time in the case of gas adsorption (desorption). According to this definition (Li et al., 2016; Zhang et al., 2018; Zhou et al., 2018a), the response and recovery time of the NiO sensor toward 30 ppm CH4 are calculated to be about 15 s and 20 s, respectively.

Figure 2D depicts the sensing response histogram of the NiO sensor to 30 ppm of various gases, including CH_3OH, CH_2O, NH_3, H_2S, and NO_2. It can be seen that the presented NiO sensor shows extremely high response to CH_4 than other potential interfering gases. The long-term stability of the sensor was also measured and shown in **Figure 2E**, inserted in **Figure 2D**, where the sensor response changes slightly and keeps at a nearly constant value during the long experimental cycles, implying an excellent longtime stability and repeatability of the sensor for CH_4 detection.

It is known to all that NiO is a typical p-type semiconducting material, and its sensing properties are predominantly controlled by the surface resistance (Wang et al., 2016). When the fabricated NiO nanoflakes sensor is exposed to air, oxygen molecules would capture free electrons to form chemisorbed oxygen in the form of O^-_{2ads}, O^-_{ads} and O^{2-}_{ads} absorbed on the sensor surface, increasing the number of electron holes of NiO surface and its conductivity. In CH_4 gas ambient, oxidation-reduction reactions would take place between the pre-adsorbed oxygen ions and CH_4 molecules, and then electrons are released back to NiO electron holes, resulting in a decreasing conductivity of the NiO nanoflakes sensor.

CONCLUSIONS

In summary, hierarchical ultrathin NiO nanoflakes were successfully synthesized via hydrothermal process and characterized by XRD, FESEM and EDS, for the purpose of fabricating highly sensitive CH_4 gas sensors. The diameter of the prepared NiO nanoflakes material is in the scope of 300 to 400 nm with thickness ranging from 10 to 15 nm. Side-heated gas sensor was fabricated with the synthesized ultrathin NiO nanoflakes and methane CH_4 sensing performances were systematically evaluated. The synthesized hierarchical ultrathin NiO nanoflakes sensor exhibited high sensitivity, low optimal operating temperature, rapid response and recovery time, excellent selectivity and stability to CH_4 gas. Moreover, good linear relationship between the sensing response and gas

concentration from 0.2 to 50 ppm was also obtained. All results indicate that the synthesized hierarchical ultrathin NiO nanoflakes may be a potential sensing material for fabricating high performance gas sensor for low concentration CH_4 detection.

AUTHOR CONTRIBUTIONS

QZ and ZL performed the experiments and analyzed the data with the help from ZW and YG. QZ and ZL wrote the manuscript with input from all authors. All authors read and approved the manuscript.

ACKNOWLEDGMENTS

This work has been supported in part by the National Natural Science Foundation of China (Nos. 51507144, 5127785), China Postdoctoral Science Foundation funded project (Nos. 2015M580771, 2016T90832) and the Chongqing Science and Technology Commission (CSTC) (No. cstc2016jcyjA0400).

REFERENCES

Cui, Y. F., Wang, C., Wu, S. J. G., Liu, Zhang, F. F., and Wang, T. M. (2011). Lotus-root-like NiO nanosheets and flower-like NiO microspheres: synthesis and magnetic properties. *CrystEngComm* 13, 4930–4934. doi: 10.1039/c1ce05389b

Gu, L. L., Xie, W. H., Bai, S. A., Liu, B. L., Xue, S., Li, Q., et al. (2016). Facile fabrication of binder-free NiO electrodes with high rate capacity for lithium-ion batteries. *Appl. Surf. Sci.* 368, 298–302. doi: 10.1016/j.apsusc.2016.01.270

Hoa, N. D., and El-Safty, S. A. (2011). Synthesis of mesoporous NiO nanosheets for the detection of toxic NO2 gas. *Chem. Eur. J.* 17, 12896–12901. doi: 10.1002/chem.201101122

Li, T. M., Zeng, W., Long, H. W., and Wang, Z. C. (2016). Nanosheet-assembled hierarchical SnO2 nanostructures for efficient gas-sensing applications. *Sens. Actuators B* 231, 120–128. doi: 10.1016/j.snb.2016.03.003

Long, H., Zeng, W., Wang, H., Qian, M. M., Liang, Y. H., and Wang, Z. C. (2018). Self-assembled biomolecular 1D nanostructures for aqueous Sodium-Ion battery. *Adv. Sci.* 5:1700634. doi: 10.1002/advs.201700634

Miao, R. Y., Zeng, W., and Gao, Q. (2017). Hydrothermal synthesis of novel NiO nanoflowers assisted with CTAB and SDS respectively and their gas-sensing properties. *Mater. Lett.* 186, 175–177. doi: 10.1016/j.matlet.2016.09.127

Schoonbaert, S. B., Tyner, D. R., and Johnson, M. R. (2015). Remote ambient methane monitoring using fiber-optically coupled optical sensors. *Appl. Phys. B* 119, 133–142. doi: 10.1007/s00340-014-6001-0

Sta, I., Jlassi, M., Kandyla, M., Hajji, M., Koralli, P., Krout, F., et al. (2016). Surface functionalization of solegel grown NiO thin films with palladium nanoparticles for hydrogen sensing. *Int. J. Hydrogen Energ.* 41, 3291–3298. doi: 10.1016/j.ijhydene.2015.12.109

Sun, X., Liu, Y. X., Gao, H. Y., Gao, P. X., and Lei, X. (2014). Bimodular high temperature planar oxygen gas sensor. *Front. Chem.* 2:57. doi: 10.3389/fchem.2014.00057

Wang, J., Zeng, W., and Wang, Z. C. (2016). Assembly of 2D nanosheets into 3D flower-like NiO: synthesis and the influence of petal thickness on gas-sensing properties. *Ceram. Int.* 42, 4567–4573. doi: 10.1016/j.ceramint.2015.11.150

Yu, F., Xu, X. L., Peng, H. G., Yu, H. J., Dai, Y. F., Liu, W. M., et al. (2015). Porous NiO nano-sheet as an active and stable catalyst for CH4 deep oxidation. *App. Catal. A* 507, 109–118. doi: 10.1016/j.apcata.2015.09.023

Zeng, W., Liu, T. M., and Wang, Z. C. (2012). Enhanced gas sensing properties by SnO2 nanosphere functionalized TiO2 nanobelts. *J. Mater. Chem.* 22, 3544–3548. doi: 10.1039/c2jm15017d

Zhang, D. Z., Chang, H. Y., Li, P., and Liu, R. (2016). Characterization of nickel oxide decorated-reduced graphene oxide nanocomposite and its sensing properties toward methane gas detection. *J. Mater. Sci. Mater. El.* 27, 3723–3730. doi: 10.1007/s10854-015-4214-6

Zhang, Y. X., Zeng, W., Ye, H., and Li, Y. Q. (2018). Enhanced carbon monoxide sensing properties of TiO2 with exposed (001) facet: a combined first-principle and experimental study. *Appl. Surf. Sci.* 443, 507–516. doi: 10.1016/j.apsusc.2018.02.036

Zheng, C. T., Ye, W. L., Sanchez, N. P., Li, C. G., Dong, L., Wang, Y. D., et al. (2017). Development and field deployment of a mid-infrared methane sensor without pressure control using interband cascade laser absorption spectroscopy. *Sens. Actuators B* 244, 365–372. doi: 10.1016/j.snb.2016.12.146

Zhou, Q., Chen, W. G., Xu, L. N., Kumr, R., Gui, Y. G., Zhao, Z. Y., et al. (2018a). Highly sensitive carbon monoxide (CO) gas sensors based on Ni and Zn doped SnO2 nanomaterials. *Ceram. Int.* 44, 4392–4399. doi: 10.1016/j.ceramint.2017.12.038

Zhou, Q., Umar, A., Sodki, E. M., Amine, A., Xu, L. N., Gui, Y. G., et al. (2018b). Fabrication and characterization of highly sensitive and selective sensors based on porous NiO nanodisks. *Sens. Actuators B* 259, 604–615. doi: 10.1016/j.snb.2017.12.050

Zhou, Q., Xu, L. N., Umar, A., Chen, W. G., and Kumr, R. (2018c). Pt nanoparticles decorated SnO2 nanoneedles for efficient CO gas sensing applications. *Sens. Actuators B* 256, 656–664. doi: 10.1016/j.snb.2017.09.206

Conflict of Interest Statement: The authors declare that the research was conducted in the absence of any commercial or financial relationships that could be construed as a potential conflict of interest.

frontiers in Chemistry

DATA REPORT
published: 14 May 2018
doi: 10.3389/fchem.2018.00165

Enhanced H_2S Gas-Sensing Performance of Zn_2SnO_4 Lamellar Micro-Spheres

Ting-Ting Xu, Ying-Ming Xu, Xian-Fa Zhang, Zhao-Peng Deng, Li-Hua Huo and Shan Gao**

Key Laboratory of Functional Inorganic Material Chemistry, Ministry of Education, School of Chemistry and Materials Science, Heilongjiang University, Harbin, China

Keywords: Zn_2SnO_4, H_2S gas, ppb-level, lamellar micro-spheres, sensitivity

INTRODUCTION

With the rapid development of industry, the discharge of sulfide gas has been increasing in recent decades, which results in severe air pollution. H_2S, as the typical representation of sulfide, is a harmful and toxic acidic gas and widely used in various industries. Even at low concentrations, it can cause hypoxia and seriously threatens the safety of human. When the concentration reaches 1 mg/L (659 ppm) or higher, inflammation or death will occur. According to the U. S. Scientific Advisory Board on Toxic Air Pollutants, the acceptable concentration of H_2S in the environment is less than 83 ppb (North Carolina Department of Environment and Natural Resources, 2003[1]). Therefore, it is necessary to fabricate gas sensors which can detect ppb-level H_2S in time to reduce the environmental pollution and harm to human.

Zinc stannate (Zn_2SnO_4) is a typical n-type ternary semiconductor, and has been employed as important multifunctional material in the fields of photocatalytic activity (Das et al., 2017), solar cells (Li et al., 2015), lithium ion batteries (Lim et al., 2016), and so forth. Especially, owing to the excellent gas-sensing performance of ZnO and SnO_2 (Sukunta et al., 2017; Zhu and Zeng, 2017; Zhu et al., 2018), the application of Zn_2SnO_4 in the field of gas sensors has attracted extensive attention (An et al., 2015; Zhao et al., 2016; Yang et al., 2017). Up to now, only one case has concerned on the detection of H_2S with Zn_2SnO_4 hollow octahedron (Ma et al., 2012), which showed the response to H_2S with the detection limit being 1 ppm at 260°C. Meanwhile, such reported Zn_2SnO_4 sensor presents poor selectivity. Apparently, the sensor cannot satisfy the need of practical application for the detection of ppb-level H_2S, especially in a complex environment involving other interfering gases due to its poor selectivity and higher working temperature. In view of the fact that gas-sensing performance of materials is highly dependent on their micro-structure and surface state (Yu et al., 2017; Zhang et al., 2018), therefore, it would be a meaningful work to prepare Zn_2SnO_4 with novel morphology to further decrease the working temperature and improve the selectivity and stability, thus performing the detection of ppb-level H_2S.

In this work, Zn_2SnO_4 lamellar micro-spheres have been synthesized by a facile ethylenediamine-assisted hydrothermal method followed by calcining at 600°C. The diameter of micro-spheres is ∼1 μm and they are composed of nanosheets with thickness of ∼85 nm. The sensor fabricated from the micro-spheres shows good response and selectivity to H_2S at 170°C, and the lowest detection limit is down to 50 ppb. Moreover, it shows good linear relationship in the range of ppb (50–1000 ppb) and ppm (3–50 ppm) level. Meanwhile, the gas-sensing mechanism is also investigated.

[1]http://daq.state.nc.us/toxics/studies/H_2S/ (accessed 2003).

OPEN ACCESS

Edited by:
Wen Zeng,
Chongqing University, China

Reviewed by:
Jun Zhang,
Qingdao University, China
Liwu Zhang,
Fudan University, China

****Correspondence:***
Zhao-Peng Deng
dengzhaopeng@hlju.edu.cn
Shan Gao
shangao67@yahoo.com

Specialty section:
This article was submitted to Nanoscience, a section of the journal Frontiers in Chemistry

Received: *12 March 2018*
Accepted: *23 April 2018*
Published: *14 May 2018*

Citation:
Xu T-T, Xu Y-M, Zhang X-F, Deng Z-P, Huo L-H and Gao S (2018) Enhanced H_2S Gas-Sensing Performance of Zn_2SnO_4 Lamellar Micro-Spheres. Front. Chem. 6:165. doi: 10.3389/fchem.2018.00165

EXPERIMENTAL

Preparation of Zn_2SnO_4 Lamellar Micro-Spheres

All the reagent were analytical grade (AR) and used as received without supplementary purification. $Zn(CH_3COO)_2{\cdot}2H_2O$ (1.2 mmol) and $SnCl_4{\cdot}5H_2O$ (0.6 mmol) were dissolved in the mixture of 20 mL deionized water and 10 mL ethylenediamine. After stirring for 30 min, 7.2 mmol NaOH was added to the above system followed by further stirring for 1 h. Then, the above turbid solution was transferred into a 50 mL Teflon-lined stainless steel autoclave and kept at 200°C for 24 h. After cooling to room temperature, the precipitate was centrifuged and washed with deionized water and ethanol for several times. White products were obtained after drying at 60°C for 12 h, which was then calcined at 600°C for 2 h in air atmosphere to obtain the Zn_2SnO_4 lamellar micro-spheres.

The characterization, sensor fabrication and measurement were listed in the Supporting Information.

RESULTS AND DISCUSSION

The FT-IR spectra of the precursor and calcined product were illustrated in Figure S1a. After calcination, the corresponding vibrations of acetate disappear. The spectrum of calcined product exhibits one peak at 3417 cm^{-1}, corresponding to the stretching vibration of water molecules. The Sn-O and Zn-O vibrations at 572 and 431 cm^{-1} in this spectrum are slightly enhanced, which indicates that the calcined product has excellent crystallinity. The TG curve of the precursor (Figure S1b) shows that the marked weight loss of 6.27% between 30 and 600°C can be attributed to the loss of water molecules and small amount of acetates. After 600°C, no obvious weight loss occurs with the increase of temperature. Therefore, the precursor is calcined at 600°C for 2 h. The XRD patterns of the precursor and calcined product are also conducted to confirm their identity and phase purity. As illustrated in **Figure 1A**, all the diffraction peaks in both precursor and calcined product are consistent with standard cubic Zn_2SnO_4 (JCPDS Card No. 24-1470). In comparison with the precursor, the calcined product presents stronger diffraction peaks and better consistency. It shows that the calcined product has better crystallinity. The surface components of the calcined product characterized by XPS spectrum indicate that the final product involves Zn, Sn and O elements (Figure S2).

As shown in **Figure 1B**, the micro-spheres of the precursor with diameter of ∼1.5 μm are composed of smooth nanosheets with thickness of ∼130 nm. After being calcined at 600°C in air, the calcined products maintain the morphology of precursor, and the diameter of the micro-spheres is slightly decreased from ∼1.5 to ∼1 μm (**Figure 1C** and Figure S3). The thickness of the nanosheets is also sharply reduced to ∼85 nm. The results shown in Figure S4 reveal that the three elements are distributed very homogeneously in the micro-spheres. **Figure 1D** shows TEM image for the Zn_2SnO_4 lamellar micro-sphere which presents a clear contrast between the dark and the pale parts, revealing that the micro-spheres are further assembled by nanosheets. The high resolution TEM (HRTEM) image in **Figure 1E** exhibits the clear parallel fringes with *d*-spacing of 0.261 nm for nanosheet, which corresponds to the (311) lattice planes of cubic Zn_2SnO_4. Meanwhile, some micro-pores appears on the surface of the nanosheets, which implies better gas performance of the lamellar micro-spheres.

Figure 2A is the response of Zn_2SnO_4 lamellar micro-spheres sensor toward 100 ppm of H_2S at different working temperatures. As can be seen, the response of sensor to H_2S decreases with the increase of working temperature. This is mainly because the adsorbed H_2S gas molecules escaped from the surface of materials easily before the reaction taking place at high operating temperature so as to a poor response as well. In other word, such commonly observed phenomenon in resistive sensors is mainly ascribed to the fact that the desorption plays dominant role at higher temperature which leads to the decrease in sensitivity. It shows that the best working temperature for the Zn_2SnO_4 sensor is 170°C, which is 90°C lower than that of Zn_2SnO_4 hollow octahedron (Ma et al., 2012). Thus, the following tests were carried out at 170°C. **Figure 2B** is the response of the sensor toward 100 ppm of CH_4, NH_3, CH_3COCH_3, HCHO, C_2H_5OH and H_2S at 170°C. The responses to the above gases are 1.04, 1.49, 1.08, 1.2, 10.95, 65.13, respectively, which show that the sensor presents the best response to H_2S than other gases. The selectivity coefficients (K_{AB}) of H_2S to other gases are 62.63, 43.71, 60.31, 54.27, 5.94, respectively, indicating excellent selectivity of the sensor to H_2S. Such highly H_2S selectivity can be attributed to the reactivities of the reducing test gases. The bond energy of 381 kJ/mol for H-SH in H_2S (Liu et al., 2009) is smaller than other inorganic gases and most of organic gases, so that H-SH bond can be easily broken to participate in the reaction with gas sensor during chemical adsorption. Given all that, the sensor has good response and selectivity to H_2S at 170°C.

The relationship between the responses of the sensor and ppb-level concentrations of H_2S and the response-recovery characteristics of the sensor to different concentrations of H_2S at 170°C are shown in **Figure 2C**. The gas response of the sensor increases in a good linear relationship from 50 to 1000 ppb ($R^2 = 0.9986$), indicating that the detection limit of the sensor is 50 ppb (response of 1.29) to H_2S. In contrast to the reported Zn_2SnO_4 octahedron sensor (Ma et al., 2012), the present sensor displays lower working temperature and ppb-level detection limit. Even compared with other preferable ternary metal oxides, such as La_2NiO_4 particles (500°C, 20 ppb, Hao et al., 2018), $K_2W_4O_{13}$ nano-wires (300°C, 0.3 ppm, Supothina et al., 2014), $Fe_2(MoO_4)_3$ nano-particles and micro-spheres (300°C, 1 ppm, Liang et al., 2016), the present material still shows better sensing performance toward H_2S. To the best of our knowledge, the detection limit of Zn_2SnO_4 lamellar micro-spheres sensor is only slightly higher than that of flower-like Bi_2MoO_6 (Cui et al., 2017) which has the lowest detection limit of 0.1 ppb to H_2S. The response of the sensor in the range from 3 to 50 ppm also increases in a good linear relationship ($R^2 = 0.9927$) (Figure S5). The responses of the sensor to 10 ppm H_2S during 5 consecutive tests at 170°C is shown in Figure S6a. It shows that the sensor keeps its initial response amplitude after 5 cycles. The sensor measurement also maintains initial response to 10 ppm H_2S with the standard error of 4.9% after 60 days (Figure S6b). These

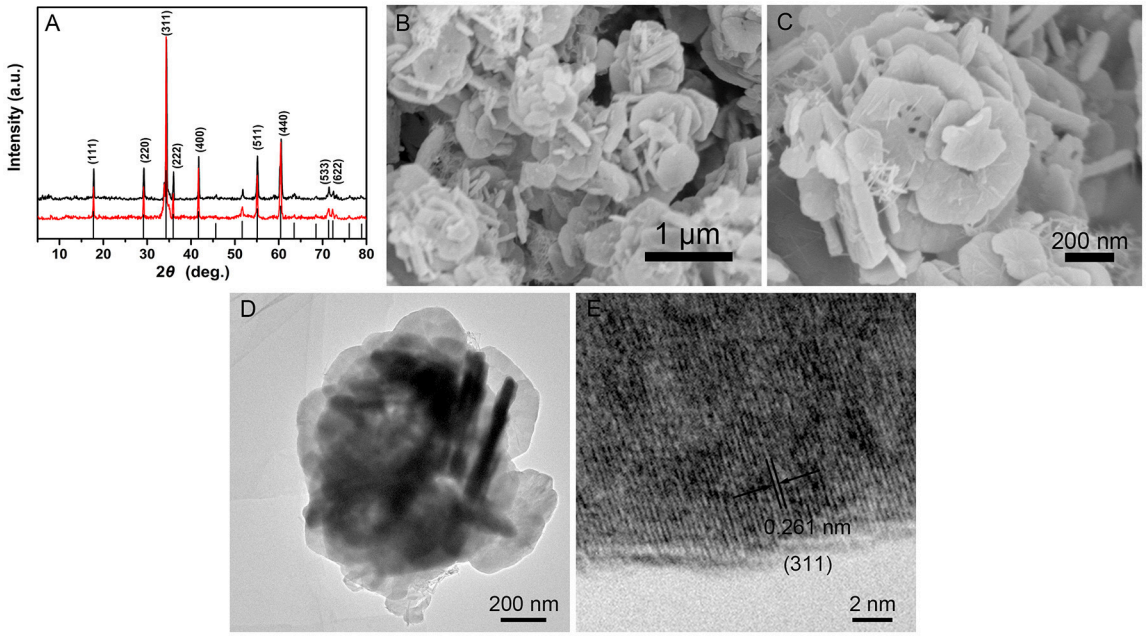

FIGURE 1 | (A) XRD patterns of the precursor and the calcined product. **(B,C)** SEM images of the calcined product. **(D,E)** TEM and HRTEM images of the calcined product.

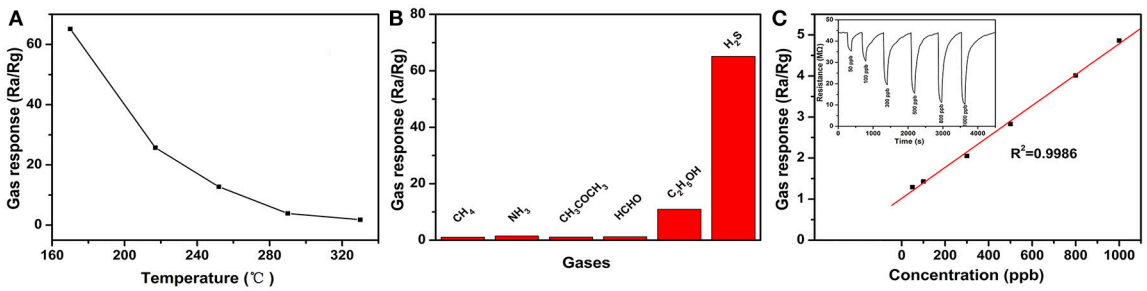

FIGURE 2 | (A) The response of Zn_2SnO_4 lamellar micro-spheres sensor toward 100 ppm of H_2S at different working temperatures. **(B)** The response of Zn_2SnO_4 hierarchical microspheres sensor toward 100 ppm of different testing gases at 170°C. **(C)** The relationship between the responses of Zn_2SnO_4 lamellar micro-spheres sensor and ppb-level concentrations of H_2S (Inset: the response-recovery characteristics of the sensor to different concentrations of H_2S at 170°C).

results indicate that this sensor has a satisfactory reproducibility and stability. Meanwhile, the influence of relative humidity on the sensor was considered at 170°C (Figure S7). It can be seen from Figure S7 that the sensor response has a small change from 1.2 to 1.4 in different humidity environment, suggesting that the influence of humidity on the sensor can be neglected at such temperature. Therefore, the present Zn_2SnO_4 lamellar micro-spheres sensor could be utilized as promising material for detecting ppb-level H_2S.

It is considered that the gas sensing property of semiconductor oxides is related to the surface adsorption oxygen, therefore, the chemical state changes of each element in the Zn_2SnO_4 sensor were analyzed before and after the sensor contacting with H_2S at 170°C. The results indicate that there is no change in the spectra of the Zn 2p and Sn 3d (Figure S8). As shown in Figures S9a,b, the O 1s spectra of Zn_2SnO_4 could be deconvoluted into three peaks at 531.9/531.8, 530.8/530.7, 529.4/529.3, corresponding to hydroxyl oxygen, surface adsorbed oxygen and lattice oxygen, respectively. The percentage of surface adsorbed oxygen drops from 30.04 to 27.01% after the sensor contacting with H_2S. The obvious decreasing of the adsorbed oxygen indicates that H_2S participates in redox reaction with the surface adsorbed oxygen. When the Zn_2SnO_4 sensor is exposed to H_2S at 170°C, the S 2p XPS spectrum displays three peaks at 168.9, 163.2 and 161.5 eV that correspond to SO_2 and sulfide (S $2p_{3/2}$ and S $2p_{1/2}$) (Figure S9c), respectively. The appearance of the three peaks indicates that H_2S is oxidized to SO_2. Combined with previous reports (Yu et al., 2015), the redox reaction engenders between H_2S and the surface adsorbed oxygen, and generates the product of SO_2.

Based on the aforementioned results, the gas sensing mechanism is speculated as follows: the resistance changes of the gas sensor are observed before and after contacting with H_2S. When the Zn_2SnO_4 sensor is exposed in air, oxygen molecules which is adsorbed on the surface of the sensor (Equation 1) captures electrons in conduction band of Zn_2SnO_4 to form of O^- at 170°C (Equation 2), and engender electron depletion layer. Then, after the sensor contacting with the H_2S, the H_2S is oxidized by the O^- on the surface of sensor and releases electrons back into the conduction band (Equations 3, 4), resulting in an increase in surface electrons and conductivity, and a decrease in resistance.

$$O_2(gas) \rightarrow O_2(ads) \quad (1)$$

$$O_2(ads) + 2e^- \rightarrow 2O^-(420 - 670\,K) \quad (2)$$

$$H_2S(gas) \rightarrow H_2S(ads) \quad (3)$$

$$H_2S(ads) + 3O^-(ads) \rightarrow SO_2 + H_2O + 3e^-(443\,K) \quad (4)$$

CONCLUSION

In conclusion, a facile ethylenediamine-assisted hydrothermal method followed by calcining at 600°C led to the formation of Zn_2SnO_4 lamellar micro-spheres which comprise of nanosheets with thickness of ∼85 nm. Such sensor exhibits excellent selectivity, sensitivity, humidity resistance and stability to H_2S at working temperature 170°C. The responses of the sensor, increased with the increasing concentrations in the range of 50–1000 ppb and 3–50 ppm exhibit good relationships with the detection limit of 50 ppb. These results indicate that the Zn_2SnO_4 lamellar micro-spheres could be utilized as promising sensor material for detecting ppb-level H_2S.

AUTHOR CONTRIBUTIONS

T-TX performed the experiments and analyzed the data with the help from Y-MX and X-FZ. Z-PD wrote the manuscript with input from all authors. L-HH and SG conceived the study. All authors read and approved the manuscript.

ACKNOWLEDGMENTS

This work is financial supported by Interational Science & Technology Cooperation Program of China (2016YFE0115100), the Project of Natural Science Foundation of Heilongjiang Province (No. B2015007), the Scientific and Technological Innovation Talents of Harbin (2016RAQXJ005), and the Young Innovation Talents of college in Heilongjiang Province (UNPYSCT-2016074). We thank the Key Laboratory of Functional Inorganic Material Chemistry, Ministry of Education, Heilongjiang University for supporting this study.

SUPPLEMENTARY MATERIAL

The Supplementary Material for this article can be found online at: https://www.frontiersin.org/articles/10.3389/fchem.2018.00165/full#supplementary-material

REFERENCES

An, D., Wang, Q., Tong, X., Zhou, Q., Li, Z., Zou, Y., et al. (2015). Synthesis of Zn_2SnO_4 via a co-precipitation method and its gas-sensing property toward ethanol. *Sens. Actuat. B* 213, 155–163. doi: 10.1016/j.snb.2015.02.042

Cui, X. L., Xu, Y. M., Zhang, X. F., Cheng, X. L., Gao, S., Zhao, H., et al. (2017). *In-situ* deposited flower-like Bi_2MoO_6 microspheres thin film based sensors for highly selective detection of ppb-level H_2S at low temperature. *Sens. Actuat. B* 247, 681–690. doi: 10.1016/j.snb.2017.03.100

Das, P. P., Roy, A., Tathavadekar, M., and Devi, P. S. (2017). Photovoltaic and photocatalytic performance of electrospun Zn_2SnO_4 hollow fibers. *Appl. Catal. B* 203, 692–703. doi: 10.1016/j.apcatb.2016.10.035

Hao, X. D., Ma, C., Yang, X., Liu, T., Wang, B., Liu, F. M., et al. (2018). YSZ-based mixed potential H_2S sensor using La_2NiO_4 sensing electrode. *Sens. Actuat. B* 255, 3033–3039. doi: 10.1016/j.snb.2017.09.127

Li, Z. D., Zhou, Y., Mao, W. T., and Zou, Z. G. (2015). Nanowire-based hierarchical tin oxide/zinc stannate hollow microspheres: enhanced solar energy utilization efficiency for dye-sensitized solar cells and photocatalytic degradation of dyes. *J. Power Sources* 274, 575–581. doi: 10.1016/j.jpowsour.2014.10.129

Liang, J. J., Zhuo, M., Guo, D., Chen, Z., Ren, W. J., Zhang, M., et al. (2016). Green and rapid synthesis of 3D $Fe_2(MoO_4)_3$ by microwave irradiation to detect H_2S gas. *Mater Lett.* 168, 171–175. doi: 10.1016/j.matlet.2016.01.048

Lim, Y. R., Jung, C. S., Im, H. S., Park, K., Park, J., Cho, W. I., et al. (2016). Zn_2GeO_4 and Zn_2SnO_4 nanowires for high-capacity lithium- and sodium-ion batteries. *J. Mater Chem. A* 4, 10691–10699. doi: 10.1039/C6TA02829B

Liu, Z., Fan, T., Zhang, D., Gong, X., and Xu, J. (2009). Hierarchically porous ZnO with high sensitivity and selectivity to H_2S derived from biotemplates. *Sens. Actuat. B* 136, 499–509. doi: 10.1016/j.snb.2008.10.043

Ma, G. X., Zou, R. J., Jiang, L., Zhang, Z. Y., Xue, Y. F., Yu, L., et al. (2012). Phase-controlled synthesis and gas-sensing properties of zinc stannate ($ZnSnO_3$ and Zn_2SnO_4) faceted solid and hollow microcrystals. *Cryst. Eng. Comm.* 14, 2172–2179. doi: 10.1039/c2ce06272k

Sukunta, J., Wisitsoraat, A., Tuantranont, A., Phanichphant, S., and Liewhiran, C. (2017). Highly-sensitive H_2S sensors based on flame-made V-substituted SnO_2 sensing films. *Sens. Actuat. B* 242, 1095–1107. doi: 10.1016/j.snb.2016.09.140

Supothina, S., Suwan, M., and Wisitsoraat, A. (2014). Hydrothermal synthesis of $K_2W_4O_{13}$ nanowire with high H_2S gas sensitivity. *Microelectron. Eng.* 126, 88–92. doi: 10.1016/j.mee.2014.06.015

Yang, H. M., Ma, S. Y., Jiao, H. Y., Chen, Q., Lu, Y., Jin, W. X., et al. (2017). Synthesis of Zn_2SnO_4 hollow spheres by a template route for high-performance acetone gas sensor. *Sens. Actuat. B* 245, 493–506. doi: 10.1016/j.snb.2017.01.205

Yu, T. T., Cheng, X. L., Zhang, X. F., Sui, L. L., Xu, Y. M., Gao, S., et al. (2015). Highly sensitive H_2S detection sensors at low temperature based on hierarchically structured NiO porous nanowall arrays. *J. Mater Chem. A* 3, 11991–11999. doi: 10.1039/C5TA00811E

Yu, Y., Xia, Y., Zeng, W., and Liu, R. (2017). Synthesis of multiple networked NiO nanostructures for enhanced gas sensing performance. *Mater Lett.* 206, 80–83. doi: 10.1016/j.matlet.2017.06.119

Zhang, Y., Zeng, W., Ye, H., and Li, Y. (2018). Enhanced carbon monoxide sensing properties of TiO_2 with exposed {001} facet: a combined first-principle and experimental study. *Appl. Surf. Sci.* 442, 507–516. doi: 10.1016/j.apsusc.2018.02.036

Zhao, Q., Ju, D., Song, X., Deng, X., Ding, M., Xua, X., et al. (2016). Polyhedral Zn_2SnO_4: synthesis, enhanced gas sensing and photocatalytic performance. *Sens. Actuat. B* 229, 627–634. doi: 10.1016/j.snb.2016.01.129

Zhu, L., Li, Y., and Zeng, W. (2018). Hydrothermal synthesis of hierarchical flower-like ZnO nanostructure and its enhanced ethanol gas-sensing properties. *Appl. Surf. Sci.* 427, 281–287. doi: 10.1016/j.apsusc.2017.08.229

Zhu, L., and Zeng, W. (2017). Room-temperature gas sensing of ZnO-based gas sensor: a review. *Sens. Actuat. A* 267, 242–261. doi: 10.1016/j.sna.2017.10.021

Conflict of Interest Statement: The authors declare that the research was conducted in the absence of any commercial or financial relationships that could be construed as a potential conflict of interest.

Advantages of publishing in Frontiers

OPEN ACCESS
Articles are free to read for greatest visibility and readership

FAST PUBLICATION
Around 90 days from submission to decision

HIGH QUALITY PEER-REVIEW
Rigorous, collaborative, and constructive peer-review

TRANSPARENT PEER-REVIEW
Editors and reviewers acknowledged by name on published articles

Frontiers
Avenue du Tribunal-Fédéral 34
1005 Lausanne | Switzerland

Visit us: www.frontiersin.org
Contact us: info@frontiersin.org | +41 21 510 17 00

REPRODUCIBILITY OF RESEARCH
Support open data and methods to enhance research reproducibility

DIGITAL PUBLISHING
Articles designed for optimal readership across devices

FOLLOW US
@frontiersin

IMPACT METRICS
Advanced article metrics track visibility across digital media

EXTENSIVE PROMOTION
Marketing and promotion of impactful research

LOOP RESEARCH NETWORK
Our network increases your article's readership